The Neutral Particle Detector on the Mars and Venus Express missions

Alexander Grigoriev

Swedish Institute of Space Physics

Kiruna

September 2007

Doctoral thesis at the Swedish Institute of Space Physics,
Kiruna, 2007
The Neutral Particle Detector on the Mars and Venus Express missions
Typeset by the author in LaTeX

IRF Scientific Report 290
ISSN 0284-1703
ISBN 978-91-7264-349-9
Printed at the Swedish Institute of Space Physics
Box 812, SE-981 28 Kiruna, Sweden
September 2007

Abstract

The Neutral Particle Detector (NPD) is a new type of instrumentation for energetic neutral atom (ENA) diagnostics. This thesis deals with development of the NPD sensor designed as a part of the plasma and neutral particle packages ASPERA-3 and ASPERA-4 on board Mars Express and Venus Express, the European Space Agency (ESA) satellites to Mars and Venus, respectively. It describes how the NPD sensors were designed, developed, tested and calibrated. It also presents the first scientific results obtained with NPD during its operation at Mars.

The NPD package consists of two identical detectors, NPD1 and NPD2. Each detector has a $9^\circ \times 90^\circ$ intrinsic field-of-view divided into three sectors. The ENA detection principle is based on the surface interaction technique. NPD detects ENA differential fluxes within the energy range of 100 eV to 10 keV and is capable of resolving hydrogen and oxygen atoms by time-of-flight (TOF) measurements or pulse height analysis.

During the calibration process the detailed response of the sensor was defined, including properties such as an angular response function and energy dependent efficiency of each of the sensor sectors for different ENA species.

Based on the NPD measurements at Mars the main scientific results reported so far are:

- observation of the Martian H-ENA jet / cone and its dynamics,
- observations of ENA emissions from the Martian upper atmosphere,
- measurements of the hydrogen exosphere density profile at Mars,
- observations of the response of the Martian plasma environment to an interplanetary shock,
- observations of the H-ENA fluxes in the interplanetary medium.

Keywords: ENA imaging, exosphere, magnetosphere, Mars, Venus, solar wind interaction

Sammanfattning

Den Neutrala Partikel Detektorn (NPD) är en ny typ av instrumentering som används för analys av energirika neutrala atomer (ENA). Denna avhandling omfattar utvecklingen av NPD-sensorn som ingår i plasma- och neutralapartikelinstrumenten ASPERA-3 och ASPERA-4 ombord på Mars Express och Venus Express, vilka är den europeiska rymdstyrelsens (ESA) satteliter till Mars och Venus. Avhandlingen beskriver hur NPD-sensorerna konstruerades, utvecklades, testades och kalibrerades. De första vetenskapliga resultaten från NPD-sensorns verksamhetstid vid Mars presenteras också.

NPD-sensorn består av två identiska detektorer, NPD1 och NPD2. Varje detektor har ett synfält på $9^\circ \times 90^\circ$ som är indelat i tre sektorer. Principen för ENA-detektering baserar sig på tekniken för växelverkan mellan ytor. NPD-sensorn detekterar flödet av ENA inom energiintervallet 100 eV till 10 keV och är kapabel att urskilda väte- och syreatomer genom "time-of-flight"-mätningar (TOF) eller pulshöjdsanalys. Under kalibreringsprocessen identifierades NPD-sensorns egenskaper som inkluderar vinkelsvarsfunktionen och den energiberoende effektiviteten för varje sensors sektor för olika ENA-typer. De huvudsakliga vetenskapliga resultaten, baserade på NPD-mätningar vid Mars och som hittills har rapporterats är:

- observationer av H-ENA strålar/koner och dess dynamik,
- observationer av ENA-emissioner från den övre delen av atmosfären,
- mätningar av vätedensitetens profil i exosfären,
- observationer av plasmamiljöns svar vid en interplanetär chock,
- observationer av H-ENA flöden i det interplanetära mediet.

Nyckelord: ENA-avbildning, exosfär, magnetosfär, Mars, Venus, solvindens växelverkan

Contents

Introduction

The solar wind is a supersonic flow of tenuous solar plasma which interacts with all bodies in our solar system. It possesses a magnetic field which is considered to be frozen in to the flowing plasma. In general every celestial body possesses a neutral gas environment of varying thickness. The interaction of the solar wind with them can be roughly divided into three types: interaction with magnetized bodies, interaction with unmagnetized bodies possessing an atmosphere, and interaction with those having negligible or no atmosphere at all. This PhD thesis is related to the solar wind interaction with unmagnetized bodies possessing an atmosphere, namely, the planets Mars and Venus. These planets no longer have a global magnetic field to deflect the solar wind, which causes atmospheric erosion through the interaction with the upper part of the planetary atmospheres.

The interaction between charged and neutral particles is a common phenomenon in space plasmas. An energetic neutral atom (ENA) is born whenever an energetic ion undergoes a charge exchange process in a collision with a neutral background atom. An ENA can also appear as a result of atmospheric and surface sputtering processes. The newly born ENA becomes independent from the surrounding plasma and the influences of magnetic and electric fields, and its trajectory is defined solely by the initial momentum and gravitational forces. With the exception of the case of very low energy (<10 eV) atoms, gravitational effects can be disregarded. Considering the case of charge exchange collision, one can assume that creation of an ENA preserves both the direction and magnitude of the energetic ion velocity before the collision. The movement of ENAs along the ballistic trajectory resembles the movement of photons in space. Hence, principles of the imaging technique used in optics can be applied to image ENAs. 'Imaging' is used to refer to the detection of the direction and wavelength of photons originating from some source of light. The term 'ENA imaging' is used for recording ENA fluxes as a function of observational direction. A global image of the object of interest can be reconstructed from a set of ENA images. In ENA imaging it is not only the angular distribution that is measured, but also the energy and mass of ENAs originating from an ENA source region. By determining ENA flux angular distribution as well as ENA energies and masses it is possible to establish plasma ion composition and distribution function remotely. This makes it possible to probe inaccessible regions in space from afar, as well as to obtain instantaneous information about the object.

ENA imaging can be used to: diagnose plasma processes on the global scale; reveal plasma boundaries resulting from the interaction of the solar wind with magnetized planets (e.g., *Williams et al.*, 1992); and characterize solar wind interaction processes with unmagnetized planets (*Lichtenegger et al.*, 2002; *Barabash et al.*, 2002; *Holmström et al.*, 2002). While electron and ion distributions in the planetary environment can only be measured locally, remote ENA imaging can give the whole picture of the interaction processes between different plasma populations and neutral background gas that result in ENA generation. Furthermore, *in situ* plasma measurements have the drawback that it is not possible to use them to resolve temporal

and spatial variations unambiguously. Remote ENA imaging, on the other hand, can reveal spatial variations. Therefore the global ENA imaging technique is an important complement to local measurements of electrons and ions. Modern planetary missions now include ENA detectors together with plasma packages.

The European Space Agency (ESA) missions towards Mars and Venus, namely Mars Express and Venus Express, carry the plasma and neutral particle packages, Analyzer of Space Plasma and Energetic Atoms (ASPERA-3 and ASPERA-4), among the scientific payload. Mars Express is Europe's first spacecraft to the Red Planet. Launched from the Baikonur launch site in Kazakhstan on board a Russian Soyuz-Fregat launcher, it travelled to Mars in seven months, going into orbit on December 25, 2003. Mars Express was inserted into a 6.5 hour elliptical near-polar orbit with apogee $\sim 3 R_M$ (where R_M stands for the radius of Mars) and perigee as low as ~265 km. Venus Express is ESA's first mission to Earth's nearest planetary neighbour, Venus. After 5 months cruise to Venus the Venus Express spacecraft entered orbit round the planet on April 11, 2006. It was inserted into a 24 hour elliptical orbit with apogee $\sim 11 R_V$ (where R_V stands for the radius of Venus) and perigee ~300 km.

The general scientific objective of both the ASPERA-3 and ASPERA-4 experiments is to study the solar wind – atmosphere interaction and to characterize the plasma and neutral gas environment in the vicinity of Mars and Venus through the use of ENA imaging and by measuring local ion and electron plasma populations. The ASPERA packages comprise 4 instruments, namely an electron spectrometer; an ion spectrometer; and two ENA sensors, the Neutral Particle Imager (NPI) and the Neutral Particle Detector (NPD) (*Barabash et al.*, 2004, 2006). NPD is an ENA detector, designed to perform mass and energy analysis of incoming ENAs, with a moderate angular resolution. This dissertation is focused on NPD development and calibration.

The thesis is organized as follows: Chapter 1 introduces the basics of ENAs along with a short description of the ENA environment of Mars and Venus. Chapter 2 provides the principles of ENA imaging followed by a review of ENA measurement techniques and ENA instrumentation examples. Chapter 3 contains a comprehensive description of the ASPERA-3 and ASPERA-4 packages that are providing plasma and ENA measurements at Mars and Venus, respectively. Chapter 4 presents a detailed design description of the NPD, followed by calibration results of both ASPERA-3 / NPD and ASPERA-4 / NPD in chapter 5. Chapter 6 reviews selected papers based on data obtained by ASPERA-3 / NPD during its operation at Mars. Finally, chapter 7 sums up the thesis and outlines future prospects. Appendices contain details on NPD operation modes, and a description of quick look NPD data display.

Chapter 1

Energetic neutral atoms in space

ENAs are neutral particles, possessing energy exceeding the thermal energy (i.e., several eV).

1.1 Production mechanisms

ENAs in space are produced by various processes of ion/atom – atom collision, mainly

- charge exchange of energetic ions with exospheric gasses in the near-planet environment or interplanetary background neutral gas,
- sputtering of atmospheric or surface materials by precipitating energetic ions or neutrals,
- back-scattering of energetic particles precipitating on the planetary upper atmosphere or surfaces.

1.1.1 Charge exchange

Charge exchange of singly-ionized plasma ions to produce ENAs is fundamental to many ENA sources. ENAs are formed in charge exchange collisions between energetic plasma ions and cold neutral gas atoms. The charge exchange process

$$A^+_{energetic} + M_{cold} \rightarrow A_{energetic} + M^+_{cold}$$

produces ENAs when an energetic (compared to thermal energies) ion $A^+_{energetic}$, collides with a cold neutral M_{cold}, resulting in an ENA and a cold ion M^+_{cold}. Species M and A may be identical (i.e., $H^+ + H \rightarrow H + H^+$, resonance charge exchange) or not (i.e., $H^+ + O \rightarrow H + O^+$). Due to the large internuclear distances during charge exchange, only negligible energy and momentum are transferred in these interactions. Hence the initial velocity of an energetic particle is only slightly changed in a charge exchange collision (*Bransden and McDowell*, 1992). Figure 1.1 illustrates the charge exchange (also known as electron pick-up) process between a fast ion and a slow atom.

The probability that a given charge exchange process will occur in a collision is expressed as a reaction cross-section. Figure 1.2 shows the charge exchange cross-sections for singly charged hydrogen and oxygen ions with cold neutral gas. In general, at low ion energies the cross-sections for charge exchange are within a range of 10^{-15}cm^2. The H^+ cross-section begins to fall off for proton energies above 10 keV and drops off steeply above 50 keV. This is a very important constraint on ENA production, and it assures that ENA hydrogen spectra will be concentrated below ~200 keV.

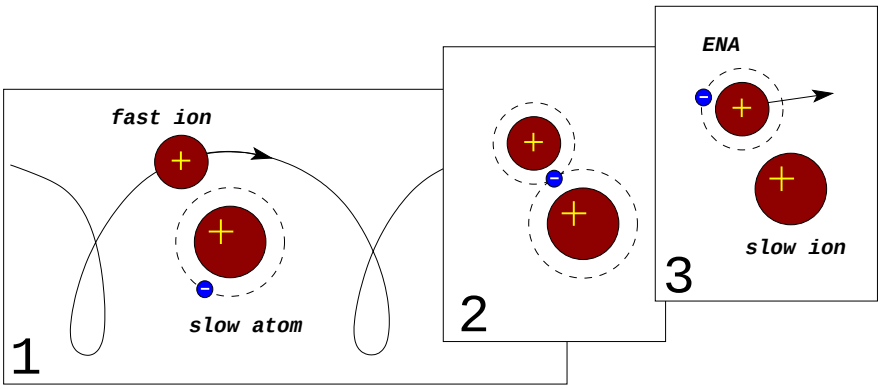

Figure 1.1: Charge exchange mechanism.

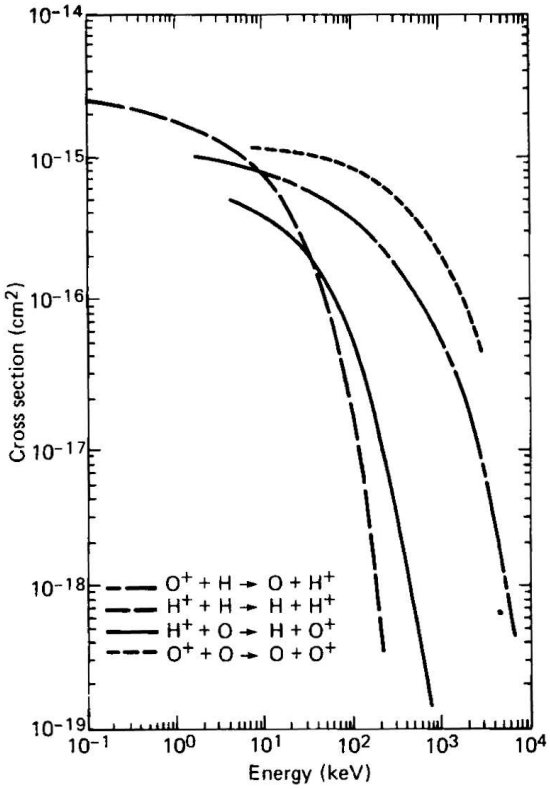

Figure 1.2: Charge exchange cross-sections of energetic H^+ and O^+ ions as a function of incident ion energy for electron pick-up from cold neutral hydrogen and oxygen atoms. From *Wurz* (2000).

1.1.2 Back-scattering

ENAs can be born during scattering, in a process of elastic and inelastic collision of energetic charged- or neutral particles with slow neutral background atoms. The ENA back-scattering production mechanism with reference to Mars is as follows:

The neutral solar wind (see Section 1.3.1) can enter the Martian upper atmosphere and reach the exobase, where it experiences elastic and inelastic collisions (*Kallio and Barabash*, 2000). It possesses the energy of the solar wind bulk flow. A fraction of the neutral solar wind

incident flux can be scattered back in the form of ENAs due to momentum transfer in collisions and cascade of charge exchange and electron stripping processes.

1.1.3 Sputtering

Two types of sputtering are present in space, namely surface and atmospheric sputtering. Surface sputtering occurs in general on the celestial bodies without atmosphere, while the atmospheric sputtering occurs on the ones possessing an atmosphere.

Atmospheric sputtering. The atmospheric sputtering mechanism with reference to Mars is shown schematically in Figure 1.3. Because the modern Mars lacks an intrinsic magnetic field, the exosphere is directly exposed to the solar wind. Hence, the solar wind convection electric field can accelerate O^+ ions, originating from ionization of the exospheric atoms, to produce 'pick-up ions'. A fraction of these O^+ pick-up ions can re-enter the Martian upper atmosphere and reach the exobase due to a large gyro-radius. After the precipitation, O^+ ions exchange charges and the resulting fast O atoms undergo elastic collisions with cold O atoms in the background gas (*Luhmann and Kozyra*, 1991). The large energy is imparted to surrounding particles through further collisions, causing atmosphere sputtering. A certain fraction of the particles which gained energy in these collisions is scattered back out of the atmosphere.

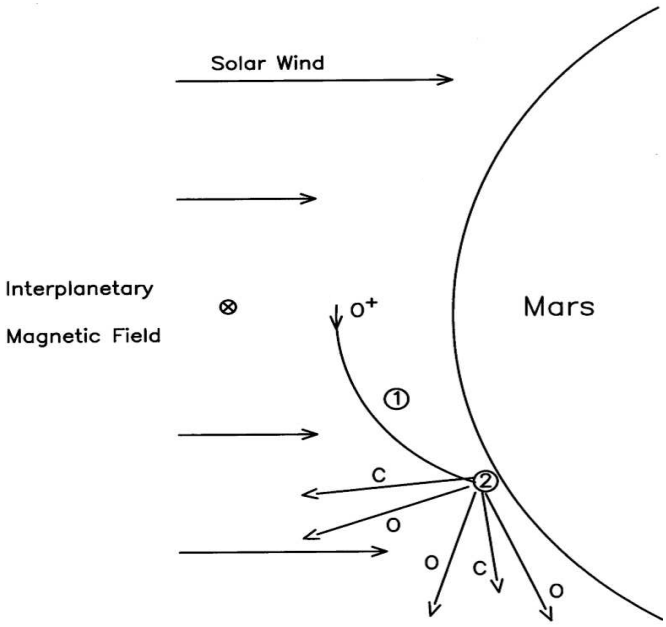

Figure 1.3: Atmospheric sputtering occurs when ionized O^+ in the upper atmosphere is accelerated by the solar wind convection electric field and strikes the exobase (step 1), causing a cascade of collisions that results in the ejection of particles in the form of ENAs (step 2). Adapted from *Kass* (1999).

Surface sputtering. In the case of surface sputtering on celestial bodies without an atmosphere, such as the Moon or Mercury, energetic ions coming directly from the solar wind as well as energized planetary ions may precipitate onto the surface, resulting in extensive sput-

tering (*Grande*, 1997; *Lukyanov et al.*, 2004). ENAs originating from the sputtering process possess energy of a few tens of eV (*Massetti et al.*, 2003).

1.2 Classification

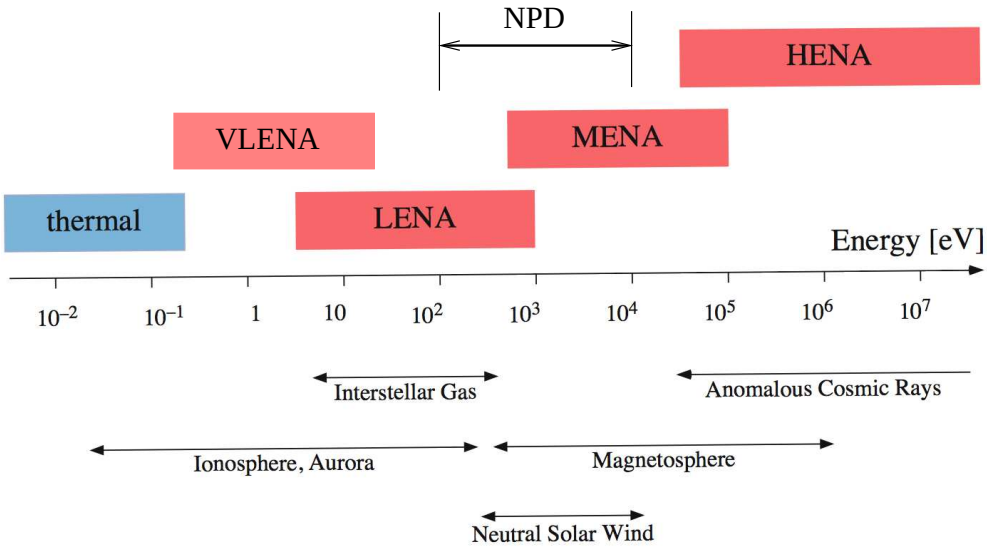

Figure 1.4: ENA classification by energy and sources. Adapted from *Wurz* (2000).

The energy range of ENAs is generally considered to cover four sub-ranges: very low-energy neutral atoms (VLENA) ~0.1 – 10 eV; low-energy neutral atoms (LENA) ~10 – 1000 eV; medium-energy neutral atoms (MENA) ~0.5 – 30 keV; and high-energy neutral atoms (HENA) ~10 – 200 keV.

This arbitrary division (with overlapping ranges) derives from the necessity of employing different experimental techniques in different energy ranges (since no single analyzer can cover the entire concerned range), rather than from the different physical natures of these ENAs. Figure 1.4 gives an overview of the different sources of energetic neutral particles that can be observed in space, together with their approximate energy range. The upper limit for HENAs is a consequence of the inherent energy and species-dependent cut-off values for ENA charge exchange cross-sections. The NPD detection range is indicated.

ENA fluxes come from different ion populations, with different compositions, flux levels and energy, and spatial, and temporal dependencies. Table 1.1 gives an overview of the typical parameters characterizing ENAs, generated near various celestial objects within the Solar system.

1.3 ENAs at non-magnetized planets

1.3.1 ENA environment of Mars

The solar wind interaction with Mars is complex and results in the production of ENAs in a wide energy range. In order to get a better understanding of such interaction, the general picture of the Martian plasma boundaries is shown in Figure 1.5.

ENA source	Energy, keV	Flux, $cm^{-2}sr^{-1}s^{-1}keV^{-1}$	Species
Intestellar medium	0.013 0.050	5×10^5	*H*
Heliospheric shock	0.2 - 1	(1-4)×10^2 $cm^{-2}sr^{-1}s^{-1}$ @ 1AU	*H*
Interplanetary shocks	10 100	$4\cdot10^1 - 10^2$ $10^{-2} - 10^{-1}$	*H*
Coronal mass ejection	2-7	10^4 @ 1AU	*H*
Martian magnetosphere	1-8 20-80	$10^5 - 10^6$ $10^{-1} - 10^1$ @ 1AU	*H, O*
Terrestrial magnetosphere	10-20 20-30	$10^3 - 10^4$ $10^1 - 10^2$ @ 5 R_E	*H, O, He*
Jovian magnetosphere	15-65	10^{-3}-10^{-2} $cm^{-2}s^{-1}keV^{-1}$ @ 100 R_J	*H, O, S*
Saturnian magnetoshere	>40	10^{-1} $cm^{-2}s^{-1}keV^{-1}$ @ 45 R_S	*H, O*
Outgassing asteroids (Phobos)	1-5	$10^4 - 10^6$	*H*

Table 1.1: Overview of different ENA population parameters (AU - astronomical unit, R_S - Saturn radius, R_E - Earth radius, R_J - Jupiter radius).

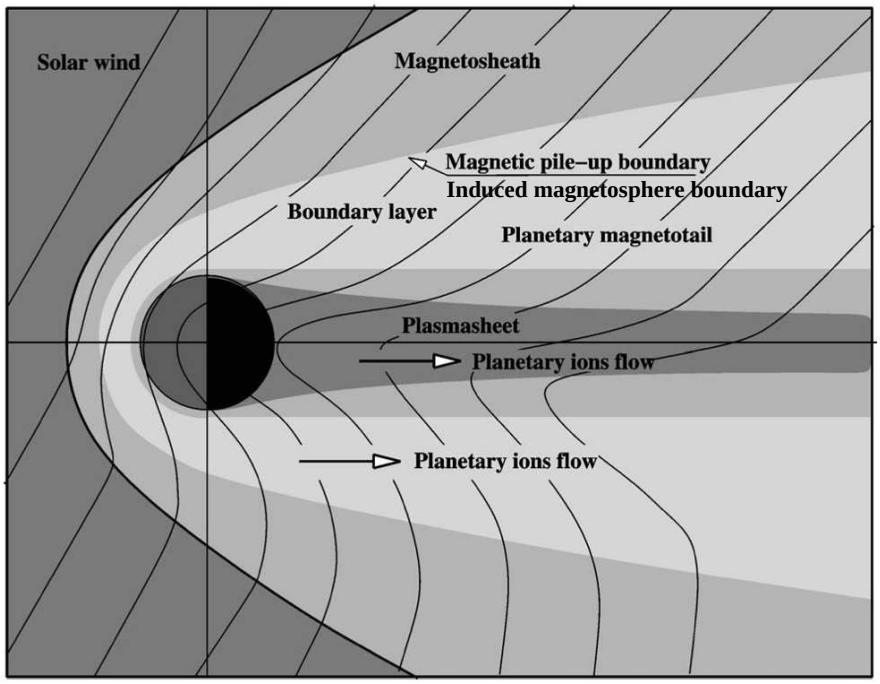

Figure 1.5: Structure of the Martian plasma environment in the plane of the interplanetary magnetic field. From *Fedorov et al.* (2006).

Mars has a very thin atmosphere with a pressure of ~7 mbar at the surface, consisting mostly of CO_2. It extends a long way out due to low gravity at Mars. The upper part of the atmosphere is partly ionized by extreme ultra-violet (EUV) / ultra-violet (UV) solar radiation. The absence of an intrinsic magnetic field (*Acuña et al.*, 1998) leads to a direct interaction of

the solar wind with the upper part of the extended neutral atmosphere of Mars. Planetary ions become picked-up by the solar wind convection electric field, which results in a significant mass-loading of the frozen-in interplanetary magnetic field (IMF). The boundary upstream and around the ionosphere, where the IMF mass-loading and draping around this obstacle occur, is called the magnetic pile-up boundary (MPB) (*Vignes et al.*, 2000) or the induced magnetosphere boundary (IMB) (*Lundin et al.*, 2004). Upstream of the IMB, the solar wind protons are thought to be the dominant ion species, while below the IMB, heavy ions of planetary origin (mostly O^+ and O_2^+) prevail. A bow shock (BS) appears upstream of the IMB, where the solar wind plasma flow is slowed from supersonic to subsonic, thermalizes and begins to divert around the obstacle. The region in-between the BS and IMB, containing both shocked solar wind ions and picked-up planetary ions, is called a magnetosheath. Behind the planet, in the planetary shadow, the plasma sheet region is located (*Rosenbauer et al.*, 1989), where the dense flow of the heavy ions can be encountered.

The neutral gas density in the solar wind interaction region where the BS and IMB are located, can reach 10^4 - 10^6 cm^{-3} due to the low gravity on Mars. The solar wind plasma can, therefore, interact strongly with the exospheric gases, mainly *H*, through the collisional interactions (Section 1.1), resulting in strong ENA production.

Nowadays the Martian plasma and ENA environment is well understood. The measurements carried out on a number of missions, such as Phobos-2 (*Lundin et al.*, 1989), MGS (*Vignes et al.*, 2000), and with the ASPERA-3 experiment on Mars Express (*Barabash et al.*, 2004, 2006) as well as numerous numerical simulations performed by *Brecht* (1997a); *Holmström et al.* (2002); *Kallio and Janhunen* (2002); *Ma et al.* (2002); *Lichtenegger et al.* (2002) complement the general picture of the Martian ENA environment.

The main sources of ENAs in the Martian environment are:

- Upstream solar wind ENAs – neutral solar wind (NSW)

  Some part of the supersonic solar wind flux is neutralized due to charge exchange with the interplanetary neutral gas. Such solar wind ENAs have been detected by the LENA instrument on board the terrestrial IMAGE mission, which is capable of looking directly towards the Sun (*Collier et al.*, 2001). Also, the undisturbed solar wind flow upstream of the Martian BS can experience charge exchange with the Martian hydrogen exosphere, extended over very long distances (exceeding 4 Martian radii, R_M).

  The resulting narrow ($\sim 10^\circ$) anti-sunward beam of solar wind ENAs, called the NSW, has the same energy as the bulk solar wind flow ($\sim$1 keV). NSW flux was likely detected with the sunward pointed ASPERA-3 / NPI sensor, right after entering Martian eclipse (*Brinkfeldt et al.*, 2006b). The planetary disk blocks solar UV photons in such a configuration, allowing NPI to avoid being solar blinded and thus detect the NSW. The NSW can reach the umbra region mostly due to thermal spreading and scattering in the upper atmosphere (*Kallio et al.*, 2006).

- Shocked solar wind

  The shocked thermalized solar wind is a strongest source of H-ENAs with an energy of a few hundreds eV. The shocked solar wind flow moves around the Martian obstacle through the comparatively dense hydrogen exosphere. Therefore charge exchange interactions between protons and cold planetary neutral species in the magnetosheath are very probable. The ENA fluxes, generated from the shocked solar wind, are sensitive to the neutral hydrogen distribution, which is controlled by the exobase temperature and density (*Holmström et al.*, 2002). Detailed modeling of the shocked solar wind ENA

production was performed by *Kallio et al.* (1997); *Holmström et al.* (2002); *Gunell et al.* (2006). Figure 1.6 shows images of H-ENA emissions near Mars simulated by *Holmström et al.* (2002) for several vantage points at different solar zenith angles.

Intense fluxes of H-ENAs emitted from the subsolar exosphere of Mars (so-called ENA jets (cones), see Section 6.1) were detected by the ASPERA-3 / NPD sensor on board Mars Express (*Futaana et al.*, 2006a). The differential flux was estimated to be $4 - 7$ $\times 10^5$ cm^{-2}sr^{-1}s^{-1} in the energy range of 0.3-3 keV/amu. These ENAs are likely to be generated through charge exchange between the shocked solar wind protons and the Martian exosphere in the subsolar region, where the solar wind plasma penetrates to its lowest altitude and where the neutral gas density is high.

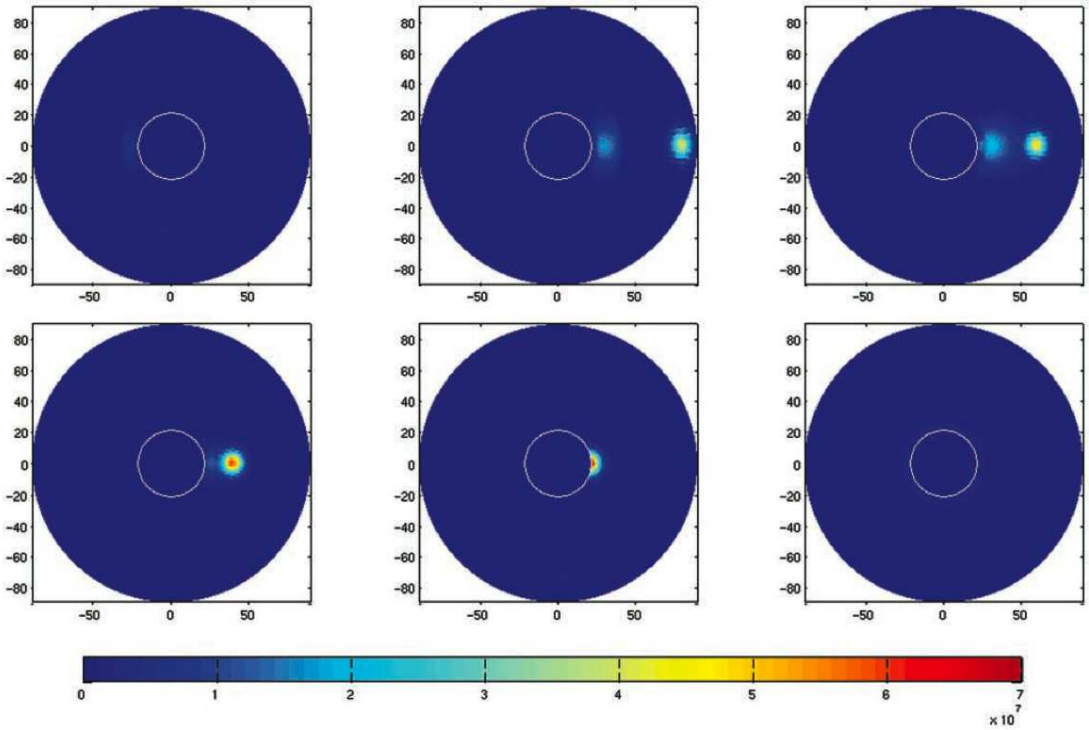

Figure 1.6: Images of ENA emissions near Mars. The look direction is toward the center of Mars. The view position is at a distance of 3 R_M. The angle of the view position to the Mars-Sun line is, from left to right: top to bottom, 80°, 100°, 120°, 140°, 160°, and 180°. The images have a field-of-view of 180° and show the intensity (cm^{-2} sr^{-1} s^{-1}) as a function of direction (q, j) in a polar format, with the q coordinate as the polar angle and j in the radial direction. The axes show the angle to the look direction, j (deg). The circle is the obstacle boundary, of radius 1.05 R_M. The up direction is perpendicular to the ecliptic plane, along the z axis. From *Holmström et al.* (2002).

- Accelerated planetary ions

  Because the Martian upper atmosphere is directly exposed to the solar wind, the cold planetary atomic and molecular species, once ionized, are being picked up and accelerated by the solar wind convection electric field and can subsequently escape the planet. A fraction of these ions can experience charge exchange reactions resulting in a specific ENA signal. *Lichtenegger et al.* (2002) and *Barabash et al.* (2002) investigated the details of such ENA fluxes associated with hydrogen pick-up and oxygen pick-up.

  Using the empirical model of the solar wind plasma flow near Mars developed by *Kallio*

(1996), *Barabash et al.* (2002) solved the kinetic equation numerically to obtain the global distribution of oxygen ions. This distribution was then converted to the corresponding ENA fluxes. The differential fluxes of oxygen ENAs were estimated for solar minimum conditions to reach $10^5\,\mathrm{cm}^{-2}\mathrm{sr}^{-1}\mathrm{s}^{-1}\mathrm{eV}^{-1}$ in the energy range 0.1-1.7 keV. It was found that the majority of oxygen ENAs have energies below 600 eV. For these energies the integral fluxes of O-ENAs could reach $10^4\,\mathrm{cm}^{-2}\mathrm{s}^{-1}\mathrm{eV}^{-1}$. Figure 1.7 shows simulated O-ENA images in a fish-eye projection, obtained for different vantage points in the noon-midnight meridian plane, and the corresponding vantage points.

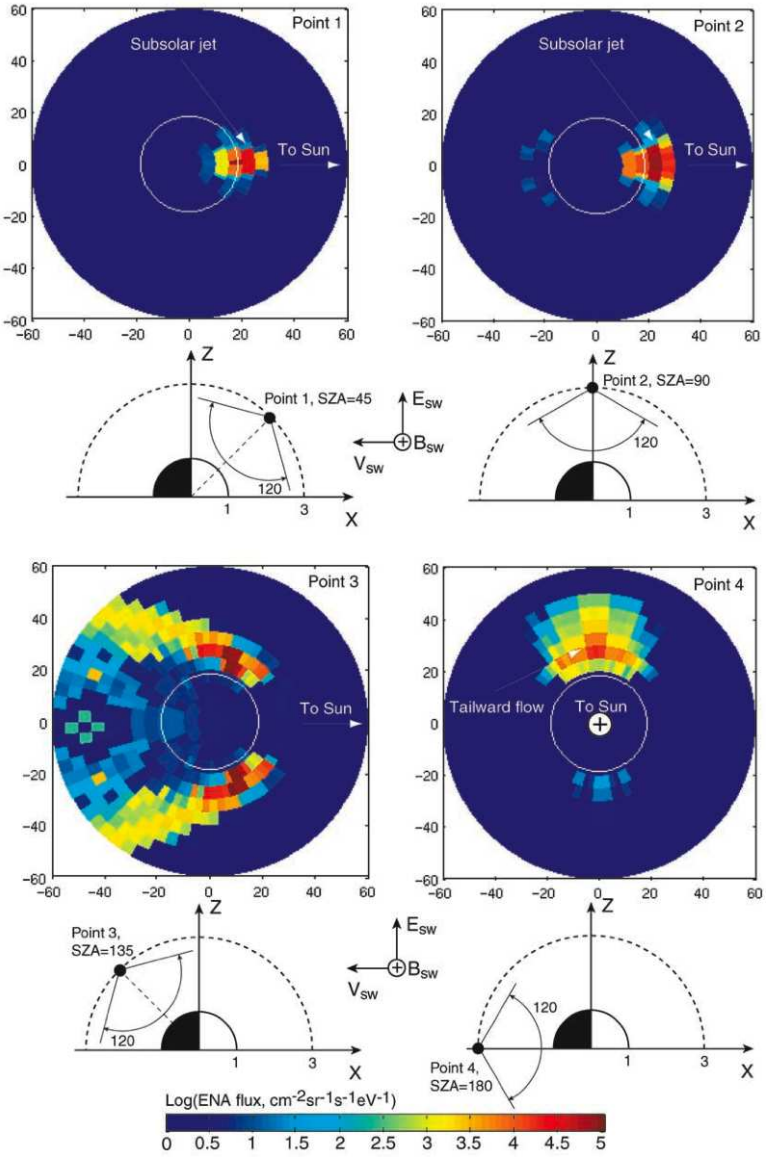

Figure 1.7: O-ENA images simulated for vantage points with different solar zenith angles (SZA). The energy range is 0.1-1.65 keV to cover the main oxygen ion population. The projection is a polar one, with the radius being the angle to the axis pointing toward the planetary center and the polar angle is the angle to the solar direction in the plane perpendicular to the planetary center direction. The position of the vantage points are shown in the inserts as well as electrical and magnetic field vectors. All points are in the OXZ plane. From *Barabash et al.* (2002).

The total ENA production rates were estimated by *Galli et al.* (2006a) from observations for both H-ENA and O-ENA to be 2-3 $\times 10^{24} s^{-1}$ and $< 10^{22} s^{-1}$, respectively. This corresponds to a total escape of both H and O as <1g/s.

- Back-scattered hydrogen (ENA albedo)

  The generation mechanism of back-scattered ENAs (H – ENA albedo) is described in Section 1.1.2. *Kallio and Barabash* (2000) used a three-dimensional Monte Carlo model to investigate the back-scattered ENAs. The ratio of the particle flux of the back-scattered ENAs to the impinging ENAs was found to be 0.58. The average energy of the back-scattered ENAs was 60% of that of the impinging ENAs.

  Yet, according to the models, some of the solar wind ions directly impact the Martian upper atmosphere near its exobase (~180 km altitude) because their gyro-radii are too large to behave as a deflected 'fluid' in the subsolar magnetosheath (*Brecht*, 1997a; *Kallio and Janhunen*, 2001) and/or because they are partially thermalized in the BS (*Kallio et al.*, 1997). These protons, reaching the exobase, experience the similar elastic and inelastic collision processes and a portion of them is scattered back as hydrogen atoms, resulting in the ENA albedo. The ENA flux generated by this proton – ENA albedo process was estimated by *Holmström et al.* (2002) to be 10^3 - 10^4 $cm^{-2}sr^{-1}s^{-1}$, i.e., negligible in comparison with the ENA albedo flux produced by precipitating hydrogen atoms.

  The H-ENA albedo on the dayside of Mars was detected by the ASPERA-3 / NPD sensor (*Futaana et al.*, 2006b). The back-scattered ENAs have energies of 0.2-2 keV with an average energy of ~1.1 keV. The differential flux of back-scattered H-ENAs was estimated to be 1.5-2.0 $\times 10^6 cm^{-2}sr^{-1}s^{-1}$.

- Sputtered O-ENAs

  The solar wind motional electric field accelerates ionized cold exospheric components producing pick-up ions (mostly H^+ and O^+). All ions are accelerated up to twice the speed of the solar wind. Thus, because of higher mass, O^+ ions reach the highest energy. Atomic O ionization to produce O^+ ions can be due to various processes, e.g., photo-ionization by UV photons ($O + h\nu \rightarrow O^+ + e^-$), photo-chemical processes in the upper atmosphere, charge exchange reactions in a collision with solar wind high energy H^+ ($O + H^{+*} \rightarrow O^+ + H^*$) and electron impact ionization.

  Because of a gyro-radius comparable with the Mars size, some of these pick-up ions can re-enter the Martian upper atmosphere and reach the exobase. After the precipitation O^+ ions charge exchange and the resulting fast O atoms undergo elastic collisions with cold O atoms in the background gas (*Luhmann and Kozyra*, 1991). The sputtering mechanism is shown schematically in Figure 1.3. The large energy is imparted to surrounding particles through further collisions, causing atmosphere sputtering. A certain fraction of the particles, gained energy in these collisions, is scattered back out of the atmosphere. This process occurs on mainly the dayside. The simulated energy spectrum of the sputtered oxygen is shown in Figure 1.8.

1.3.2 ENA environment of Venus

The ENA environment of Venus is very similar to that of Mars. This is because both planets are non-magnetized and the solar wind can directly interact with the upper atmospheres. ENAs are produced in charge exchange collisions between solar wind protons and neutral atoms in

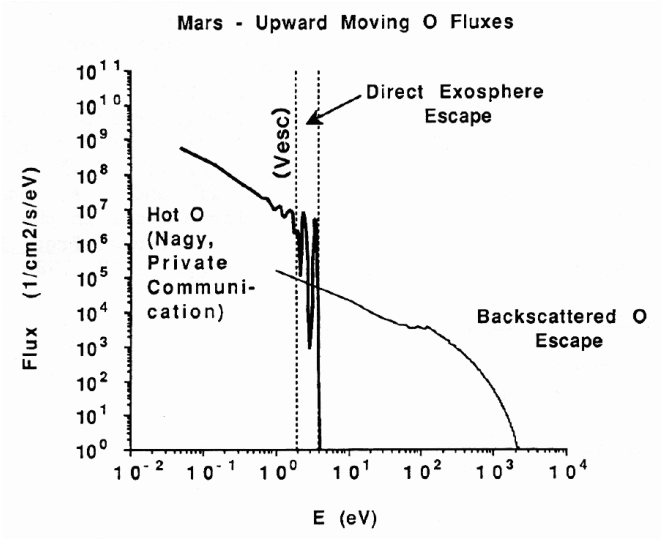

Figure 1.8: Calculated low energy flux from the pick-up O^+ ion precipitation. From *Luhmann and Kozyra* (1991).

the upper part of the atmospheres of the planets. Of course, the planetary environments differ considerably. The Venusian atmospheric pressure is about 90 bar at the surface, while the Martian one is about 7 mbar at the surface. But as the gravity of Venus is about 3 times larger than that of Mars, the Venusian barometric scale height is lower than the Martian one.

The ENA flux and production rates at Venus are lower than at Mars even though the solar wind flux is greater at Venus. The reason for this is that the neutral gas density at relevant heights is lower in the exosphere of Venus that at Mars. The neutral density falls off more rapidly with altitude at Venus, due to its stronger gravity field. The dominant contribution to the neutral density at high altitudes at Mars during solar minimum conditions is the large hydrogen corona (*Krasnopolsky and Gladstone*, 1996). The hydrogen density at Mars is greater than that at Venus everywhere above the exobase, and hydrogen is by far the most important specie for ENA production at Mars (*Holmström et al.*, 2002). The ENA production rate at Mars at solar maximum conditions is about the same as that at Venus.

Gunell et al. (2005) compared ENA production rate for Mars and Venus (Table 1.2). At solar minimum a lower ENA production rate is expected for Venus. At solar maximum the ENA production rate for both planets is expected to be comparable, as the neutral density at Mars decreases at high altitudes.

The ionopause altitude at Venus is not well known for solar minimum conditions (*Luhmann*, 1992). It is thought to vary with the solar cycle, but since all *in situ* measurements were made during solar maximum conditions this variation is still unconfirmed.

Gunell et al. (2005) have investigated the ENA emissions as a function of ionopause distance by scaling the ionopause altitude in the plasma model. The ENA flux from the local emission maximum near the planet decreases with increasing ionopause altitude, since with a higher ionopause altitude the protons pass through a region with lower neutral density. This also affects the ENA production and escape rates. The ionopause is thought to be close to the lower end of that range at solar minimum because of lower ionospheric pressure (*Luhmann*, 1992).

Venus Express has arrived at Venus during solar minimum conditions. The ASPERA-4 instrument provides ENA images of the solar wind – Venus interaction region. Such images

	Venus IP 250 km	Venus IP 400 km	Mars Holmström	Mars MHD (Gunell)	unit
Production rate	$7.8 \cdot 10^{24}$	$5.6 \cdot 10^{24}$	$1.7 \cdot 10^{25}$	$\begin{cases} 2.4 \cdot 10^{25}, & \text{min} \\ 5.1 \cdot 10^{24}, & \text{max} \end{cases}$	s^{-1}
Escape rate	$5.3 \cdot 10^{24}$	$4.0 \cdot 10^{24}$	$1.5 \cdot 10^{25}$		s^{-1}
Precip. rate	$2.2 \cdot 10^{24}$	$1.2 \cdot 10^{24}$	$1.4 \cdot 10^{24}$		s^{-1}
Max. flux	$5.8 \cdot 10^{10}$	$3.8 \cdot 10^{10}$	$3 \cdot 10^{11}$	$1.1 \cdot 10^{11}$, min	$sr^{-1}m^{-2}s^{-1}$

Table 1.2: A comparison of ENA fluxes at Venus and Mars. Values for Venus are given for ionopause (IP) altitudes 250 km and 400 km respectively. Venusian upper atmosphere is approximately the same independent of the solar cycle. The values for Mars from *Holmström et al.* (2002) are all for solar minimum conditions. Values from the MHD simulation of Mars were taken from *Gunell et al.* (2006). "Max. flux" refers to the maximum flux in an ENA image of the interaction region downstream of the BS. Solar minimum and maximum conditions are denoted by "min" and "max" respectively. From *Gunell et al.* (2005).

have been simulated (Figure 1.9) through the integration of the ENA production along lines-of-sight (LOS) to a virtual ENA instrument (*Fok et al.*, 2004; *Gunell et al.*, 2005). The ENA images are generated by evaluating LOS integrals in the same way as has previously been done to simulate ENA images of the Martian environment (*Holmström et al.*, 2002; *Gunell et al.*, 2006). *Gunell et al.* (2005) have used a semi-analytical magnetohydrodynamics (MHD) model (*Biernat et al.*, 1999, 2001) to describe the plasma flow around Venus, and a neutral gas density model based on published data from measurements. The maximum flux observed at 3 R_V (R_V denotes the Venus radius), coming from the interaction region on the dayside of Venus is 5.8 $\times 10^{10}$ $sr^{-1}m^{-2}s^{-1}$, which occurs for the lowest ionopause altitude, i.e., 250 km at the subsolar point. The ENAs that are produced in the solar wind upstream of the BS are not included in this number. For higher ionopause altitudes (400 km) the ENA flux decreases and is below 3.8 $\times 10^{10}$ $sr^{-1}m^{-2}s^{-1}$. The corresponding number for Mars at solar minimum conditions, computed by *Holmström et al.* (2002), is about 3 $\times 10^{11}$ $sr^{-1}m^{-2}s^{-1}$, which is five times larger than the value obtained for Venus with an ionopause altitude of 250 km.

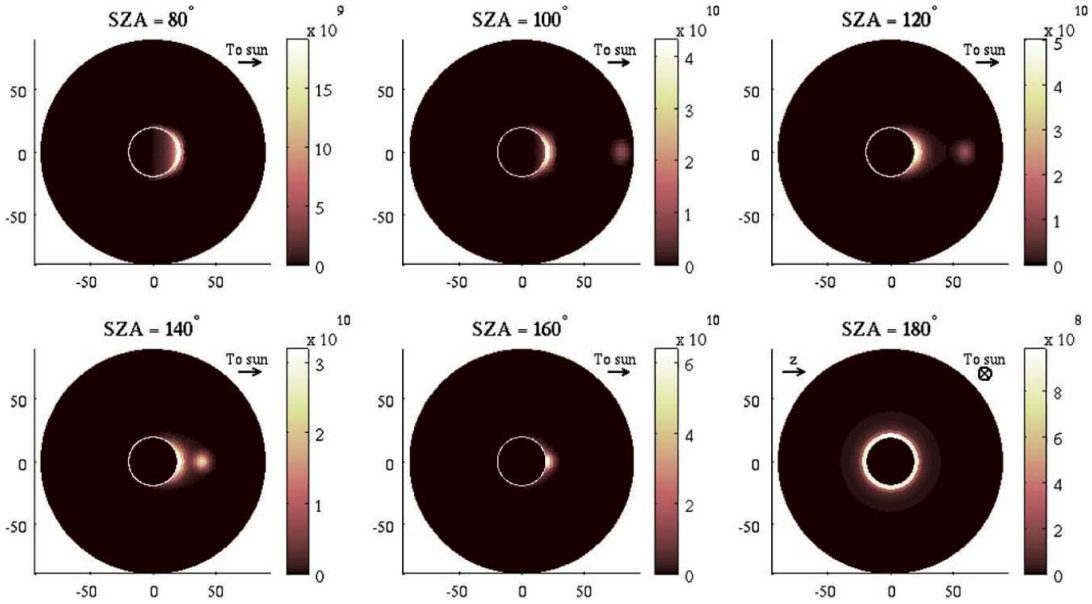

Figure 1.9: ENA images of Venus from vantage points 3 R_V from Venus (planetocentric distance) and solar zenith angles θ = 80°, 100°, 120°, 140°, 160°, and 180°. The ENA flux is shown in units of $sr^{-1}m^{-2}s^{-1}$, and the axes show the polar angle in degrees. The altitude of the ionopause is 250 km at the subsolar point. The dominant contribution to the ENA flux comes from a region between the ionopause and the BS on the day-side of Venus, except in the lower right panel where θ = 180°, and this region is occulted by Venus. The second maximum toward the right side of the images with 100° < θ < 140°, is produced upstream of the BS in the solar wind. Each image has its own colour scale. From *Gunell et al.* (2005).

Chapter 2

Energetic neutral atoms detection

2.1 ENA imaging

The capability to detect ENAs with high mass, energy and angular resolutions constitutes the basis of ENA imaging (*Gruntman*, 1997). By recording ENA fluxes as a function of observational direction, one can reconstruct a global image of a remote object of interest. An ENA image is a two-dimensional (2D) map of the ENA fluxes given by LOS integrals of the ion distribution convolved with the neutral density through the whole plasma volume. An ENA's ability to fly along straight lines resembles the photon's movement in space. Thus the ENA imaging concept resembles that used in optical instruments.

All ENA imaging instruments can be classified within three groups, namely non-imaging detectors, one-dimensional (1D) imaging instruments and 2D imaging instruments. Non-imaging detectors have a well defined but narrow field-of-view (FOV) and no intrinsic imaging capability (like telescopes). To obtain a 1D "image" with a non-imaging detector, the latter can be installed on a scanning platform or make use of a spin of a spacecraft to point the detector in the desired direction. Combining both the spacecraft spin and the scanning platform allows us to obtain a 2D image with a non-imaging detector. But as the image is being obtained sequentially, pixel by pixel, total image accumulation time can be very long, as it equals the number of pixels composing the image, multiplied by a pixel accumulation time. In a 1D imaging scheme, an ENA imager records the arrival direction of particles only in one dimension, with the second dimension being narrowly collimated. To scan over an object of interest and obtain a 2D image, the 1D imager can either be placed on a scanning platform or make use of the spacecraft spin. A 2D ENA imager records the arrival direction of a particle in two dimensions simultaneously, while pointing at the object of interest. It can have a sufficiently large FOV to cover the entire object and is typically located on a three-axis stabilized spacecraft. Time resolution of a 2D imager can be very high (if counting statistics allows), as it obtains a 2D image momentarily. However the angular resolution is not high. Charge particle rejection becomes a challenging problem.

The 1D imager is a compromise between a non-imaging ENA detector with a narrow FOV and long image accumulation time, and the 2D imager with a large FOV but complex instrumentation. 1D imaging has therefore become most common.

ENA imaging (only 1D and 2D imaging schemes) can be divided into two groups, one obtaining non-inverted images and another one obtaining inverted images. Both concepts are shown schematically in Figure 2.1. The object plane on the plot is a remote object of interest. The image plane is the plane onto which a non-inverted or inverted image is mapped. The

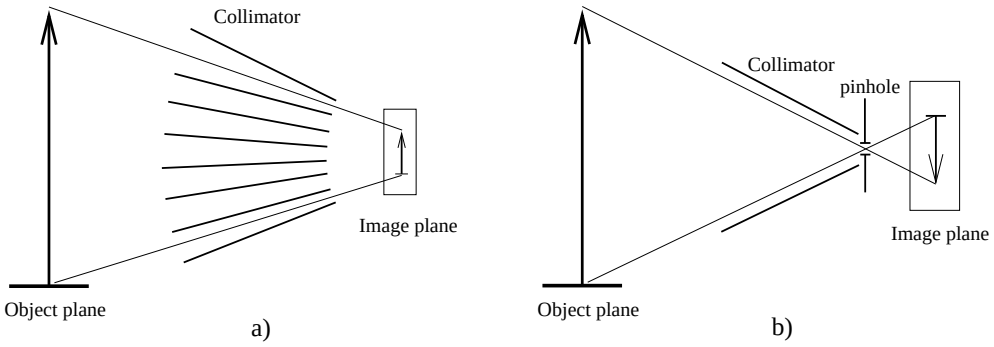

Figure 2.1: ENA imaging concepts: non-inverted (a) and inverted (b) image.

image plane can be a position sensitive detector. The aperture of a non-inverting instrument (Figure 2.1a) is a long narrow slit. Imaging is performed in one dimension, while the second dimension is collimated by charge particle rejection plates to a small angle, corresponding to a width of 1 pixel. This configuration resembles a set of telescopes placed parallel to each other. Wrapping the aperture slit around 360° allows us to obtain a 360° viewing plane (as in the NPI imager, Section 3.2.3).

Another way is to use the pinhole camera concept (Figure 2.1b), where imaging is achieved by letting an incoming particle pass through a small aperture (pinhole) and impinge on a 1D or 2D imaging detector, located at a certain distance apart from the pinhole. From an impact location on the image plane of the detector the arrival direction of an incoming particle can be estimated. The advantage of this concept is that we can obtain a large FOV with sufficiently good angular resolution. However, this technique requires longer accumulation times due to the small aperture size. A larger pinhole size allows us to decrease the accumulation time, but compromises an angular resolution of the image (blurring). The typical area of the pinhole may range from 1 mm^2 to 1 cm^2. A pinhole camera itself does not provide any information on the mass or energy of the registered particles. Additional information is obtained by combining the pinhole imaging concept with different ENA detection techniques (see Section 2.5).

ENA imaging provides images of the plasma region under investigation and gives the observer spectral, compositional and spatial information. ENA imaging is a powerful technique for obtaining the temporal and spatial evolution of space plasmas on a global scale and is complementary to local plasma measurements.

The ENA flux, originating from charge exchange, that reaches the observer from a given direction, is a LOS integral of the ion distribution convolved with the neutral density through the whole plasma volume. Other mechanisms of ENA production are reviewed in Chapter 1. Considering only the prevalent mechanism, namely charge exchange, the uni-directional differential flux $f_i(E)$ (in units of $cm^{-2}sr^{-1}s^{-1}keV^{-1}$) of charge exchange neutrals is then given by an integral along the LOS in equation 2.1, assuming no loss.

$$f_i(E) = \sum_k \sigma_{ik}(E) \int_l j_i(E,l)\, n_k(l)\, dl \tag{2.1}$$

where $\sigma_{ik}(E)$ denotes the energy-dependent charge exchange cross sections for involved various ion i and neutral k species. $j_i(E,l)$ is the directional singly charged ion flux along the LOS at each point l for species i within the source volume, $n_k(l)$ is the density of the component k of the neutral gas. The sum extends over all constituents of the neutral gas contributing to

the charge exchange. The extinction of ENAs due to re-ionization by EUV/UV photons or collisions with electrons, ions and neutral particles along the way is not included. This approximation is valid for ENAs traveling through a so-called 'ENA thin' or 'ENA transparent' medium, where interaction of ENAs with the medium is negligible.

As soon as an ENA image is accumulated, extraction of the quantitative information from the image, which contains an admixture of information on energetic ion and cold neutral distributions, requires deconvolution of the sum of $j_i(E,l)\, n_k(l)$ products from the integral 2.1. Parameterized models of the ion distribution of the observed plasma volume as well as the density distribution of the neutral gas are needed. Different image processing techniques to recover plasma distribution parameters of the remote object can be used.

One approach to interpreting an ENA image is a forward modeling technique. In one model a set of initial parameters is chosen and is used together with another model to simulate an ENA image, which is compared with the observed one. The model parameters are changed until a simulated ENA image which matches the recorded ENA image is obtained (*Chase and Roelof*, 1995). The forward modeling technique can be rather time consuming if the models contain large numbers of parameters to change.

Another approach is extraction of the original ion distribution information from ENA images using an ENA image deconvolution technique (*Roelof and Skinner*, 2000; *Perez et al.*, 2000). This is a method which allows deconvolution of the sum of $j_i(E,l)\, n_k(l)$ products. This technique is usually very fast, although it is much more complicated mathematically than the forward modeling, as it uses inverted equations of the models. *Roelof and Skinner* (2000) developed (for investigating the terrestrial ring current) several algorithms to extract the parameters of the model ion distribution by minimizing the differences between a simulated image and an observed image or set of images. Even if the information in the image is insufficient to determine all details of the ion distribution, the developed algorithms can still often provide a quantitative estimate of the range of ion intensities or densities on a time scale comparable to the exposure time required to acquire the images themselves.

The ENA imaging technique can be used for remote sensing of planetary magnetospheres, and it has been successfully applied to the terrestrial magnetosphere (*Mitchell et al.*, 2000; *Pollock et al.*, 2000; *Moore et al.*, 2000). Apart from the Earth, it has been considered for Saturn (*Curtis and Hsieh*, 1989), for the Martian plasma environment (*Holmström et al.*, 2002; *Barabash et al.*, 2002) and for that of Venus (*Gunell et al.*, 2005). ENA imaging technique was also used to image ENA production resulting from the interaction of Titan's exosphere with Saturn's magnetosphere (*Amsif et al.*, 1997; *Dandouras and Amsif*, 1999).

2.2 Principle functions of ENA instruments

In order to detect ENAs and obtain a sufficiently good signal-to-noise ratio, an ENA sensor has to be able to perform the following basic functions:

- detection of incoming ENAs with angular, and preferably energy and mass, resolution,
- rejection of charged particles,
- suppression of EUV/UV photon background.

LENA / MENA detection is usually performed by ionization of neutral particles by means of interaction with foils or conversion surfaces, followed by detection of ionized components. Depending on which particular ENA sensor detection technique is used, certain angular, energy and mass resolutions can be achieved. Typically, one can achieve an angular resolution of 5° –

40° in one direction and 1° – 10° in another one (in the case of a 1D imager), energy resolution $\Delta E/E$ of 30% – 50% for H-ENA and the ability to distinguish between H-ENA and O-ENA.

Charged particle background should be removed from the incident flux prior to detection, because incident energetic charged particles and ENAs of the same energy and species are indistinguishable to a particle detector (*McEntire and Mitchell*, 1989). Often, the local ion and electron fluxes in the ENA detector environment can exceed the ENA flux to be diagnosed. A deflector of the ENA sensor prevents ions and electrons from entering the instrument. Charged particle rejection factor of $>10^3$ is typically required.

Suppression of EUV/UV photon fluxes is vital for every ENA instrument because EUV/UV photons cause photo-electron emission from every lit surface. Emitted photo-electrons can consequently be registered by particle detectors (e.g., MCP detectors) used for incident ENA trajectory and energy determination. Moreover, EUV/UV photons can trigger particle detectors directly. Therefore, an intensive UV flux can induce an unacceptably high noise background in the ENA measurements and therefore has to be rejected. A typical UV photon rejection factor of $>10^5$ is required.

Other ENA instrument requirements are:

- large geometrical factor, $>10^{-3}$ cm^{2}sr / pixel,
- sufficiently wide dynamic range. The ENA sensor should ideally be capable of detecting ENA fluxes of up to 10^7 cm^{-2}sr^{-1}s^{-1} in a covered energy range. Thus, particle counting rate would range up to $\sim 10^4$ counts/s.

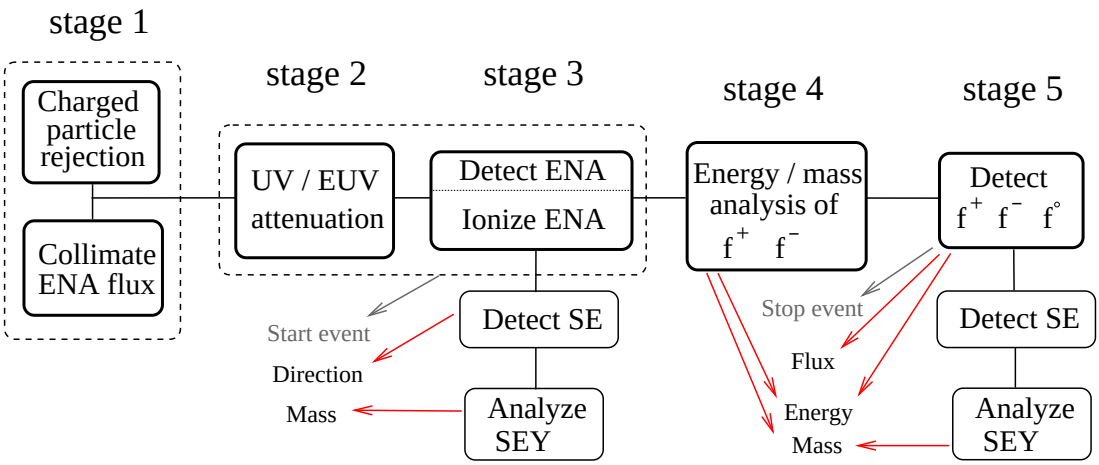

Figure 2.2: Principle functions of a generic ENA instrument are shown. For details see text.

The schematic structure of a conventional ENA instrument is shown in Figure 2.2. The instrument performs several basic functions which are shown as a sequence of stages. The first stage is a deflection system, which rejects charged particle fluxes and collimates the incoming ENA flux.

At the second stage EUV/UV photon flux attenuation is performed, followed by either an ENA detection or an ENA ionization, release of secondary electrons, and/or generation of a start event for the TOF measurement, at the third stage. Mapping secondary electrons to a position sensitive particle detector can also give the direction of an incoming ENA. Analysis of secondary electron yield (SEY) can also provide a crude mass resolution. Very often UV photon flux attenuation is performed at the same time with an ENA ionization, i.e., stages 2

and 3 are combined (e.g., thin foils provide both UV rejection and ENA ionization).

At the fourth stage the ionized fraction of neutrals, i.e. positively and/or negatively charged particles (f^+ and f^-, respectively), can be analyzed for energy and/or mass. If this stage is present, then either ion energy or mass or both can be obtained. Otherwise, a particle mass can be derived by means of secondary electron yield analysis, and particle energy can be calculated from the TOF measurement and estimated mass information.

At the fifth stage the ionized components (and in some cases neutral fraction as well) are detected at a low-energy particle detector (e.g., MCP) directly, striking the detector, or indirectly, striking a surface optimized for high secondary electron yield, with consecutive detection of released secondary electrons. Analysis of secondary electron yield would give also a crude mass resolution. A stop timing signal is obtained at this stage for the TOF measurements, yielding incident ENA velocity. Combining this information with that of a particle mass, the ENA energy can be derived.

The first three stages are present in the vast majority of LENA/MENA detecting sensors. Any of the other stages or a combination of these can also be present, depending on the practical design of the sensor. In order to increase an EUV/UV photon rejection factor, UV attenuation can be done during any other stage, if feasible. There is a detailed description of stages 1, 2, 3 in the following sections.

2.3 Deflection systems

For most missions on which ENA instruments are flown, there are likely to be significant local charged particle fluxes at the location of the spacecraft. In fact, for magnetospheric missions one has to assume the local energetic charged particle fluxes in the ENA imager environment to be orders of magnitude higher than the ENA flux to be measured. Charged particles have to be prevented from entering the ENA instrument or greatly reduced prior to any interaction with a detector in an ENA imager. This is because for most particle detectors the detection of charged particles is similar to that of ENAs of the same energy. Charged particles up to a certain energy can be prevented from reaching a detector by deflecting them out of the path of the ENAs in the entrance system of an ENA imager and absorbing them in the structure. This can be realized with either electric or magnetic fields, or both.

Electric fields are normally used for charged particle rejection. The first element of an ENA instrument is typically a mechanical collimator, which defines the overall FOV of the instrument. The collimator can be built in a such way as to consist of two or more closely spaced parallel metallic plates of length L and separation D, and serve also as an electrostatic deflector. If these plates are biased with high voltages of alternate polarity, transverse electric field is created in-between the plates, and charged particles can be deflected to the collimator plates and be absorbed, while the ENAs are not affected. Charged particles with energy below the rejection energy E_e will be deflected to the collimator plates. E_e is defined by the applied voltage V between two adjacent plates and the geometrical dimensions of those, according to equation 2.2 (*McEntire and Mitchell*, 1989). Fringe electric fields can be ignored, if $L \gg D$.

$$E_e = qV\left[1+\left(\frac{L}{4D}\right)^2\right] \tag{2.2}$$

where q stands for the elementary charge. For example, for $V = 10$ kV, $L = 0.12$ m and $D = 0.004$ m, the propagation of ions and electrons of energy $E_e/q < 570$ kV beyond the deflection plates is prevented.

Permanent magnets can also be included in the collimator. With a magnetic field strength B, and magnet length L_m, particles with mass m and energy below the rejection energy E_b will be deflected into the collimator structure, according to equation 2.3 (*Wurz*, 2000).

$$E_b/q = \frac{qB^2}{2m}\left(\frac{D^2 + L_m^2}{2D}\right)^2 \tag{2.3}$$

For example, for B = 0.01 T, L_m = 0.02 m and D = 0.004 m, electrons with energy $\leqslant$24 keV are prevented from moving beyond the deflection system. Magnets have an advantage of zero power consumption. However, in order to deflect ions or high energy electrons higher magnetic field strengths and, hence, larger/heavier magnets are required as well as a magnetic shield that can be unacceptably heavy for space-borne instrumentation. Therefore permanent magnets are used primarily to deflect incident electrons away from the detector.

A charged particle rejection factor of $\geqslant 10^3$ is achievable by means of the deflection techniques described. In practice, it is not enough to deflect incoming ions to hit a plate in the collimating system, since the deflected ions and, in particular, electrons may scatter further into the instrument and cause an increase of background signal. Thus, roughening of the deflection plates or anti-scatter serration is an important part of a deflection system design.

2.4 UV rejection

UV photon fluxes in the interplanetary environment can be large (especially at distances less than 2 astronomical units (AU) to the Sun), with a dominant line being H Lyman-α at 1216 Å. This radiation is resonantly scattered on neutral hydrogen atoms in the planet's exosphere to create widespread Lyman-α emissions from the planetary corona, with intensities, e.g. at Earth, ranging from $\sim 5\times10^7$ to 10^9 photons·cm^{-2}sr^{-1}s^{-1} depending on the vantage point and observation directions (*McEntire and Mitchell*, 1989). EUV/UV photons have sufficient energy to stimulate low-energy particle detectors, such as MCP or channel electron multiplier (CEM). Since there is a direct optical path from the exterior into an ENA detector, UV fluxes can cause unacceptable background count rates and thus severely disturb ENA measurements or even, at most, damage an ENA sensor. Therefore, incident UV photon flux attenuation down to acceptable levels is a very important aspect of an ENA imager design. There are different techniques to counter intensive UV flux, depending on the energy range of the ENA sensor, as shown in Figure 2.3 (*Funsten et al.*, 1998).

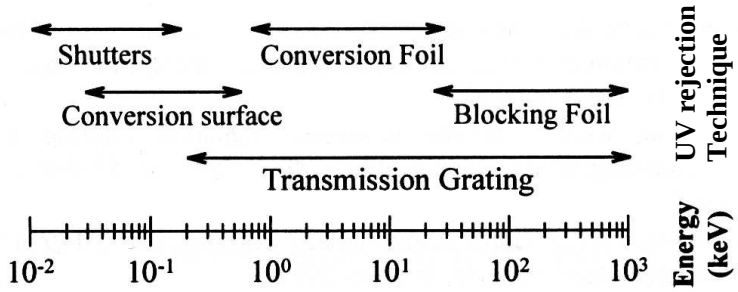

Figure 2.3: Applicability of UV rejection techniques for different ENA energy ranges. Adapted from *Funsten et al.* (1998).

Thick UV blocking foils (~10-15 μg/cm^2) in front of an imaging ENA detector screen out a large fraction of UV flux, though allowing only high energetic neutrals to pass through

(*Mitchell et al.*, 1998). Such foils have to be thick enough to block the UV photons efficiently, but still be thin enough to allow the passage of ENAs without blurring the image. These conflicting demands result in blocking foils with only moderate photon suppression factors in the range of 10 to 10^3, depending on foil thickness (*Hsieh et al.*, 1991).

Thin (<10 μg/cm^2) and ultra-thin conversion foils (~1 μg/cm^2) have low UV attenuation factors, and allow LENA/MENA to penetrate. ENAs, converted to ions after passing the foils, can be separated from UV photons afterwards, by means of electrostatic deflection.

Low energy ENAs cannot penetrate foils. Hence, for lower energy ranges, surface interaction techniques are utilized. A solution to separate LENAs from the incoming UV photon flux is to convert LENAs to negative ions on low work function surfaces and subsequently deflect them electrostatically to separate newly created ions from the ambient UV (*Gruntman*, 1993).

Another way to separate UV photon flux and ENA flux is to mount free-standing transmission gratings over an ENA imager aperture. Transmission gratings consist of a set of parallel bars supported by a large mesh grid. The gratings with a period of 200 nm, 100-140 nm bar width and, therefore, 100-60 nm slit width were developed and investigated (*Funsten et al.*, 1995). Such gratings act as a diffraction filter to suppress incident UV radiation, while permitting ENA transmission. Figure 2.4 shows UV transmission through gold gratings as a function of wavelength. A Lyman-α flux transmission factor of 4×10^{-5} is achieved (*McComas et al.*, 1998). More efficient UV suppression (by a factor of up to 10^7) is achieved by two sequentially located and perpendicularly oriented gratings, as the UV suppression is lower in the dimension along the slit. The total geometric transparency of the grating, i.e, transmission to ENA fluxes, ranges from 0.08 to 0.15 (*Funsten et al.*, 1995).

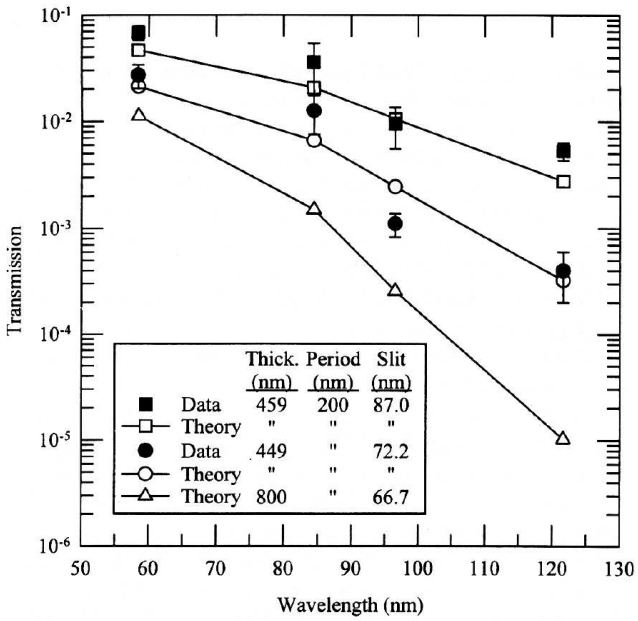

Figure 2.4: Plots of measured (solid symbols) and calculated (open symbols and lines) UV transmission through gold gratings as functions of wavelength. From *McComas et al.* (1998).

This technique differs importantly from previously suggested thin foil/surface interaction in that the large EUV/UV flux is rejected prior to ENA detection, and therefore, it is not necessary to extract the small signal from very large background counting rates.

For even lower energy range a high frequency shutter technique can be used. A very high

suppression factor for incident EUV/UV photon flux is achieved, as the shutters perform velocity filtering of the incoming particles and are basically closed during the detection time window (see Section 2.5.3).

Blackening of ENA detector internal structure surfaces as well as deflection plates allows the scattered EUV/UV photon flux to be attenuated. Furthermore, utilizing TOF coincidence techniques in an ENA imager allows further reduction of background noise caused by UV photons.

2.5 ENA detection and analysis: Instrument examples

Various ENA ionization techniques are utilized in ENA instrumentation for different energy ranges. Detectors for MENA or the high energy part of the LENA range (>600 eV) use thin/ultra-thin foils in order to convert an incoming ENA to an ion in a foil passage. Different detection techniques are needed for the low energy part of the LENA range. This is because such low energy (<600 eV) is insufficient for a particle to penetrate through an ultra-thin foil. Several approaches are now possible. One approach is to use a particle interaction with a conversion surface upon scattering to initiate detection. Different implementations of particle–surface interaction processes have led to development of a number of techniques. Some of them are discussed below, namely ENA detection based on ENA-to-negative ion conversion, particle reflection, secondary ion emission, and kinetic emission of secondary electrons. Another approach is to use high frequency shutters. These ENA detection concepts are reviewed in the following sections, complemented by examples of ENA instrumentation utilizing the respective ENA detection techniques.

2.5.1 Foils

The ionization of incoming ENAs while passing through one or several thin foils is the most well-developed technique with heritage from ion spectroscopy. In ENA instrumentation, foils play a three-fold role: they serve for ENA ionization, for incident EUV/UV radiation attenuation and for producing secondary electrons to generate a detection event. In order to allow passage of ENAs through a foil, it must be freestanding without a solid substrate support and, at the same time, be mechanically robust to withstand vibrations and acoustic shocks during the rocket launch. A high-transparency (90%-95%) metal grid usually provides the required foil support with slight reduction of the effective area of the foil. Materials such as carbon or silicon are often used for thin foil production, since low atomic number materials reduce scattering and energy losses of penetrating particles. Ultra-thin foils of carbon are characterized by high mechanical strength and technological simplicity. Foil composition is usually optimized to maximize UV suppression while providing high secondary electron yield (*Hsieh et al.*, 1991). Different units are used for foil thickness, μg/cm^2 and Å. Foils of different thickness are used in space-borne ENA detecting instrumentation: thick (>10 μg/cm^2), thin (1-10 μg/cm^2) and ultra-thin ($\leqslant$1 μg/cm^2). Foils as thin as ~20 Å (~0.1 μg/cm^2) have been reported by *McComas et al.* (1991).

ENA penetration of a thin foil results in particle energy loss, scattering, possible change of the initial charge state, and emission of electrons from the foil surface (*Gruntman*, 1997). Figure 2.5 gives an overview of processes which occur during an ENA passage through a thin foil. ENA scattering (i.e., deviation of the final direction of flight from the initial one by the angle ϕ) and energy loss occur due to collisions and interactions with solid body electrons

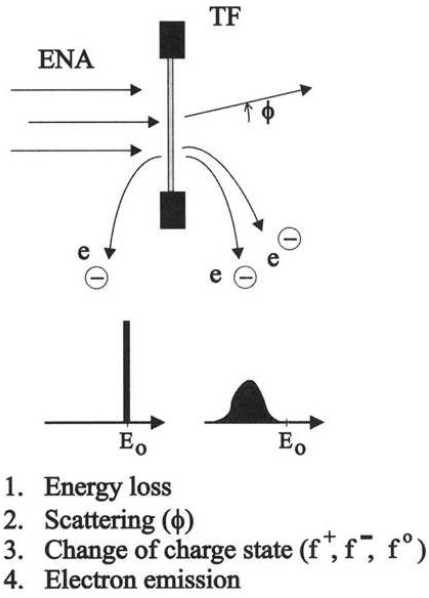

Figure 2.5: ENA penetration through a thin foil (TF) results in particle energy loss, scattering, possible change of particle charge state (fractions f^+, f^-, f°), and secondary electron emission (backward and forward). From *Gruntman* (1997).

and lattice ions. These interactions are a statistical process, and an incident monoenergetic and collimated particle beam would be characterized by energy and angular distributions after leaving the foil.

An incident particle loses its initial charge after passing through the first 2-3 atomic layers in the foil, and the exit charge state does not therefore depend on the initial charge. An incident ENA can either be stripped to a positive ion (f^+) or emerge as a negative ion (f^-), or stay neutral (f°). ENA ionization efficiency as well as the charge state of a particle exiting the foil, are a function of particle species and energy (*McComas et al.*, 1998), as shown in Figure 2.6.

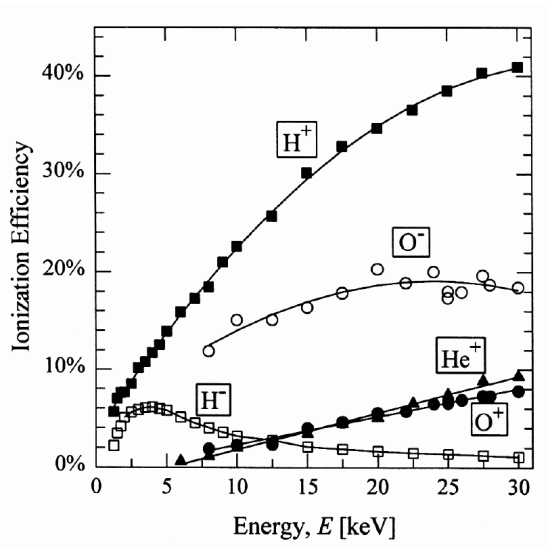

Figure 2.6: Ionization efficiency for H, He, and O as a function of energy. From *McComas et al.* (1998).

Secondary electron emission occurs from both sides of the foil, forward and backward, while the particle penetrates it (*Gruntman*, 1997). Electron emission can be used to provide a Start event in a conventional TOF spectrometer designed for MENA detection and using thick (10-15 μg/cm^2) foil, allowing efficient blocking of background EUV/UV photon flux. Meanwhile, in LENA instruments utilizing ultra-thin foils, the photon flux is only partially attenuated. As the foils are directly exposed to the incoming radiation, photo-electrons emitted from foils used for coincidence and TOF measurements, that are able to trigger MCP detectors, can increase the background count rate during the ENA measurement. This is because photo-electrons are indistinguishable from the secondary electrons emitted from a thin foil by ENA passage.

A concept of a foil-based ENA imager (*Funsten et al.*, 1995) for a spinning spacecraft, designed to detect ENAs in the energy range 0.9 – 30 keV, is shown in Figure 2.7. ENAs

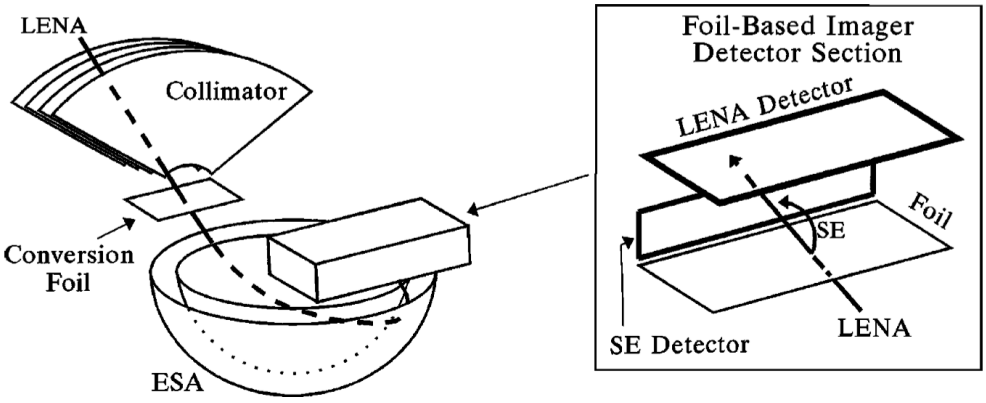

Figure 2.7: Schematic of an ENA imager, based on the ENA stripping in an ultra-thin foil. LENA – ENA in the energy range of 0.9 – 30 keV, ESA – electrostatic analyzer, SE – secondary electron. From *Gruntman* (1997).

pass a collimator that sets an arrival angle, and then transit an ultra-thin (~1.1 μg/cm^2) carbon foil. Newly formed ions enter a hemispheric electrostatic analyzer and are subsequently analyzed for energy per charge (E/q). The electrostatic analyzer also effectively rejects EUV/UV photons. Ions that pass through the electrostatic analyzer enter an ion detector, located at the exit focal plane of the analyzer. The ion detector (Figure 2.7 right panel) is a combination of another ultra-thin foil and two MCP position-sensitive detectors. An ion transits this second foil, yielding secondary electrons, detected by one of the MCP detectors, and is detected at the second MCP detector. Measurement of the coordinates of both electron and particle impact positions allows reconstruction of the trajectory of the incident ENA. The time interval between electron and particle detection establishes the velocity of the ion and can be employed for effective suppression of noise counts. Since the ion energy is selected by the electrostatic analyzer, the ENA mass can be determined. The instrument instantaneous FOV is $120^\circ \times 2^\circ$ with $120^\circ \times 360^\circ$ coverage during one spacecraft spin and a nominal pixel resolution of $2^\circ \times 2^\circ$. Estimated energy resolution $\Delta E/E$ is ~10% for 5 keV H-ENA.

2.5.2 Surface interaction

Currently, several methods are employed for particle detection based on surface interaction.

Ionization

Direct detection of ENAs with energies below a few hundred eV is not feasible. Since secondary electron emission, on which most of the particle detectors rely, gives useful secondary electron yield only at particle energies in excess of a few hundred eV, conversion of atoms into charged particles is necessary. One approach to ionize LENAs is based on an atom-to-negative ion surface conversion (*Gruntman*, 1993). The concept is shown schematically in Figure 2.8.

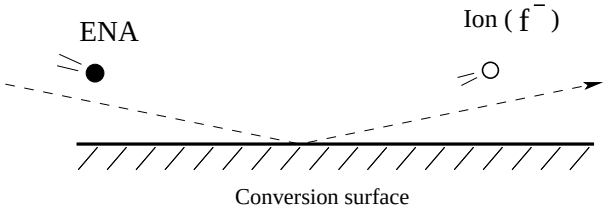

Figure 2.8: Schematic view of a neutral-to-negative ion conversion process.

The first instrument to use an atom-to-negative ion conversion technique is the IMAGE / LENA instrument (*Moore et al.*, 2000), designed to detect ENA in the energy range of ~10-750 eV. The instrument concept is shown in Figure 2.9.

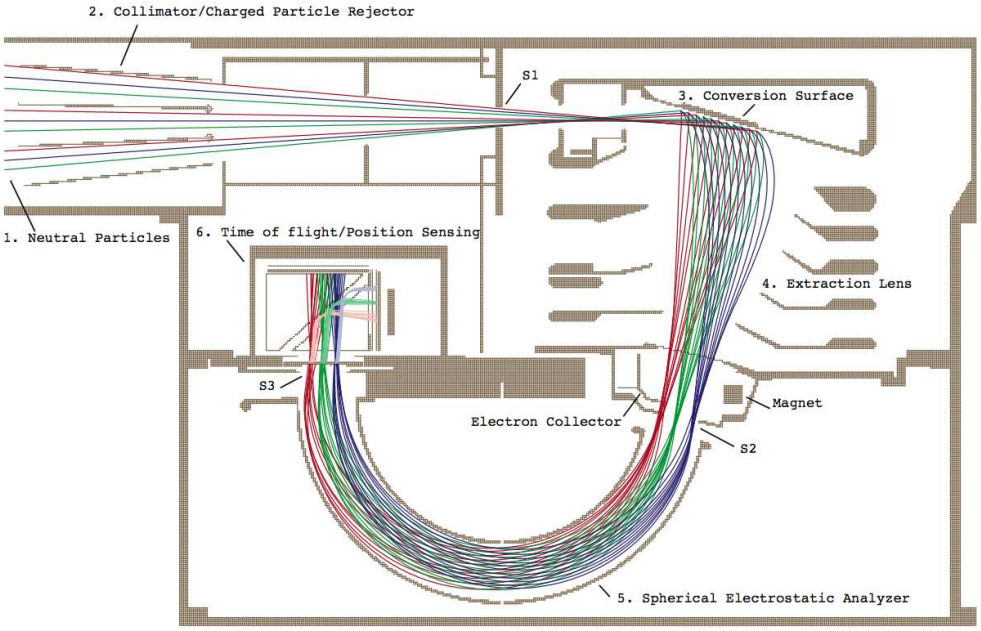

Figure 2.9: The IMAGE / LENA principle schematics and ray-tracing. Adapted from *Moore et al.* (2000).

The ENA trajectories are depicted by color lines, corresponding to different energies. All incoming particles enter a collimator and charge particle rejection system, designed to reject charged particles with an energy of ⩽100 keV/q. Incoming neutrals pass through a ~1 cm^2 pinhole, strike a near-conical tungsten conversion surface at a shallow angle of 15°, where a considerable fraction of nearly specularly reflected particles becomes negatively charged.

The ionized fraction of the neutrals is accelerated and collected by an ion extraction lens that focuses them spatially and disperses in energy. A broom magnet in front of an electrostatic

analyzer removes electrons with energies of below 200 keV. Accelerated negatively-charged ions, mapped onto the electrostatic analyzer entrance, are delivered to a TOF sensor and 2D imaging system, that sorts the particles by polar angle of arrival and energy. The imaging TOF subsystem contains $\sim 2\ \mu g/cm^2$ carbon foils at the entrance aperture, placed in the focal plane of the electrostatic analyzer. Upon striking the carbon foil, the negative ions produce secondary electrons, which provide a start pulse as well as the azimuth and radial position information. Particles (both ions and neutrals) exit the carbon foil and proceed to a Stop MCP.

As a result, a direct correlation between the azimuth direction and the position on the plane of the carbon foil is achieved, allowing the original arrival direction of an ENA to be deduced. In a similar manner, energy information is extracted from the radial impact position. EUV/UV photon rejection is done by means of an electrostatic analyzer. LENA provides a $90° \times 8°$ FOV with a pixels size of $8° \times 8°$. Energy resolution $\Delta E/E \sim 100\%$ and mass resolution $\Delta M/M \sim 0.25$ are achieved.

Reflection

The basic concept for detecting ENA by means of ENA reflection on a reflection surface with following detection at a MCP detector is shown in Figure 2.10.

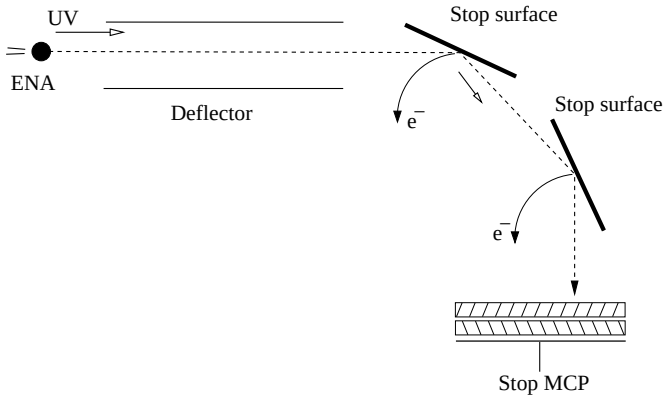

Figure 2.10: ENA deflection on a reflection surface.

The LENA / MENA strikes a reflection surface at a shallow angle ($< 30°$) and leaves it as a negatively (f^-) or positively (f^+) charged particle or neutral ($f°$). The emerging particles proceed to another reflection on a second reflection surface. Finally, a certain fraction of emerging particles (f^+, $f°$) strikes a MCP position-sensitive detector. Negatively charged particles as well as photo-electrons are repelled from the MCP detector by means of a retarding grid in front of the MCP, or negative potential of the MCP front surface.

This approach was used in the Prelude In Planetary Particle Imaging (PIPPI)–MCP instrument on ASTRID, the first dedicated ENA instrument to detect magnetospheric ENAs (*Barabash*, 1995; *Barabash et al.*, 1998) and in Neutral Particle Imager (NPI) of the ASPERA-3 / ASPERA-4 packages on Mars Express and Venus Express missions (*Barabash et al.*, 2004, 2006).

The PIPPI imager comprises two sensor heads, namely PIPPI–SSD, a high energy detector and PIPPI–MCP, a low energy detector (Figure 2.11). The latter is dedicated to measuring 0.1-70 keV LENA/MENA by means of ENA conversion into secondary particles, followed by detection at an imaging MCP detector.

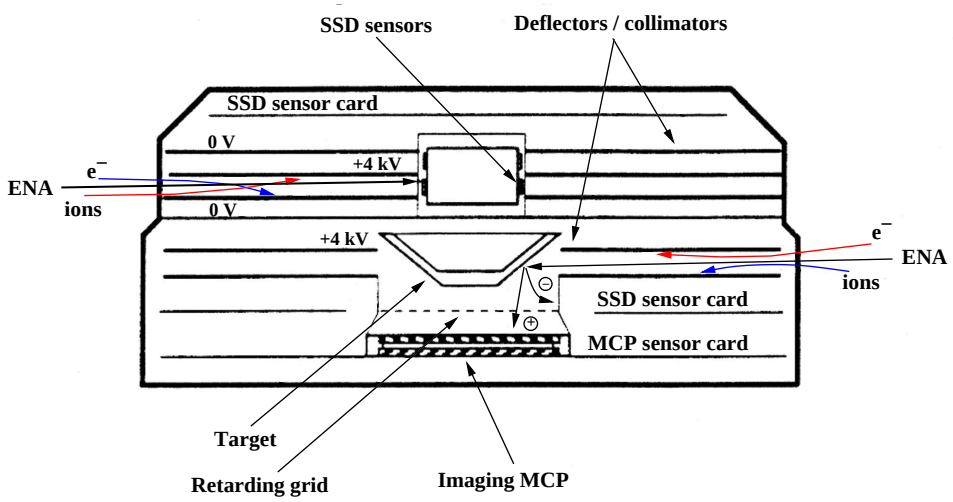

Figure 2.11: The PIPPI sensor head schematics. From *Barabash* (1995).

The PIPPI–MCP deflection system was designed to reject charged particles with energy $\leqslant 70$ keV/q. The space between collimation disks is divided into 32 sectors each with $9^\circ \times 18^\circ$ FOV. Neutrals, passing through the deflection system, strike a 32-sided cone target at $\sim 20^\circ$ angle of incidence, producing secondary particles, that are further detected by a MCP detector. UV suppression is achieved by blackening the collimator plates and by selection of the target block coating. Secondary and photo-electrons are retarded by the potential of the front surface of the MCP, operating in the ion detection mode. The sensor provides a FOV of $9^\circ \times 360^\circ$ and covers almost 4π in a half satellite spin period (with a spacecraft rotation plane perpendicular to the 360° viewing plane).

Advantages of such instrumentation are simplicity and the possibility of obtaining a high angular resolution in one dimension. The application field is, however, rather constrained as such instruments normally have low sensitivity and do not have sufficient UV rejection efficiency, or capability for energy- or mass analysis.

Secondary ion emission

Figure 2.12 shows an approach for detecting ENA in very low energy ranges making use of secondary ion sputtering from a sensitive surface by incident ENA.

The first instrument utilizing secondary ion emission for detection of ENAs in a very low energy range is the GAS experiment on board Ulysses, the interstellar neutral helium detector (*Witte et al.*, 1992). It is designed to measure interstellar neutral helium flux directly in the energy range of 30-100 eV. Schematic cross-sections of the GAS sensor head are shown in Figure 2.13.

Incoming particles first pass electrostatic deflection systems, which serve as filters against charged particles. Incident ENA are converted into secondary ions and electrons upon hitting the lithium fluoride (LiF) surface. When bombarded with neutral helium atoms, the yield of Li^+ from the surface is much higher than that of F^- because of the better momentum transfer from He to Li. As LiF is an ionic crystal, the efficiency for secondary ion production is comparatively high and is about 10^{-2} for incident ENA energy around 80 eV. Towards lower energies the

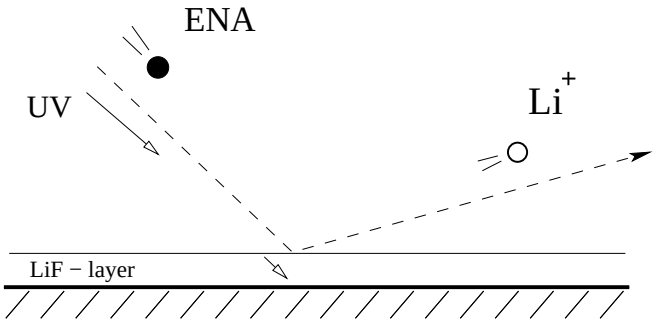

Figure 2.12: Schematic view of a secondary ion sputtering from a LiF layer. LiF is transparent to UV radiation, thus UV is suppressed.

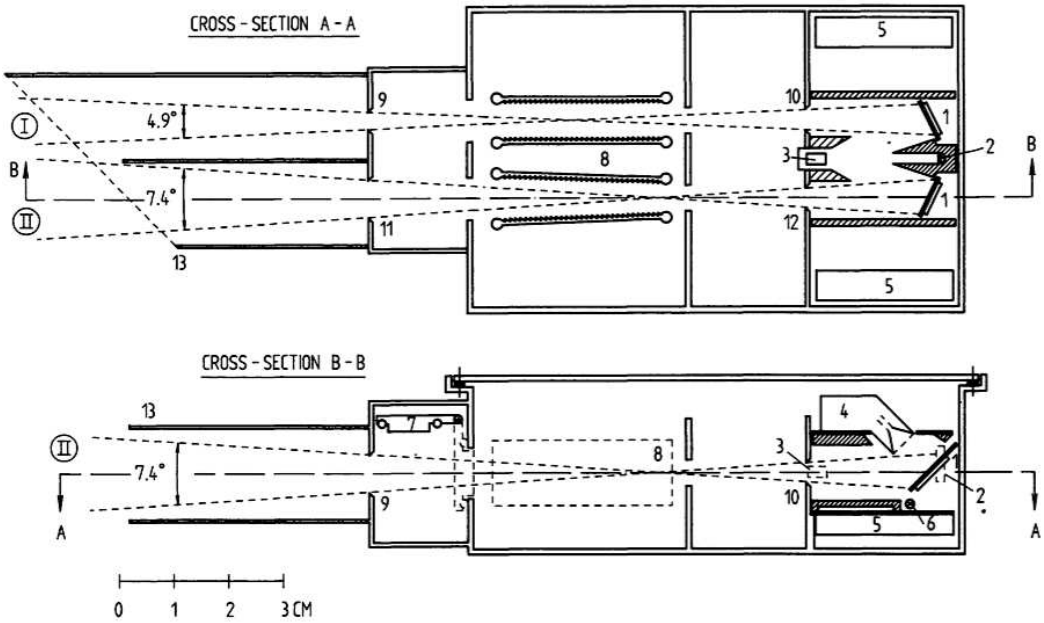

Figure 2.13: Cross-sections of the Ulysses / GAS sensor head (schematic): 1) conversion plate with heater, evaporated with lithium-fluoride (LiF), 2) quartz crystal for monitoring the LiF evaporation process, 3) furnace with LiF supply, 4) CEM, 5) CEM electronics, 6) tungsten filaments to stimulate the CEMs, 7) vacuum-tight cover in closed (dashed lines) and open position, 8) electrostatic deflection system, 9,10,11, and 12) circular apertures defining the field of view of channel I and II, 13) light baffle. From *Witte et al.* (1992).

efficiency falls off rapidly. Therefore, an instrument based on LiF as a conversion surface is only useful for neutral helium detection if the incident particle energy is above ~30 eV and if there are no much heavier atoms (e.g., *O*) to be detected. It is ideal for detection of interstellar neutrals as interstellar *He* population is next most abundant after *H* and its energy range is well defined.

Since LiF is transparent to UV radiation, Lyman-α photons have a low photo-electron yield from the LiF surface. To keep the surface transparency to UV radiation high, the LiF cover is refurbished periodically.

The yielded Li^+-ions are accelerated by the electric field to a particle detector, and at the same time photo-electrons are suppressed. Therefore, a detector system based on the release of Li^+-ions from a LiF surface is very insensitive to UV photons. An integrated turn-table

together with the rotation of a spacecraft allow coverage of the whole celestial sphere. The advantages of the secondary ion emission instrumentation are an ability to detect He ENAs in a very low energy range, and a sufficiently high UV photon rejection factor. However this type of instrumentation allows particle detection with no capability for mass analysis and very limited energy analysis using the sputtering threshold energy and the change in the apparent energy of incident ENAs due to the orbital motion of the spacecraft.

Secondary electron emission

A newly-developed method for detecting ENA in low and medium energy ranges is based on the kinetic emission of secondary electrons upon a particle scattering from a dedicated surface. The basic principle of this approach is shown schematically in Figure 2.14. ENAs strike a Start surface at a shallow angle of incidence of $\sim 15^{\circ}$. Secondary electrons, yielded from the surface and detected at a Start MCP detector, give a start signal for a TOF measurement. The reflected particles of any charge state proceed towards the second, Stop surface, and strike it nearly normally to reduce TOF path length variation. Secondary electrons released from the Stop surface, detected at a Stop MCP detector, give a stop signal for the TOF measurement. The energy dependence of the secondary electron yield limits this technique to low energies of >100 eV.

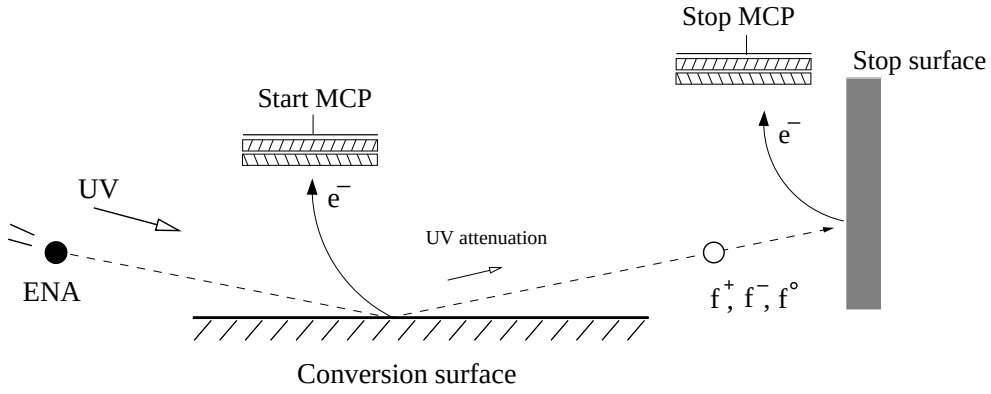

Figure 2.14: Schematic view of a TOF spectrometer, based on kinetic emission of secondary electrons.

The ASPERA-3 / ASPERA-4 NPD sensors, described in this thesis in Chapter 4, utilize this concept of ENA detection (*Barabash et al.*, 2004, 2006). The main advantage of this technique is the high efficiency obtained, as no particle separation by charge is required after ENA reflection on the Start surface. Comparatively simple design and the light weight of the instrumentation allow it wide applicability.

2.5.3 High frequency shutters

If one replaces a conventional carbon foil and conversion surface (used in TOF mass spectrometers) with high frequency shutters (*Funsten et al.*, 1995) one can build ENA sensors without intrinsic energy range limitations, and ones that are more robust against EUV/UV. Figure 2.15 illustrates two different implementations of a shutter-based ENA direct detection technique.

In Figure 2.15(a) two shutters, separated by a distance d, are involved. Each shutter is a set of plates, one plate is stationary and the other is movable. Each plate has an aperture, the width of which is less than half the travel distance of the moving plate. The oscillating

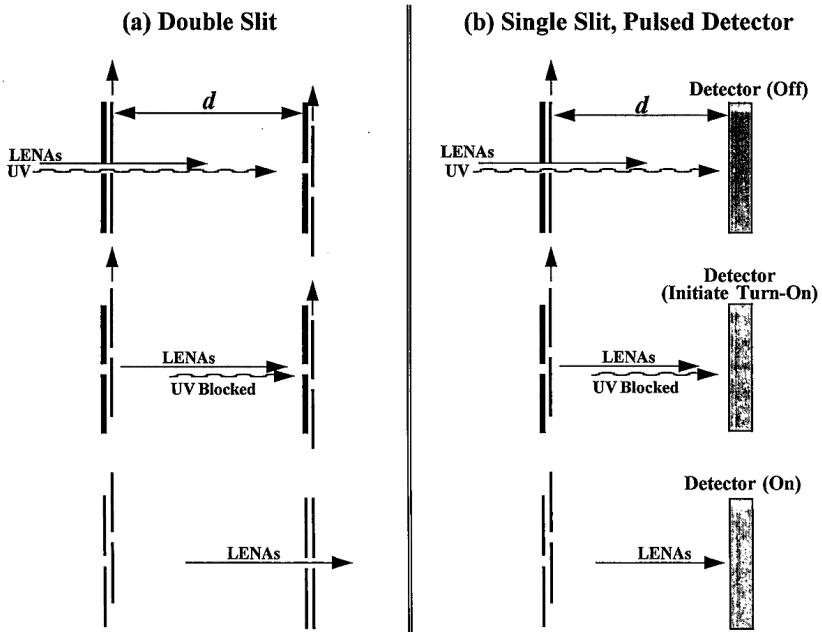

Figure 2.15: Schematic views of using high frequency shutters in ENA detection. From *Funsten et al.* (1995).

plates of both shutters are 180° out of phase. UV trapping proceeds as shown in panel (a). The apertures of the first shutter plates are aligned (i.e., shutter is opened), so that both ENAs and UV photons can enter the region between the shutters. The apertures of the second shutter plates are misaligned (i.e., shutter is closed), so that UV photons cannot enter the detector region. Next, both shutters are closed, so the region between the shutters acts as a light trap in which UV photons are absorbed. Finally, the second shutter is opened, so that ENAs can enter the detector region. This cycle is repeated. The typical time period when the shutters are closed is set to be much longer than that with opened shutters; UV photon flux is absorbed and photo-electrons are removed by means of electrostatic deflection during this period.

The technique illustrated in Figure 2.15(b) is similar, except the second shutter is replaced with a detector that is electrically gated to operate only when the shutter is closed and to shut off when the shutter is opened. An incoming ENA is identified by having it pass through the opened shutter (at that moment a start signal is generated) and then by measuring the elapsed time until the particle hits a particle detector at a given distance. Basic shutter 'open' state time is much shorter than that of the 'closed' state and the free-field path d is sufficiently long. Hence, the UV-induced signal in the detector can be clearly separated from the one caused by ENAs, as the particles arrive a while after the shutter closes. This results in ENA detection while UV photon flux is rejected.

The first space-borne instrumentation utilizing the concept based on Micro-Electro-Mechanical System (MEMS) technology, is under development (*Brinkfeldt et al.*, 2006a). It is shown in Figure 2.15(b). The verification of the technique will be first performed using MEMS shutters in an ion spectrometer. The expected ion energy range is ~5-100 eV/q, energy resolution ~15%. The sensor typical oscillating frequency is in the range of 100-300 kHz. Duty cycle of the sensor times MEMS transparency is designed to be $>10^{-5}$, which will place constraints on a lower detection limit of the ENA flux. Flight verification of the instrument is due to be done during the PRISMA mission in 2008 (*Wieser et al.*, 2006).

Chapter 3

The ASPERA-3 and ASPERA-4 experiments

The Analyzer of Space Plasmas and Energetic Atoms (ASPERA)-3 experiment (Figure 3.1) on board the European Space Agency (ESA) Mars Express mission is a comprehensive plasma diagnostics package to measure ENAs, electrons and ions with a wide angular coverage from a three-axis stabilized platform (*Barabash et al.*, 2004). The ASPERA-4 experiment (Figure 3.2) on board the Venus Express mission is a replica of the ASPERA-3 package.

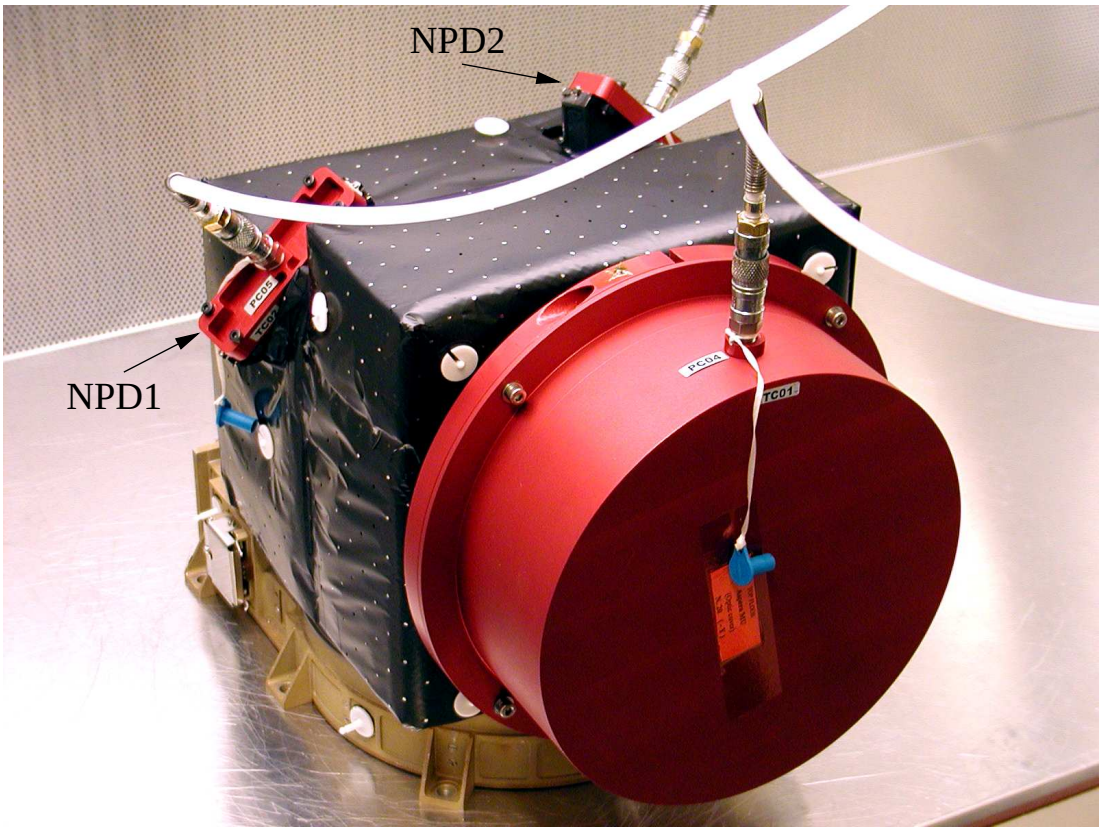

Figure 3.1: Main unit of the ASPERA-3 flight instrument, covered with black multi-layer insulation (MLI). The NPD with GN_2 purging tubes connected is identified. All sensors have red protective covers.

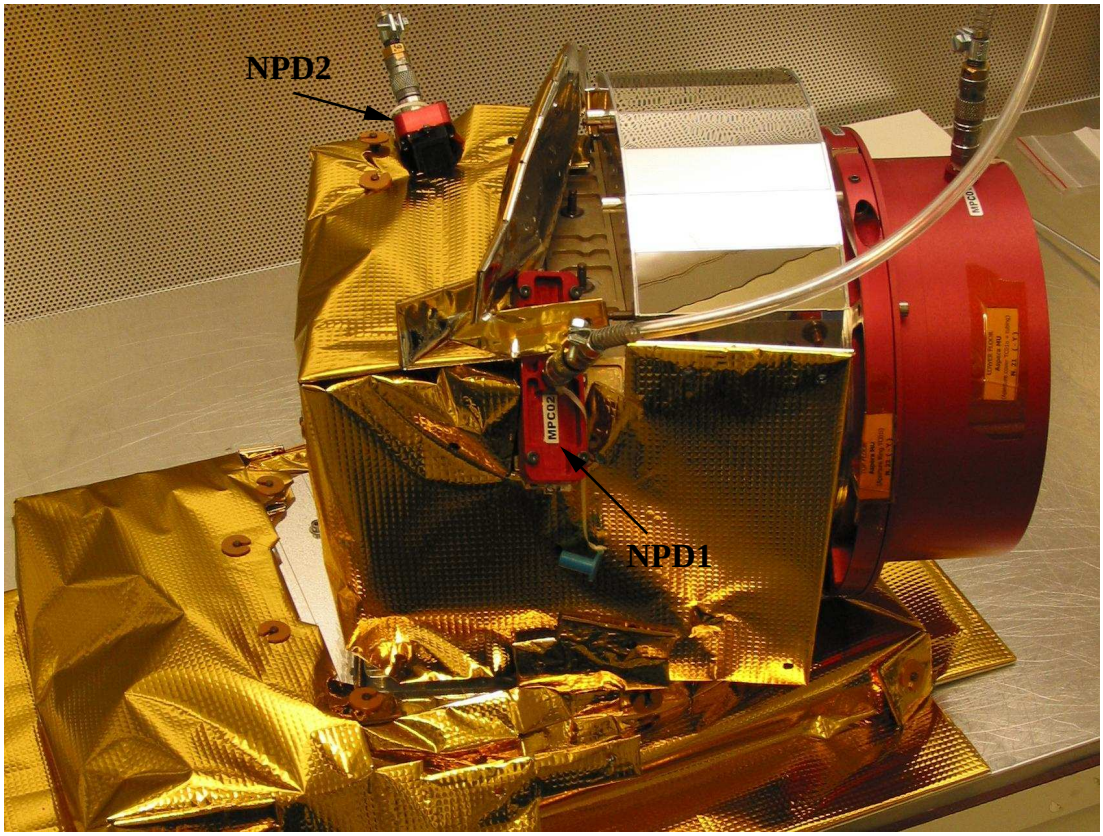

Figure 3.2: Main unit of the ASPERA-4 flight instrument, covered with white MLI. The NPD with GN_2 purging tubes connected is identified. All sensors have red protective covers.

3.1 Scientific objectives

3.1.1 ASPERA-3

The studies of the solar wind – atmosphere interaction address the fundamental question: How strongly do the interplanetary plasma and electromagnetic fields affect the Martian atmosphere? This question is already coupled with the problem of what happened to the Martian water that once flowed in numerous channels? As we know from the experience of our Earth, together with an inventory of organic compounds and external energy sources, liquid water is a fundamental requirement for life as we know it. Therefore, a clear understanding of the fate of the Martian water is a crucial issue in resolving the problem of whether or not life existed on Mars in the past.

In order to study the processes related to the impact of the solar wind – Mars interaction on the atmosphere, the ASPERA-3 experiment was designed to measure electrons and ions in the hot plasma energy range, as well as to provide remote sensing (diagnostics) of the plasma–neutral gas interaction via ENA measurements.

The general scientific objective of the ASPERA-3 experiment is to study the solar wind–atmosphere interaction and to characterize the plasma and neutral gas environment within the space near Mars through the use of ENA imaging and by measuring local ion and electron plasma populations.

The general scientific task can be subdivided into specific scientific objectives, listed in

Scientific objectives	Associated measurements	Measurement requirements
Determine the instantaneous global distributions of plasma and neutral gas near the planet	ENAs originating from the shocked solar wind	Measure the ENA flux in the energy range tens of eV - few keV with 4π coverage. ENA flux > 10^4 $cm^{-2}s^{-1}keV^{-1}$ Measure the upstream solar wind parameters
Study plasma induced atmospheric escape	ENAs originating from the inside of the magnetosphere	Mass resolving (H / O) ENA measurements in the energy range up to tens of keV. ENA flux > 10^3 $cm^{-2}s^{-1}keV^{-1}$
Investigate the modification of the atmosphere through ion bombardment	ENA albedo	Mass resolving (H / O) ENA measurements in the energy range down to tens of eV from the nadir direction ENA flux > 10^6 $cm^{-2}s^{-1}keV^{-1}$ (100 eV)
Investigate the energy deposition from the solar wind to the ionosphere	Precipitating ENAs	ENA measurements in the energy range tens of eV - few keV. ENA flux > 10^4 $cm^{-2}s^{-1}keV^{-1}$
Search for the solar wind – Phobos interactions	ENAs originating from Phobos	ENA measurements in the energy range tens of eV - few keV with 4π coverage ENA flux 10^4 $cm^{-2}s^{-1}keV^{-1}$
Define the local characteristics of the main plasma regions	Ions and electron measurements of hot plasma	Ion and electron measurements in the energy range few eV - tens of keV with 4π coverage

Table 3.1: The ASPERA-3 scientific objectives

Table 3.1, together with the corresponding instrument requirements.

The key objectives of the ASPERA-3 experiment are:

1. to determine as precisely as possible the total ion escape (particles/s) for the major ion species (O^+, O_2^+, CO_2^+),
2. to study momentum, energy and mass deposition from the solar wind into the upper atmosphere / ionosphere and its response (sputtering),
3. to investigate the morphological structure of the Martian interaction region and define its local plasma characteristics.

3.1.2 ASPERA-4

The ASPERA-4 experiment is designed to study ENAs, ions and electrons from Venus orbit. The scientific objectives of the ASPERA-4 experiment are similar to those of the ASPERA-3 experiment. The specific scientific questions are:

- What is the structure of the solar wind interaction region?
- How is the Venus atmosphere coupled with the solar wind? How is mass added to and removed from the atmosphere due to this coupling?
- The previous question is connected to the issue of "where did the water go?" The early atmosphere must have contained water equivalent to a global ocean a few meters deep as follows from the H/D ratio consideration (*Donahue and Hartle*, 1992). Could the solar wind interaction have contributed to the water escape (mainly increasing H escape)? Is the process the same as for the water escape from Mars?

- What is the mass composition of the escaping plasma?

- What is the neutrals – plasma interaction on Venus? How does the presence of the neutral gas affect plasma dynamics?

- What are similarities and differences in the solar wind interaction with Mars?

The ASPERA-4 experiment is the first at Venus to cover such a wide range of scientific objectives in the area of the solar wind interaction. The other unique feature of the ASPERA-4 experiment is that it is a replica of the ASPERA-3 experiment orbiting Mars. The combination of the observations made by two identical instruments at two non-magnetized planets exhibiting a similar type of solar wind interaction (but differing significantly in terms of interplanetary conditions, atmospheric characteristics, and size and mass) opens up completely new perspectives for comparative magnetospheric studies.

3.2 Instrument overview

As the ASPERA-4 package (Figure 3.2) is a replica of the ASPERA-3 one, this section describes both the ASPERA-3 and the ASPERA-4 instruments. The packages are designed to work in different environments, hence there are certain differences between them, listed below.

Mechanically, ASPERA-3 / ASPERA-4 consists of two units, the Main unit and the Ion Mass Analyzer (IMA). The Main unit comprises three sensors (the Neutral Particle Imager, the Neutral Particle Detector, the Electron Spectrometer (ELS)) and a digital processing unit (DPU), shown in Figure 3.3. The Main unit is located on a turnable platform of a mechanical scanner. The scanner sweeps the three sensors, mounted on it, through 180° to give 4π steradian coverage (ideally) when the spacecraft is 3-axis stabilized. In practice, part of the FOV is blocked by the spacecraft body. All electrical interfaces of the instrument with the spacecraft are made through the scanner.

IMA is an improved version of the ion mass spectrographs Freja/TICS, Mars-96/ASPERA-C/IMIS and Planet-B/IMI (*Norberg et al.*, 1998). IMA is a stand alone instrument with its own DPU and high voltage (HV) power supplies. Since IMA is not accommodated on the scanner, electrostatic sweeping is used to achieve ±45° elevation coverage. Electrically, IMA interfaces only the Main unit.

Total mass of the ASPERA-4 instrument is 9.00 kg; the Main unit flight model mass without thermal hardware is 6.63 kg, while the mass of the IMA flight model is 2.37 kg without thermal hardware. The maximum power consumption is 18 W. The Main unit envelope is $350 \times 263 \times 288$ mm; for IMA it is $287 \times 187 \times 165$ mm.

Total mass of the ASPERA-3 instrument is 8.2 kg, the power consumption is 13.5 W, and the envelopes are $359 \times 234 \times 393$ mm and $255 \times 150 \times 150$ mm for the Main unit and IMA, respectively.

The ENA sensors (NPI, NPD) of the ASPERA-3 / ASPERA-4 instruments complement each other. The NPI is designed to provide ENA measurements with relatively high angular resolution, but no mass and energy discrimination, while the NPD performs mass and energy analysis of the incoming ENAs, but the angular resolution is crude. This approach also gives the necessary redundancy as well as the independent cross-checking that is necessary for such measurements in a new environment. The charged particle sensors not only provide characterisation of the local plasma environment, but also support ENA measurements in terms of charged particle background and inter-calibrations. The ELS sensor represents a new genera-

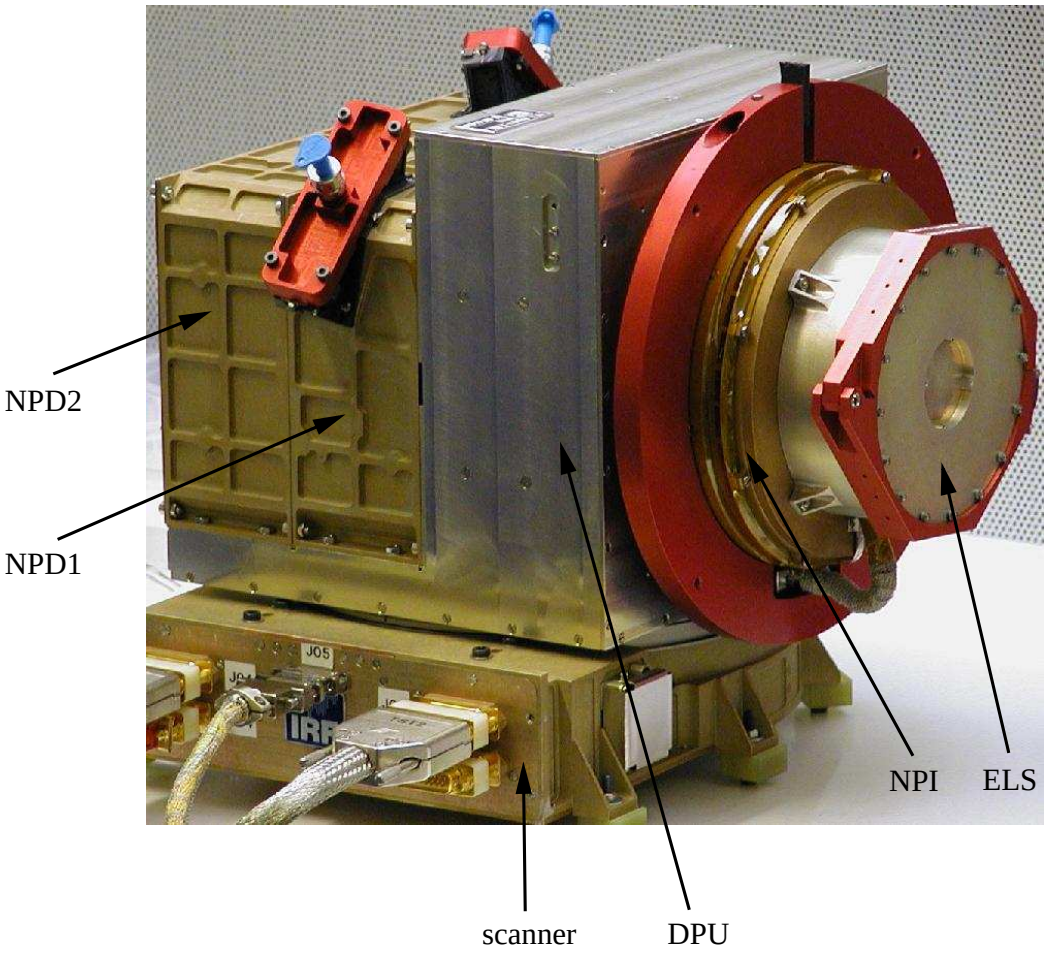

Figure 3.3: ASPERA-3 main unit. The NPD and ELS apertures are covered with protective covers (red). The NPI protective cover has been removed to show the NPI and ELS sensors.

tion of ultra-light, low-power electron sensors. It is a standard top-hat electrostatic analyzer in a very compact design and with high energy resolution.

The ASPERA-3 / ASPERA-4 instrument design, while based on a modular structure, demonstrates a high degree of packaging and sharing of the internal resources. The instrument DC/DC converters are shared between all 5 units, including the two identical NPD sensors. The DPU mechanical structure also serves as a carrying support for mounting the NPD sensors and the NPI, which in turn is carrying the ELS. The internal walls that separate the DPU, NPI and both NPD sensors have been replaced by conductive kapton foils to minimise mass, while maintaining sufficient electromagnetic shielding.

Table 3.2 summarizes the ASPERA-3 / ASPERA-4 instrument performance.

The differences between the ASPERA-3 and the ASPERA-4 instruments are mainly due to the environments they are designed to be immersed in. As Mars is located more than twice as far from the Sun as Venus, the solar thermal flux delivered to the Mars Express spacecraft orbiting Mars as well as all on board instruments is much lower than that for Venus Express orbiting Venus. The thermal design is therefore different: the ASPERA-3 multi-layer insulation (MLI) outermost layer is black kapton, while for ASPERA-4 it is white kapton. ASPERA-4 is also equipped with a radiator covered by optical secondary reflection (OSR) mirrors (Figure 3.2).

Parameter	NPI	NPD	ELS	IMA
Particles to be measured	ENA	ENA	Electrons	Ions
Energy range, keV/q	~0.1 - 60	0.1 - 10	0.01 - 20	0.01 - 30
Energy resolution, $\Delta E/E$	–	0.5	0.08	0.07
Resolved masses, amu	–	1, 16	–	1, 2, 4, 8, 16, >32
Intrinsic field-of-view	$9^\circ \times 344^\circ$	$9^\circ \times 180^\circ$	$10^\circ \times 360^\circ$	$90^\circ \times 360^\circ$
Angular resolution (FWHM)	$4.6^\circ \times 11.5^\circ$	$5^\circ \times 30^\circ$	$10^\circ \times 22.5^\circ$	$4.5^\circ \times 22.5^\circ$
G-factor / pixel, cm^2sr	2.5×10^{-3} (ε not incl.)	6.2×10^{-3} (ε not incl.)	7×10^{-5}	1.6×10^{-6}
Efficiency, ε, %	~1	1-15	Inc. in G	Inc. in G
Time resolution (full 3D), s	32	32	32	192
Mass[a], kg	0.7	1.3[b]	0.3	2.37
Power, W	0.8	1.5	0.6	3.5

[a] ASPERA-4
[b] 2 sensors

Table 3.2: The baseline performance of the NPI, NPD, ELS and IMA sensors. FWHM stands for full width at half maximum, G-factor a geometrical factor.

Open surface treatment is also different. Those ASPERA-4 surfaces, not covered by MLI, are covered with PCBE white paint. The radiation requirements were also different for the two missions, 5 kRad for Mars Express and 30 kRad for Venus Express. In order not to change the component selection, the point shielding (tantalum) was used to protect ASPERA-4 components which were not sufficiently radiation hard. To protect the ASPERA-4 / ELS electronics an aluminum protecting skirt was introduced around the entire sensor.

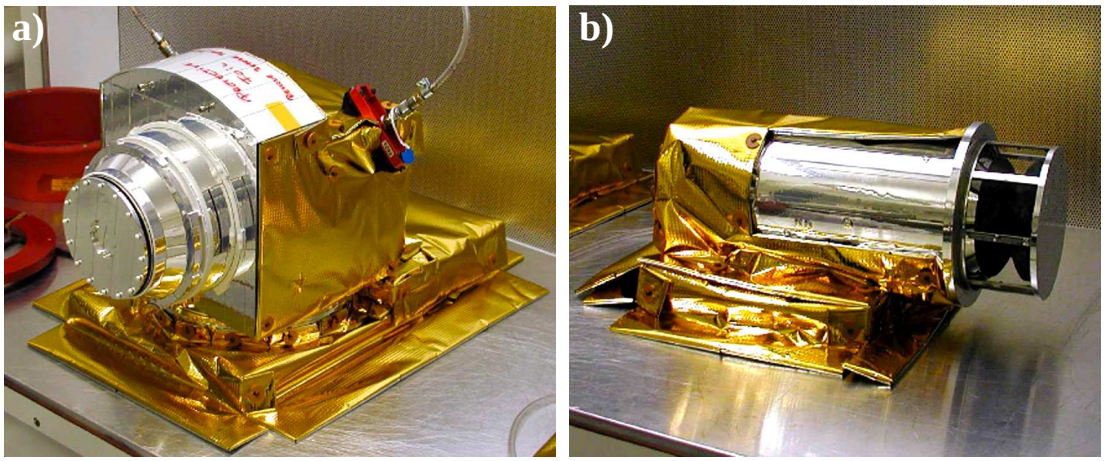

Figure 3.4: The ASPERA-4 overall configuration with the Main unit (left) and IMA (right). The NPI protective cover has been removed to show both the NPI and ELS sensors. From *Barabash et al.* (2007b).

3.2.1 The Ion Mass Analyzer (IMA)

IMA is a top-hat electrostatic analyzer (Figure 3.5a) resolving H^+, He^{++}, He^+, O^+ and molecular ions in the energy range 10 eV/q - 30 keV/q. Being located separately from the scanner, it

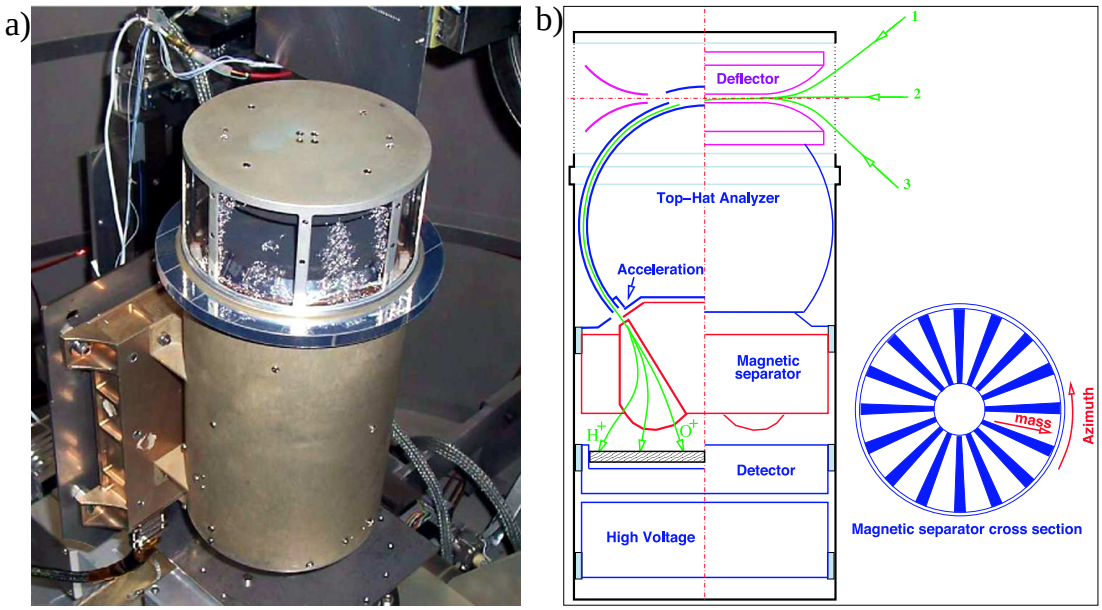

Figure 3.5: Photograph (a) and a cross-section (b) of the IMA sensor. Adapted from *Barabash et al.* (2007b).

is equipped with an electrostatic deflector to scan over elevation. The principal diagram of the instrument is shown in Figure 3.5b. Ions first pass through a grounded grid and enter the deflection system comprising two curved electrodes that deflect ions arriving in the instrument over elevation range ±45° (shown as trajectories 1, 2 and 3) and over 360° azimuthal FOV into the entrance of the top-hat analyzer. The latter selects only ions with a given energy according to the interplate voltage of the analyzer's hemispheres. The ions, passed through the electrostatic analyzer, exit the annular space separating the hemispheres and travel through the magnetic velocity analyzer section (magnetic separator). The cut of this section in the azimuthal plane is shown on the right side of Figure 3.5b. The magnets are shown as blue wedges. Sixteen gaps between the magnets correspond to 16 azimuthal sectors of the instrument of 22.5° each. In the magnetic mass analyser, the ions pass through a static, cylindrical magnetic field, which deflects them outward, away from the central axis of the analyzer system. The lighter the ions, the stronger its trajectory bending. As the ions leave the magnetic mass analyzer, they are registered at the MCP detector with a position sensitive anode. A system of 32 concentric rings measures the radial impact position, which corresponds to the ion mass, and 16 sector anodes measure azimuthal impact position, which corresponds to the ion azimuth entrance angle. To measure light ions, such as H^+, at low energies, which have too small gyro-radius to reach the MCP, the ions can be post-accelerated in the gap between the electrostatic analyzer exit and the magnet assembly entrance. Varying the post-acceleration voltage allows one to select the mass range and to adjust the mass resolution.

The IMA sensor also includes an IMA DPU and a HV unit, providing the MCP bias and sweep voltages for all electrodes. Energy range sweeps from 30 keV down to 10 eV over 96 logarithmically equidistant steps. The polar angle is scanned from −45° up to +45° over 16 steps. The time to complete a full 3D spectrum is 192 s.

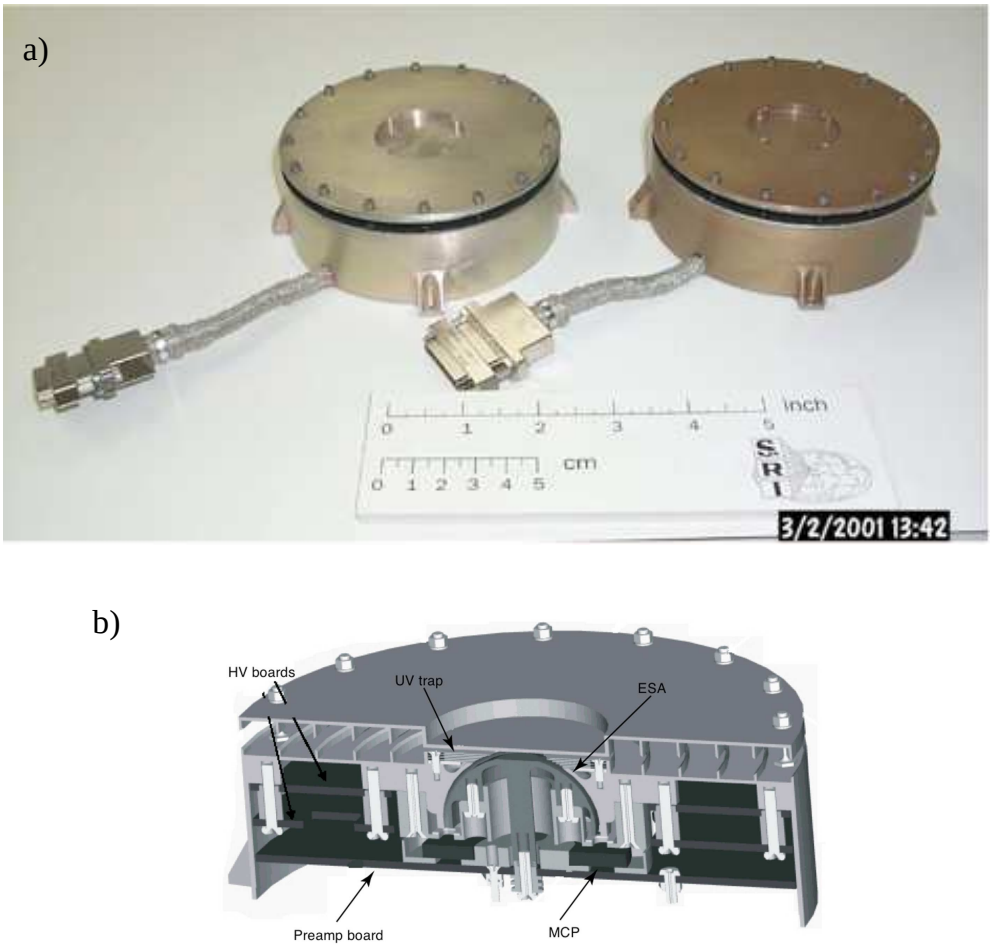

Figure 3.6: Photograph (a) and cut-off view (b) of the ELS sensor. Adapted from *Barabash et al.* (2006).

3.2.2 The Electron Spectrometer (ELS)

ELS is a top-hat electrostatic analyzer to measure electrons in the energy range 10 eV - 20 keV entering over 360° FOV (Figure 3.6a). It comprises a collimator system and a spherical top-hat electrostatic analyzer with the radii of the inner and outer hemispheres equal to 14.9 mm and 15.9 mm respectively (Figure 3.6b).

Entering electrons are deflected into the spectrometer by a positive potential on the inner hemisphere. A spectral measurement is achieved by stepping the plate voltage. The time of one energy sweep, consisting of 128 steps, is four seconds. The ELS sweep is fully programmable within the constraint of the maximum decay rate of 32 steps/s. The electrons, filtered by energy, are detected by an MCP detector. There are 16 anodes behind the MCP defining 16 azimuthal sectors of 22.5° each.

ELS was designed to be sun blind, so that it may operate during exposure to direct sunlight. EUV/UV photon flux is minimized through the use of a series of light baffles in the collimator and a series of light traps at the entrance to the spherical deflection plates. Photo-electrons are reduced by use of a special coating, based on a modified Ebanol-C process, applied to the deflection surface, light trap and the collimator system (*Johnstone et al.*, 1997). To eliminate the photo-electron flux, a retarding grid is introduced between the MCP and the analyzer exit.

3.2.3 The Neutral Particle Imager (NPI)

NPI (Figure 3.7a) is designed to measure ENAs with a relatively high angular resolution. All incoming particles, entering over 360° FOV, pass between two 150 mm diameter disks separated by a 3 mm gap. The disks and radial spokes in-between them collimate the incoming beam over the elevation and azimuth angle to give a pixel of $9° \times 18°$ FOV and $4.5° \times 11.5°$ full width at half maximum (FWHM). The 5 kV potential between the grounded and biased disks results in a strong electric field, which sweeps away charged particles with energy less than 60 keV.

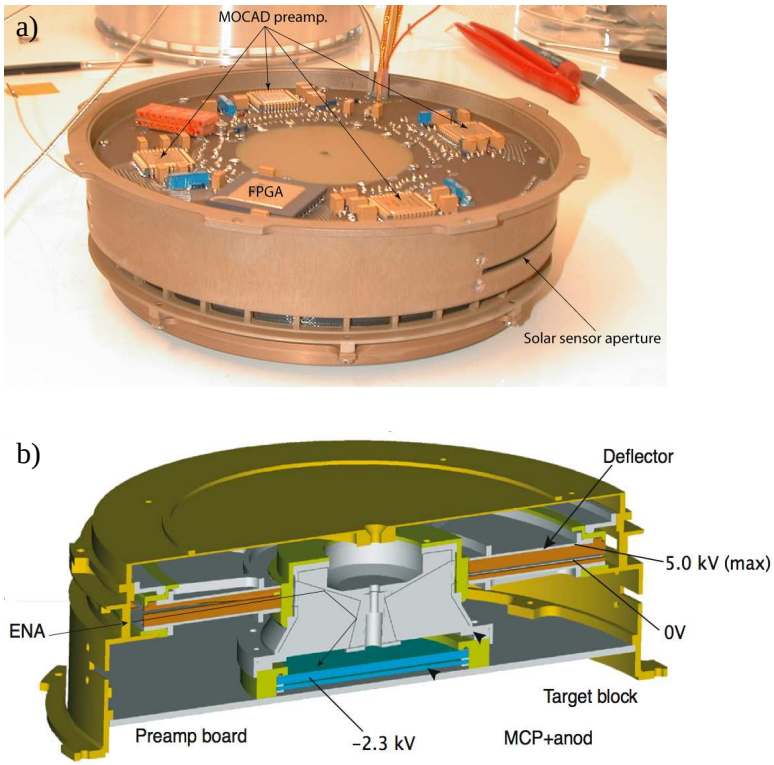

Figure 3.7: Photograph (a) and cut-off view (b) of the NPI sensor. Adapted from *Barabash et al.* (2006).

Neutrals that pass through the deflector system hit a 32-sided conical target at a grazing angle of incidence of ~30°. On impact with the target block the incident neutral can either be reflected in positive, negative or neutral charge state, or produce secondary particles. The secondaries can be both ions and electrons. The particles, leaving the target, are then detected by an MCP detector followed by a 32 sector anode. The MCP operates in an ion mode with a negative bias of -2.3 kV applied to the front side and thus detects both positive and neutral particles reflected as well as sputtered off the target, while electrons are repelled. The internal view of the NPI sensor is shown in Figure 3.7b. The UV suppression is based on the target material selection, blackening of the internal surfaces, and the MCP mode operation. The NPI is located on the scanner platform. Ideally it can cover 4π *sr* in a 180° scan, whereas approximately a half of its FOV is blocked by the spacecraft body. Also two sectors are mechanically blocked to accommodate the ELS cable.

3.2.4 The Digital Processing Unit (DPU) and the scanner

The DPU includes two boards: the DPU board itself and a Housekeeping (HK) board. These are connected together with the sensor control electronics and a power supply via a common bus system with 8 address- and 16 data lines. The bus also includes control-, analog- and power supply lines. The software is built around a real-time system with a scheduler and an interrupt handler. All executable routines are defined inside a routing table, which resides in an Electrically Erasable Programmable Read Only Memory (EEPROM) and can be modified during the flight. In this way new or modified software routines can be stored inside a free area of the EEPROM, verified and added to the operating software by including their start address into this routing table. A macro feature of the telecommand (TC) handler offers the possibility to generate sequences of standard TCs automatically according to a pre-defined list, reducing the need for complex TC groups to be up-linked over and over again. Besides detector activation and parameter control, compression and averaging of measurement data allow the reduction of the amount of telemetry generated.

The scanner platform (Figure 3.8) was originally designed for the ASPERA-C experiment on the Russian Mars-96 mission. Some modifications were made for ASPERA-3 on Mars Express as well as for ASPERA-4 on Venus Express, most of them concerned with optimization of the performance during long-term operations and reduction of its mass.

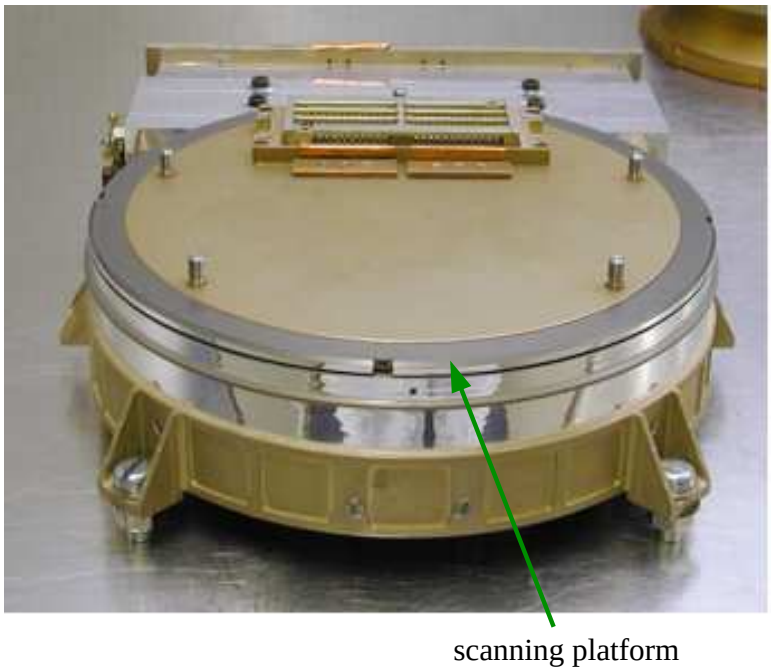

Figure 3.8: The ASPERA-3 scanner. Adapted from *Barabash et al.* (2006).

The scanner serves as a bearing structure for the ELS, NPI, NPD sensors and the DPU, as well as providing all electrical interfaces with the spacecraft. It constitutes the 0° to 180° rotating platform on which the sensors as well as the DPU, HV power supply (HV PS), HK and DC/DC boards are situated. Rotation is accomplished by means of a worm gear mechanism. The scan platform is made as a plug-in unit for the sensor assembly.

Chapter 4

The Neutral Particle Detector (NPD)

The Neutral Particle Detector (Figure 4.1) developed for the ESA Mars Express and Venus Express missions is a compact, low weight (~650 g), high efficiency TOF sensor to image low and medium energy ENAs that result from the solar wind interaction with the Martian / Venusian exospheres. The ASPERA-3/ASPERA-4 packages each contain two identical NPD detectors. NPD is a pinhole camera with a $9° \times 90°$ intrinsic field-of-view. The measurement principle is based on a surface interaction technique. The sensor is capable of resolving hydrogen (H) and oxygen (O) atoms and provides measurements of an ENA differential flux over the energy range of 100 eV - 10 keV with a coarse angular resolution of $5° \times 30°$ and total efficiency of 1-16%.

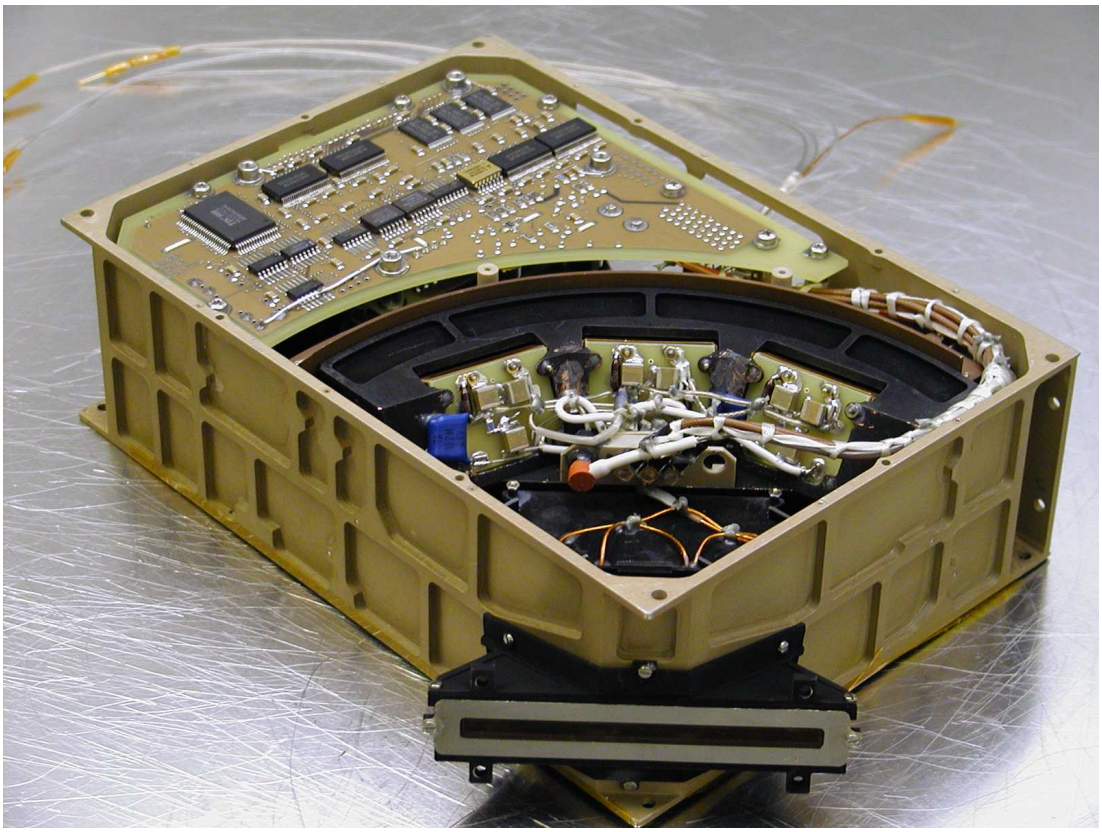

Figure 4.1: The NPD flight model. The cover has been removed.

4.1 The measurement technique

Figure 4.2 provides a conceptual view of the detector. Incoming ENA particles pass between two parallel deflector plates (shown in red), separated by a 3.0 mm gap with an inter-plate electric potential difference of up to 10 kV, and enter a pin-hole of 3.0×4.5 mm^2 size. Charged particles (ions [f^+] and electrons [f^-]) with an energy of $\leqslant$70 keV/q are swept away by the transverse electric field created between the plates. The collimated ENA beam emerging from the pinhole hits a Start surface (shown in grey) at a 15° grazing angle, causing secondary electron emission. The angle between an ENA trajectory and the Start surface is chosen to provide a maximal ENA reflection from the surface as well as a high secondary electron yield. Secondary electrons are transported by a system of collecting grids (shown as green boxes) to one of two Start MCP assemblies (inside the green boxes), giving a start event. The incident ENAs, reflected from the Start surface nearly specularly, hit a Stop surface. The emerging beam contains both neutral and ionized components since the charge state equilibrium is established during the interaction with the surface. No further separation by charge is made in order to increase the total efficiency. Therefore particles of any charge state–negative, neutral, positive–

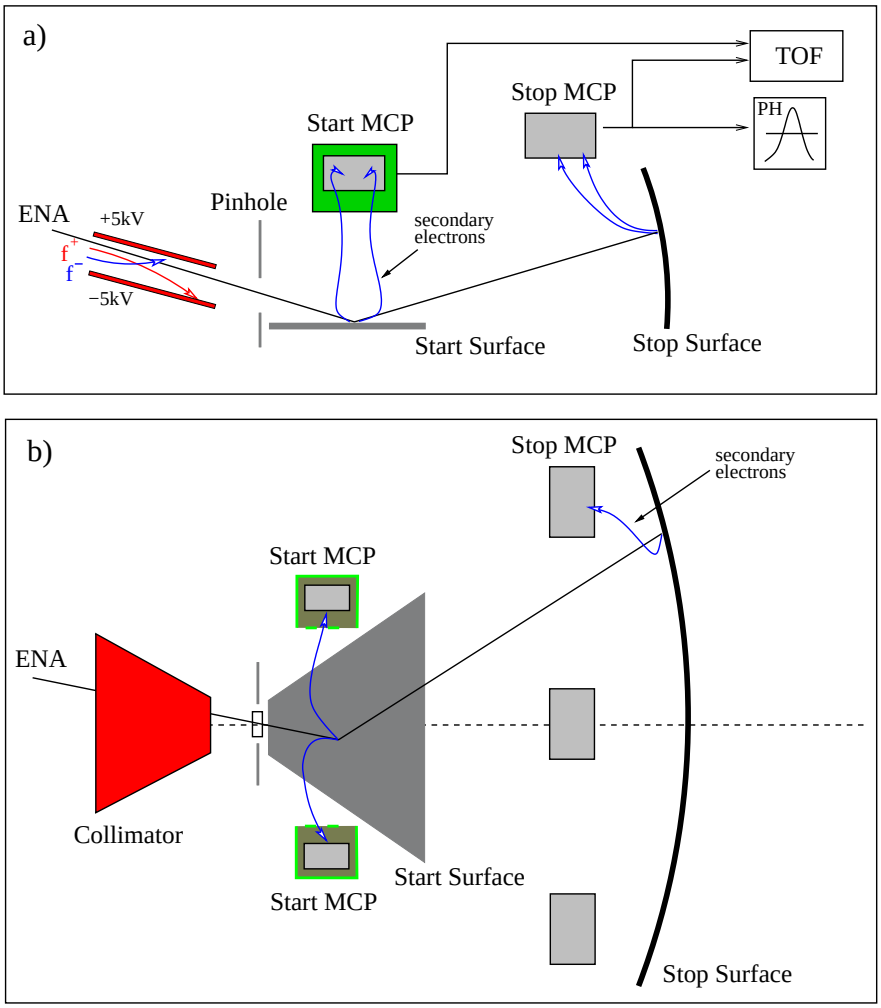

Figure 4.2: The principle design of the NPD sensor. a) view from the side, b) view from the top. For details see the text.

impact the Stop surface. A black line depicts an ENA trajectory. Secondary electrons yielded from the Stop surface accelerate towards one of three Stop MCP assemblies, mapping the position of the impact, and produce a stop event. The start and stop signals are then used for TOF measurements. The particle velocity is defined by the TOF over a fixed distance between the Start and Stop surfaces of on average about 8 cm. Three Stop MCPs give an angular resolution of roughly 30° within the 90° azimuth acceptance angle. The secondary electron yield from the Stop surface depends on the atomic mass number of a neutral and, therefore, is different for ENAs of different mass moving with the same velocity. The pulse height (PH) distribution analysis of the stop signals can be used to estimate the mass (*H* or *O*) utilizing this phenomenon. Moreover, the difference in the TOF between *H* and *O* atoms is sufficient for direct mass identification within the particular energy range. UV suppression is provided by properties of the Start and the Stop surface coatings as well as by the coincidence between start and stop signals within a defined TOF window. Figure 4.3 shows a 3D model of NPD with the main components identified.

4.2 NPD mechanical design

NPD consists of several functional units, namely, a deflector, Start unit, Stop unit, Stop surface, housing, and electronics (Figure 4.4).

The sensor is enclosed in a rectangular chassis with a size of $200 \times 140 \times 60$ mm (Figure 4.4e). The top and bottom sides are closed by an aluminum plate and/or kapton membranes with a conductive coating. The deflector housing (Figure 4.4a) is a triangular box, located in

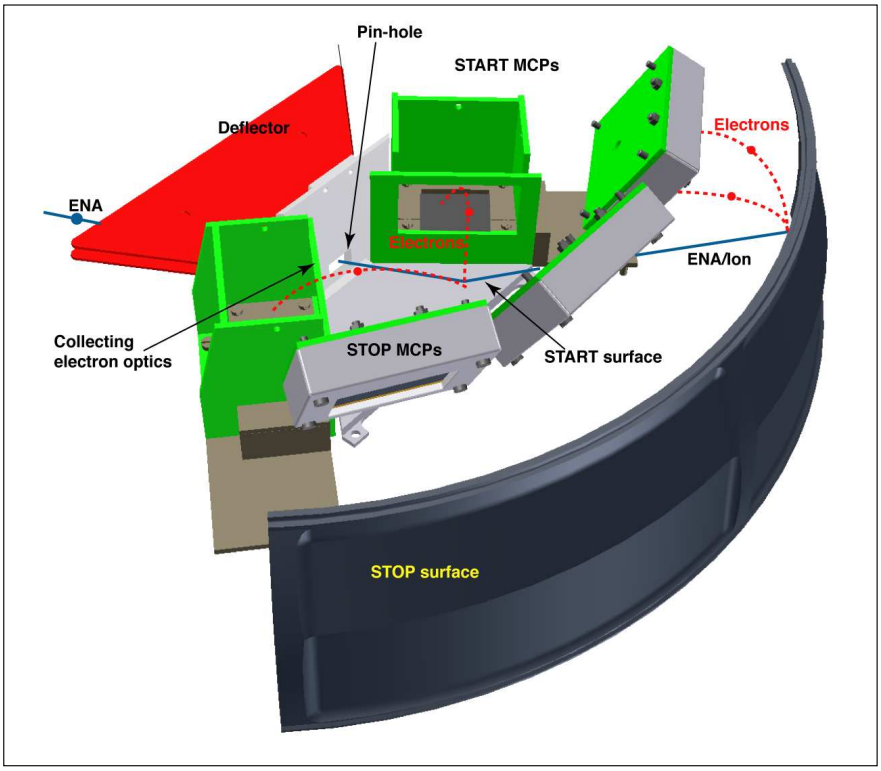

Figure 4.3: The 3D model of the NPD sensor.

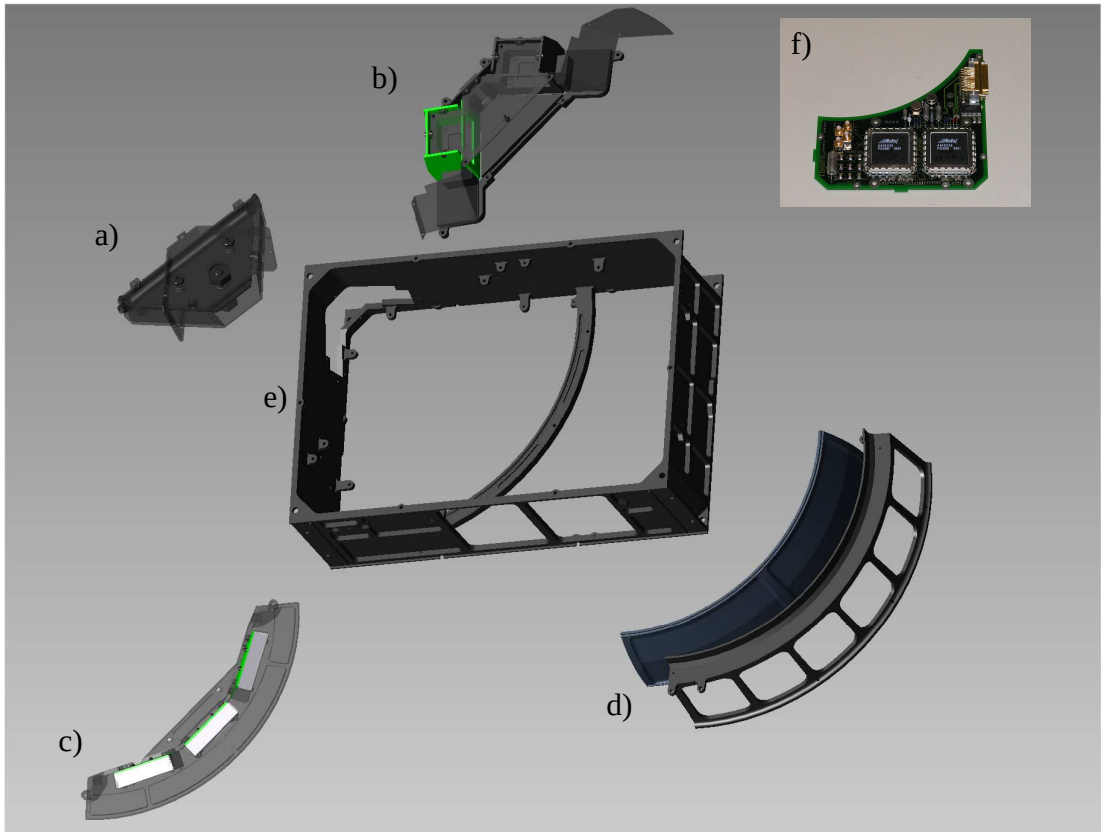

Figure 4.4: NPD functional units. a - Deflector, b - Start unit, c - Stop unit, d - Stop surface with a holder, e - housing (chassi), f - electronics.

the upper left corner of the chassis. The opening is covered by a highly transmitting (>90%) stainless grid. The collimator plates are located parallel to each other inside the deflector. A strong transverse electric field is created across the incoming beam path when plates are biased. The central deflector plane is inclined 15° away from the Start surface plane.

The Start unit (Figure 4.4b) is located next to the deflector. The entire unit is electrically insulated from the chassis. The Start surface, two MCP assemblies, electron optics system and the pinhole plate are placed on the Start unit frame. High voltage- and signal cables, and the electron optics system bias cable, are attached to the corresponding connectors on one side of the unit. The connectors and parts of the MCP electronics boards, exposed to the ion beam emerging from the Start unit, are closed by grounded blackened (Ebanol-C) shields.

The Stop unit (Figure 4.4c) is located next to the Start unit. It comprises a frame holding three MCP detectors. The frame is electrically coupled to the chassis. High voltage- and signal cables are attached to the connector on the back side of the frame.

The Stop surface (Figure 4.4d) is located next to the Stop unit. The Stop surface is part of a sphere of 108 mm radius to cover all possible particle trajectories from the Start unit.

All sensor elements are fixed to the outer shell of the mechanical structure (chassis). This configuration provides easy access to all elements, mechanical stiffness, and minimizes the structural mass.

Four signal cables are guided from the Start and Stop units through the sensor and connected to the electronics package (Figure 4.4f) located in the opposite corner to the deflector. All high voltage cables as well as the electron optics bias cable bypass the sensor and connect

to the Main unit HV board. The Start and Stop MCP detectors are biased separately. The digital electronics connection with the Main unit DPU is performed via a MDM-37 connector.

The sensor has a quite large empty space between the Start unit and the Stop surface as well as in the electronics compartment, and is therefore very light. The high voltage is generated externally, in the Main unit HV PS.

Pointing of the NPD sectors FOVs (Dir0, Dir1, Dir2) is shown in Figure 4.5, depicted by black arrows.

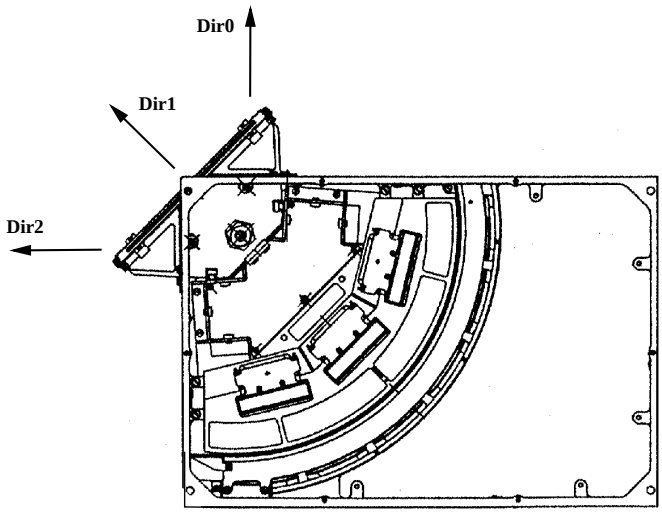

Figure 4.5: Engineering drawing of NPD. The black arrows depict the pointing of the NPD sectors.

The NPD package is comprised of two identical sensors, NPD1 and NPD2. It covers a hemisphere (half a hemisphere per sensor) when placed on a scanning platform, which performs 180° sweeps (see Figure 3.3). A conductive kapton film provides an electrical screening between the units mounted together.

Main unit HV PS. The ASPERA-3 / ASPERA-4 Main unit HV PS provides high voltages for the NPD1 and NPD2 sensors as well as for NPI. Each NPD sensor is connected to an individual HV PS which is built around two base supplies. The base supply uses a conventional coil transformer followed by a custom-made doubler. The first single polarity HV PS provides base voltage from 0 to +3 kV regulated further by two AMPTEK HV601B optocouplers to bias the Start and Stop MCP assemblies individually. The second double polarity HV PS provides two voltages from 0 to ±5 kV for the NPD deflector electrodes. The regulation accuracy is 256 steps for each range, which is sufficient for this application.

Assembled NPD sensor. Figure 4.6 shows a cross-section of a 3D model of NPD with the main units depicted by arrows, and an incoming ENA trajectory (as a pink line). Figure 4.7 shows the NPD flight model with covers removed to exhibit the main elements.

4.2.1 Deflector

The NPD deflection system is an electrostatic deflector, consisting of a pair of parallel plates located inside the grounded deflector housing. Commandable potentials of up to ±5 kV are

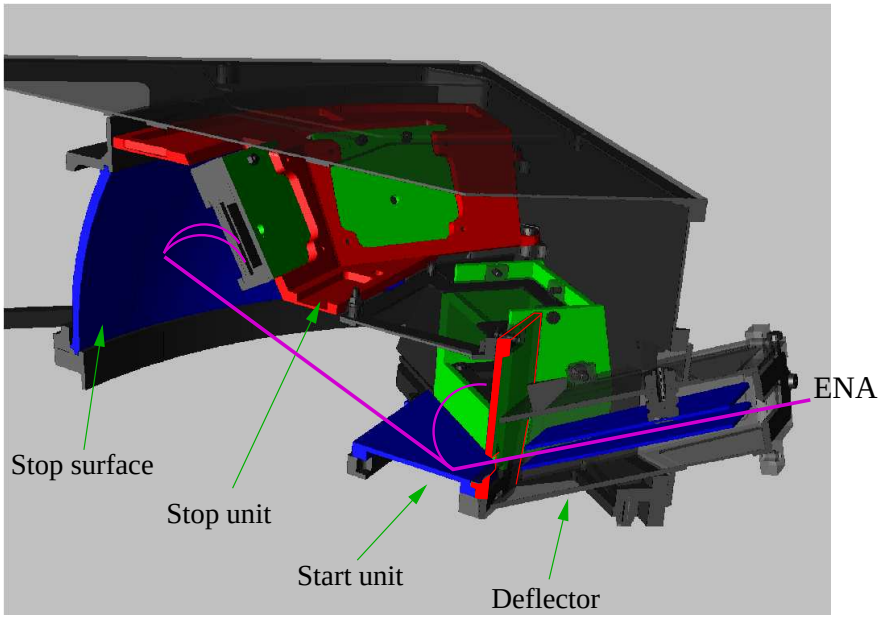

Figure 4.6: Cross-section of a 3D model of NPD. Main units are depicted by arrows.

applied to the plates to sweep charged particles with energies $\leqslant$70 keV/q into the plates (excluding them from the detector). Each deflection electrode is a blackened aluminum plate of a trapezoidal shape with serrations to inhibit forward scattering of incident particles. Figure 4.8 shows a cross-section of a 3D model of the NPD deflector with the lower half cut away. The deflector electrodes are visible inside the housing. The entrance slit has dimensions of 3.0 mm $\times$ 70.0 mm. It is covered by a stainless steel grid in order to prevent electric field leakage outside the deflector housing.

Charged particles with energy below the cut-off energy E_e will be rejected. E_e of an electrostatic deflector, consisting of two parallel plates of the length L and a gap D in-between, can be estimated roughly by Equation 2.2. The lengths of the deflector electrodes (along the incoming beam path) are 30.0 and 31.0 mm. The gap between the electrodes is 3.0 mm. The maximum potential supplied by the Main unit HV PS on the deflection plates is $\pm$5 kV. Therefore, all charged particles with energy up to $\sim$70 keV/q, will be swept away, while passing through the deflector. Energetic charged particles with energy above E_e can pass through the deflector, but they are not registered as valid events due to their very short TOF. Detailed investigation of the sensor response to high energy particles is given in Section 4.7.

4.2.2 Start unit

The Start unit consists of the pinhole plate, the Start surface (see Section 4.2.4), the electron optics system to collect and guide secondary electrons toward the Start MCPs, and two Start MCP detectors. The Start unit is shown in Figure 4.9. The left panel is a 3D model of the Start unit. All key elements are depicted by arrows. The Start surface is not shown. By a system of collecting grids (shown in blue), secondary electrons emitted from the Start surface are transported to one of two MCP assemblies (inside blue boxes), giving a start event. The right panel shows a photo of a completely integrated Start unit. Figure 4.10 shows the key elements of the Start unit during integration. Panel (a) shows the Start unit from above. Two

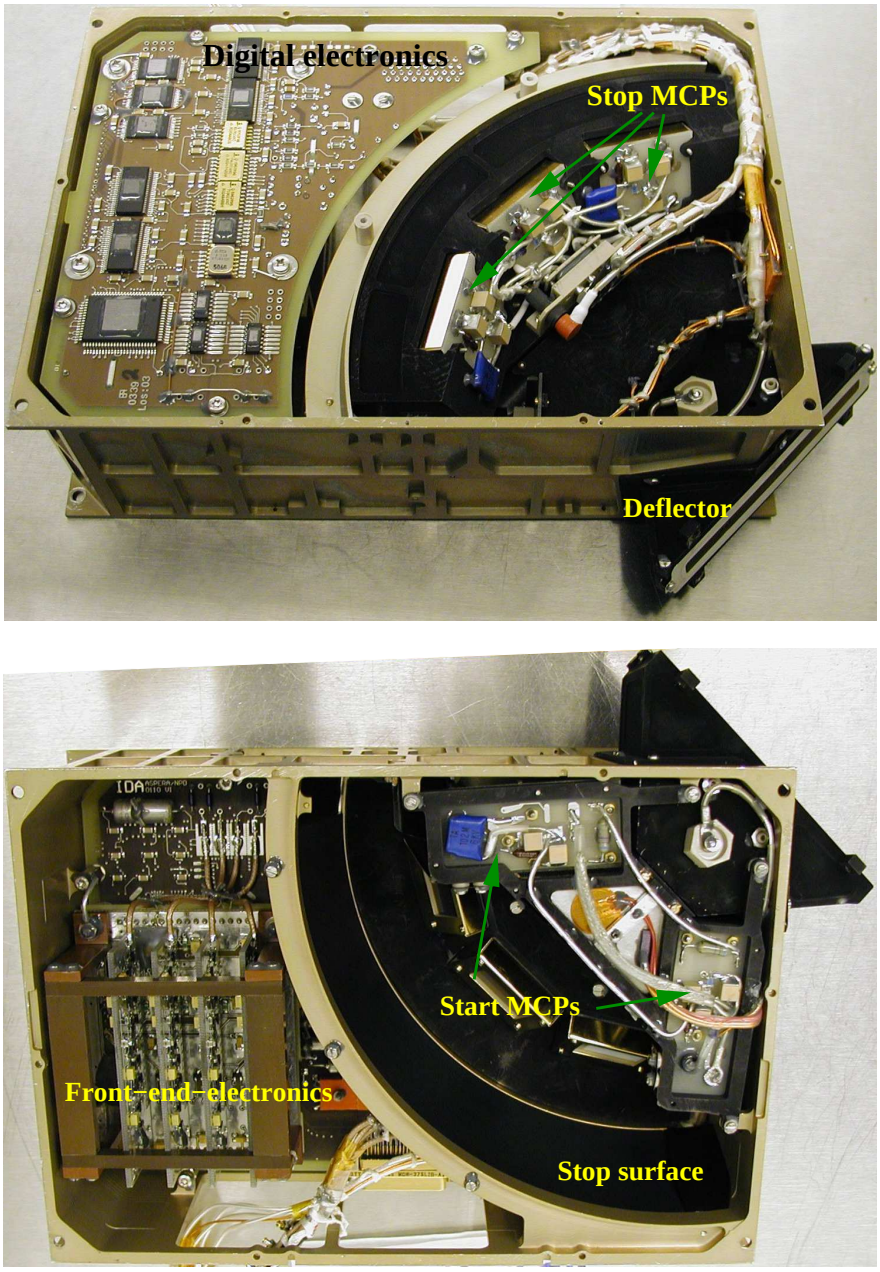

Figure 4.7: NPD flight model with the main elements shown.

MCP assemblies are located aside the trapezoidal Start surface. The pinhole is attached in front of the latter. Panel (b) shows parts of the electron optics system. Panel (c) shows a view of the completed Start unit from below. The electronics of the MCP detectors is depicted by arrows. In the center of the Start unit frame can be seen a trapezoidal aluminum plate with a temperature sensor and a heater attached (see details in the following section). The plate is attached to the bottom side of the Start surface. Panel (d) shows this plate on its own.

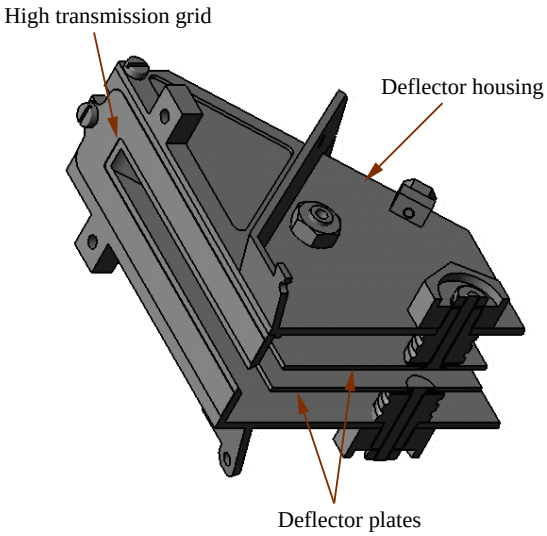

Figure 4.8: Cross-section of a 3D model of the deflector.

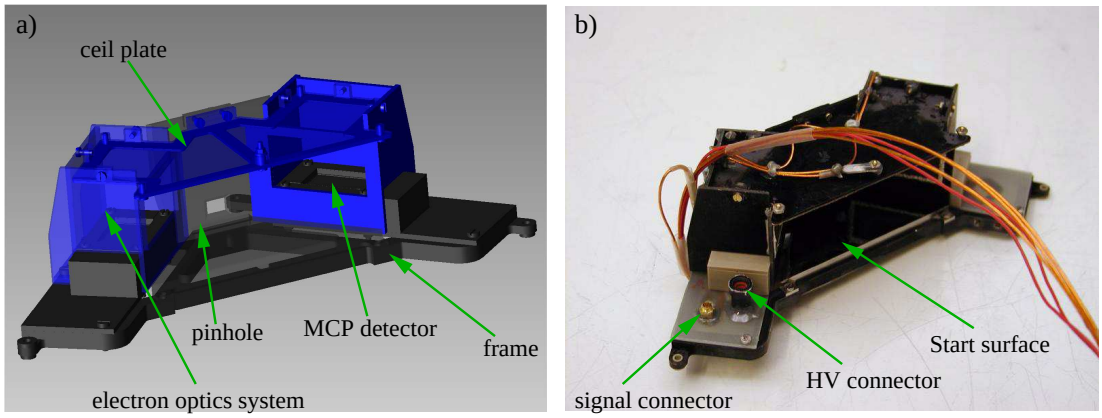

Figure 4.9: The Start unit assembly. (a) 3D model of the Start unit with key elements depicted by arrows. The Start surface is not shown. (b) a photo of the integrated Start unit.

Electron optics system

The main purpose of the Start unit electron optics (Figure 4.9a, colored blue) is to provide an effective transport of secondary electrons yielded from the Start surface to Start MCPs located inside the cages, preventing direct exposure of the MCP detectors to UV photons coming into the sensor. Figure 4.11 shows an electrical model of the electron optics system. The cages, main elements of the optics, have openings toward the Start surface closed by highly transparent (91%) golden grids. The grids are biased with +50 V. All inner sides of the cages have the same potential as the Start unit frame (+12 V). Small electrodes, biased differently (+20 V), are embedded into the inner back sides of the cages. The top horizontal plate of the electron optics, located above the Start surface, has a negative potential of -12 V to repel electrons towards the cages. All potentials are set with respect to that of the Start unit frame. The entire Start unit is biased positively (+12 V), to prevent secondary and photo-electrons yielded from the Start surface from reaching the Stop unit. The front side of the MCP detectors is biased by +300 V.

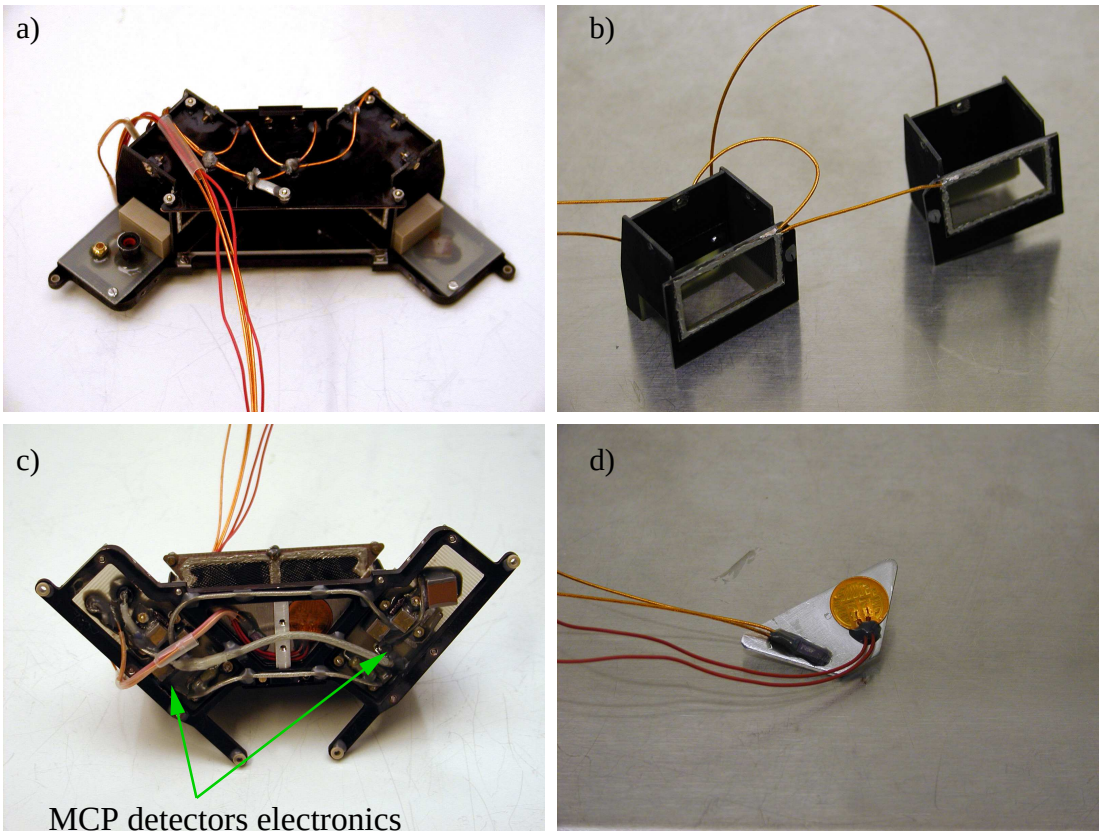

Figure 4.10: (a) the Start unit from above; (b) electron optics system cages; (c) the Start unit from below; (d) an aluminum plate with a heater and a temperature sensor attached.

As proven by ion ray-tracing, the Start electron optics introduces minor disturbance to the reflected ions leaving the Start surface with an energy above 80 eV. Figure 4.12 shows the results of the electron and ion ray-tracing in the Start electron optics assembly. The electron collection efficiency of the optics varies from 80% to 95% depending on the azimuth angle of incident ENAs.

The heater and the temperature sensor

The heater is intended for Start surface pre-conditioning in space. The surface performance was investigated during thermal vacuum testing performed at IKI, Moscow. The thermal cycling included five heating cycles from +15° to +90° and back to +15° and five cooling cycles from +15° to -60° and back to +15° with a temperature gradient of 1°C/min. The surface performance was measured before and after the tests. He^+ beams of different incident energy were used. Figure 4.13 show TOF spectra before (panel a) and after (panel b) the thermal cycling. The black, yellow, and green curves show the TOF spectra obtained during the tests using ion beams of energies of 500 eV, 1500 eV, and 2500 eV, respectively. The vertical red lines show the position of the corresponding peaks obtained before the test. The energy loss at the surface was found to reduce by several per cent after the thermal vacuum test. A hydrogen recoil peak (a small bump on the 500 eV He^+ TOF spectrum at ~210 ns) decreased as well as the electron event peak (at ~50 ns, it is caused by secondary electrons yielded from the Start surface reaching the Stop unit). These improvements are related to the cleaning during

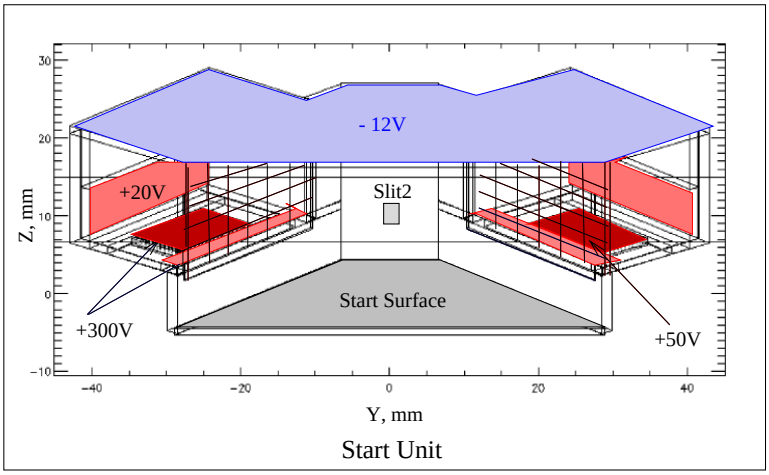

Figure 4.11: An electrical model of the Start unit electron optics system.

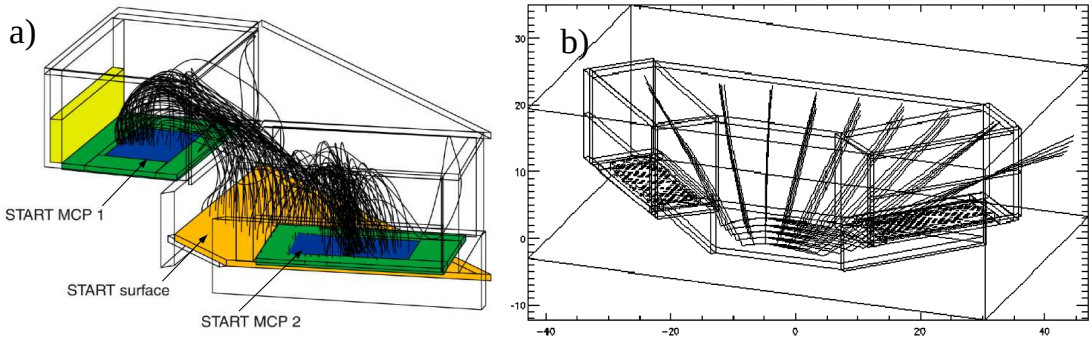

Figure 4.12: The ray-tracing of the trajectories of secondary electrons (panel a) and 80 eV ions (panel b) in the Start unit electron optics system.

heating cycles.

The heater is a 0.4 W flexible Termofoil^{TM} MINCO heater (see Figure 4.10d) without temperature regulation to heat the Start surface when powered with +5V. It allows an increase of the Start surface temperature by ~50° above the ambient. The heater operation is commandable.

The temperature sensor AD590J is used to monitor the Start surface temperature continuously. It reflects the Start surface temperature and can be used to monitor the NPD temperature when the heater, located close to it, is switched off. Both the heater and the temperature sensor are attached to a thin aluminum plate (Figure 4.10d), which is located in a pocket inside the Start surface and is pressed tightly to a bottom side of the latter. Using the intermediate aluminum plate between the Start surface and the heater helps avoid hot spot heating as well as making the heater easy to replace.

4.2.3 Stop unit

The Stop unit registers secondary electrons yielded from the Stop surface (Section 4.2.4), produces stop signals and provides a coarse analysis of the direction of an incoming ENA. It comprises an aluminum frame (Figure 4.14) to hold MCP detectors and three identical MCP detectors with some passive HV components.

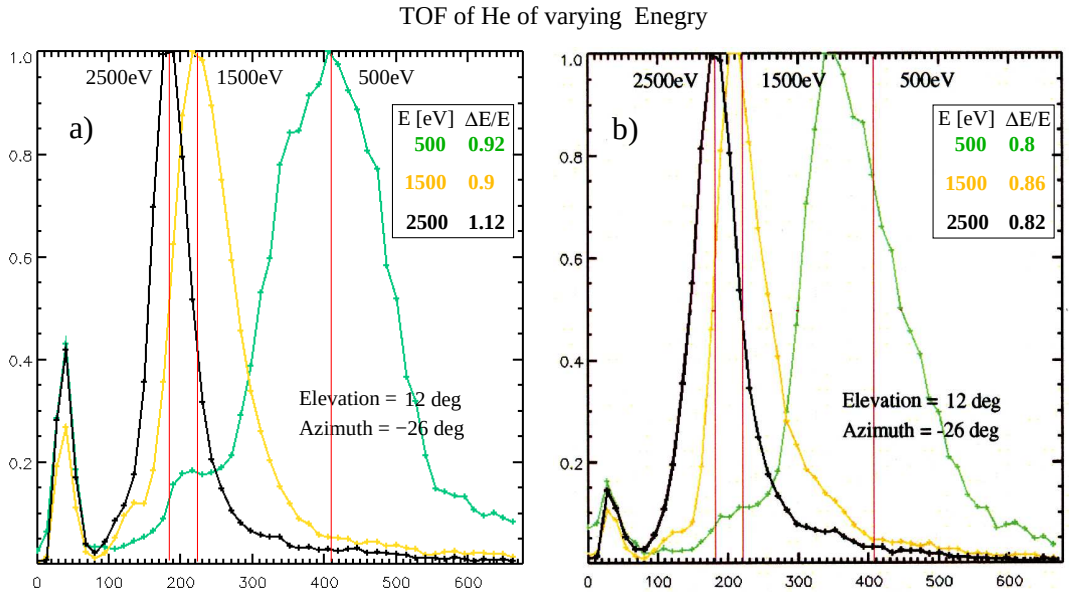

Figure 4.13: TOF analysis of different energy beams made a) before and b) after the thermal vacuum test. The vertical red lines show the position of the corresponding peaks obtained before the test.

The frame is fixed right above the Stop surface in such a way as to achieve the highest secondary electron collection efficiency. Every MCP detector is shielded by a grounded gold-plated cover to inhibit electric field leakage outward from the biased MCPs through the MCP assembly holders. The electric potential of all of the MCP front surfaces is kept the same and is about +300 V in order to effectively collect secondary electrons released from the Stop surface. Each MCP detector produces a stop pulse with a magnitude proportional to the amount of secondary electrons reaching the MCP detector simultaneously. The MCP bias is commandable and is nominally in the range of 2750 to 3100 V.

Figure 4.15 shows different views of the assembled Stop unit. The MCP detector supporting electronics and connectors are located at the back of the Stop unit (left panel). The Stop unit MCP detectors are shown in the right panel. The frame is blackened to inhibit UV reflections and photo-electron yield.

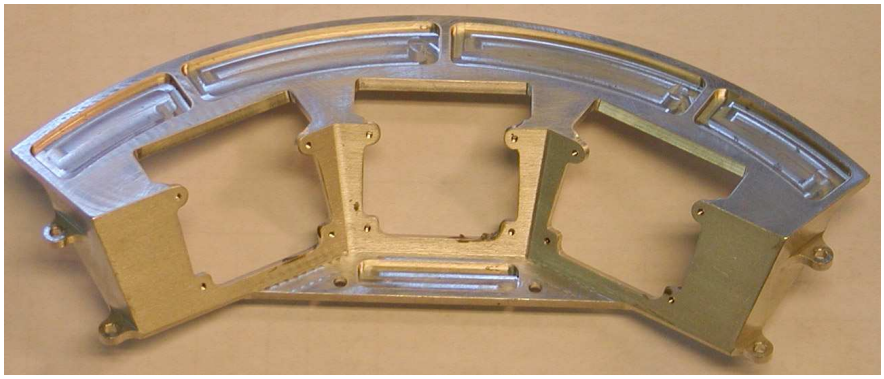

Figure 4.14: The Stop unit frame.

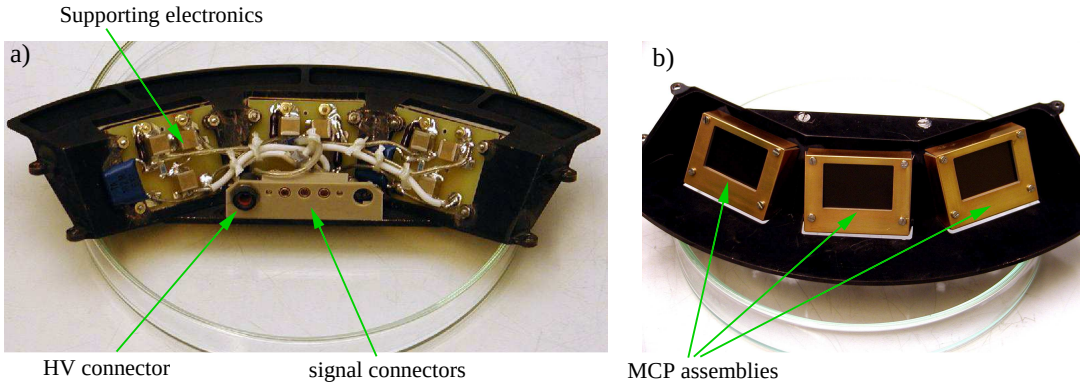

Figure 4.15: The Stop unit assembly: a) back side with the MCP detector electronics and connectors depicted by arrows, b) front side of the Stop unit with facing MCP detectors.

4.2.4 Surfaces

The selection of the Start and Stop surfaces was the most challenging part of the NPD development. Extensive studies have been performed at University of Bern, Switzerland (*Jans*, 2000), and Brigham Young University, USA, to optimize the performance of the surfaces, which must satisfy a number of requirements, namely, high secondary electron yield, high UV absorption even at grazing incident angles, high particle reflection coefficient (Start surface), low angular scattering (Start surface) and low photo-electron yield.

A multi-layer coating composed of a thin layer of Cr_2O_3, covered by a thicker layer of MgF and topped with a thin layer of WO_2, was used for the Start surface (Figure 4.16). The coating was optimized for the absorption of the 121.6 nm Lyman-α line at an incident angle of $\sim 15^\circ$. It was applied on a titanium substrate polished down to 100 Å roughness. The reflection coefficient was about 30%. The Start surface is of a trapezoidal shape. A pocket in the surface substrate is used to accommodate the temperature sensor and the heater.

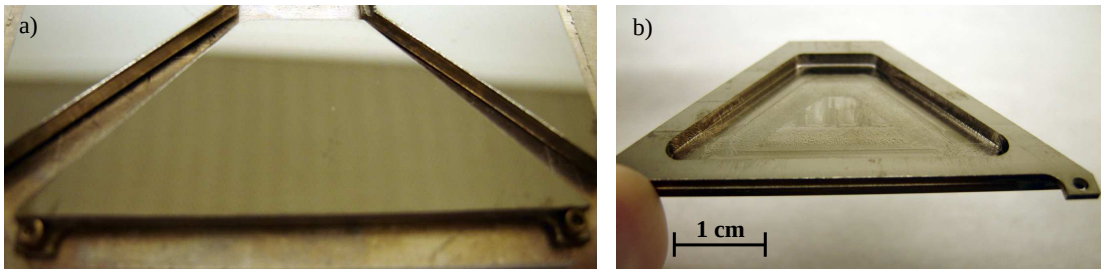

Figure 4.16: The NPD Start surface, view from the top (a) and bottom (b).

The Stop surface (Figure 4.17) is part of a graphite sphere (roughness around 100 nm) covered by a MgO layer of ~500 nm thickness. This combination has a very high secondary electron yield, low photo-electron yield, and high UV absorption. Much effort has been expended into increasing the stability of the MgO coating against moisture absorption. It was established that polishing the graphite down to the roughness of about 100 nm improves the surface stability, so no problems related to surface performance were encountered during assembly, integration, and verification (AIV) activities (i.e., due to absorption of air humidity).

Thus, the Stop surfaces did not require special maintenance to retain their stability and preserve the surface properties unchanged from their calibrated state.

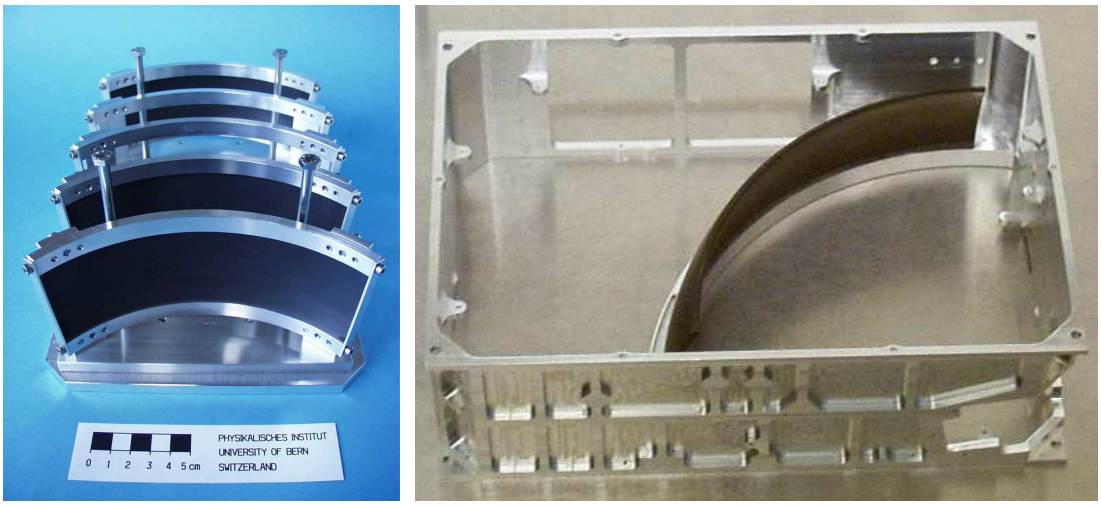

Figure 4.17: The Stop surface in a NPD chassi (right panel). The left panel shows a batch of Stop surfaces in a transport container.

4.3 Electronics

Each NPD sensor is an "intelligent" device and its electronics perform a substantial portion of the data pre-processing. The NPD electronics consist of two boards: Front-end electronics (FEE, Figure 4.18a) and digital TOF electronics (DigTOF, Figure 4.18b). All high voltages are provided and controlled externally.

The FEE block diagram and typical signal shapes are shown in Figure 4.19. Pulses from four MCP anodes (one Start and three Stops) are fed to discrete-charge sensitive preamplifiers based on fast MOS FET (frequency cut-off at 6 GHz) and followed by operational amplifiers. The wave shaper generates a fast logic pulse for the Time-to-Digital converter (TDC) of the DigTOF board, and fast Texas TLV1562 video Analog-to-Digital converters (ADC) perform a pulse height analysis. The signals are up-shifted by 0.8 V to reach the ADC working range of 0.8 – 3.8 V. Four Digital-to-Analog converters (DAC) provide input threshold control. The thresholds are commandable. The FEE provides a theoretical TOF resolution of 0.1 ns that is well within the limits of what is required for this measurement technique (1 ns).
DigTOF electronics serve a number of tasks, including:

- TOF measurement from one start to one out of three stop signals,
- serving FEE and initiating analog-to-digital conversion of stop pulses,
- coincidence check and selection of valid TOF – pulse height pairs,
- events counting,
- three different data types buffering in Static Random Access Memory (SRAM),
- interfacing DigTOF to DPU.

DigTOF is realized in two Field Programmable Gate Arrays (FPGA) Actel 54SX32. Figure 4.20 shows the DigTOF block diagram focused on the functionality of the diffirent componets and FPGA subroutines.

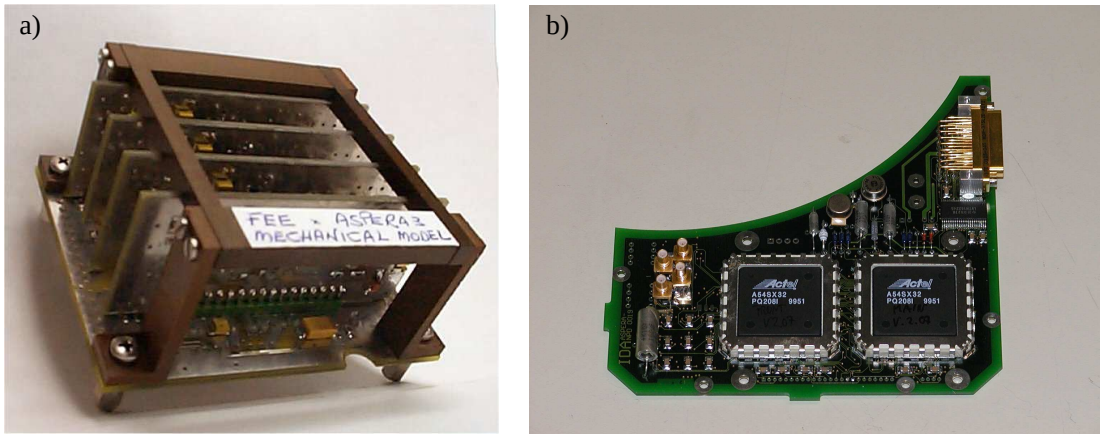

Figure 4.18: Technological models of a) Front-end electronics (FEE) and b) digital TOF electronics (DigTOF) are shown.

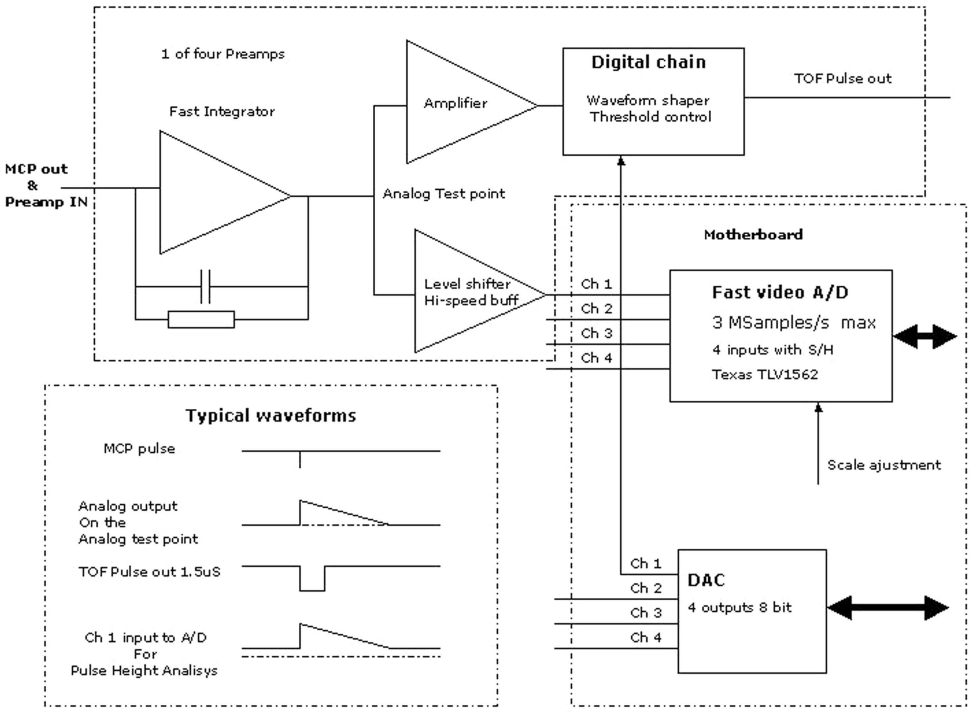

Figure 4.19: Front-end electronics block diagram.

The occurrence of a start signal followed by a stop signal leads to a TOF measurement in the TDC and generation of a data item with uncorrected TOF information. The time obtained is then corrected to compensate for a possible temperature drift. The TDC calibration is performed continuously using a 6 MHz clock supplied by the DPU, and the calibration constants are continuously updated at DigTOF. The TDC control and TOF correction are performed by a TDC Management unit, a part of FPGA. The final time data item is a TOF value with 12-bit binary time information. Parallel to this, a sampling process by FEE ADC follows the occurrence of a stop signal, thus generating a 10-bit data item with information of both direction and

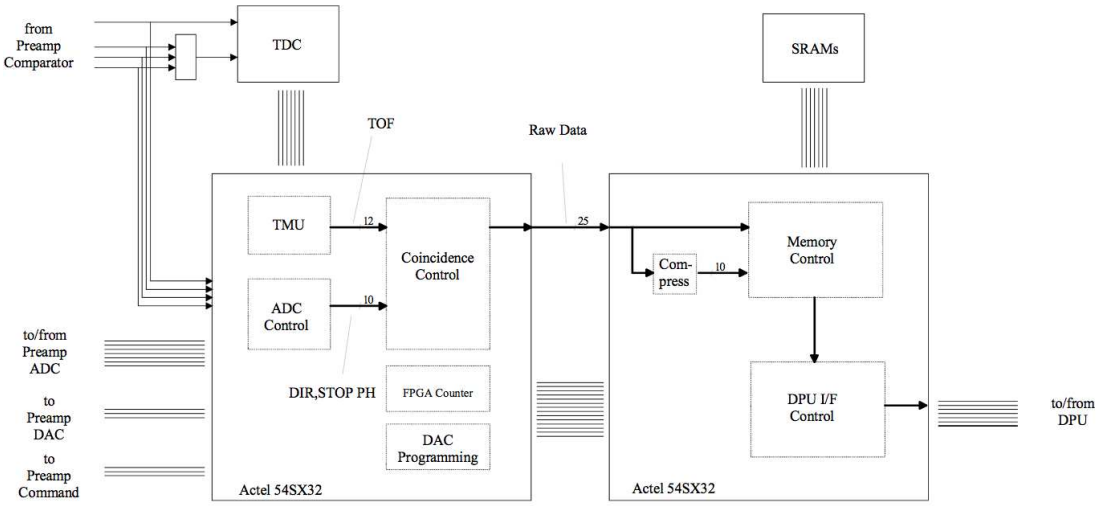

Figure 4.20: Digital TOF electronics block diagram.

8-bit stop pulse height. The coincidence control checks then for a valid coincidence of these two data items and additionally flags an occurrence of more then one start or stop signal during the TOF measurements. NPD registers a 'valid event' when a signal from one (and only one) Stop detector corresponds to one start event within the given TOF window. This now leads to a 25-bit raw data item formation that is used for the pending storing process. The memory control has to handle three different memory areas in the SRAM. For the binning array, the raw data is compressed into 10-bit data that represents the bin number inside the array. The respective bin is incremented by one up to the bin depth of 65535 (16 bit). For the raw data array, incoming raw data items are successively stored until this array is filled completely (512 entries). The PH array is filled in the same way as the binning array, but with the compressed stop pulse height data together with the respective direction. All data arrays are filled in parallel. The binning array is excluded, if the coincidence (1 Start – 1 Stop event) does not fit. Readout and the following initialization of these arrays are performed by using burst read access from the DPU. Several 16-bit event counters and two registers facing the preamplifier board are also implemented in FPGAs. One of these registers is used to program FEE DACs, the other one for directly commanding FEE. All control, counter and memory data are accessible from the DPU over 16-bit registers; physically the connection to the DPU is a 16-bit bus.

4.4 MCP assembly

There are five MCP detectors in each NPD: two Start and three Stop MCP assemblies. Figure 4.21 shows the Start (panel a) and the Stop (panel b) MCP assemblies. Micro-channel plates are known as high gain, low noise, two-dimensional detectors of charged particles and electromagnetic radiation. MCP is an array of solid state electron multipliers (*Wiza*, 1979) consisting of millions of microscopic electron multipliers (10^5 - 10^7 channels/cm^2) all fused together in a solid array. Typical channel diameter is 6 - 25 μm. The operational principle of the MCP detector is shown in Figure 4.22 (panel a). Panel (b) shows a cross-section of a 3D model of a Stop MCP assembly.

Each NPD MCP assembly comprises a pair of standard 'Photonis' custom cut rectangu-

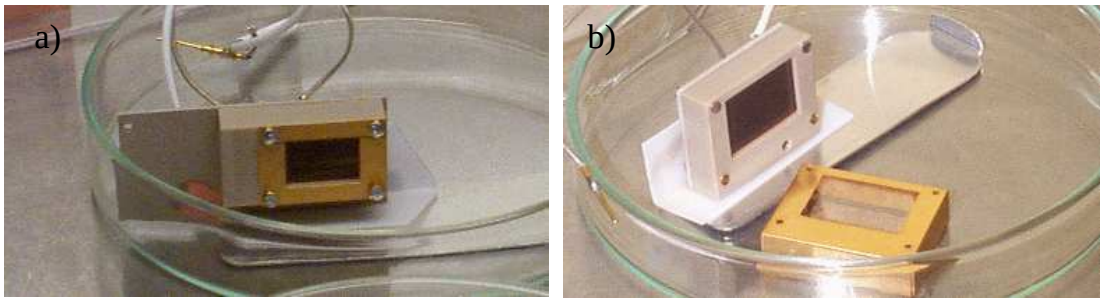

Figure 4.21: (a) Start and (b) Stop MCP assemblies.

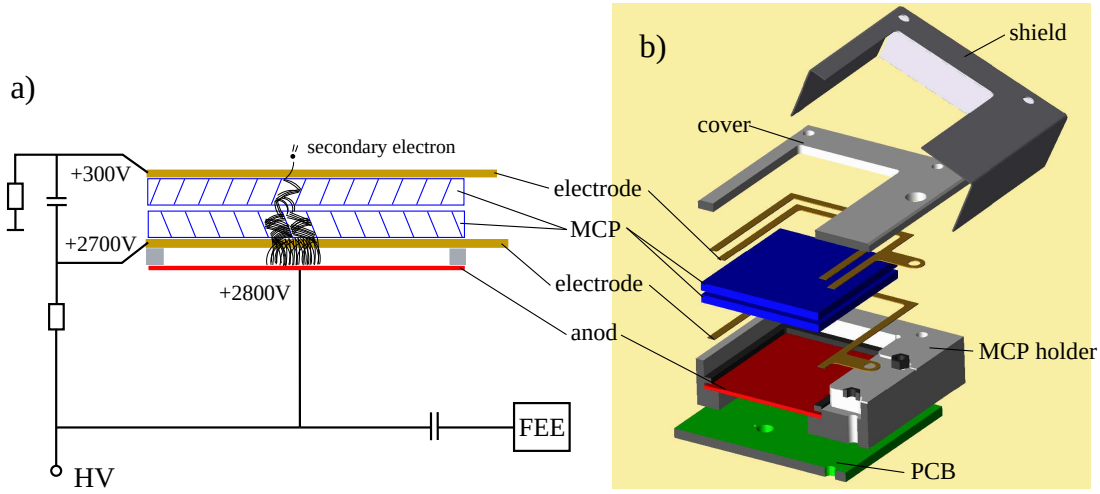

Figure 4.22: (a) MCP detector operation principle. Arrows depict major elements. (b) Cross-section of a 3D model of a Stop MCP assembly.

lar MCP plates of 1.0 mm thickness. MCPs operate in a chevron configuration to avoid an ion feedback. Secondary electrons reaching the MCP detector are attracted by the +300 V potential of the front surface of the first MCP. As soon as an electrons enter the MCP channels, it collides with the channel wall resulting in secondary electrons. The resultant secondary electrons are accelerated down the channel by the electric field of the bias high voltage applied across the plates. Further collisions with the channel walls produce more secondary electrons. Finally, an electron cloud is formed and extracted from the output side of the MCP and accumulates by an anode, separated from the rear side of MCP by a gap of 1 mm. The anode potential is ~100 V higher than that of the back of the MCP and is about +2800 V. The collected charge is transferred to FEE through a decoupling capacitor. The typical gain of the MCP detectors is in the range of (6 - 8) $\times 10^6$.

The size of the Start and Stop MCP detectors is different. The Start MCP is 8×12 mm, and the Stop MCP is 16×12 mm. Also, Start and Stop MCP detectors are connected differently. Both Start MCP detectors possess a common anode to efficiently collect secondary electrons yielded from different regions of the Start surface. Stop MCP detectors possess equal potential on the front MCP surfaces providing an evenly distributed electric field over the Stop surface in order to allow an angular response. MCP resistance differs between Stop MCP assemblies. Therefore, a certain resistor R was chosen for each Stop MCP assembly to provide the same MCP voltage across the plates in all three Stop MCP assemblies.

Start MCP detectors (two assemblies) and Stop MCP detectors (three assemblies) are controlled by two tele-commands independently.

4.5 Data formats

The sensor hardware mode is always the same but DigTOF generates in parallel two data flows (formats), namely, raw event data (RAW) and binned matrix data (BIN). Depending on the settings, the DPU reads out one of the flows. Thus, the sensor operates either in the RAW mode or in the BIN mode.

The RAW mode. The data buffer contains 512 data entries. Each 32-bit depth item corresponds to one recorded event. Incoming raw data items are stored sequentially until the data buffer is filled completely. Each data entry contains uncompressed TOF values with a 0.5 ns resolution as well as information about the direction, magnitude (pulse height) of a stop signal, and a coincidence flag (see Table A.1). The TOF spectral resolution is reduced by the DPU from 0.5 ns to 1 ns. The TOF window of 1 ns to 2048 ns is defined. PH data values are scaled to 255 levels.

The BIN mode. Both TOF and PH data are accumulated for each of three directions. TOF of valid events (one Start – one Stop) is stored in 16 logarithmically divided TOF bins. The size of the TOF bins and their location in the TOF space are shown in Table A.1. A stop signal magnitude value is stored in 16 linearly divided PH bins. The data buffer is an array of $16 \times 16 \times 3$ 16-bit counters. TOF is measured in the range of 50 to 1900 ns. The lower TOF limit allows for a cut off of electron events ('Start' electrons reaching the Stop unit). The higher TOF limit defines the upper energy of the range in question, i.e., no significant fluxes of *O* ENAs of an energy above 10 keV are expected in the region where ASPERA-3 / ASPERA-4 performs measurements. The matrix of $16 \times 16 \times 3$ can be reduced to $16 \times 2 \times 3$ comprising 16 TOF steps and two PH steps for three directions (see Appendix A.1).

The TOF mode. The RAW event data is post-processed by the DPU in TOF mode in order to reduce the bit-rate. The NPD sampling is fixed to 0.5 s. The direction and TOF of the correlated signals is extracted from the RAW data 32-bit words by DPU. The TOF spectrum resolution is downgraded to 8 ns, resulting in 256 linearly divided 8-bit TOF bins for every direction. Each of 256×3 16-bit counters is increased by one when addressed by 8-bit TOF and 2-bit direction. After accumulation, 16-bit counter values are log-compressed to 8 bits (Appendix A.2).

The PH mode. There is also an engineering data flow. The data buffer in PH mode contains 16×3 16-bit counters addressed by pulse height values.

Each of the NPD sensors (NPD1 and/or NPD2) can be set independently to any operation mode or be disabled (masked out). Data is not received by the DPU from the masked-out sensor. The NPD sampling time is commandable and equals $2^n \times 62.5$ ms, where n=1, 2, … 7; but nominally is 1 sec. The basic sampling periods are 0.5, 1.0, 2.0 sec (8, 16, 32 sampling periods of 62.5 ms), which correspond to three scanner rotation periods, 32, 64, and 128 s.

The NPD electronics also include linear counters to monitor the performance. Every start and stop event is counted by a corresponding 16-bit counter. There are four counters available

in every mode to count start events (Start counter) and stop events (Stop0, Stop1, Stop2 counters). In RAW mode two additional counters are used. The Tof counter is used to count valid events. Again, a 'valid event' is produced when a signal from one (and only one) Stop detector corresponds to one start event within the given TOF window. The Raw counter is used to count ADC conversion events.

4.6 Instrument level qualification

The NPD sensors were flight qualified on the instrument level as well as on the sensor level (vibration test). The environment tests on the instrument level included a mechanical test, electromagetic compatibility (EMC) test, and thermal vacuum (TVAC) test. The protoflight approach was used, meaning the hardware was tested to the qualification levels. The qualification level is usually 1.4 times the highest load the component should ever experience in operation (for mechanical test).

Mechanical test. Mechanical test is called sometimes a vibration test. It was done in order to simulate vibration caused by the rocket engine during the launch. Vibration was simulated in three transverse directions. The standard testing procedure included: sine vibrations over a specified frequency range to search for resonances, and random vibrations simulating the real mechanical environment during the launch.

Figure 4.23 shows ASPERA-4 mounted on a vibration table, with accelerometers depicted by arrows. Mechanical tests of ASPERA-4 were performed on an LDS964LS electro-dynamic vibrator with LDS 1200 $\times$1200 sliding table. An electrical functional test of the instrument was performed every time a given vibration test was over.

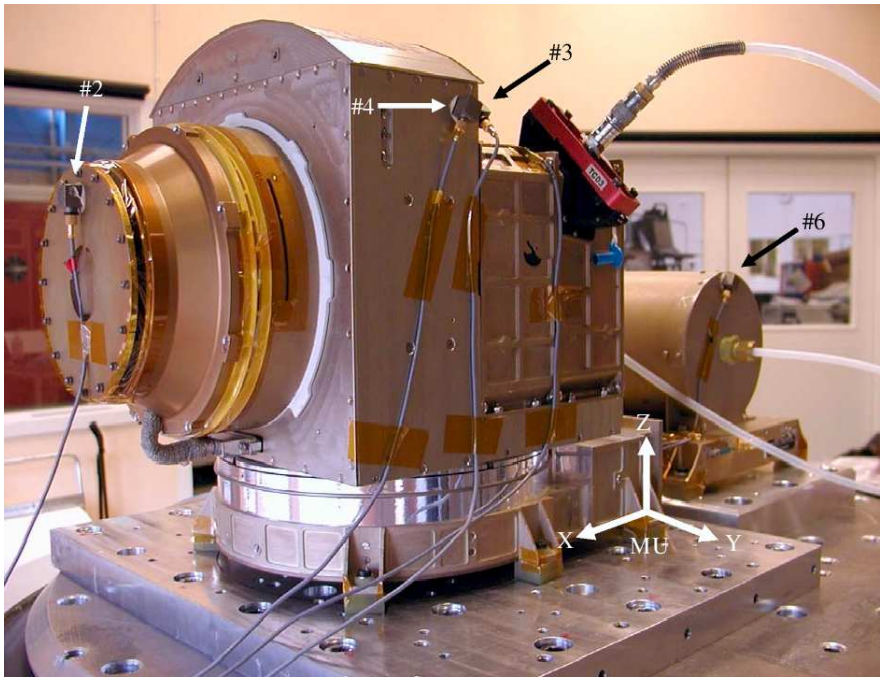

Figure 4.23: ASPERA-4 mounted on a vibration table. Arrows depict accelerometers. GN_2 purging tubes are connected between the test sessions.

EMC test. The purpose of the EMC test was to verify the electromagnetic susceptibility and emissive properties of the ASPERA-3/ASPERA-4 instruments. It was done in order to prove an electromagnetic compatibility of devices with the spacecraft systems as well as other sensors on board the spacecraft. The testing sequence included measurements of electromagnetic radiation of the instrument and identification of whether it is resistant to external electromagnetic radiation in a certain frequency and magnitude range. During the EMC test the instrument was running in different modes defined by the given EMC test.

TVAC test. The purpose of the TVAC test was to verify the capability of the ASPERA-3 / ASPERA-4 instruments to withstand the thermal load to which the units were to be exposed during their operational lifetime. This test mostly affects electrical components and movable parts. The ambient temperature varied cyclically over the defined temperature interval. Figure 4.24 show the temperature cyclogram (panel a) and measured temperature profiles (panel b). The instrument functionality was verified in vacuum over the required temperature range (-30° to +50° centigrade) for a temperature variation of 1°/min (Figure 4.25).

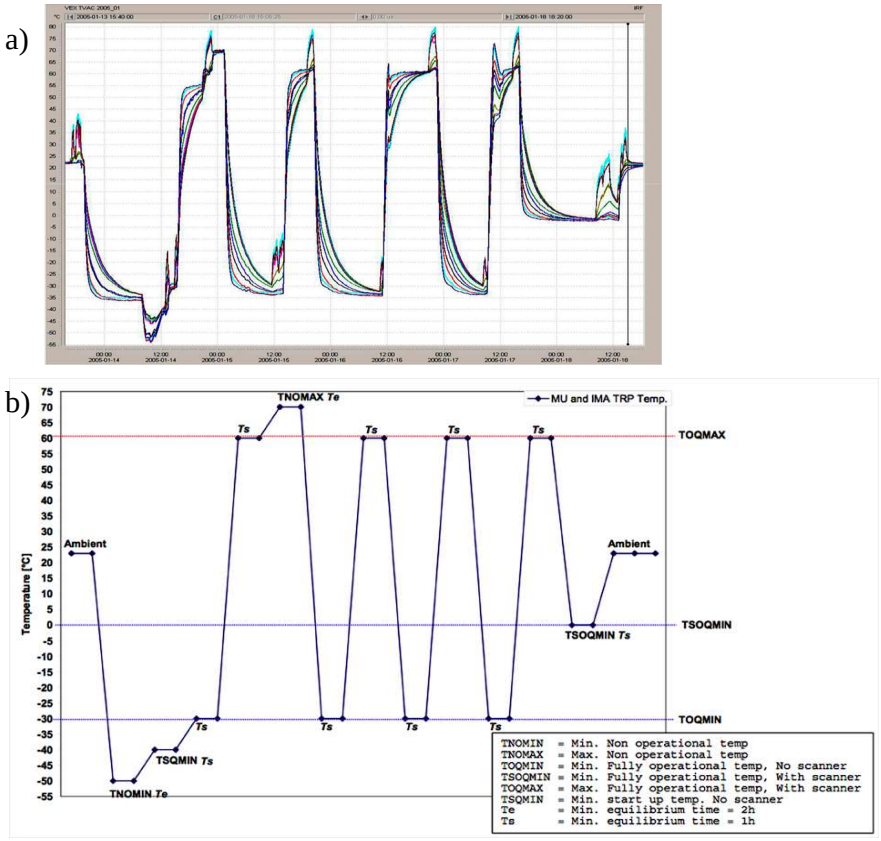

Figure 4.24: TVAC test of ASPERA-4. The measured (a) and predefined (b) temperature profiles are shown.

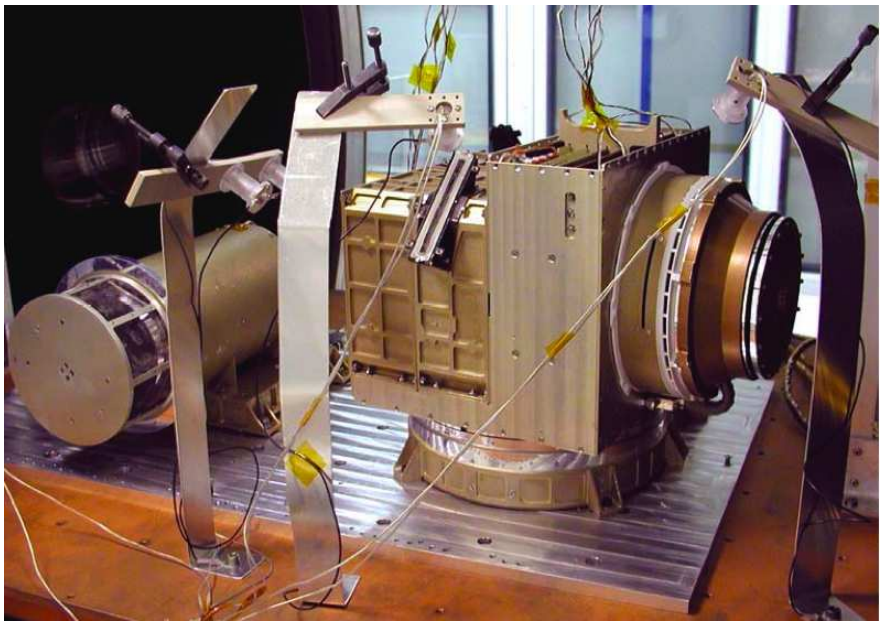

Figure 4.25: The ASPERA-4 instrument mounted in a vacuum chamber during the TVAC test. The small ion guns to simulate particle flux are also visible.

4.7 NPD response to high energy particles

The NPD deflection system cut-off energy is ~70/q keV, hence particles of higher energy (>100 keV) can pass through the deflector and produce scattered particles of lower energy that could be detected by the NPD. We performed simulations of the scattering of high energy protons on a mono-crystal tungsten (W) surface covered with a thin layer of WO_2 (simulating the Start surface). The simulations were based on the 'The Stopping and Range of Ions in Matter' (SRIM) code (*Ziegler et al.* (1985); www.srim.org).

The NPD geometry was used in the simulation process. As many as 16730 projectile particles of energy of 100 keV were injected at a grazing angle of 15° to the surface plane. Scattered particles were collected and both angular- and energy distributions were analyzed. Figure 4.26 shows the energy distribution of the particles for all scattering angles.

Figure 4.27 shows the energy distribution of particles which can reach the Stop surface. Note that particles scattered approximately specularly (i.e., towards the Stop surface) lose more than half of their initial 100 keV energy. A number of particles in the energy range of 0.1 – 10 keV (the NPD energy band) that reached the Stop surface was ~170. Hence, the amount of high energy protons that can be detected by the NPD sensor is ⩽1% of the incoming flux.

If the typical differential flux of 100 keV H^+ ions is $10^3 cm^{-2}sr^{-1}s^{-1}keV^{-1}$ (such particles can be born at a distant shock, travel along magnetic field lines and reach the sensor), then we estimate that the detected integral flux number will be less than $10 - 10^2$ $cm^{-2}sr^{-1}s^{-1}$. This flux is several orders of magnitude lower than the expected ENA flux in the energy range of 0.1 – 10 keV. The ENA flux in the Martian environment is in the range of $10^4 - 10^5$ $cm^{-2}sr^{-1}s^{-1}$ as reported by *Futaana et al.* (2006b); *Galli et al.* (2006b) (see Chapter 6). Moreover, the simulated energy spectrum of high energy H^+ differs from that of the detected ENA signals (*Galli et al.*, 2006a). Therefore, we conclude that high energy H^+ can be disregarded as a source of intense ENA signal at Mars.

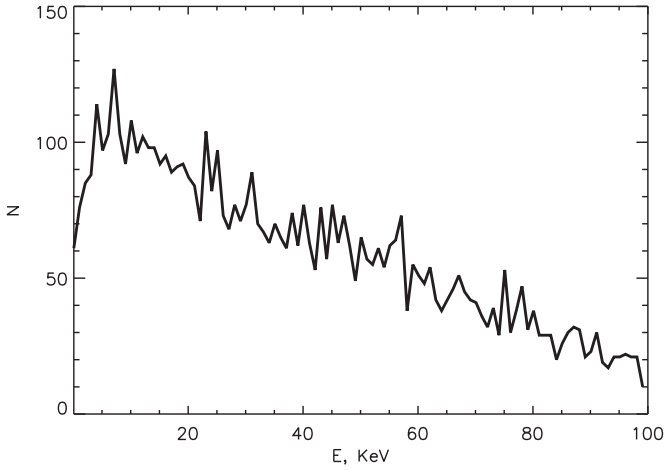

Figure 4.26: Simulated energy distribution of *H* particles with an inital energy of 100 keV, scattered on the Start surface in all directions.

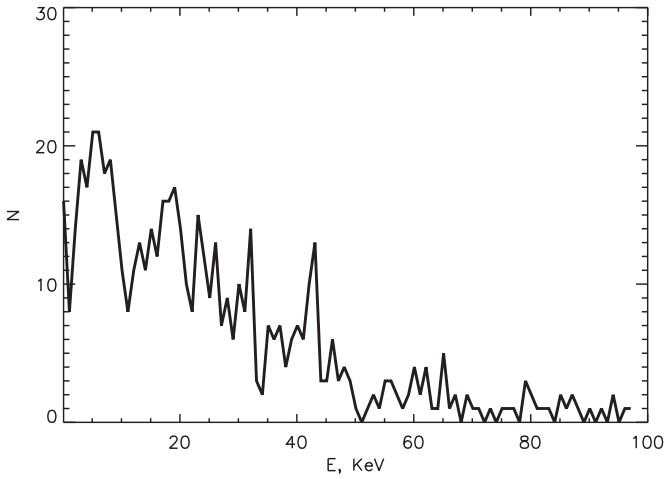

Figure 4.27: Simulated energy distribution of 100 keV H, scattered on the Start surface, which can reach the Stop surface.

This page is left intentionally blank

Chapter 5

The NPD calibrations

5.1 Introduction

The calibration of NPD is performed in order to define the detailed characteristics of the sensors, such as the angular response function, efficiency, geometric factor of each of the sensor's sectors. The NPD sensors were calibrated using ion beam facilities. The ion beam is easily to operate and its absolute intensity is easier to monitor than an ENA beam. ENAs or ions interacting with the Start surface, lose their initial charge state within a few Å of the material and achieve a charge equilibrium which does not depend on the initial charge. Therefore, an ENA instrument calibration can be performed using an incoming ion beam. The results of the sensor calibrations using the ion beam can be directly applied to ENAs (except deflector system calibrations, which in any case were out of scope of the calibrations).

5.1.1 Calibration facilities

The NPD sensors were calibrated at the Swedish Institute of Space Physics (IRF, Kiruna) using its ion beam facilities. The calibration facility includes two ion sources with energies of 0.4 – 25 keV and 0.02 – 50 keV that provide large diameter ($\leqslant$10 cm) parallel beams of selected energy and mass and with variable intensity. The systems are also equipped with turn-tables having four degrees of freedom. The system used for the NPD particle calibration is the PSX-2751 50 keV Ion Source from Peabody Scientific. It is capable of producing a parallel ion beam of a flat profile with an energy of up to 50 keV/q. The system can be run in three different energy ranges, namely 0.05 – 1.3 keV/q, 1.0 – 15 keV/q, and 15 – 50 keV/q. Ions are produced in a duoplasmatron in discharge between an anode and a filament, coated with Ba_2CO_4 to increase electron emission. The ion species are defined through injection of the corresponding gas into the duaplasmatron. To increase the ionization efficiency, a strong magnetic field is applied in the axial direction of the duoplasmatron. Emitted electrons spiral along the magnetic field lines towards the anode and produce long ionization paths. The duoplasmatron is kept under positive HV potential defining the ion beam energy. Ions are extracted from the duoplasmatron / source through an extraction electrode and pass through a three-element Einzel focusing lens, which collimates the diverging ion beam into a parallel beam. The focal length of the lens can be optimized by adjusting the voltage of the lens. The ions then enter an $E \times B$ Wien filter. The Wien filter is based on transverse magnetic and electric fields. The electric field can be varied to balance the magnetic force so that only ions of the desired velocity (mass) can pass through the filter. Exiting the Wien filter, the ions are accelerated in an acceleration gap to achieve the final

beam energy. The beam is then guided through a 90° electrostatic analyzer, with a central radius of 12.7 cm, in order to select ions within a narrow energy band and reject a neutralized fraction of the beam. The electrostatic analyzer in the system has an energy resolution of 1%. To permit broadening of the ion beam that emerges from the electrostatic analyzer (~10 mm in diameter), a defocus lens first diverges the beam and then a focus lens collects the diverging beam into a parallel beam used for calibrations (Figure 5.1). Both lenses are three-element Einzel lenses of different sizes. A retractable Faraday cup provides measurements of the ion beam intensity as well as, indirectly, the beam location. It is mounted inside the vacuum tank. The Faraday cup closes the beam outlet completely during the current measurements. A fraction of the outgoing beam is neutralized by charge exchange between the ions and residual gas in the drift tube. The neutral part of the beam does not exceed 3% of the total beam intensity.

The maximally achievable beam divergence is derived from the geometry of the ion source (see Figure 5.1). The distance between the electrostatic analyzer exit and the aperture is ~1.7 m, the electrostatic analyzer exit diameter ~10 mm, the aperture diameter 36 mm, and the distance between the exit aperture and the turn-table ~1.8 m, the maximal divergence of the ion beam is thus estimated to be less than 2°. The ion beam spot at the center of the vacuum chamber, where the instrument is located, can thus vary between 10 - 60 mm in diameter.

The system produces quite stable and homogeneous over profile (±10%) ion beam. During the calibrations no direct beam profiling was performed.

5.1.2 Calibration setup

Each of the NPD units was calibrated on a sensor level. The calibration setup and coordinate system are shown in Figure 5.1. The sensor, mounted on the turn-table inside the vacuum chamber, was subjected to parallel ion beams of different energies and masses. The turn-table allows the sensor to sweep in the azimuthal plane over $[-45°, 45°]$ and in the elevation plane over $[-7.5°, 7.5°]$, with 1° steps. The turn-table can also be translated across the incident ion beam in both vertical and horizontal directions.

Angles α, β denote the azimuth angle and elevation angle, respectively. The angular position, $\alpha = \alpha_0$ and $\beta = \beta_0$, shown in Figure 5.1, corresponds to the sector Dir1 pointing. In such a way the deflector plates are placed horizontally, i.e., normally to the turn-table rotation axis. Definition of the NPD sectors (Dir0, Dir1, and Dir2) pointing is shown in Figure 4.5. The geometrical pin-hole area of the sensor is $A_G = 3.0 \times 4.5 \times \cos 15° = 13.04$ mm^2, where 15° is the inclination of the pin-hole with respect to the entering beam (see Figure 5.2).

Figure 5.2 shows the cross-section of the sensor through the pin-hole and sector Dir1. All key elements are identified. A thin black line shows an incoming beam trajectory through the collimator, the pin-hole, towards the Start surface and then to the Stop surface. The azimuthal rotation axis of the sensor is co-aligned with the rotation axis of the turn-table and passes through the pin-hole geometrical center. It is normal to the deflector plane of NPD. In such a configuration the NPD pin-hole is kept well inside the ion beam during the azimuthal scanning, i.e., no translation of the sensor across the ion beam is required. The vertical shift of the sensor aperture during elevation scanning is also small with regard to the ion beam spot size.

The sensor calibrations were performed with the following setup:

- Deflector electrodes were grounded because the sensor was calibrated using ions,
- Ion beam intensity was set to keep the Start MCP count rate $\leqslant 5 \times 10^3$ s^{-1},
- Pressure in the vacuum chamber was $\leqslant 4 \times 10^{-7}$ mbar.

The calibration objectives together with the ion beam species and energy settings are given in

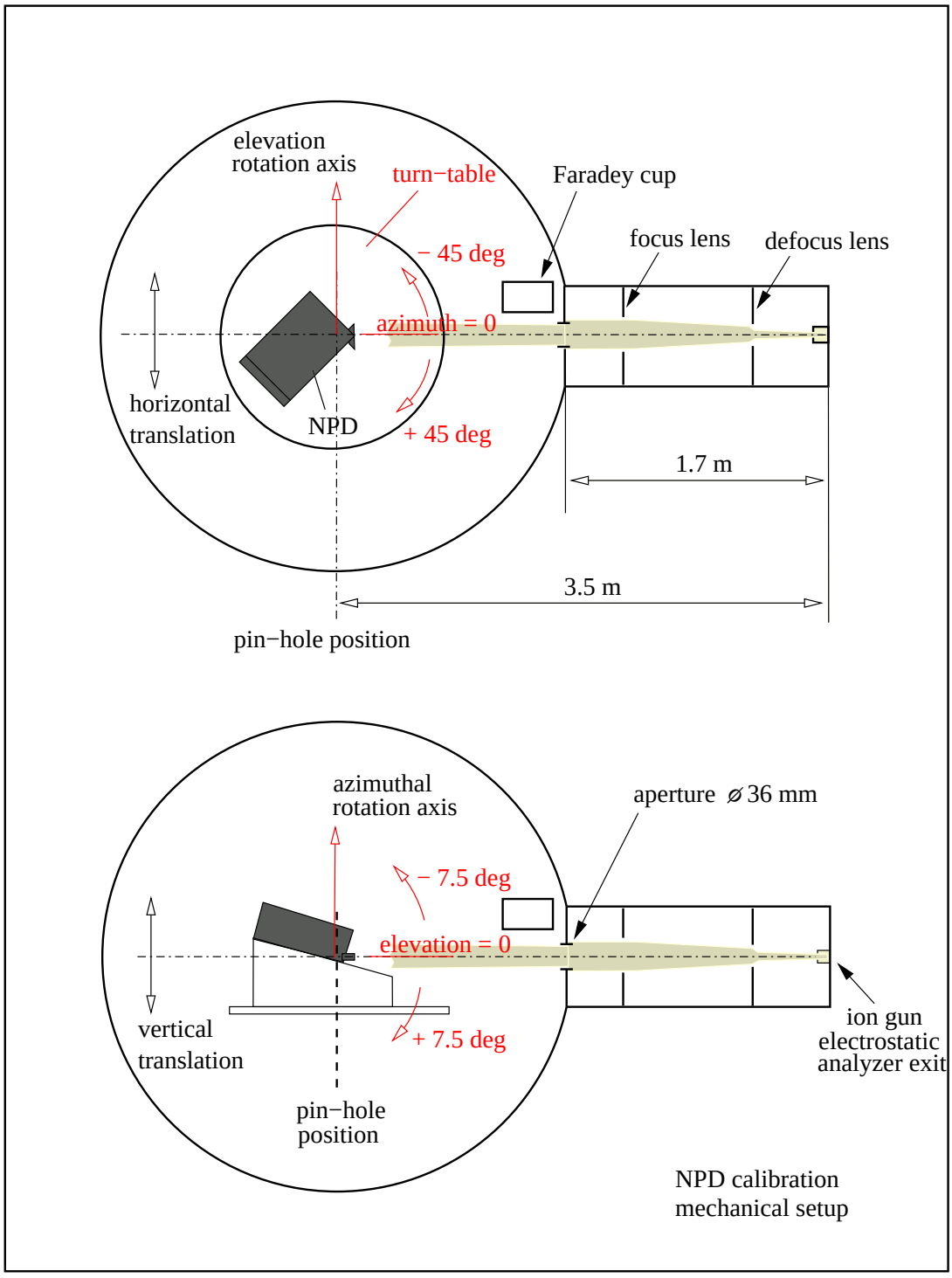

Figure 5.1: NPD calibration mechanical set up and coordinate system; view from the top (the upper part) and from aside (the lower part).

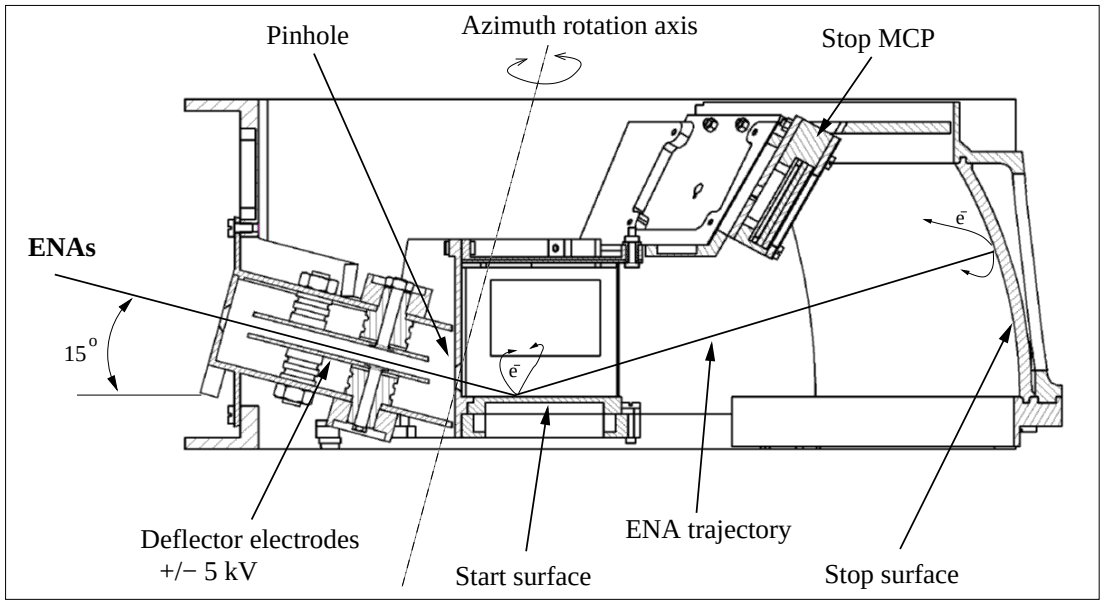

Figure 5.2: The instrument cross section, showing the azimuthal rotation axis.

Tables 5.1 and 5.20 respectively for the ASPERA-3 / NPD and ASPERA-4 / NPD.

5.2 Theoretical principles

5.2.1 MCP characterization

Before the calibration of the NPD sensor, MCP characterization was performed. MCP detector characterization and tests included:

- HV test. MCP detector should withstand the bias voltage at least 10% above the nominal.
- Analysis of MCP count in dependency on the bias voltage and threshold level, and determination of the working point, i.e., the nominal bias voltage at which MCP count saturates.
- Dark noise determination under the nominal bias.
- Pulse height distribution analysis of MCP output signal in order to identify the sensitivity threshold level for FEE. The nominal bias is applied.

5.2.2 Beam characterization

The ion beam characterization is performed in order to provide accurate calibrations of the sensor efficiency. Beam monitoring in the system is provided by a retractable Faraday cup. It is not possible to monitor the ion beam continuously during the measurements. Therefore, the ion beam should be stable, and parallel. Its spatial distribution should be homogeneous.

The ion source provides a sufficiently stable beam (Section 5.1.1). The stability was verified before each calibration run. The average value of the ion beam current measured before and after the run was obtained and used in calculations.

To avoid the possible errors in the absolute calibrations of the sensor efficiency associated with the beam intensity variations over the spot, a special transverse scan was implemented

for the efficiency calibration (see Section 5.3.3). Also errors due to measurements with a non-parallel ion beam are taken into account by this scan procedure. Defocused ion beams can otherwise lead to wrong estimation of the ion current density at the Faraday cup and the sensor.

5.2.3 Geometrical Factor calculation

The geometrical factor, (G), of a sensor is the integral of the effective area $A_{eff}(\bar{\Omega})$ in the direction $\bar{\Omega}$ of the sensor's aperture over the sensor field-of-view

$$G = \int A_{eff}(\bar{\Omega})\, d\Omega$$

From simple spherical trigonometry the elementary solid angle $d\Omega$ will be given in the α, β coordinates as $d\Omega = \cos\alpha\, d\alpha\, d\beta$. We thus obtain the geometrical factor expression for NPD as

$$G = \int_{\alpha}\int_{\beta} A_{eff}(\alpha,\beta)\cos\alpha\, d\alpha\, d\beta, \tag{5.1}$$

where the integrals are over the sensor field-of-view. We assume that A_{eff} can be presented by the expression

$$A_{eff}(\alpha,\beta) = \varepsilon(E)\cdot f(\alpha,\beta)\cdot A_o \tag{5.2}$$

where ε is the efficiency and depends only on energy (see Section 5.2.4), $f(\alpha,\beta)$ is a function which defines the shape of the angular response and max $f(\alpha,\beta)|_{\alpha,\beta}$=1, and A_o is the pin-hole area at the maximum $f(\alpha,\beta)$, i.e., A_o=$A(\alpha_o,\beta_o)$. α_o,β_o are the azimuth and elevation at which $f(\alpha_o,\beta_o)$=1. Therefore,

$$G = \int_{\alpha}\int_{\beta} \varepsilon(E)\cdot A_o\cdot f(\alpha,\beta)\cos\alpha\, d\alpha\, d\beta$$

By defining a pure geometrical factor G_o (with the efficiency excluded) as

$$G_o = A_o \int_{\alpha}\int_{\beta} f(\alpha,\beta)\cos\alpha\, d\alpha\, d\beta \tag{5.3}$$

we obtain the total geometrical factor as

$$G = \varepsilon(E)\cdot G_o \tag{5.4}$$

The efficiency can thus be measured separately from the angular response, which avoids possible errors due to beam intensity variations over the spot. The calibration principle becomes simple. We sweep the sensor over the beam over elevation and azimuth and normalize the recorded count rate to the maximum value. Defining the azimuth and elevation of the maximum count rate, (α_o, β_o), we also define the effective area at these angles. We assume

$$\begin{aligned} A_{eff}(\alpha,\beta) &= A_{eff}(\alpha_o,\beta_o)\,\frac{f(\alpha,\beta)}{f(\alpha_o,\beta_o)} \\ &= A_{eff}(\alpha_o,\beta_o)\cdot f(\alpha,\beta) \\ &= \varepsilon(E)\cdot A_o\cdot f(\alpha,\beta) \end{aligned} \tag{5.5}$$

$$f(\alpha,\beta) = \frac{C(\alpha,\beta)}{C(\alpha_o,\beta_o)} \tag{5.6}$$

where $C(\alpha,\beta)$ is the count rate at the azimuth α and elevation β. G can be calculated finally as

$$\begin{aligned} G &= A_{eff}(\alpha_o,\beta_o)\int_\alpha\int_\beta f(\alpha,\beta)\cos\alpha\, d\alpha\, d\beta \\ &= \varepsilon(E)\cdot A_o\int_\alpha\int_\beta \frac{C(\alpha,\beta)}{C(\alpha_o,\beta_o)}\cos\alpha\, d\alpha\, d\beta \end{aligned} \tag{5.7}$$

5.2.4 Efficiency

The sensor efficiency ε depends on a number of factors such as particle mass and energy, MCP bias voltage, surface properties and conditions, etc. MCP characterization was performed and the working point was defined prior to the tests. All tests were performed at this working point, i.e., MCP bias was fixed. ε is measured for different incident ion species at different energies.

If the calibrating ion beam has the current density, j, which is constant over the effective pin-hole area, the following expression can be written

$$\begin{aligned} C(\alpha,\beta) &= \frac{j}{q}\cdot A_{eff}(\alpha,\beta) \\ &= \frac{j}{q}\cdot\varepsilon\cdot A_o\cdot f(\alpha,\beta) \\ &= \frac{dI}{dA}\cdot\frac{\varepsilon}{q}\cdot A_o\cdot f(\alpha,\beta) \end{aligned} \tag{5.8}$$

where q is the elementary charge, I is the beam current, dA the area element over the beam spot. Note that $j = \frac{dI}{dA}$ may vary over the beam spot (not homogenous beam). Rewriting the expression in the form

$$\begin{aligned} \varepsilon\cdot dI &= q\cdot\frac{C(\alpha,\beta)}{A_o\cdot f(\alpha,\beta)}\cdot dA \\ &= \frac{q}{f(\alpha,\beta)}\cdot dC(\alpha,\beta) \end{aligned} \tag{5.9}$$

where $dC(\alpha,\beta)$ is the count rate over an elementary area over the beam spot, we can integrate both sides and get the expression for the efficiency

$$\varepsilon = \frac{C_{Total}(\alpha,\beta)}{f(\alpha,\beta)}\cdot\frac{q}{I} \tag{5.10}$$

where $C_{Total}(\alpha,\beta)$ is the total count rate integrated over the whole beam spot A_{beam}.

$$\begin{aligned} C_{Total}(\alpha,\beta) &= \gamma\int_{A_{beam}} dC(\alpha,\beta) \\ &= \gamma\sum_i\sum_j C_{ij}(\alpha,\beta) \end{aligned} \tag{5.11}$$

where i, j - the indexes over coordinates in the plane perpendicular to the beam.

$$\gamma = \frac{A_{pixel}}{A_{geom}} \tag{5.12}$$

where A_{pixel} = 4.5 × 3.0 mm – a characteristics of the sweep, A_{geom} is a projection of the pin-hole on the plane normal to the beam direction and depends on sensor direction. If the measurement performed at $\alpha = \alpha_o$ and $\beta = \beta_o$,

$$\varepsilon = q \cdot \frac{C_{Total}(\alpha_o, \beta_o)}{I} \tag{5.13}$$

This expression does not depend on the area and thus can be applied even for non-homogenuos beams. In practice, it implies that it is sufficient to cover the beam spot fully with the effective pin-hole size pixels and record the total number of counts. In principle, it is not even necessary to make the measurements at the maximum of the angular response function. If the efficiency ε_m was measured at the azimuth α_m and elevation β_m, the sensor efficiency at α_o, β_o is given by the obvious relation

$$\varepsilon = \frac{\varepsilon_m}{f(\alpha_m, \beta_m)} \tag{5.14}$$

5.2.5 Energy resolution

Dependency of the particle time-of-flight T_M on the initial particle energy E and mass M can be expressed as

$$\begin{aligned} T_M &= L \cdot \frac{\sqrt{M}}{\sqrt{E - \Delta E_{loss}}} \\ &= L \cdot \frac{\sqrt{M}}{\sqrt{E}\sqrt{1-K}} \\ &= 720 \cdot L(cm) \cdot \frac{\sqrt{M(amu)}}{\sqrt{E(eV) - \Delta E_{loss}(eV)}} \\ &= 720 \cdot L(cm) \cdot \frac{\sqrt{M(amu)}}{\sqrt{E(eV)}\sqrt{1-K}} \end{aligned} \tag{5.15}$$

where L is the TOF distance, ΔE_{loss} the energy loss when a particle interacts with the Start surface, T_M in ns, $K = \Delta E_{loss}/E$ the relative energy loss.

TOF measurements are performed for hydrogen and oxygen species in a range of particle energies from 0.1 keV to 10 keV. TOF spectra are shown in Sections 5.4.6, 5.5.6. Using the position of the maximum of the TOF spectra, we can obtain the TOF dependence on the particle initial energy and define the energy loss.

5.2.6 Mass resolution

Hydrogen and oxygen atoms are assumed to be the most probable species to be detected in the Martian and Venusian plasma environments.

Because of the large difference in velocity (for the same energy) and relatively narrow TOF window (50 ns - 1900 ns), TOF measurements alone can be used for mass identification. Indeed, TOF below 240 ns corresponds to either hydrogen with an energy above 580 eV or oxygen above 10 keV. The oxygen ENA fluxes with such high energies are very low because planetary ions do not have enough room to get accelerated in the small region with sufficiently high exospheric densities. Therefore, TOFs below 240 ns can come only from hydrogen. TOF above 650 ns can only come from oxygen because the instrument efficiency is very low for 100 eV hydrogen and such slow atoms cannot be detected by NPD. Inside the TOF range of 240 - 650 ns other mass resolving techniques are required, for example pulse height analysis.

PH analysis

PH analysis is based on the secondary electron yield dependency on the ENA atomic number for different species with the same velocity. Particles of different mass and the same velocity yield different amounts of secondary electrons from the Stop surface, which was optimized for high secondary electron yield. The heavier the ions, the higher the secondary electron yield. The more secondary electrons reach the Stop MCP simultaneously, the higher the output signal, because electrons hit different MCP channels. The higher the secondary electron yield, the higher the magnitude of the analog stop signal produced which is analyzed by a fast 8-bit ADC. Hydrogen atoms yield fewer secondary electrons from the Stop surface than equally fast oxygen atoms. Each 8-bit pulse height value is reduced to 4 bit resolution (16 levels or channels) in the BIN mode.

Figure 5.3 shows pulse height distributions from *H* (the red curve) of an energy of 0.3 keV and *O* (the black curve) of an energy of 5.0 keV (both species possess approximately the same velocity) measured in the BIN mode. Both distributions are normalized to have the same area of 1.

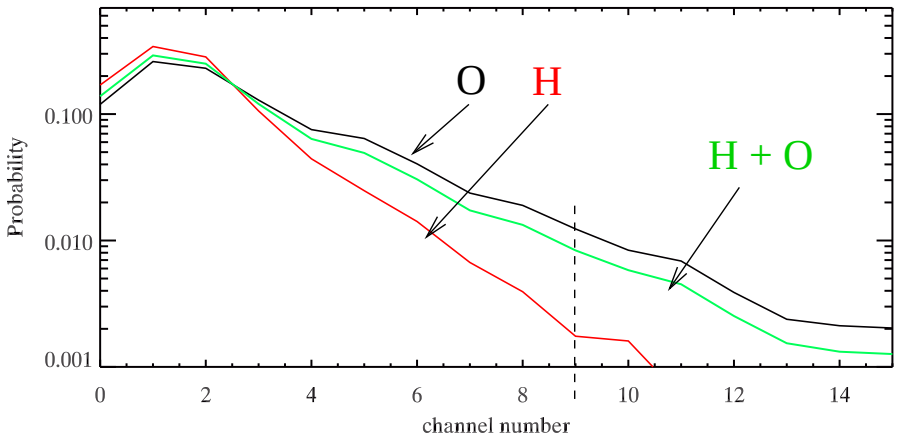

Figure 5.3: Pulse height distributions from *H* (the red line) and *O* (the black line) with the same velocity are shown. Both distributions are normalized to have the same area of 1. The green line shows a pulse height distribution from a mixture of *H* and *O* normalized to have the area equal to 1 as well. The dashed line is set to the channel $N = 9$. *O* gives a larger count in the range of channels 9 - 15.

As can be seen, areas of the tail parts of the pulse height distributions (integrated over the channels from an arbitrary chosen channel *N* to 15) are different. *H* atoms produce signals of lower amplitude and consequently give shorter tails in the pulse height distribution than heavier *O*. Hence, the ratio of the tail to the total area of the distribution is larger for *O* than for *H*. In the case of a mixture of *H* and *O* atoms, the pulse height distribution is a sum of the distribution from *H* and *O*. The green line in Figure 5.3 shows a pulse height distribution from a mixture of 50% *H* and 50% *O*. The distribution is normalized to have an area of 1. The tail part of this distribution comprises partly *H* and partly *O* counts. If a measured pulse height distribution has no counts in the tail part while the count rate is reasonably high ($\sim$1 kHz), the incoming particles are hydrogen. However, if the tail does contain some counts, the incoming flux may contain a mixture of *H* and *O*. Let us show how one can deduce the mass composition of the incoming flux during in-flight measurements from the pulse height distribution for *H* and *O* obtained in the calibrations. The probability for hydrogen and oxygen to produce counts in

the tail part are, respectively,

$$P_H = \frac{\sum_{i=N}^{15} C_i^H}{\sum_{i=0}^{15} C_i^H} \tag{5.16}$$

$$P_O = \frac{\sum_{i=N}^{15} C_i^O}{\sum_{i=0}^{15} C_i^O} \tag{5.17}$$

where C_i^H and C_i^O are the respective amount of counts in the i-th bin of the pulse height distribution for H and O. Numbers P_H, P_O, and N are defined in the calibrations. The total number of counts N_{tail} from each specie in the tail region thus becomes

$$N_{tail}^H = P_H \cdot N_{Total}^H \tag{5.18}$$

$$N_{tail}^O = P_O \cdot N_{Total}^O \tag{5.19}$$

where N_{Total}^H and N_{Total}^O are the total amount of counts for H and O, respectively. In the case of measuring a mixture of H and O, we know the number N_{Total}^{H+O} and the relative amount of counts in the tail region R,

$$\begin{aligned} R &= \frac{\sum_{i=N}^{15} C_i^{H+O}}{\sum_{i=0}^{15} C_i^{H+O}} = \frac{\sum_{i=N}^{15} (C_i^H + C_i^O)}{N_{Total}^{H+O}} = \frac{N_{tail}^H + N_{tail}^O}{N_{Total}^{H+O}} \\ &= \frac{P_H \cdot N_{Total}^H + P_O \cdot N_{Total}^O}{N_{Total}^{H+O}} \end{aligned} \tag{5.20}$$

Keeping in mind $N_{Total}^H + N_{Total}^O = N_{Total}^{H+O}$, we arrive at

$$N_{Total}^O = \frac{R - P_H}{P_O - P_H} \cdot N_{Total}^{H+O} \tag{5.21}$$

$$N_{Total}^H = \frac{P_O - R}{P_O - P_H} \cdot N_{Total}^{H+O} \tag{5.22}$$

Channel N is defined in such a way as to minimize the value of $\frac{P_H}{P_O}$. The values of N, P_O, P_H are defined for every NPD sector during calibrations. Note, the method works only for good statistics. This PH analysis is used in the BIN mode (due to good signal statistics achievable in this mode) for the on board data reduction (see Appendix A.1).

Example. Let a total count of valid events N^{H+O}_{Total}=1000 be detected by sector Dir1 of the sensor during the sampling time Δt. P_H=0.12·10^{-2} and P_O=1.25·10^{-2} as calculated during the calibrations. Let the ratio R be calculated as 0.01.

Hence, the *O* fraction is $N^{O}_{Total} = (0.01 - 0.12 \cdot 10^{-2}) / (1.25 \cdot 10^{-2} - 0.12 \cdot 10^{-2}) \cdot 1000 = \sim 779$. The counts from *H* are: $N^{H}_{Total} = 1000 - 779 = 221$.

5.3 Measurement principles

5.3.1 MCP characterization

Figure 5.4 shows the characterization setup of the MCP detectors.

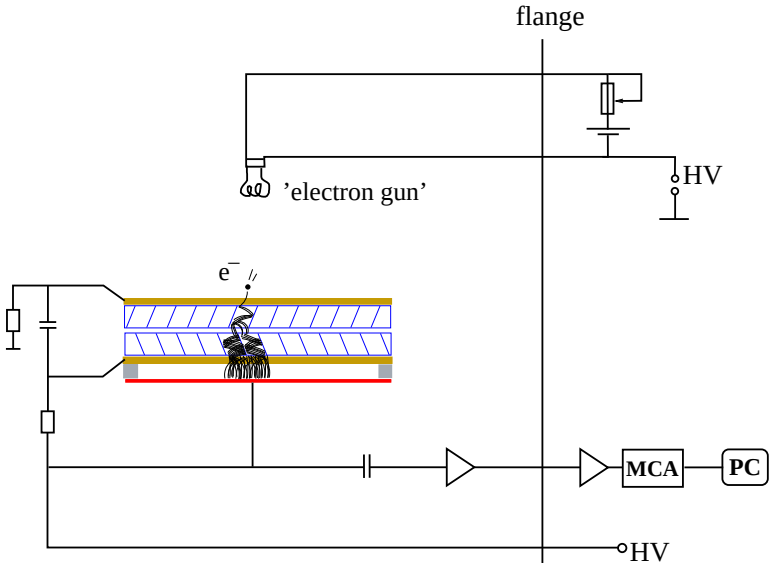

Figure 5.4: MCP characterization was done in the following configuration: MCA - multi-channel analyzer, PC - computer.

First the Start MCP assembly was inserted into a vacuum chamber, then it was changed for the Stop MCP assembly. A small electron gun was used to produce an electron beam to stimulate MCP detectors. MCP output signal was analyzed by means of a multi-channel analyzer MCA8000. Bias of Start MCP U^{Start} and of Stop MCP U^{Stop} were changed in the range of 2300 - 2900 V.

5.3.2 Angular response measurements

During the angular response measurements the sensor worked in the BIN mode, i.e., valid events (1 Start and 1 Stop) were counted. NPD modes are described in Section 4.5. The angular response was measured for different energies for both *H* and *O* species.

The sensor was translated to the center of the ion beam spot and set to a default position, shown in Figure 5.1. An azimuthal scan was performed in the range of $\alpha = [-45°, +45°]$, with steps $\Delta\alpha$=5°. An elevation scan was performed in the range of $\beta = [-7.5°, +7.5°]$, with steps $\Delta\beta$=1.5° for the ASPERA-3 / NPD, and in the range of $\beta = [-6°, +6°]$, with steps $\Delta\beta$=1.0° for the ASPERA-4 / NPD. Accumulation time *t* was set to 1 s per pixel. The angles α_o, β_o

were calculated afterwards by finding the angular position corresponding to the maximum of the angular response function.

5.3.3 Efficiency

During the efficiency measurements, the sensor worked in the BIN mode. Absolute efficiency measurements were performed for fixed angles α_m, β_m which may be different from α_o, β_o, for various energies and species (see Tables 5.1 and 5.20). The instrument response was integrated over the beam spot, performing a scan of an area larger than the ion beam spot at the NPD location. No beam intensity variation over a small area of 3.0×4.5 mm^2 (pin-hole size) is assumed.

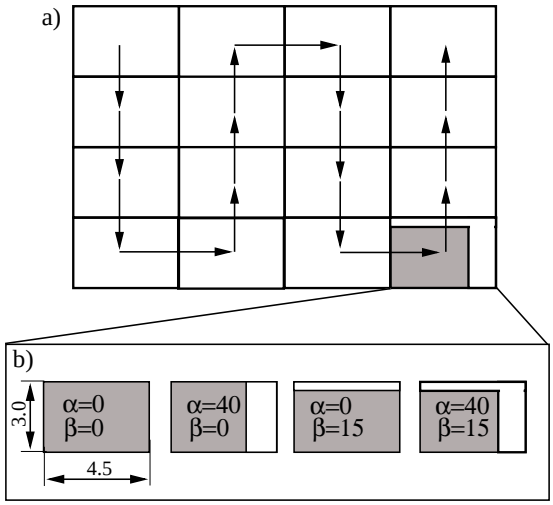

Figure 5.5: a) Scan sequence of the NPD sensor during efficiency test. Arrows depict direction of shift of the sensor aperture; b) a pin-hole effective area (shown in grey) for different azimuthal and elevation angles.

Scan procedure The ion beam spot location was found by scanning along the x- and y-axis. Then the sensor was translated to the center of the spot. Then a scan sequence was initiated (shown in Figure 5.5(a)). The very first and last measurements are made in the center of the scanning matrix, i.e., in the center of the ion beam spot. The pinhole zigzagged as shown in Figure 5.5(a) over the area $A = 60 \times 63$ mm^2 covering the ion beam spot entirely (its size is estimated to be $\leqslant$60 mm^2 in diameter at the position of the NPD). The turn-table translation steps are chosen to correspond to the pin-hole size as 3.0 mm and 4.5 mm in vertical and horizontal planes, respectively. The integrated count rate $C_{Total}(\alpha_m,\beta_m)$ is calculated according to equation 5.11. The pin-hole effective area $A(\alpha,\beta)$ dependency on the azimuth and elevation angles is shown schematically in Figure 5.5(b).

5.3.4 Energy resolution

Measurements are made in the RAW mode. TOF spectra are accumulated during the efficiency calibration scans. The long exposure time allows us to obtain spectra with good statistics.

5.3.5 Mass resolution

Pulse height spectra accumulated during the efficiency measurements are used. The NPD electronics worked in the BIN mode (Section 4.5) and produced both TOF and pulse height data. A long exposure time allows us to obtain spectra with good statistics.

5.4 ASPERA-3 / NPD calibration results

5.4.1 Calibration objectives

The ASPERA-3 / NPD calibration objectives are given in Table 5.1.

N	Calibrated parameter/ function	Ion beam		Comment
		Energy, keV	Species	
1	MCP characterization	5.0	*O*	Determine nominal bias of the Start / Stop MCP detectors.
2	Efficiency measurements	5.0, 3.0, 1.3, 0.7, 0.5, 0.3	*H*, *O*	Energy / mass dependent efficiency ε for sectors Dir0/Dir1/Dir2
3	Angular response	0.3, 1.3	*H*, *O*	Azimuthal and elevation resolution The geometrical constant G_o estimation
4	Geometrical factor G	5.0, 3.0, 1.3, 0.7, 0.5, 0.3	*H*, *O*	Derived from: 1. the angular response, 2. the efficiency measurements
5	Energy and mass resolution	5.0, 3.0, 1.3, 0.7, 0.5, 0.3	*H*, *O*	TOF and PH distribution functions
6	Heater and temperature sensor characterization			Start surface heating
7	EMC related disturbances			Functional test on the ASPERA-3 level

Table 5.1: The ASPERA-3 / NPD calibration objectives.

5.4.2 MCP characterization

The MCP assemblies were tested up to 3100 V bias. The working point, i.e., a nominal MCP bias, was defined. Figure 5.6 shows the Start, Stop0, Stop1, Stop2 MCP detectors count versus MCP bias for the NPD1 (left panel) and NPD2 (right panel) sensors.

The working point of NPD1 is defined as 2750 V for both Start and Stop MCP detectors. Calibration of NPD1 was performed at this MCP bias.

The working point of NPD2 is defined as 2750 V for both Start and Stop MCP detectors. Calibration of NPD2 was performed at this MCP bias.

Though the saturation was not reached, the nominal bias was chosen at the point where the curve derivative decreased. The lower bias was chosen to reduce a risk of discharge.

5.4.3 Efficiency measurements

Accumulation time t was set to 1.0 s. Efficiency measurements are performed for azimuthal α_m, and elevation β_m angles. Tables 5.2 and 5.3 shows the angles α_m and β_m, the pin-hole effective area, and the values of the angular response function at these angles for the NPD1 and NPD2 sensors, respectively.

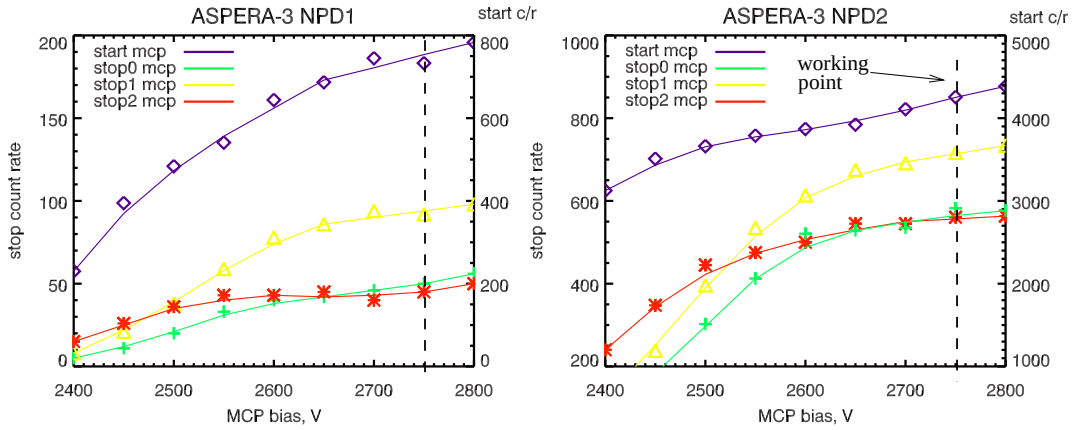

Figure 5.6: The Start, Stop0, Stop1, Stop2 MCP detector count versus a MCP bias for the NPD1 (left panel) and NPD2 (right panel) sensors. The dashed lines depict the working points.

Sensor	Sector	α_m, deg	β_m, deg	$A(\alpha_m,\beta_m)$, mm^2	$f(\alpha_m,\beta_m)$	
					0.3 keV H	0.3 keV O
NPD1	Dir0	40.0	0.0	10.0	0.43	0.69
	Dir1	0.0	0.0	13.0	0.77	0.73
	Dir2	−40.0	0.0	10.0	0.39	0.72

Table 5.2: Azimuth and elevation angles α_m, β_m at which the efficiency was measured. $A(\alpha_m,\beta_m)$ the pin-hole effective area at these angles. $f(\alpha_m,\beta_m)$ is a value of the function defining the shape of the angular response. It is calculated for the angles α_m, β_m from the angular response measurements for 0.3 keV H and 0.3 keV O for NPD1 (Section 5.4.4).

Efficiency ε_m was calculated according to Equations 5.11 and 5.13:

$$\begin{aligned} \varepsilon_m &= q \cdot \frac{C_{Total}(\alpha_m,\beta_m)}{I} \\ &= \frac{q}{I} \cdot \gamma \cdot \sum_i \sum_j C_{ij}(\alpha_m,\beta_m) \end{aligned}$$

where i, j - the indexes over coordinates in the plane perpendicular to the beam, γ is defined by Equation 5.12, $A_{geom} = A(\alpha_m,\beta_m)$.

Then the efficiency was recomputed for angles α_o, β_o by Equation 5.14. Tables 5.4 and 5.5 show the efficiency $\varepsilon(\alpha_o,\beta_o)$ of NPD1 and NPD2, respectively.

Figures 5.7 and 5.8 show the NPD sensors' efficiency profiles together with the best fittings by the function

$$\ln(y) = a_0 + a_1 \cdot x + a_2 \cdot \ln(x) \tag{5.23}$$

where $x = \ln(E)$, $y = 10^4 \cdot \varepsilon$, and E an incident ion energy in units of eV.

The plots presented are valid for the energy range of 0.3 - 5.0 keV for both H and O. Tables 5.6 and 5.7 show the coefficients for the efficiency fittings for NPD1 and NPD2, respectively.

Sensor	Sector	α_m, deg	β_m, deg	$A(\alpha_m,\beta_m)$, mm^2	$f(\alpha_m,\beta_m)$
					1.3 keV H
NPD2	Dir0	40.0	0.0	10.0	0.67
	Dir1	0.0	0.0	13.0	0.84
	Dir2	−40.0	0.0	10.0	0.60

Table 5.3: The format is the same as in Table 5.2. $f(\alpha_m,\beta_m)$ is calculated from the angular response for 1.3 keV H of NPD2 (Section 5.4.4).

ASPERA-3 / NPD1							
Efficiency $\varepsilon(\alpha_o,\beta_o)$, $\times 10^{-2}$							
	E, keV	5.0	3.0	1.3	0.7	0.5	0.3
O	Dir0	–	8.86	3.17	0.67	–	0.02
	Dir1	–	7.89	2.12	0.73	–	0.03
	Dir2	–	8.57	3.63	0.79	–	0.03
H	Dir0	–	9.07	7.67	2.70	–	0.44
	Dir1	–	5.26	3.69	1.70	–	0.40
	Dir2	–	10.10	9.54	3.44	–	0.59

Table 5.4: Absolute efficiency of the ASPERA-3 / NPD1 versus ion mass and energy.

5.4.4 Angular response

Figures 5.9 and 5.11 shows the angular response of the NPD1 sensor for 0.3 keV H and 0.3 keV O, respectively. Each figure shows the angular response of the sectors Dir2, Dir1, Dir0 (from left to right). The upper row is the measured azimuth-elevation response. The second row from the top shows the fitting of the measured and smoothed data, normalized to have the peak magnitude equal to 1. The contours show the polynomial fits based on the function

$$f(x,y) = \sum k_{ji} \cdot x^i \cdot y^j \tag{5.24}$$

where x and y are azimuth and elevation angles scaled as $x = \alpha/5 + 10$, $y = \beta + 6$. k_{ji} are coefficients.

Functions are valid in the range of α [-45, 45], and β [-4, 6] degrees. The third row shows the azimuthal responses at β=β_o and the bottom row shows the elevation responses at α=α_o. Diamonds show the measured and smoothed data. The fittings are shown by thick lines. FWHM

ASPERA-3 / NPD2							
Efficiency ε (α_o, β_o), $\times 10^{-2}$							
	E,keV	5.0	3.0	1.3	0.7	0.5	0.3
O	Dir0	13.25	8.27	2.75	0.19	0.19	0.06
	Dir1	9.10	6.75	2.42	0.64	0.29	0.02
	Dir2	17.80	10.23	3.83	0.37	0.15	0.05
H	Dir0	7.00	6.78	4.06	2.36	1.25	0.36
	Dir1	4.88	4.58	2.92	1.69	0.98	0.35
	Dir2	9.48	9.48	5.68	3.10	1.63	0.57

Table 5.5: Absolute efficiency of the ASPERA-3 / NPD2 versus ion mass and energy.

ASPERA-3 / NPD1						
	H			*O*		
	a_0	a_1	a_2	a_0	a_1	a_2
Dir0	-38.96	-4.31	38.71	-76.60	-7.71	69.81
Dir1	-30.47	-3.37	30.67	-66.16	-6.48	59.96
Dir2	-36.62	-4.10	36.85	-73.10	-7.43	67.09

Table 5.6: Coefficients for the NPD1 efficiency fitting (Equation 5.23).

ASPERA-3 / NPD2						
	H			*O*		
	a_0	a_1	a_2	a_0	a_1	a_2
Dir0	-33.57	-3.76	33.77	-57.66	-5.11	50.56
Dir1	-26.62	-2.87	26.80	-65.54	-6.62	60.13
Dir2	-32.24	-3.65	32.87	-72.71	-7.04	65.39

Table 5.7: Coefficients for the NPD2 efficiency fitting (Equation 5.23).

is given for each profile. The values of k_{ji} for the fit in Figure 5.9 are given in Table 5.8. The values of k_{ji} for the fit in Figure 5.11 are given in Table 5.9.

Figures 5.10 and 5.12 show the azimuthal profiles for respectively 0.3 keV *H* and 0.3 keV *O* of all three sectors of the NPD1 sensor plotted altogether. The dashed lines show the total angular coverage of the NPD1 sensor in the azimuthal plane. All responses are normalized to have the peak maximum equal to 1.

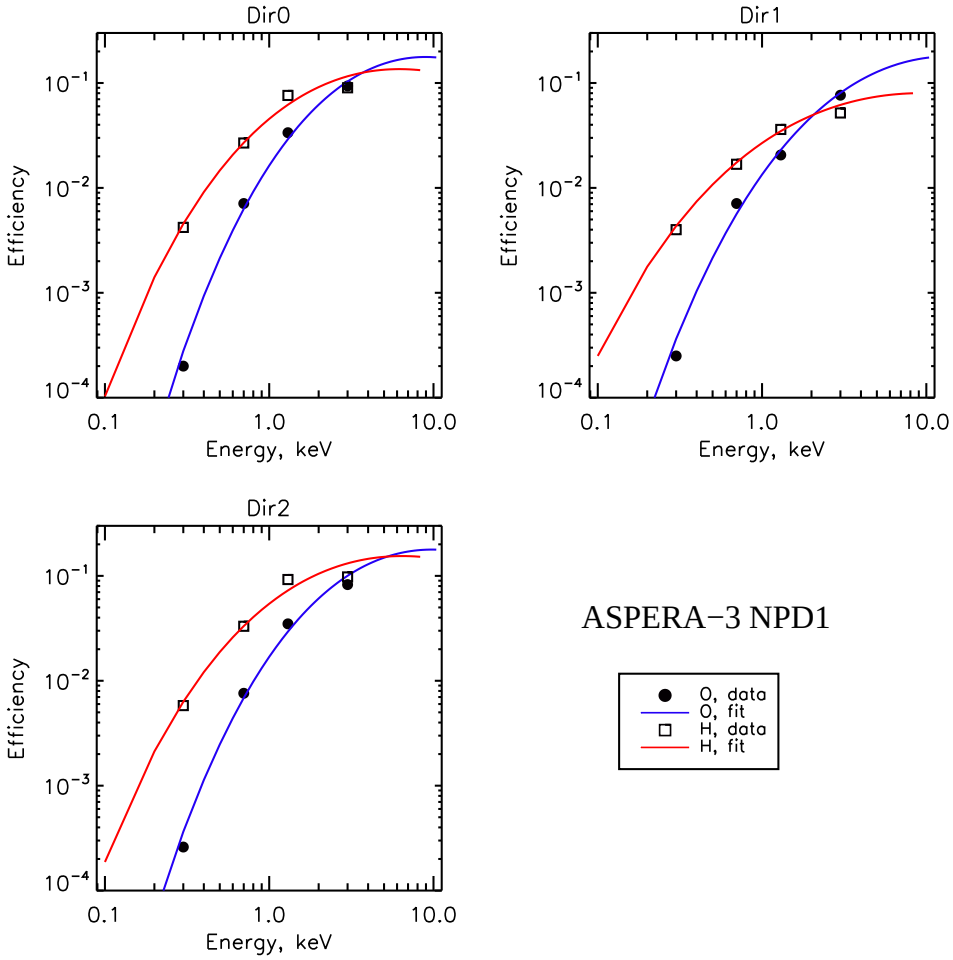

Figure 5.7: The NPD1 absolute efficiency $\varepsilon(\alpha_o, \beta_o)$ as a function of the ion energy and mass for different sectors. Least-square fittings are shown by lines.

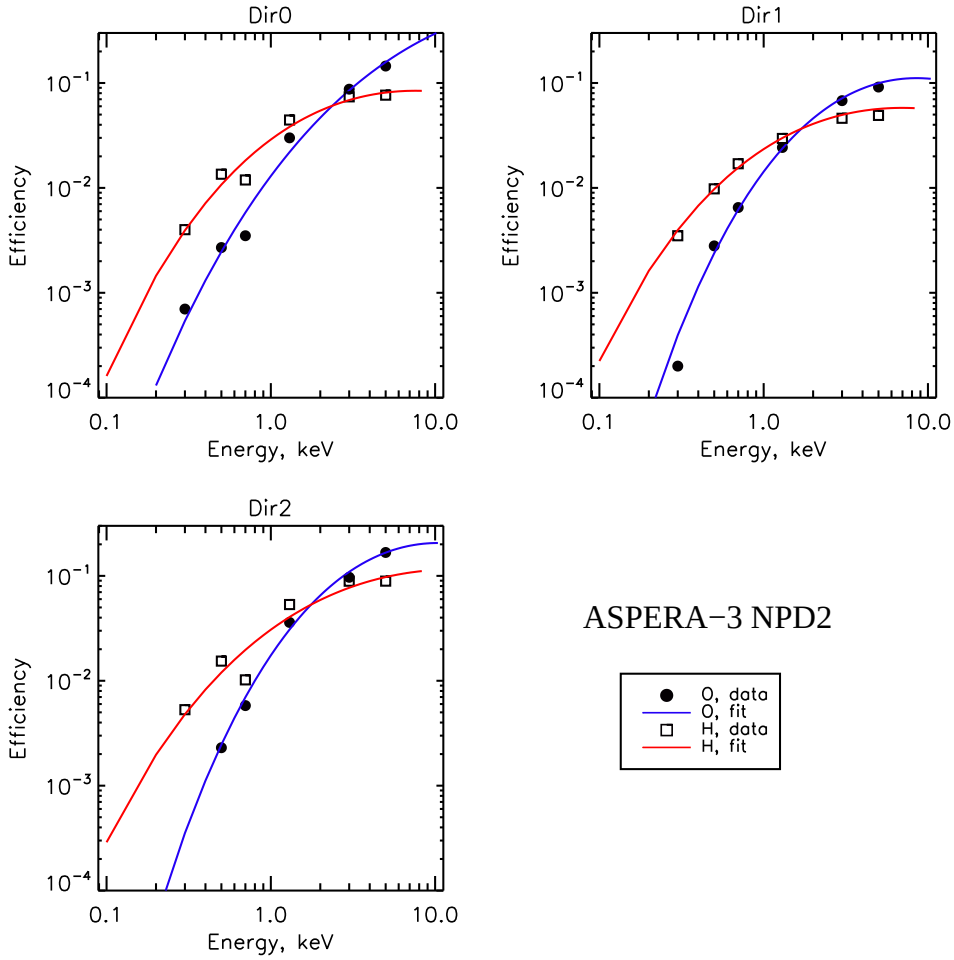

Figure 5.8: The NPD2 absolute efficiency $\varepsilon(\alpha_o, \beta_o)$ as a function of the ion energy and mass for different sectors. Least-square fittings are shown by lines.

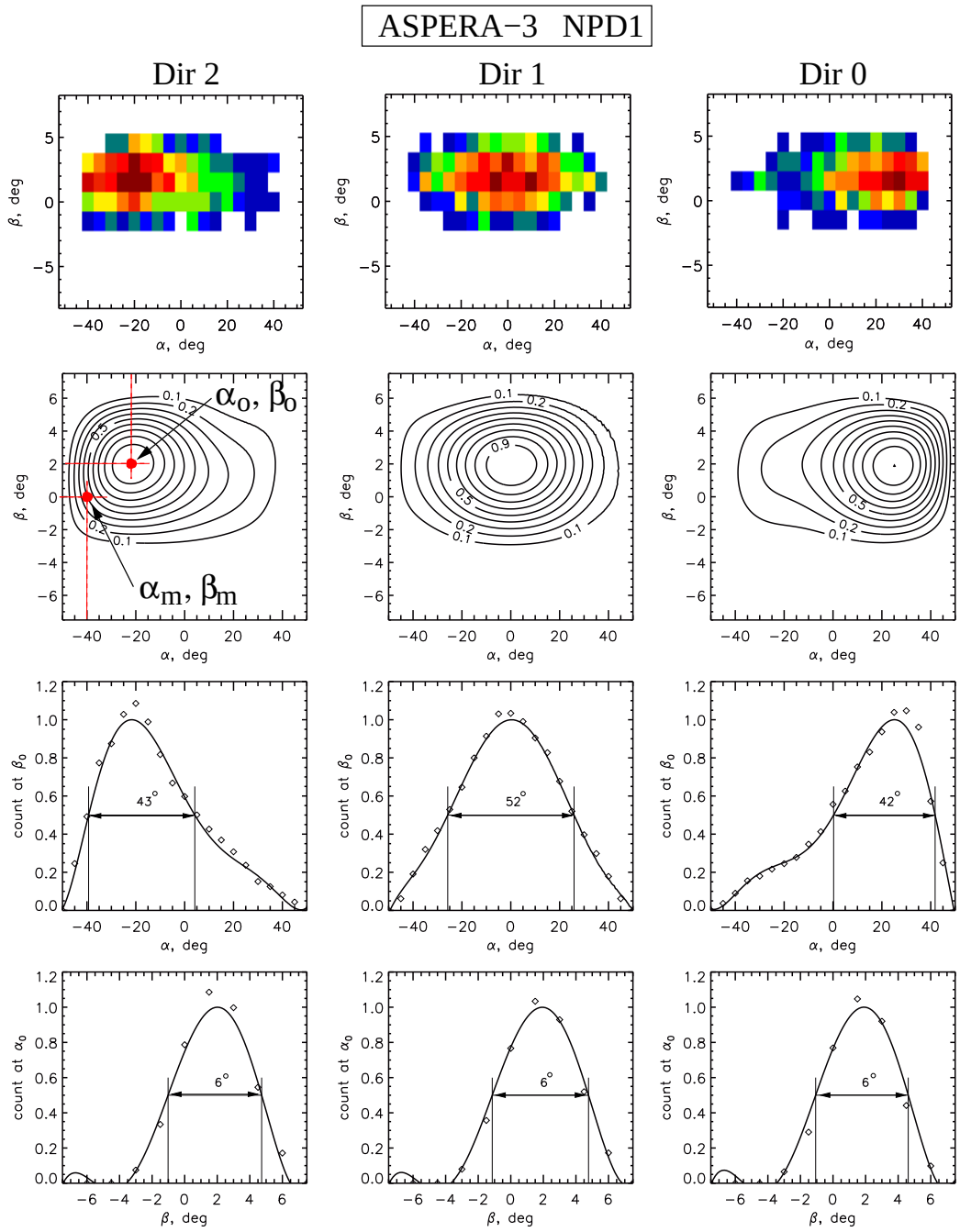

Figure 5.9: Angular response of the NPD1 sensor for 0.3 keV *H* given for the sectors Dir2, Dir1, Dir0 (from left to right). The upper row shows the measured azimuth-elevation response. The second row from the top shows the fitting of the measured and smoothed data. The third and fourth rows show the cross-sections of the angular response function at β_o and α_o, respectively. FWHM is given for each profile. Two red dots depict the angular positions corresponding to the position α_m, β_m at which the efficiency measurements have been performed, and to the position α_o, β_o of the maximum of the azimuth-elevation response function.

k_{ji}	i=0	i=1	i=2	i=3	i=4	i=5	i=6
j=0	1.55e-03	-2.62e-02	3.02e-02	-1.22e-02	2.27e-03	-1.99e-04	6.59e-06
j=1	-6.42e-03	1.11e-01	-1.26e-01	4.90e-02	-8.74e-03	7.30e-04	-2.31e-05
j=2	3.08e-03	-4.07e-02	4.12e-02	-1.44e-02	2.60e-03	-2.33e-04	8.07e-06
j=3	-5.80e-04	5.89e-03	-5.11e-03	1.46e-03	-2.58e-04	2.58e-05	-1.00e-06
j=4	5.09e-05	-3.68e-04	2.21e-04	-1.98e-05	2.64e-06	-6.68e-07	4.17e-08
j=5	-2.14e-06	1.06e-05	-1.80e-06	-2.86e-06	6.01e-07	-3.18e-08	9.48e-11
j=6	3.50e-08	-1.28e-07	-4.37e-08	8.50e-08	-1.79e-08	1.26e-09	-2.69e-11
j=0	7.91e-04	-1.80e-02	2.35e-02	-1.05e-02	1.99e-03	-1.72e-04	5.54e-06
j=1	-3.97e-03	1.10e-01	-1.46e-01	6.41e-02	-1.17e-02	9.56e-04	-2.91e-05
j=2	1.75e-03	-4.86e-02	6.61e-02	-3.02e-02	5.89e-03	-5.20e-04	1.71e-05
j=3	-3.75e-04	1.12e-02	-1.54e-02	7.09e-03	-1.37e-03	1.19e-04	-3.87e-06
j=4	3.71e-05	-1.15e-03	1.59e-03	-7.29e-04	1.40e-04	-1.20e-05	3.86e-07
j=5	-1.68e-06	5.24e-05	-7.24e-05	3.32e-05	-6.35e-06	5.43e-07	-1.73e-08
j=6	2.83e-08	-8.81e-07	1.22e-06	-5.56e-07	1.06e-07	-9.08e-09	2.89e-10
j=0	3.60e-02	-6.98e-02	5.14e-02	-1.87e-02	3.40e-03	-2.94e-04	9.58e-06
j=1	-4.28e-02	2.21e-01	-2.56e-01	1.11e-01	-2.06e-02	1.70e-03	-5.10e-05
j=2	1.42e-02	-4.03e-02	4.13e-02	-2.04e-02	4.86e-03	-5.06e-04	1.87e-05
j=3	-2.16e-03	1.89e-03	-6.06e-04	8.42e-04	-4.11e-04	5.90e-05	-2.59e-06
j=4	1.67e-04	1.01e-04	-2.97e-04	8.07e-05	7.43e-06	-2.84e-06	1.58e-07
j=5	-6.35e-06	-1.12e-05	2.18e-05	-7.82e-06	5.87e-07	3.83e-08	-3.95e-09
j=6	9.45e-08	2.53e-07	-4.54e-07	1.77e-07	-2.05e-08	4.44e-10	2.69e-11

Table 5.8: k_{ji} coefficients for the polynomial fit (Equation 5.24) for the angular response of NPD1 for 0.3 keV *H*.

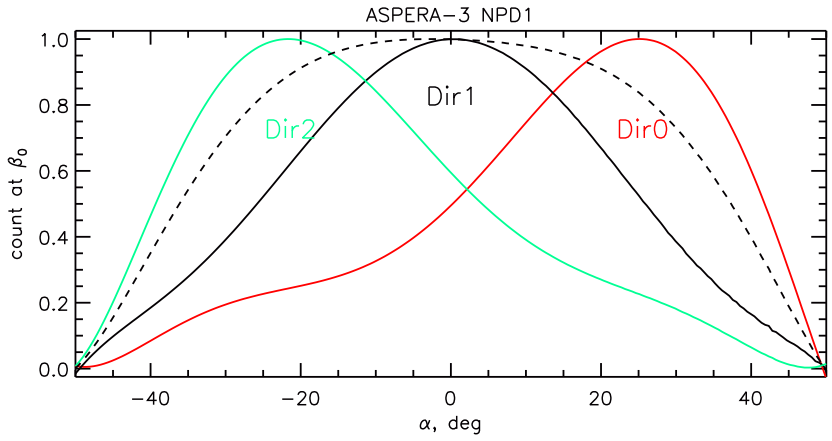

Figure 5.10: The azimuthal responses of each sector of NPD1 measured for 0.3 keV *H*. The dashed line shows the total angular coverage of the NPD1 sensor in the azimuthal plane. All responses are normalized to have the peak maximum equal to 1.

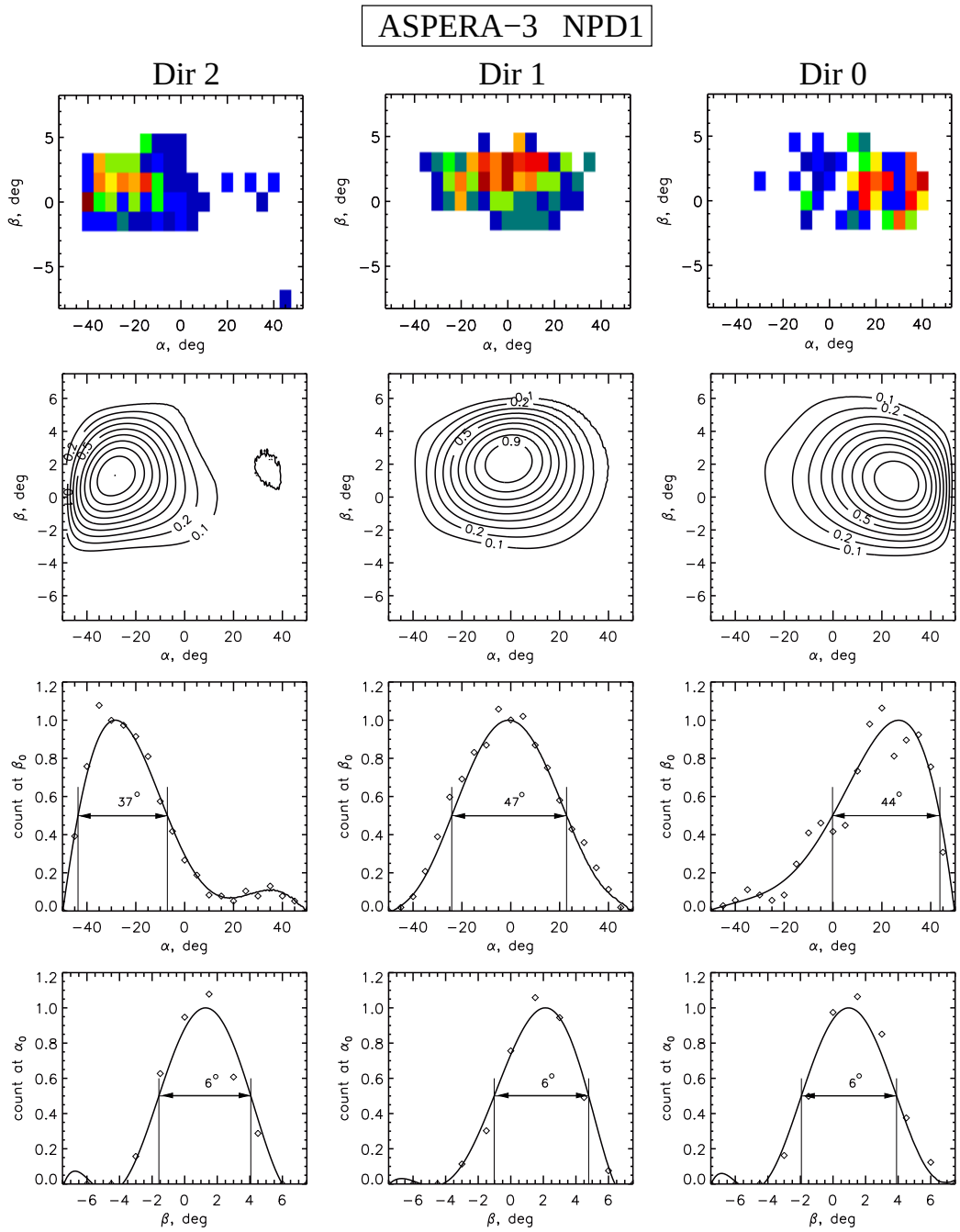

Figure 5.11: Angular response of the NPD1 sensor for 0.3 keV *O* given for the sectors Dir2, Dir1, Dir0 (from left to right). The format is the same as in Figure 5.9.

k_{ji}	i=0	i=1	i=2	i=3	i=4	i=5	i=6
j=0	2.32e-03	-3.85e-02	4.05e-02	-1.38e-02	2.11e-03	-1.51e-04	4.06e-06
j=1	-6.13e-03	6.23e-02	-5.17e-02	1.22e-02	-7.30e-04	-4.74e-05	4.41e-06
j=2	3.14e-03	-3.25e-02	2.87e-02	-8.23e-03	1.01e-03	-5.50e-05	1.10e-06
j=3	-6.27e-04	7.29e-03	-7.25e-03	2.54e-03	-4.19e-04	3.36e-05	-1.07e-06
j=4	5.83e-05	-7.38e-04	7.84e-04	-3.00e-04	5.48e-05	-4.81e-06	1.63e-07
j=5	-2.56e-06	3.56e-05	-4.00e-05	1.63e-05	-3.14e-06	2.86e-07	-9.87e-09
j=6	4.27e-08	-6.62e-07	7.84e-07	-3.36e-07	6.65e-08	-6.12e-09	2.12e-10
j=0	3.13e-04	1.75e-02	-2.84e-02	1.39e-02	-2.85e-03	2.58e-04	-8.49e-06
j=1	3.34e-04	-1.24e-01	1.85e-01	-8.65e-02	1.72e-02	-1.51e-03	4.87e-05
j=2	-6.05e-04	8.94e-02	-1.32e-01	6.10e-02	-1.19e-02	1.04e-03	-3.28e-05
j=3	6.65e-05	-1.67e-02	2.51e-02	-1.18e-02	2.39e-03	-2.13e-04	6.95e-06
j=4	9.86e-07	1.33e-03	-2.05e-03	9.92e-04	-2.06e-04	1.89e-05	-6.30e-07
j=5	-3.37e-07	-4.79e-05	7.65e-05	-3.80e-05	8.10e-06	-7.59e-07	2.58e-08
j=6	9.74e-09	6.38e-07	-1.07e-06	5.48e-07	-1.20e-07	1.14e-08	-3.93e-10
j=0	-1.14e-02	3.52e-02	-3.49e-02	1.41e-02	-2.76e-03	2.56e-04	-8.92e-06
j=1	5.55e-02	2.21e-01	-4.88e-01	2.79e-01	-6.05e-02	5.62e-03	-1.89e-04
j=2	-3.73e-02	-2.60e-02	1.35e-01	-9.23e-02	2.25e-02	-2.27e-03	8.19e-05
j=3	8.67e-03	-3.18e-03	-1.61e-02	1.35e-02	-3.61e-03	3.87e-04	-1.45e-05
j=4	-8.95e-04	6.67e-04	1.03e-03	-1.04e-03	2.94e-04	-3.26e-05	1.25e-06
j=5	4.20e-05	-3.70e-05	-3.54e-05	4.07e-05	-1.19e-05	1.33e-06	-5.15e-08
j=6	-7.31e-07	6.69e-07	5.16e-07	-6.33e-07	1.86e-07	-2.10e-08	8.16e-10

Table 5.9: k_{ji} coefficients for the polynomial fit (Equation 5.24) for the angular response of NPD1 for 0.3 keV *O*.

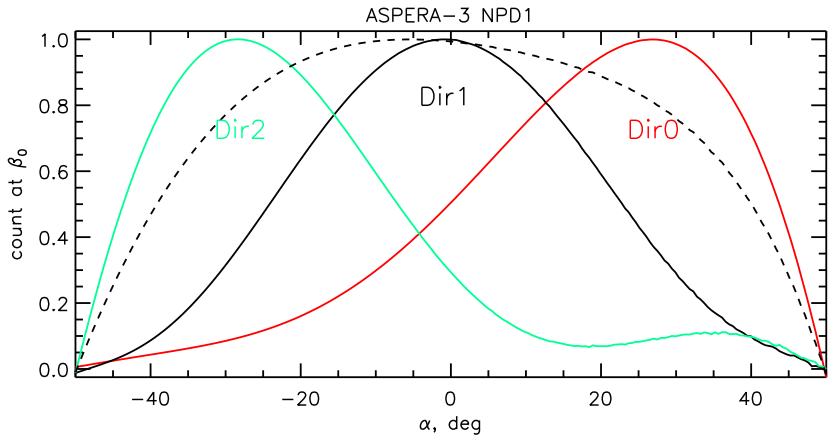

Figure 5.12: The azimuthal responses of each sector of NPD1 measured for 0.3 keV *O*. The dashed line shows the total angular coverage of the NPD1 sensor in the azimuthal plane. All responses are normalized to have the peak maximum equal to 1.

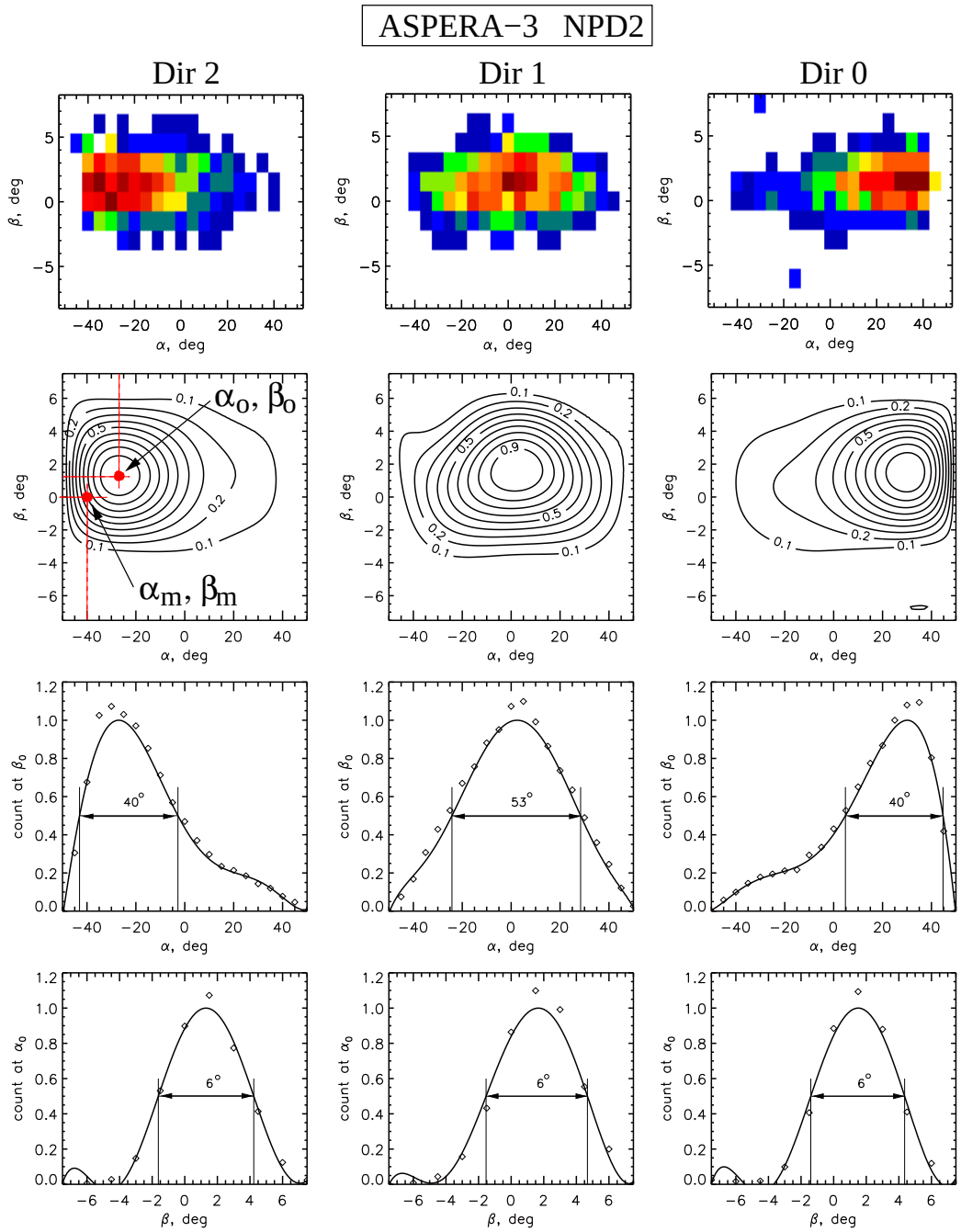

Figure 5.13: Angular response of the NPD2 sensor for 1.3 keV *H* given for the sectors Dir2, Dir1, Dir0 (from left to right). The format is the same as in Figure 5.9.

Figure 5.13 shows the angular response of the NPD2 sensor for 1.3 keV *H*. The format is the same as in Figure 5.9. The values of coefficients k_{ji} for the fit in Figure 5.13 are in Table 5.10.

Figure 5.14 shows the azimuthal profiles for 1.3 keV *H* of all three sectors of the NPD2 sensor plotted altogether. The dashed line shows the total angular coverage of the NPD2 sensor in the azimuthal plane. All responses are normalized to have the peak maximum equal to 1.

k_{ji}	i=0	i=1	i=2	i=3	i=4	i=5	i=6
j=0	-3.06e-03	6.42e-02	-1.06e-02	-7.82e-03	2.70e-03	-2.98e-04	1.11e-05
j=1	3.28e-04	5.36e-02	-9.67e-02	4.60e-02	-9.01e-03	7.86e-04	-2.53e-05
j=2	3.56e-04	-2.15e-02	3.04e-02	-1.23e-02	2.24e-03	-1.93e-04	6.31e-06
j=3	-1.79e-04	4.70e-03	-5.00e-03	1.70e-03	-2.88e-04	2.45e-05	-8.25e-07
j=4	2.84e-05	-4.93e-04	4.33e-04	-1.27e-04	2.01e-05	-1.71e-06	5.99e-08
j=5	-1.77e-06	2.53e-05	-2.09e-05	5.95e-06	-9.09e-07	7.56e-08	-2.60e-09
j=6	3.80e-08	-5.03e-07	4.28e-07	-1.29e-07	2.00e-08	-1.60e-09	5.18e-11
j=0	6.58e-03	-3.82e-02	4.64e-02	-2.02e-02	3.90e-03	-3.44e-04	1.14e-05
j=1	-3.53e-02	8.96e-02	-9.31e-02	3.02e-02	-3.41e-03	1.04e-04	1.94e-06
j=2	2.16e-02	-1.63e-02	3.04e-03	8.13e-03	-3.27e-03	4.06e-04	-1.62e-05
j=3	-4.50e-03	3.00e-03	-7.68e-05	-2.03e-03	7.75e-04	-9.53e-05	3.80e-06
j=4	4.21e-04	-3.33e-04	8.40e-05	1.54e-04	-6.60e-05	8.40e-06	-3.40e-07
j=5	-1.83e-05	1.72e-05	-7.70e-06	-4.64e-06	2.43e-06	-3.24e-07	1.33e-08
j=6	3.02e-07	-3.30e-07	1.96e-07	3.99e-08	-3.17e-08	4.51e-09	-1.90e-10
j=0	3.04e-04	-3.35e-02	4.69e-02	-2.25e-02	4.48e-03	-3.94e-04	1.27e-05
j=1	-5.25e-03	2.51e-01	-3.45e-01	1.59e-01	-2.97e-02	2.44e-03	-7.40e-05
j=2	2.96e-03	-4.39e-02	5.07e-02	-2.24e-02	4.43e-03	-4.06e-04	1.40e-05
j=3	-4.03e-04	2.25e-03	-4.33e-04	-2.76e-05	-6.96e-05	1.74e-05	-9.95e-07
j=4	1.67e-05	7.88e-07	-2.65e-04	1.43e-04	-1.88e-05	3.30e-07	3.85e-08
j=5	1.05e-07	-2.36e-06	1.46e-05	-7.64e-06	1.06e-06	-3.19e-08	-1.24e-09
j=6	-1.31e-08	3.05e-08	-2.23e-07	1.18e-07	-1.58e-08	3.70e-10	2.57e-11

Table 5.10: k_{ji} coefficients for the polynomial fit (Equation 5.24) for the angular response of NPD2 for 1.3 keV *H*.

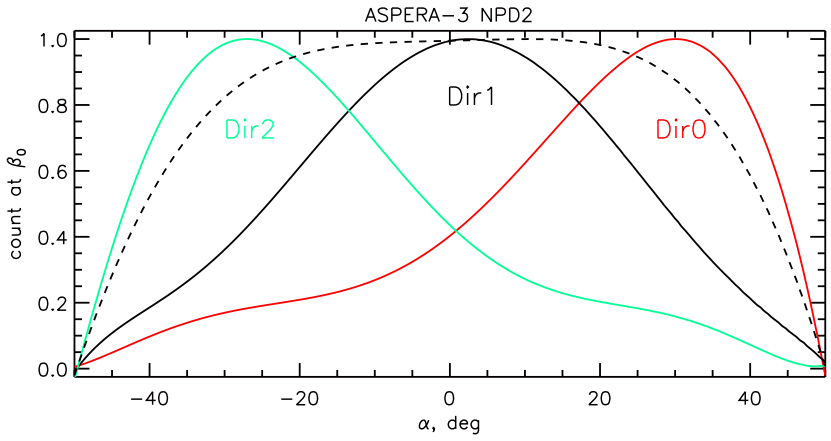

Figure 5.14: The azimuthal responses of each sector of NPD2 measured for 1.3 keV *H*. The dashed line shows the total angular coverage of the NPD2 sensor in the azimuthal plane. All responses are normalized to have the peak maximum equal to 1.

		H			*O*		
Sensor	Sector	α_o, deg	β_o, deg	A_o, mm^2	α_o, deg	β_o, deg	A_o, mm^2
NPD1	Dir0	25.0	1.9	11.80	27.0	0.9	11.66
	Dir1	0.0	2.0	13.03	−1.0	2.1	13.03
	Dir2	−22.0	2.0	12.10	−29.0	1.3	11.46

Table 5.11: Angles α_o, β_o for different sectors, and corresponding effective aperture area for these angles are given. α_o, β_o are calculated from the angular response for 0.3 keV *H* and 0.3 keV *O* of the NPD1 sensor.

		H		
Sensor	Sector	α_o, deg	β_o, deg	A_o, mm^2
NPD2	Dir0	30.0	1.5	11.25
	Dir1	3.0	1.7	13.02
	Dir2	−27.0	1.3	11.61

Table 5.12: Angles α_o, β_o for different sectors, and corresponding effective aperture area for these angles are given. α_o, β_o are calculated from the angular response for 1.3 keV *H* of the NPD2 sensor.

Table 5.11 shows the angles α_o, β_o which correspond to the maximum of the angular response function of the NPD1 sensor for 0.3 keV *H* and 0.3 keV *O*. The effective aperture area at these angles is also shown.

Table 5.12 shows the angles α_o, β_o which correspond to the maximum of the angular response function of the NPD2 sensor for 1.3 keV *H*. The effective aperture area at these angles is also shown.

Tables 5.13 and 5.14 show the pure geometrical constant G_o of the NPD1 and NPD2 sensors, respectively, calculated according to Equation 5.3.

G_o, $\times 10^{-3}$, cm^{2}sr						
	H			*O*		
Sensor	Dir0	Dir1	Dir2	Dir0	Dir1	Dir2
*NPD*1	8.76	11.45	9.34	8.94	10.45	7.13

Table 5.13: Pure geometrical factor G_o computed from the angular response for 0.3 keV *H* and 0.3 keV *O* of the NPD1 sensor. Efficiency ε is not included.

G_o, $\times 10^{-3}$, cm^{2}sr			
	H		
Sensor	Dir0	Dir1	Dir2
*NPD*2	8.98	12.77	9.06

Table 5.14: Pure geometrical factor G_o computed from the angular response for 1.3 keV *H* of the NPD2 sensor. Efficiency ε is not included.

5.4.5 Geometrical factor

The total geometrical factors $G = G_o \cdot \varepsilon(E)$ (in units of $cm^2 sr$) of the NPD1 and NPD2 sensors are shown in Tables 5.15 and 5.16, respectively.

NPD1 / ASPERA-3							
Geometrical factor G, $\times 10^{-4}$							
	E, keV	5.0	3.0	1.3	0.7	0.5	0.3
O	Dir0	–	9.05	2.58	0.56	–	0.02
	Dir1	–	8.29	2.51	0.62	–	0.04
	Dir2	–	7.35	2.25	0.53	–	0.03
H	Dir0	–	10.43	5.34	2.33	–	0.42
	Dir1	–	6.76	3.83	1.93	–	0.48
	Dir2	–	13.03	6.87	3.11	–	0.61

Table 5.15: The absolute geometrical factor of the ASPERA-3 / NPD1 sensor, computed from the fit function of the efficiency of NPD1 and pure geometrical factors (Table 5.13).

NPD2 / ASPERA-3							
Geometrical factor fit G, $\times 10^{-4}$							
	E, keV	5.0	3.0	1.3	0.7	0.5	0.3
O	Dir0	11.46	6.82	1.85	0.45	0.18	0.03
	Dir1	12.64	9.01	3.00	0.79	0.31	0.05
	Dir2	15.11	9.64	2.55	0.54	0.19	0.03
H	Dir0	7.65	6.46	3.61	1.75	1.05	0.39
	Dir1	7.54	6.21	3.55	1.86	1.19	0.52
	Dir2	10.36	8.77	4.96	2.45	1.48	0.57

Table 5.16: The absolute geometrical factor of the ASPERA-3 / NPD2 sensor, computed from the fit function of the efficiency of NPD2 and pure geometrical factors (Table 5.14).

5.4.6 Energy resolution

Figures 5.15, 5.16 show TOF spectra obtained by the NPD1 sensor for H and O ion beams, respectively, for different energies. Figures 5.17, 5.18 show TOF spectra obtained by the NPD2 sensor for H and O ion beams, respectively, for different energies.

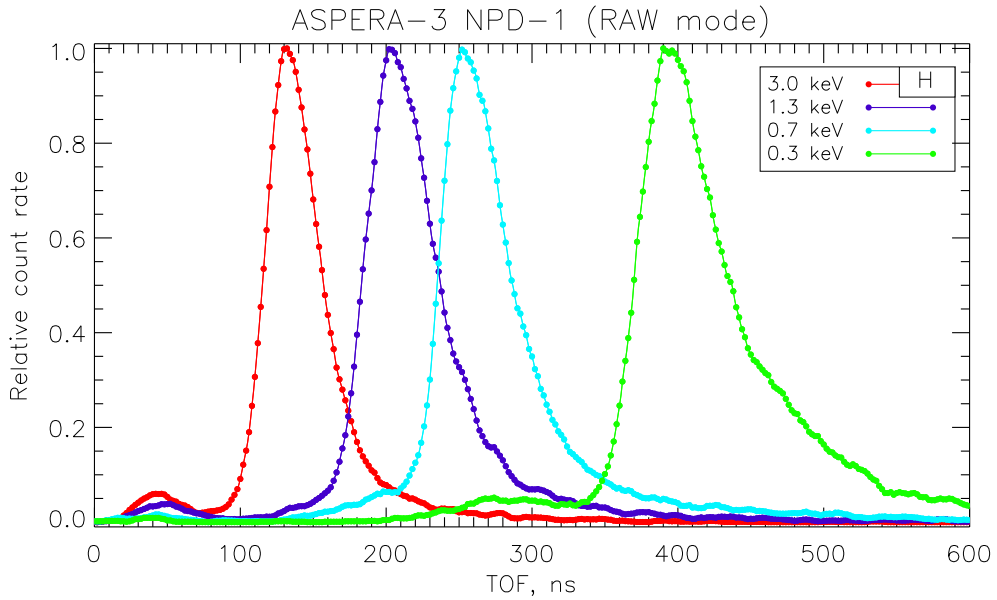

Figure 5.15: The NPD1 TOF spectra for *H* beams of different energies.

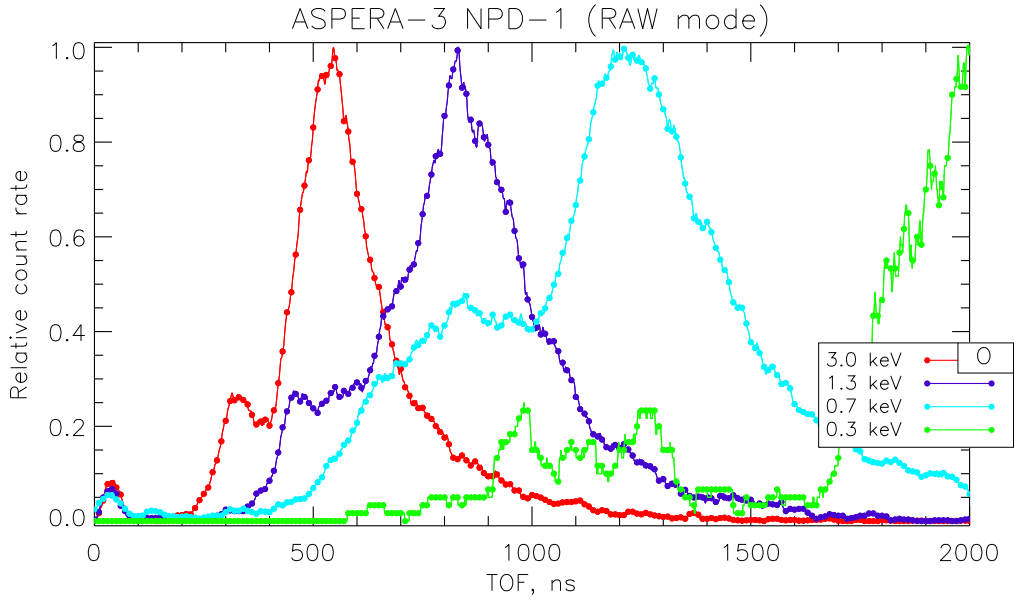

Figure 5.16: The NPD1 TOF spectra for *O* beams of different energies.

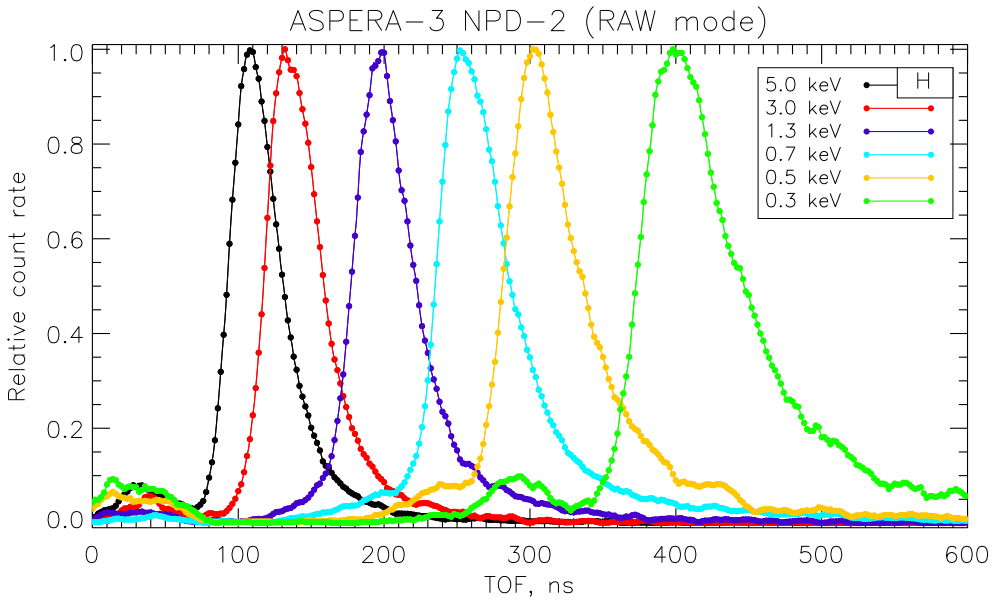

Figure 5.17: The NPD2 TOF spectra for *H* beams of different energies. The reason for the structure in the 0.3 keV TOF spectrum (at ~300 ns) is as yet unclear. It can perhaps be due to electronic disturbances.

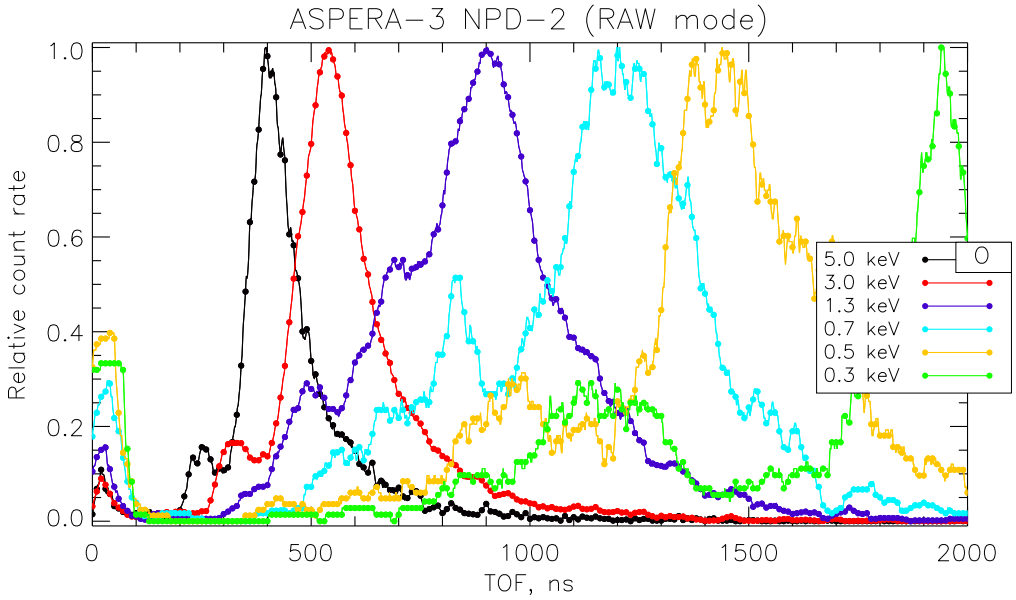

Figure 5.18: The NPD2 TOF spectra for *O* beams of different energies.

Figures 5.19 and 5.20 show the TOF spectrum maximum as a function of the incident ion beam energy for the NPD1 and NPD2 sensors, respectively. The error bars show FWHM of the TOF spectra. The dashed lines show ideal theoretical dependencies $T_M = f(E)$ (Equation 5.15) with no energy loss, i.e., ΔE_{loss}=0. The solid lines show the best fits assuming the TOF distance L equal to 80 mm. These curves can be expressed by Equation 5.15.

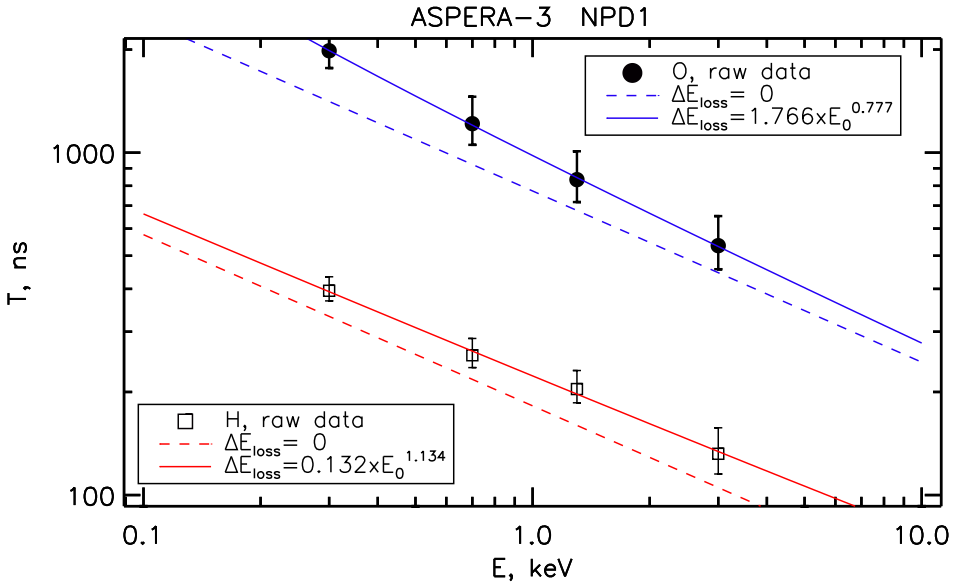

Figure 5.19: The NPD1 TOF spectrum maximum as a function of the initial energy E_o. Open squares and solid circles show experimental data for H and O beams, respectively. The dashed lines depict the dependences with no energy loss, $\Delta E_{loss} = 0$. The solid lines show the best fit.

Table 5.17 shows ΔE_{loss} as a function of the initial particle energy E_o for both NPD sensors. The incident ion energy loss during interaction with the Start surface is clearly energy dependent.

Figures 5.21 and 5.22 show the energy loss ΔE_{loss} (panels a) and the relative energy loss $K = \Delta E_{loss}/E$ (panels b) of the NPD1 respectively NPD2 sensor graphically.

Figure 5.23 shows the estimation of the energy resolution of the NPD1 and NPD2 sensors. The energy resolution is defined as double FWHM of the TOF spectra, normalized to the TOF peaks.

	m	ΔE_{loss}		m	ΔE_{loss}
NPD1	O	$1.766E_o^{0.777}$	NPD2	O	$1.365E_o^{0.820}$
	H	$0.132E_o^{1.134}$		H	$0.112E_o^{1.154}$

Table 5.17: Energy loss ΔE_{loss} as a function of the initial energy E_o and ion species.

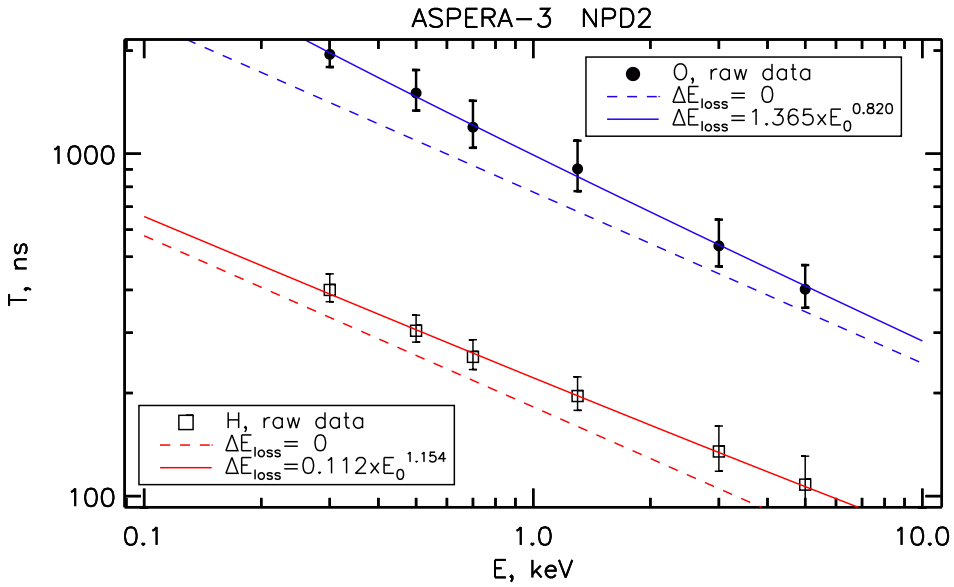

Figure 5.20: The NPD2 TOF spectrum maximum as a function of the initial energy E_o. Open squares and solid circles show experimental data for H and O beam, respectively. The dashed lines depict the dependences with no energy loss, $\Delta E_{loss} = 0$. The solid lines show the best fit.

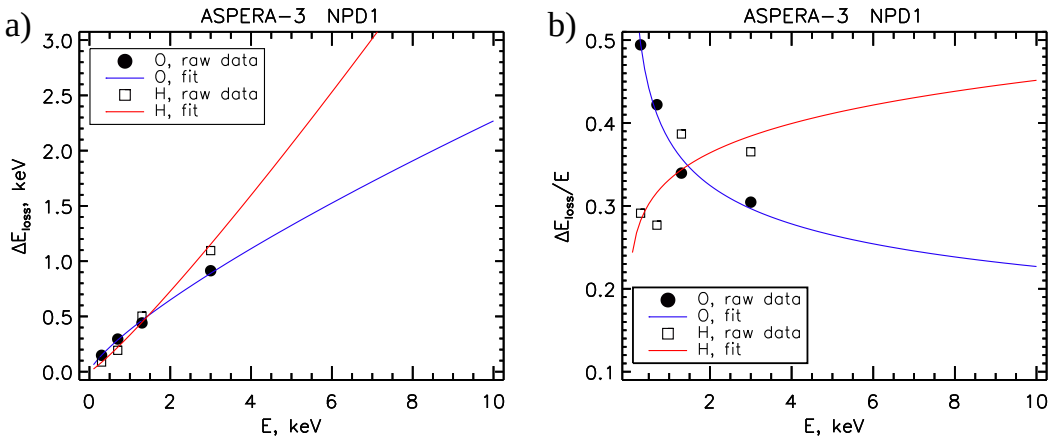

Figure 5.21: (a) Energy loss ΔE_{loss} and (b) relative energy loss $K = \Delta E_{loss}/E$ are plotted as a function of the initial energy E_o for NPD1.

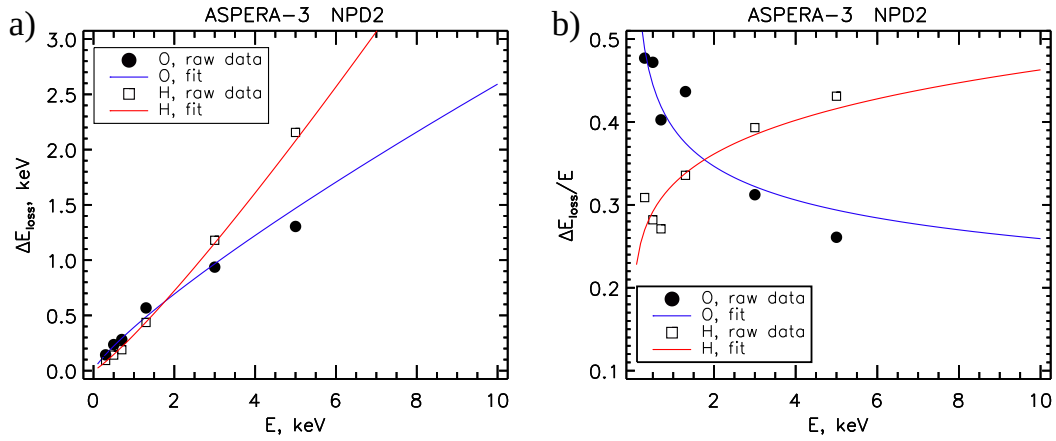

Figure 5.22: (a) Energy loss ΔE_{loss} and (b) relative energy loss $K = \Delta E_{loss}/E$ are plotted as a function of the initial energy E_o for NPD2.

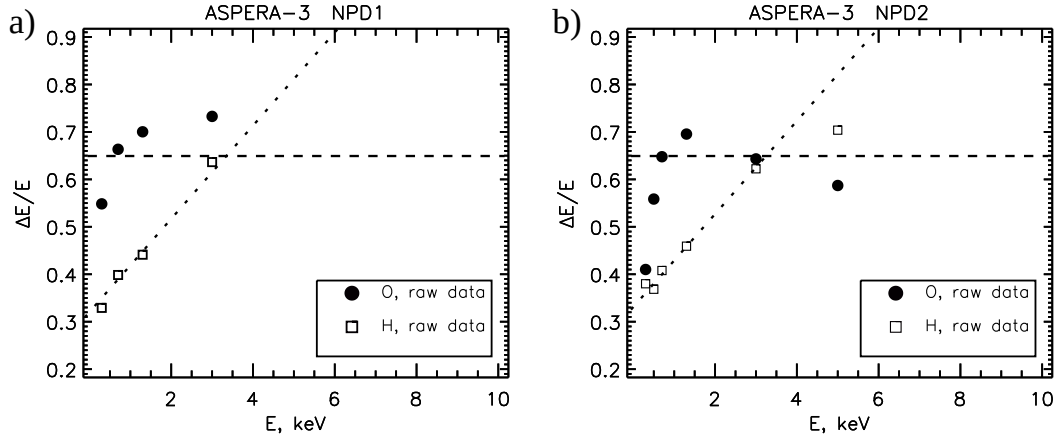

Figure 5.23: Energy resolution $\Delta E/E$ as a function of the initial energy E_o is plotted for different ion species; for a) the NPD1 and b) the NPD2 sensors. The dashed and dotted lines are to guide the eye.

5.4.7 Mass resolution

As seen in Figures 5.19 and 5.20, TOF for *H* and *O* overlap in the range of ~260 - 650 ns for the energy range of 100 eV - 10 keV. Particles with TOF in the range of >650 ns are assumed to be *O*. Particles with TOF less than 260 ns are assumed to be *H*. Table 5.18 shows TOF ranges in which *O* and *H* species can be identified directly from TOF measurements. PH analysis is required to distinguish between the species inside this TOF range.

ASPERA-3				
	NPD1		NPD2	
	$T_M(RAW)$	T_M (BIN)	T_M (RAW)	T_M (BIN)
H	< 261 ns	< 7 ch	< 268 ns	< 7 ch
O	> 663 ns	> 10 ch	> 665 ns	> 10 ch

Table 5.18: Identification of *O* and *H* species from TOF measurements. TOF values are shown for two modes, RAW and BIN. T_M shows the TOF in ns in the RAW mode and the channel number in the BIN mode.

Table 5.19 shows the values of *N* indicating the channel number above which mostly *O* atoms give a considerable tail in the pulse height distribution, and P_O, P_H indicating probability for *O* and *H* atoms respectively to produce stop signals of a magnitude higher than level *N*. Channel *N* is defined in such a way as to minimize the value of $\frac{P_H}{P_O}$.

ASPERA-3						
	NPD1			NPD2		
	Dir0	Dir1	Dir2	Dir0	Dir1	Dir2
N	9	11	10	12	9	11
P_H, $\times 10^{-2}$	0.03	0.00	0.38	0.93	0.12	0.33
P_O, $\times 10^{-2}$	0.63	0.08	5.42	6.11	1.25	7.62

Table 5.19: Value *N* indicates a number of a channel above which mostly *O* atoms give a considerable tail in pulse height distribution. P_H and P_O are the probabilities for *H* and *O*, respectively, to produce stop signals of a magnitude higher than level *N*.

Figures 5.24 and 5.25 show pulse height distributions from 0.3 keV *H* (the red curve) and 3.0 keV *O* (the black curve) for NPD1 and that from 0.3 keV *H* (the red curve) and 5.0 keV *O* (the black curve) for the NPD2 sensor, respectively, in the logarithmic scale.

5.4.8 Heater and temperature sensor characterization

The heater is for the Start surface conditioning (Section 4.2.2). The heater increases temperature of the Start surface by 50° over the ambient temperature. It takes ~2 hours to reach the equilibrium maximum temperature of the Start surface. Temperature sensors were verified after the NPD integration with the ASPERA-3 package during TVAC test (Section 4.6).

5.4.9 Dark noise

Electromagnetic disturbances during communication of the DPU with the spacecraft were measured after the NPD integration with the ASPERA-3 package. Electromagnetically induced noise at biased MCP detectors is ⩽20 c/s for non-correlated counts. TOF coincidence totally removes this noise.

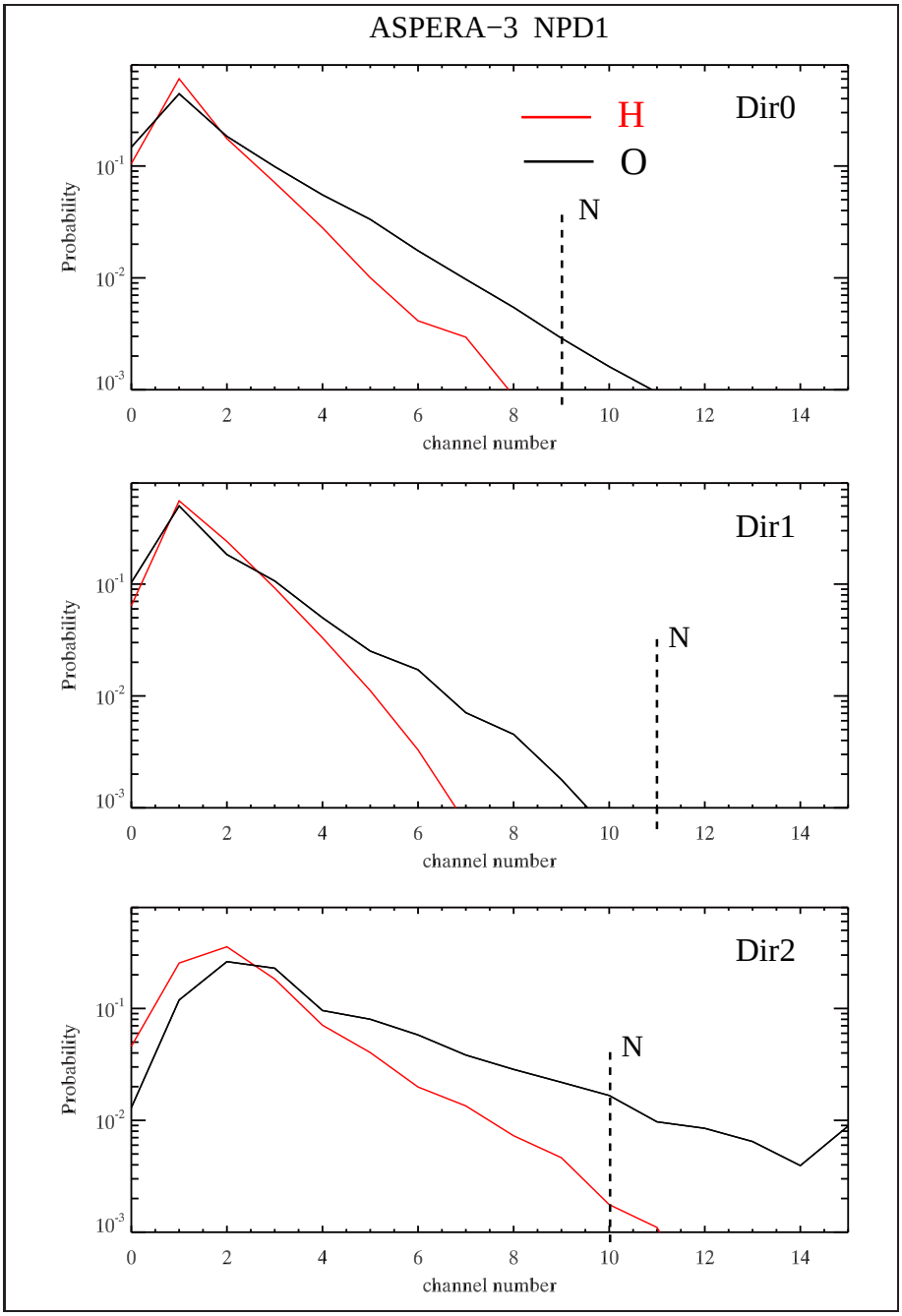

Figure 5.24: Pulse height distributions from 0.3 keV *H* (the red curve) and 3.0 keV *O* (the black curve) are shown for sectors Dir0, Dir1, Dir2 (from top to bottom) of the ASPERA-3 / NPD1. Plots are shown in the logarithmic scale. Both distributions are normalized to have the same area equal to 1. The dashed lines show channel *N* values. The threshold for the NPD1 Dir1 was erroneously set to channel 11.

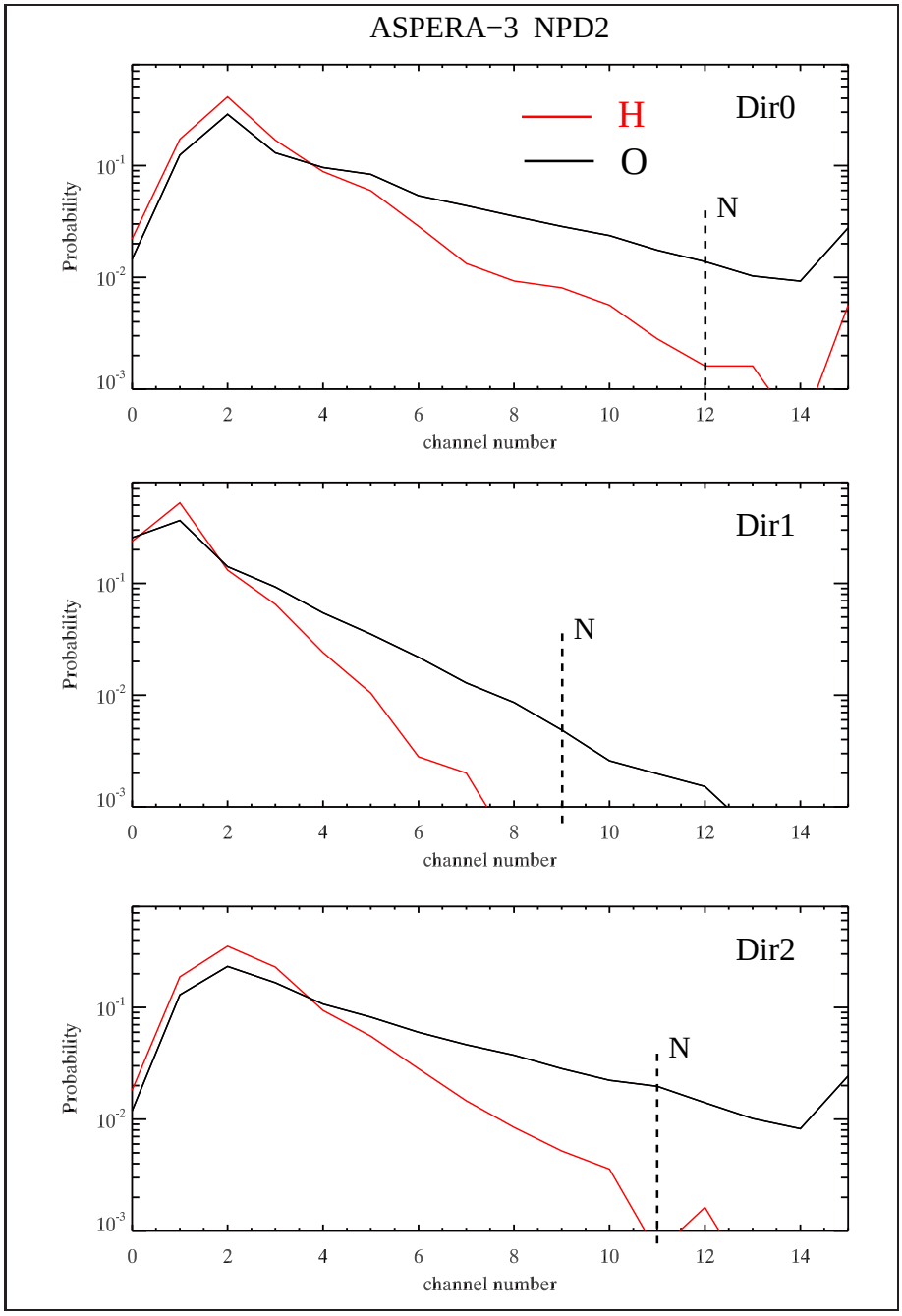

Figure 5.25: Pulse height distributions from *H* and *O* of about the same velocity are shown for all sectors of the ASPERA-3 / NPD2. The format is the same as in Figure 5.24.

5.5 ASPERA-4 / NPD calibration results

5.5.1 Calibration objectives

The ASPERA-4 / NPD calibration objectives are given in Table 5.20.

N	Calibrated parameter/ function	Ion beam		Comment
		Energy, keV	Species	
1	MCP characterization	5.0	*O*	Determine nominal bias of the Start / Stop MCP detectors.
2	Efficiency measurements	(10.0), 5.0, 3.0, 1.3, 0.7, 0.5, 0.3, (0.1)	*H*, *O*	Energy / mass dependent efficiency ε for sectors Dir0/Dir1/Dir2
3	Angular response	(10.0), 5.0, 3.0, 1.3, 0.7, 0.5, 0.3, (0.1)	*H*, *O*	Azimuthal and elevation resolution The geometrical constant G_o estimation
4	Geometrical factor G	(10.0), 5.0, 3.0, 1.3, 0.7, 0.5, 0.3, (0.1)	*H*, *O*	Derived from: 1. the angular response 2. the efficiency measurements
5	Energy and mass resolution	5.0, 3.0, 1.3, 0.7, 0.5, 0.3	*H*, *O*	TOF and PH distribution functions
6	Heater and temperature sensor characterization			Start surface heating
7	EMC related disturbances			Functional test on the ASPERA-4 level

Table 5.20: The ASPERA-4 / NPD calibration objectives.

5.5.2 MCP characterization

The MCP assemblies were tested up to 3100 V bias. The working point, i.e., nominal MCP bias, was defined. Figure 5.26 shows the Start, Stop0, Stop1, Stop2 MCP detectors count versus MCP bias for the NPD1 (left panel) and NPD2 (right panel) sensors.

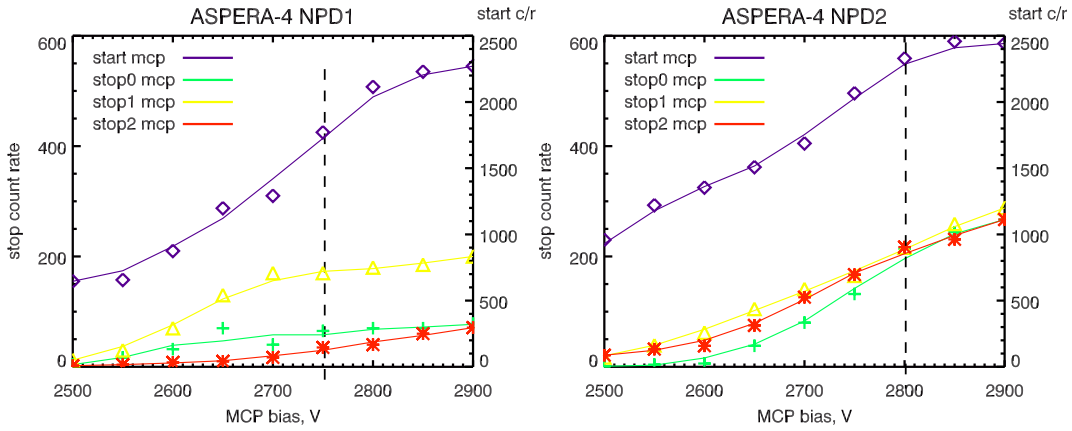

Figure 5.26: The Start, Stop0, Stop1, Stop2 MCP detector count versus MCP bias for the NPD1 (left panel) and NPD2 (right panel) sensors. The dashed lines depict the working points.

The working point of NPD1 is defined as 2750 V for both Start and Stop MCP detectors.

Calibration of NPD1 was performed at this MCP bias.

The working point of NPD2 is defined as 2800 V for both Start and Stop MCP detectors. Calibration of NPD2 was performed at this MCP bias.

Though the saturation was not reached, the nominal bias was chosen at the point where the curve derivative decreased. The lower bias was chosen to reduce a risk of discharge.

5.5.3 Efficiency measurements

Accumulation time t was set to 1.0 s. Efficiency measurements are performed for azimuthal α_m, and elevation β_m angles. Table 5.21 shows the angles α_m and β_m, the pin-hole effective area, and the values of the angular response function at these angles for both the NPD1 and NPD2 sensors.

Sensor	Sector	α_m, deg	β_m, deg	$A(\alpha_m,\beta_m)$, mm^2	$f(\alpha_m,\beta_m)$
NPD1	Dir0	40.0	0.0	10.0	0.64
	Dir1	0.0	0.0	13.0	0.88
	Dir2	−40.0	0.0	10.0	0.58
NPD2	Dir0	35.0	0.0	10.7	0.86
	Dir1	0.0	0.0	13.0	0.93
	Dir2	−35.0	0.0	10.7	0.87

Table 5.21: Azimuth and elevation angles α_m, β_m at which the efficiency was measured. $A(\alpha_m,\beta_m)$ the pin-hole effective area at these angles. $f(\alpha_m,\beta_m)$ is a value of the function defining the shape of the angular response, calculated from the angular response measurements for 1.3 keV H for both the NPD1 and NPD2 sensors (Section 5.5.4).

Efficiency ε_m was calculated according to Equations 5.11 and 5.13:

$$\begin{aligned} \varepsilon_m &= q \cdot \frac{C_{Total}(\alpha_m,\beta_m)}{I} \\ &= \frac{q}{I} \cdot \gamma \cdot \sum_i \sum_j C_{ij}(\alpha_m,\beta_m) \end{aligned}$$

where i, j - the indexes over coordinates in the plane perpendicular to the beam, γ is defined by Equation 5.12, $A_{geom} = A(\alpha_m,\beta_m)$.

Then the efficiency was recomputed for angles α_o, β_o by Equation 5.14. Tables 5.22 and 5.23 show the efficiency $\varepsilon(\alpha_o,\beta_o)$ of NPD1 and NPD2, respectively.

ASPERA-4 / NPD1									
Efficiency ε (α_o, β_o), $\times 10^{-2}$									
	E, keV	10.0	5.0	3.0	1.3	0.7	0.5	0.3	0.1
O	Dir0	18.39	10.49	13.94	4.60	0.57	0.33	–	–
	Dir1	12.29	10.04	5.77	1.82	0.50	0.18	0.04	–
	Dir2	13.88	7.56	5.77	1.54	0.26	0.13	–	–
H	Dir0	–	7.54	16.27	5.80	3.58	2.27	0.48	–
	Dir1	–	4.45	6.61	3.31	1.69	1.19	0.44	0.04
	Dir2	–	5.24	6.83	2.93	1.43	1.02	0.39	–

Table 5.22: Absolute efficiency of the ASPERA-4 / NPD1 versus ion mass and energy.

ASPERA-4 / NPD2								
Efficiency ε (α_o, β_o), $\times 10^{-2}$								
	E, keV	5.0	3.0	1.3	0.7	0.5	0.3	0.1
O	Dir0	9.41	6.44	1.19	0.21	0.03	0.01	–
	Dir1	6.45	4.83	1.24	0.26	0.04	0.03	–
	Dir2	15.02	11.89	4.72	0.69	0.08	0.03	–
H	Dir0	5.27	4.89	2.38	2.37	0.47	0.18	–
	Dir1	3.89	3.99	2.31	1.53	0.54	0.17	0.01
	Dir2	9.17	8.62	4.95	1.38	1.20	0.47	–

Table 5.23: Absolute efficiency of the ASPERA-4 / NPD2 versus ion mass and energy.

Figures 5.27 and 5.28 show the NPD sensors' efficiency profiles together with the best fittings by the function

$$\ln(y) = a_0 + a_1 \cdot x + a_2 \cdot \ln(x) \tag{5.25}$$

where $x = \ln(E)$, $y = 10^4 \cdot \varepsilon$, and E an incident ion energy in units of eV.

The plots presented are valid for the energy range of 0.3 - 5.0 keV for H, and the energy range of 0.3 - 10.0 keV for O. Tables 5.24 and 5.25 show the coefficients for the efficiency fit-function for NPD1 and NPD2, respectively.

NPD1 / ASPERA-4						
	H			O		
	a_0	a_1	a_2	a_0	a_1	a_2
Dir0	-35.27	-4.02	35.81	-68.98	-7.01	63.49
Dir1	-29.37	-3.42	30.29	-57.65	-5.36	51.43
Dir2	-27.05	-2.81	26.87	-63.18	-5.68	55.23

Table 5.24: Coefficients for the NPD1 efficiency fitting (Equation 5.25).

NPD2 / ASPERA-4						
	H			O		
	a_0	a_1	a_2	a_0	a_1	a_2
Dir0	-36.60	-3.83	35.33	-95.06	-9.18	84.09
Dir1	-27.67	-2.58	26.15	-61.80	-5.55	53.98
Dir2	-32.29	-3.44	31.96	-87.42	-8.83	79.46

Table 5.25: Coefficients for the NPD2 efficiency fitting (Equation 5.25).

5.5.4 Angular response

Examples of the angular responses for 1.3 keV H and 1.3 keV O are shown only. The angular responses have been also measured for several other energies (see Table 5.20) for both NPD sensors. The values of coefficients k_{ji} for the respective fits are collected in the file *vex_npd1_npd2_angular response.dat* and available on the ASPERA-3 / ASPERA-4 server.

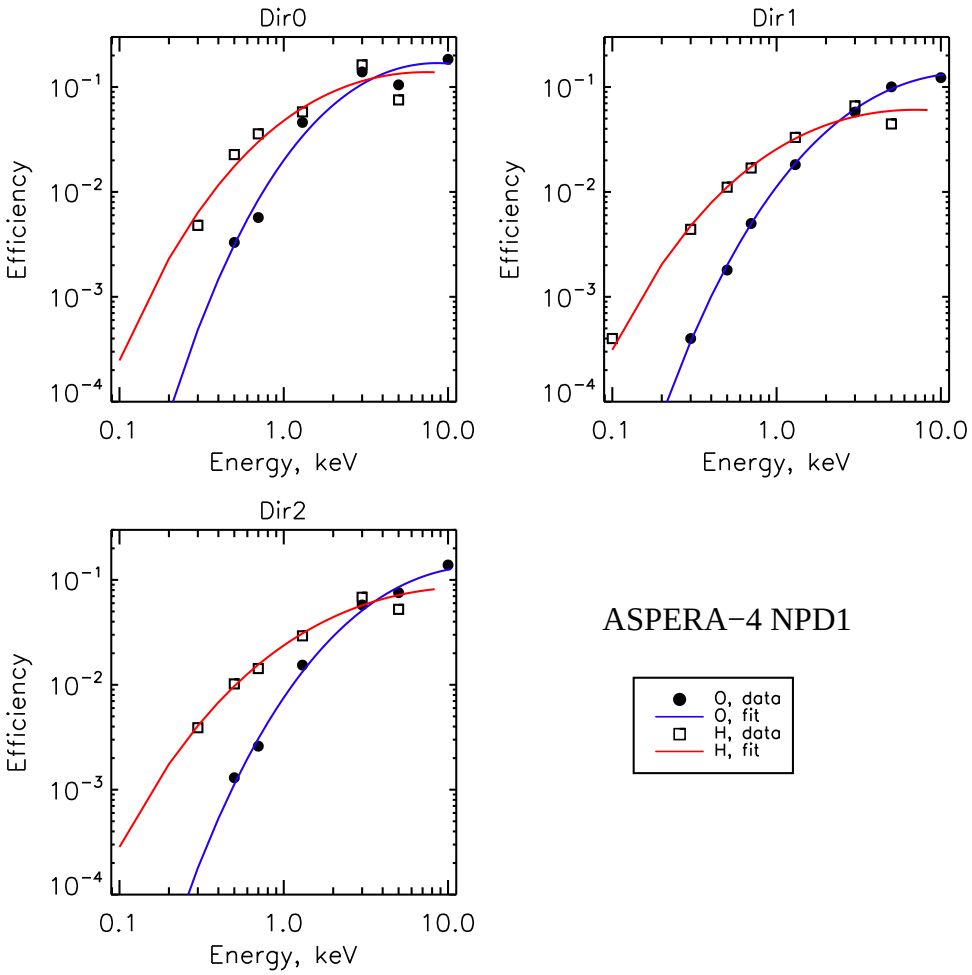

Figure 5.27: Absolute efficiency $\varepsilon(\alpha_o, \beta_o)$ of NPD1 is plotted in dependency on the ion mass and energy for different sectors. Least-square fitting functions are shown by lines.

Figures 5.29 and 5.31 show the angular responses of the NPD1 sensor for 1.3 keV *H* and 1.3 keV *O*, respectively. Each figure shows the angular response of the sectors Dir2, Dir1, Dir0 (from left to right). The upper row is the measured azimuth-elevation response. The second row from the top shows the fitting of the measured and smoothed data, normalized to have the peak magnitude equal to 1. The contours show the polynomial fits based on the function

$$f(x,y) = \sum k_{ji} \cdot x^i \cdot y^j \tag{5.26}$$

where x and y are azimuth and elevation angles scaled as $x = \alpha/5+10$, $y = \beta + 6$. k_{ji} are coefficients.
Functions are valid in the range of α [-45, 45], and β [-4, 6]. The third row shows the azimuthal response at $\beta=\beta_o$ and the bottom row shows the elevation response at $\alpha=\alpha_o$. Diamonds show the measured and smoothed data. The fittings are shown by thick lines. FWHM is given for each profile. The values of k_{ji} for the fit in Figure 5.29 are in Table 5.26. The values of k_{ji} for the fit in Figure 5.31 are in Table 5.27.

Figures 5.30 and 5.32 show the azimuthal profiles for respectively 1.3 keV *H* and 1.3 keV *O* of all three sectors of the NPD1 sensor plotted altogether. The dashed lines show the total

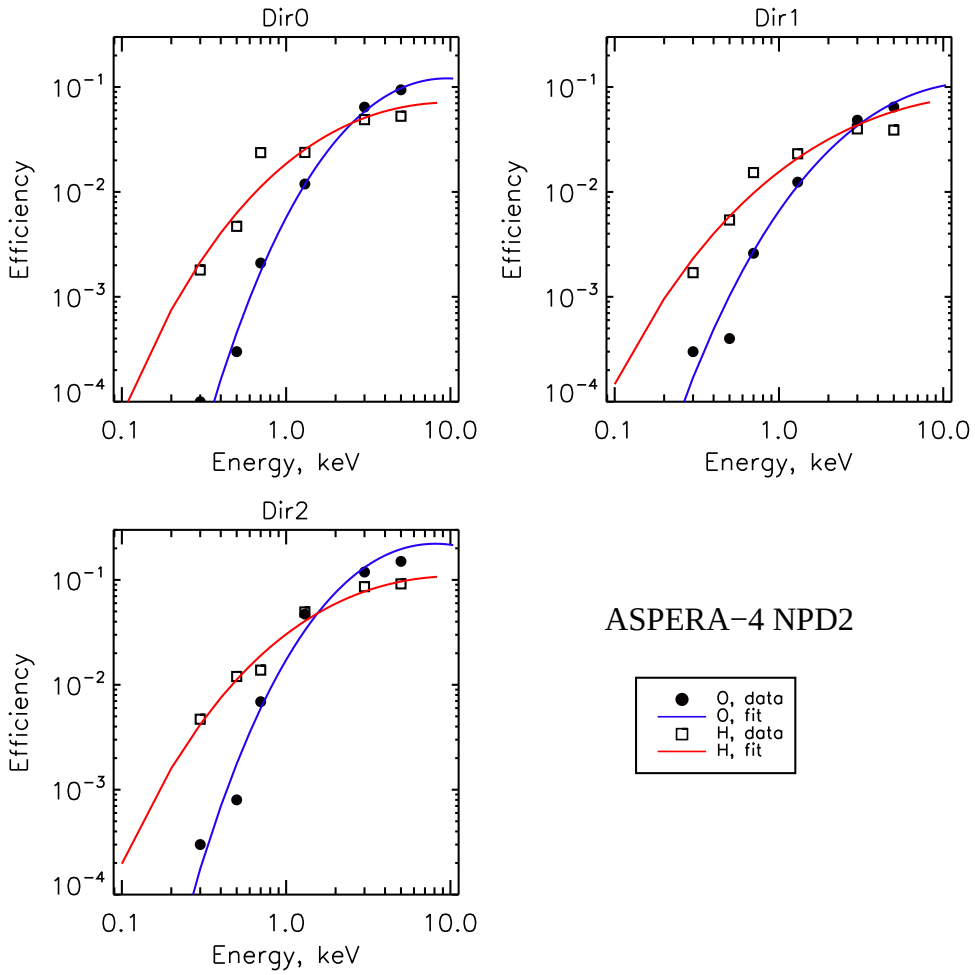

Figure 5.28: Absolute efficiency $\varepsilon(\alpha_o, \beta_o)$ of NPD2 is plotted in dependency on the ion mass and energy for different sectors. Least-square fitting functions are shown by lines.

angular coverage of the NPD1 sensor in the azimuthal plane. All responses are normalized to have the peak maximum equal to 1.

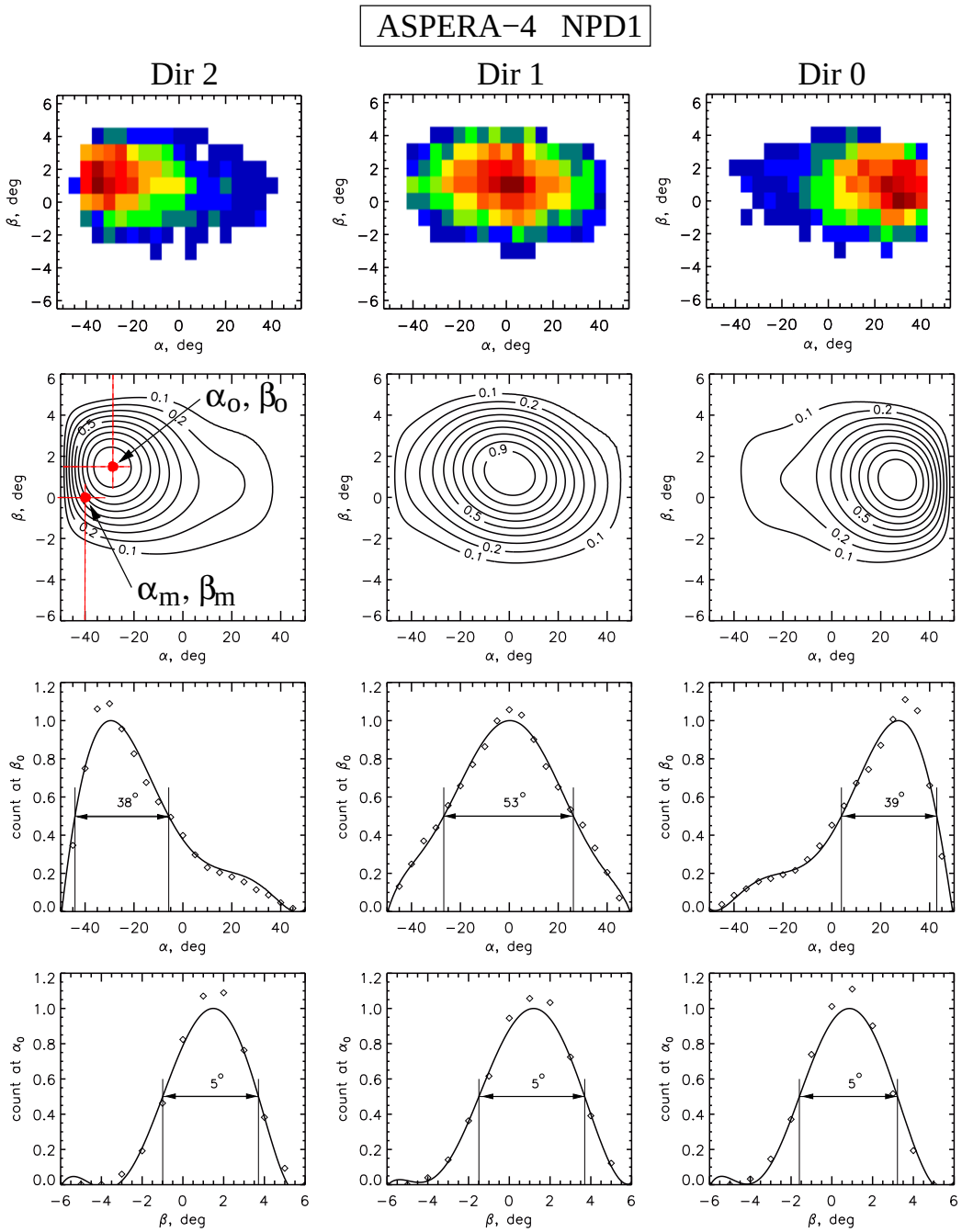

Figure 5.29: Angular response of the NPD1 sensor for 1.3 keV *H* given for the sectors Dir2, Dir1, Dir0 (from left to right). The upper row shows the measured azimuth-elevation response. The second row from the top shows the fitting of the measured and smoothed data. The third and fourth rows show the cross-sections of the angular response function at α_o and β_o, respectively. FWHM is given for each profile. Two red dots depict the angular positions corresponding to the position α_m, β_m at which the efficiency measurements have been performed, and to the position α_o, β_o of the maximum of the azimuth-elevation response function.

Dir	j	i=0	i=1	i=2	i=3	i=4	i=5	i=6
0	0	-4.52e-04	6.90e-03	-7.35e-03	2.82e-03	-4.35e-04	2.89e-05	-6.92e-07
	1	1.60e-03	-2.63e-02	2.94e-02	-1.24e-02	2.12e-03	-1.57e-04	4.22e-06
	2	-1.19e-03	1.92e-02	-2.15e-02	8.96e-03	-1.44e-03	9.81e-05	-2.39e-06
	3	2.66e-04	-3.78e-03	4.05e-03	-1.68e-03	2.59e-04	-1.63e-05	3.57e-07
	4	-2.47e-05	2.91e-04	-2.92e-04	1.24e-04	-1.79e-05	9.93e-07	-1.67e-08
	5	9.72e-07	-8.12e-06	6.76e-06	-3.07e-06	3.82e-07	-1.19e-08	-1.82e-10
	6	-1.31e-08	3.65e-08	1.24e-08	2.04e-09	1.84e-09	-4.14e-10	1.98e-11
1	0	-1.09e-04	3.53e-04	1.03e-05	-4.93e-04	1.19e-04	-9.61e-06	2.58e-07
	1	-5.38e-03	1.02e-01	-1.11e-01	4.07e-02	-6.02e-03	3.84e-04	-8.84e-06
	2	2.38e-03	-3.98e-02	4.00e-02	-1.45e-02	2.15e-03	-1.39e-04	3.27e-06
	3	-4.47e-04	6.88e-03	-6.65e-03	2.42e-03	-3.53e-04	2.19e-05	-4.87e-07
	4	3.91e-05	-5.63e-04	5.25e-04	-1.90e-04	2.66e-05	-1.55e-06	3.11e-08
	5	-1.58e-06	2.17e-05	-1.94e-05	6.92e-06	-9.21e-07	4.89e-08	-8.32e-10
	6	2.42e-08	-3.18e-07	2.74e-07	-9.55e-08	1.20e-08	-5.65e-10	7.09e-12
2	0	1.18e-03	-1.91e-02	1.91e-02	-6.10e-03	7.41e-04	-3.51e-05	4.64e-07
	1	-1.38e-02	2.30e-01	-2.37e-01	7.65e-02	-9.40e-03	4.51e-04	-6.12e-06
	2	4.67e-03	-7.04e-02	6.80e-02	-2.08e-02	2.58e-03	-1.33e-04	2.22e-06
	3	-6.44e-04	8.72e-03	-7.87e-03	2.30e-03	-2.98e-04	1.74e-05	-3.71e-07
	4	4.41e-05	-5.36e-04	4.48e-04	-1.24e-04	1.73e-05	-1.18e-06	3.07e-08
	5	-1.50e-06	1.64e-05	-1.26e-05	3.30e-06	-5.07e-07	4.08e-08	-1.24e-09
	6	2.01e-08	-2.03e-07	1.43e-07	-3.52e-08	6.22e-09	-5.86e-10	1.99e-11

Table 5.26: k_{ji} coefficients for the polynomial fit (Equation 5.26) for the angular response of NPD1 for 1.3 keV *H*.

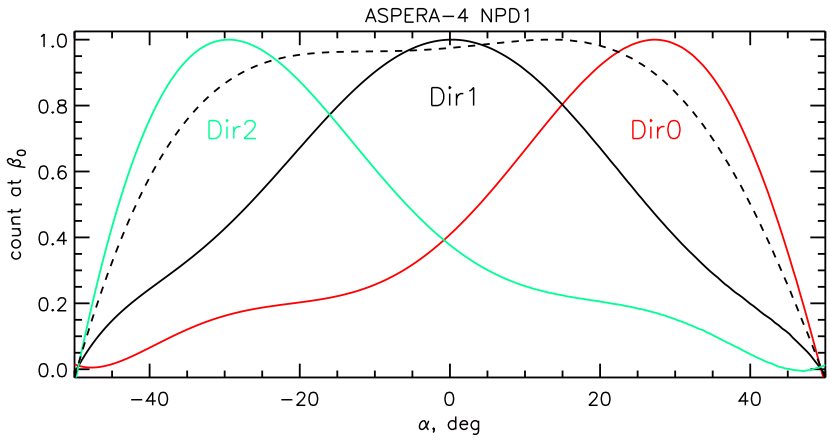

Figure 5.30: The azimuthal responses of each sector of NPD1 measured for 1.3 keV *H*. The dashed line shows the total angular coverage of the NPD1 sensor in the azimuthal plane. All responses are normalized to have the peak maximum equal to 1.

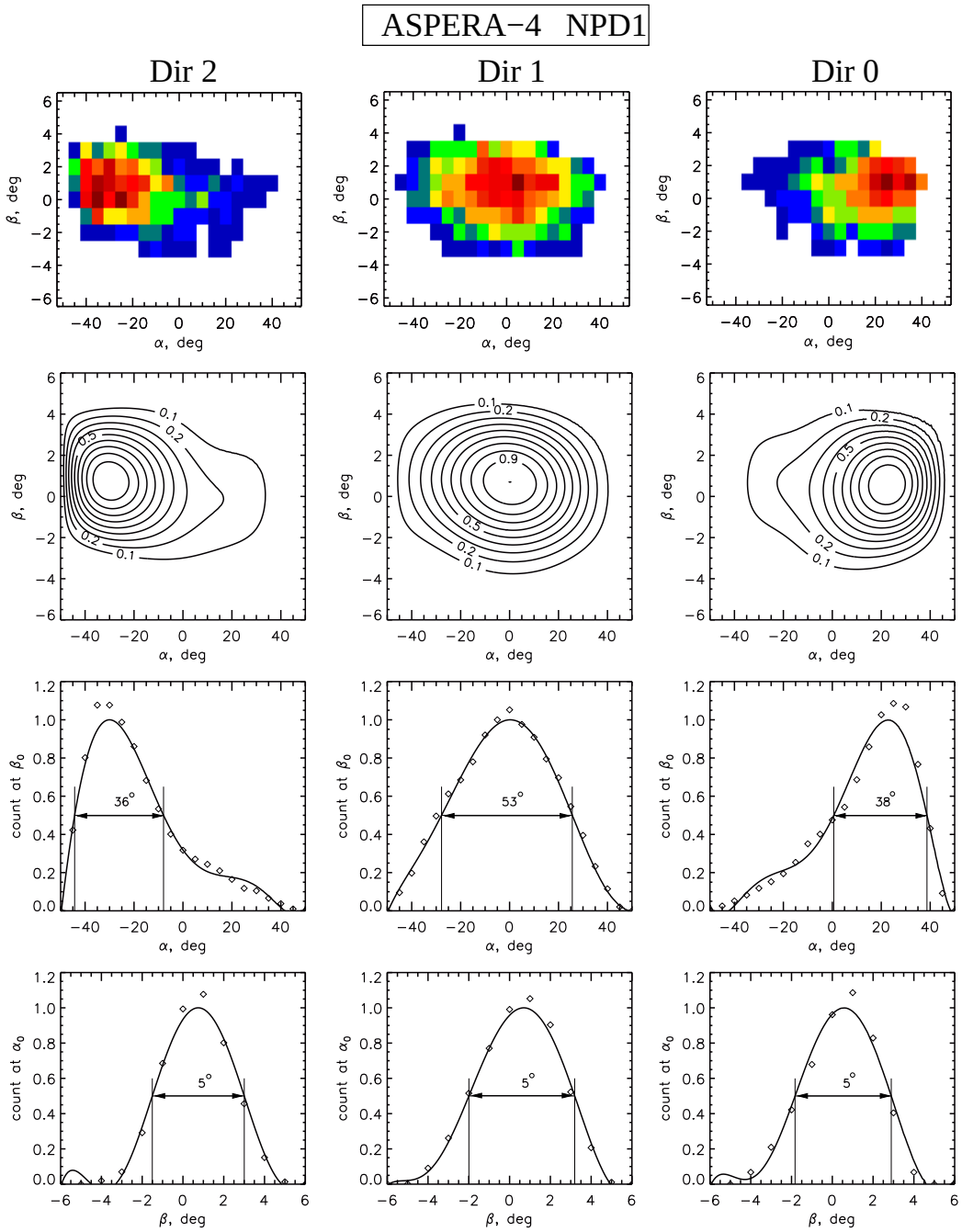

Figure 5.31: Angular response of the NPD1 sensor for 1.3 keV *O* given for the sectors Dir2, Dir1, Dir0 (from left to right). The format is the same as in Figure 5.29.

Dir	j	i=0	i=1	i=2	i=3	i=4	i=5	i=6
0	0	-1.47e-03	2.34e-02	-2.54e-02	9.26e-03	-1.40e-03	9.36e-05	-2.29e-06
	1	6.26e-03	-9.75e-02	1.03e-01	-3.57e-02	5.08e-03	-3.14e-04	6.96e-06
	2	-4.02e-03	6.75e-02	-7.36e-02	2.63e-02	-3.81e-03	2.39e-04	-5.38e-06
	3	8.70e-04	-1.51e-02	1.67e-02	-6.03e-03	8.79e-04	-5.53e-05	1.25e-06
	4	-8.25e-05	1.45e-03	-1.63e-03	6.02e-04	-8.86e-05	5.60e-06	-1.26e-07
	5	3.47e-06	-6.22e-05	7.08e-05	-2.66e-05	3.96e-06	-2.51e-07	5.68e-09
	6	-5.32e-08	9.64e-07	-1.11e-06	4.28e-07	-6.42e-08	4.08e-09	-9.21e-11
1	0	-9.63e-05	1.58e-03	-1.99e-03	8.26e-04	-1.82e-04	1.78e-05	-6.10e-07
	1	8.90e-04	3.46e-03	-1.25e-02	7.76e-03	-1.23e-03	6.90e-05	-1.12e-06
	2	-1.34e-03	2.30e-02	-2.44e-02	7.96e-03	-1.23e-03	9.11e-05	-2.57e-06
	3	3.19e-04	-6.60e-03	7.37e-03	-2.44e-03	3.77e-04	-2.76e-05	7.71e-07
	4	-3.20e-05	7.11e-04	-8.10e-04	2.71e-04	-4.21e-05	3.10e-06	-8.64e-08
	5	1.45e-06	-3.33e-05	3.84e-05	-1.30e-05	2.04e-06	-1.50e-07	4.19e-09
	6	-2.42e-08	5.67e-07	-6.60e-07	2.28e-07	-3.59e-08	2.64e-09	-7.35e-11
2	0	1.06e-03	-3.14e-02	3.98e-02	-1.62e-02	2.71e-03	-2.00e-04	5.44e-06
	1	-1.55e-02	3.32e-01	-3.73e-01	1.36e-01	-2.02e-02	1.31e-03	-3.08e-05
	2	4.94e-03	-8.51e-02	8.42e-02	-2.64e-02	3.45e-03	-1.96e-04	3.97e-06
	3	-6.60e-04	7.89e-03	-5.66e-03	9.33e-04	-1.15e-05	-6.77e-06	3.46e-07
	4	4.48e-05	-2.85e-04	-1.22e-05	1.19e-04	-3.07e-05	2.78e-06	-8.55e-08
	5	-1.53e-06	1.50e-06	1.34e-05	-1.00e-05	2.08e-06	-1.72e-07	4.98e-09
	6	2.07e-08	8.16e-08	-3.43e-07	2.10e-07	-4.13e-08	3.30e-09	-9.37e-11

Table 5.27: k_{ji} coefficients for the polynomial fit (Equation 5.26) for the angular response of NPD1 for 1.3 keV *O*.

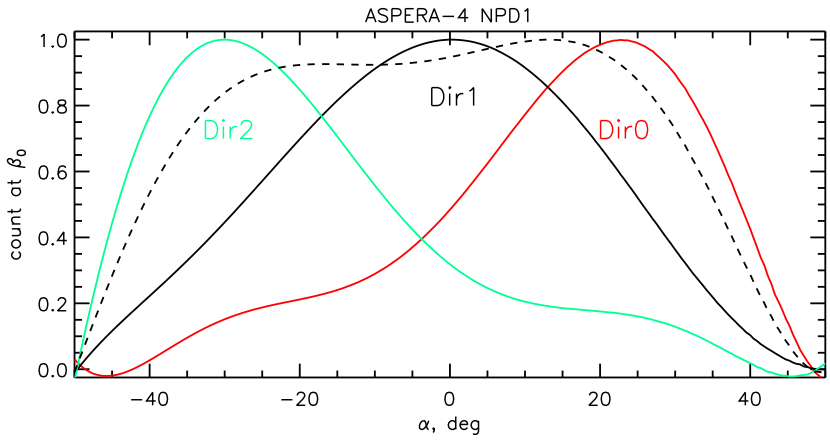

Figure 5.32: The azimuthal responses of each sector of NPD1 measured for 1.3 keV *O*. The dashed line shows the total angular coverage of the NPD1 sensor in the azimuthal plane. All responses are normalized to have the peak maximum equal to 1.

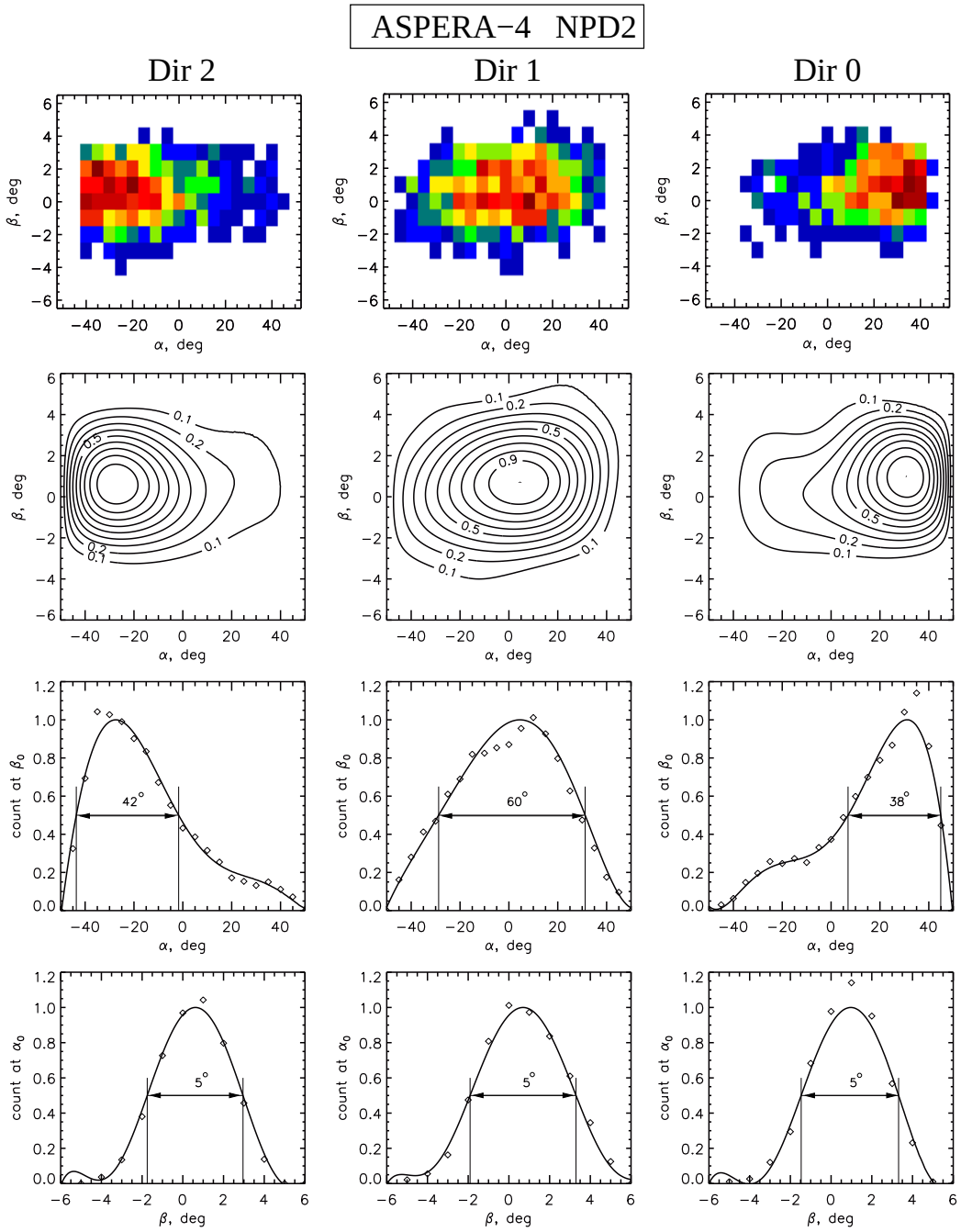

Figure 5.33: Angular response of the NPD2 sensor for 1.3 keV *H* given for the sectors Dir2, Dir1, Dir0 (from left to right). The format is the same as in Figure 5.29.

Figures 5.33 and 5.35 show the angular responses of the NPD2 sensor for 1.3 keV *H* and 1.3 keV *O*, respectively. The format is the same as in Figure 5.29. The values of coefficients k_{ji} for the fit in Figure 5.33 are in Table 5.28. The values of coefficients k_{ji} for the fit in Figure 5.35 are in Table 5.29.

Figures 5.34 and 5.36 show the normalized azimuthal profiles for respectively 1.3 keV *H* and 1.3 keV *O* of all three sectors of the NPD2 sensor plotted altogether. The dashed lines show the total angular coverage of the NPD2 sensor in the azimuthal plane.

Dir	j	i=0	i=1	i=2	i=3	i=4	i=5	i=6
	0	-4.66e-03	2.52e-02	-2.62e-02	1.00e-02	-1.65e-03	1.22e-04	-3.32e-06
	1	2.11e-02	-3.65e-02	1.35e-02	-1.49e-03	-1.82e-04	3.84e-05	-1.59e-06
	2	-1.39e-02	2.10e-02	-4.68e-03	-2.39e-04	3.30e-04	-4.48e-05	1.73e-06
0	3	3.24e-03	-3.84e-03	-1.74e-04	5.81e-04	-1.69e-04	1.76e-05	-6.06e-07
	4	-3.37e-04	3.08e-04	1.13e-04	-9.79e-05	2.37e-05	-2.27e-06	7.44e-08
	5	1.60e-05	-1.03e-05	-9.79e-06	6.29e-06	-1.37e-06	1.23e-07	-3.88e-09
	6	-2.81e-07	1.03e-07	2.53e-07	-1.40e-07	2.84e-08	-2.42e-09	7.36e-11
	0	-4.74e-03	-1.19e-02	1.34e-02	-3.53e-03	3.72e-04	-1.43e-05	5.98e-08
	1	1.70e-04	3.69e-02	-4.81e-02	2.51e-02	-4.80e-03	3.82e-04	-1.08e-05
	2	9.07e-03	-1.09e-02	6.16e-03	-2.75e-03	5.25e-04	-4.23e-05	1.22e-06
1	3	-2.53e-03	3.25e-03	-8.32e-04	5.46e-05	1.57e-05	-2.73e-06	1.14e-07
	4	2.60e-04	-3.97e-04	6.19e-05	2.57e-05	-9.21e-06	9.77e-07	-3.38e-08
	5	-1.17e-05	2.02e-05	-1.77e-06	-2.39e-06	7.01e-07	-6.94e-08	2.30e-09
	6	1.93e-07	-3.68e-07	1.39e-08	5.80e-08	-1.58e-08	1.51e-09	-4.93e-11
	0	5.97e-04	-8.31e-03	1.12e-02	-4.47e-03	6.53e-04	-3.90e-05	8.01e-07
	1	-4.61e-03	1.57e-01	-2.26e-01	9.99e-02	-1.68e-02	1.21e-03	-3.15e-05
	2	9.79e-09	-2.02e-02	4.47e-02	-2.19e-02	3.98e-03	-3.09e-04	8.62e-06
2	3	1.90e-04	-6.09e-04	-3.44e-03	2.18e-03	-4.59e-04	3.98e-05	-1.22e-06
	4	-2.40e-05	2.05e-04	1.37e-04	-1.32e-04	3.24e-05	-3.07e-06	9.96e-08
	5	1.12e-06	-1.06e-05	-3.52e-06	4.84e-06	-1.29e-06	1.27e-07	-4.24e-09
	6	-1.83e-08	1.72e-07	5.33e-08	-7.82e-08	2.12e-08	-2.11e-09	7.08e-11

Table 5.28: k_{ji} coefficients for the polynomial fit (Equation 5.26) for the angular response of NPD2 for 1.3 keV *H*.

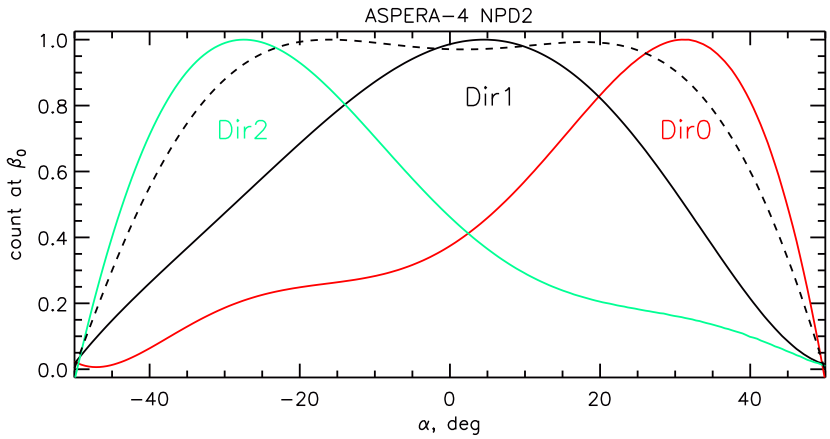

Figure 5.34: The azimuthal responses of each sector of NPD2 measured for 1.3 keV *H*. The dashed line shows the total angular coverage of the NPD2 sensor in the azimuthal plane. All responses are normalized to have the peak maximum equal to 1.

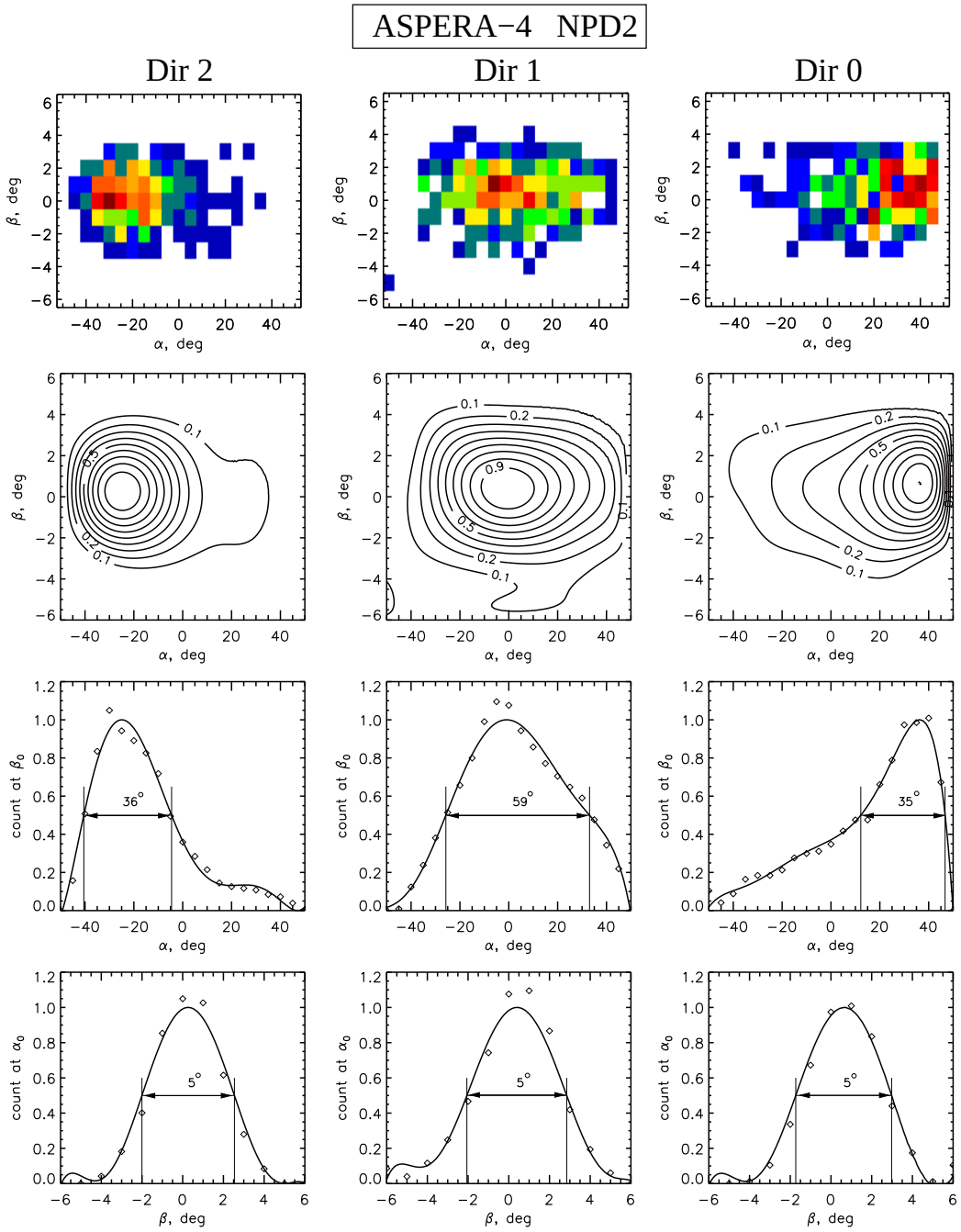

Figure 5.35: Angular response of the NPD2 sensor for 1.3 keV *O* given for the sectors Dir2, Dir1, Dir0 (from left to right). The format is the same as in Figure 5.29.

Dir	j	i=0	i=1	i=2	i=3	i=4	i=5	i=6
0	0	-5.76e-03	9.96e-02	-1.03e-01	3.83e-02	-6.36e-03	4.87e-04	-1.39e-05
	1	5.66e-03	-9.95e-02	7.12e-02	-2.30e-02	4.03e-03	-3.45e-04	1.10e-05
	2	-1.81e-03	3.03e-02	-7.54e-03	3.67e-04	-1.22e-04	2.65e-05	-1.34e-06
	3	2.21e-04	-2.80e-03	-2.96e-03	1.74e-03	-2.82e-04	1.78e-05	-3.72e-07
	4	-8.94e-06	-2.22e-05	6.55e-04	-3.14e-04	5.13e-05	-3.48e-06	8.40e-08
	5	-1.01e-07	1.31e-05	-4.44e-05	2.00e-05	-3.25e-06	2.25e-07	-5.59e-09
	6	9.40e-09	-4.07e-07	9.80e-07	-4.27e-07	6.94e-08	-4.82e-09	1.21e-10
1	0	1.10e-02	4.33e-01	-3.64e-01	1.10e-01	-1.56e-02	1.04e-03	-2.67e-05
	1	2.01e-02	-4.19e-01	3.26e-01	-8.89e-02	1.12e-02	-6.68e-04	1.54e-05
	2	-5.95e-03	1.15e-01	-7.92e-02	1.78e-02	-1.61e-03	5.23e-05	-1.34e-07
	3	7.19e-04	-1.20e-02	5.16e-03	2.01e-04	-2.62e-04	3.07e-05	-1.06e-06
	4	-4.08e-05	5.41e-04	1.00e-04	-2.29e-04	5.72e-05	-5.18e-06	1.59e-07
	5	1.02e-06	-9.09e-06	-1.96e-05	1.55e-05	-3.36e-06	2.86e-07	-8.52e-09
	6	-7.96e-09	-6.74e-10	4.84e-07	-3.15e-07	6.45e-08	-5.35e-09	1.57e-10
2	0	3.77e-02	-1.00e-01	9.23e-02	-3.25e-02	5.14e-03	-3.73e-04	1.01e-05
	1	-5.19e-02	3.85e-01	-4.18e-01	1.53e-01	-2.43e-02	1.74e-03	-4.65e-05
	2	1.91e-02	-1.21e-01	1.19e-01	-3.67e-02	5.28e-03	-3.63e-04	9.62e-06
	3	-3.25e-03	1.74e-02	-1.53e-02	3.79e-03	-4.54e-04	2.83e-05	-7.29e-07
	4	2.80e-04	-1.34e-03	1.08e-03	-2.19e-04	2.02e-05	-1.00e-06	2.35e-08
	5	-1.17e-05	5.27e-05	-4.08e-05	7.29e-06	-5.18e-07	1.70e-08	-2.81e-10
	6	1.87e-07	-8.23e-07	6.29e-07	-1.08e-07	6.74e-09	-1.49e-10	7.94e-13

Table 5.29: k_{ji} coefficients for the polynomial fit (Equation 5.26) for the angular response of NPD2 for 1.3 keV *O*.

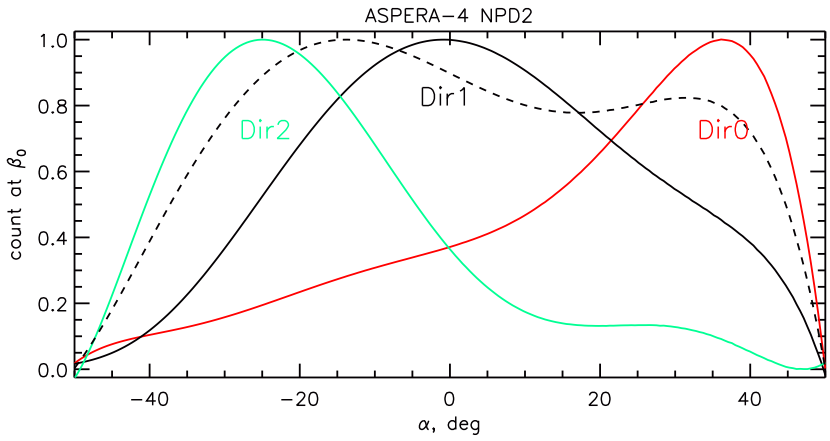

Figure 5.36: The azimuthal responses of each sector of NPD2 measured for 1.3 keV *O*. The dashed line shows the total angular coverage of the NPD2 sensor in the azimuthal plane. All responses are normalized to have the peak maximum equal to 1.

		H			*O*		
Sensor	Sector	α_o, deg	β_o, deg	A_o, mm^2	α_o, deg	β_o, deg	A_o, mm^2
NPD1	Dir0	27.0	0.9	11.62	23.0	0.6	12.00
	Dir1	0.0	1.1	13.04	0.0	0.7	13.04
	Dir2	−29.0	1.5	11.40	−30.0	0.8	11.29
NPD2	Dir0	32.0	1.1	11.06	36.0	0.7	10.55
	Dir1	5.0	0.9	12.99	−1.0	0.4	13.04
	Dir2	−27.0	0.6	11.62	−25.0	0.2	11.82

Table 5.30: Angles α_o, β_o for different sectors, and corresponding effective aperture area for these angles are given. α_o, β_o are calculated from the angular response for 1.3 keV *H* and 1.3 keV *O* for both NPD1 and NPD2 sensors.

Table 5.30 shows the angles α_o, β_o which correspond to the maximum of the angular response functions of both NPD sensors for 1.3 keV *H* and 1.3 keV *O*. The effective aperture area at these angles is also shown.
Table 5.31 shows the pure geometrical constant G_o of both the NPD1 and NPD2 sensors, calculated according to Equation 5.3.

G_o, $\times 10^{-3}$, cm^{2}sr						
	H			*O*		
Sensor	Dir0	Dir1	Dir2	Dir0	Dir1	Dir2
*NPD*1	6.94	10.33	6.71	6.98	10.10	6.01
*NPD*2	6.79	12.10	7.56	6.43	11.36	6.25

Table 5.31: Pure geometrical factor G_o computed from the angular response for 1.3 keV *H* for both NPD1 and NPD2 sensors. Efficiency ε is not included.

5.5.5 Geometrical factor

The total geometrical factors $G = G_o \cdot \varepsilon(E)$ (in units of $cm^2 sr$) of the NPD1 and NPD2 sensors are shown in Tables 5.32 and 5.33, respectively.

NPD1 / ASPERA-4									
Geometrical factor G, $\times 10^{-4}$									
	E, keV	10.0	5.0	3.0	1.3	0.7	0.5	0.3	0.1
O	Dir0	11.82	10.20	7.42	2.30	0.49	0.10	–	–
	Dir1	13.79	9.80	6.65	1.85	0.51	0.20	0.03	–
	Dir2	8.01	5.87	3.83	0.83	0.20	0.07	–	–
H	Dir0	–	9.18	7.79	4.47	2.13	1.27	0.49	–
	Dir1	–	6.47	5.33	3.34	1.90	1.13	0.50	0.03
	Dir2	–	4.40	3.80	2.01	1.08	0.69	0.31	–

Table 5.32: The absolute geometrical factors of the ASPERA-4 / NPD1 sensor, computed from the fit functions of the efficiency of NPD1 and pure geometrical factors of NPD1 derived from the angular responses for respective energies.

NPD2 / ASPERA-4								
Geometrical factor G, $\times 10^{-4}$								
	E, keV	5.0	3.0	1.3	0.7	0.5	0.3	0.1
O	Dir0	7.99	4.37	0.84	0.14	0.05	0.003	–
	Dir1	9.17	5.40	1.28	0.32	0.13	0.02	–
	Dir2	14.19	8.73	2.06	0.35	0.11	0.01	–
H	Dir0	4.67	3.79	1.84	0.90	0.56	0.21	–
	Dir1	7.42	5.64	2.57	1.26	0.70	0.28	–
	Dir2	7.29	6.29	3.14	1.40	0.79	0.30	–

Table 5.33: The absolute geometrical factor of the ASPERA-4 / NPD2 sensor, computed from the fit function of the efficiency of NPD2 and pure geometrical factors of NPD2 derived from the angular responses for respective energies.

5.5.6 Energy resolution

Figures 5.37, 5.38 show the TOF spectra obtained by the NPD1 sensor for *H* and *O* ion beams, respectively, for different energies. Figures 5.39, 5.40 show the TOF spectra obtained by the NPD2 sensor for *H* and *O* ion beams, respectively, for different energies.

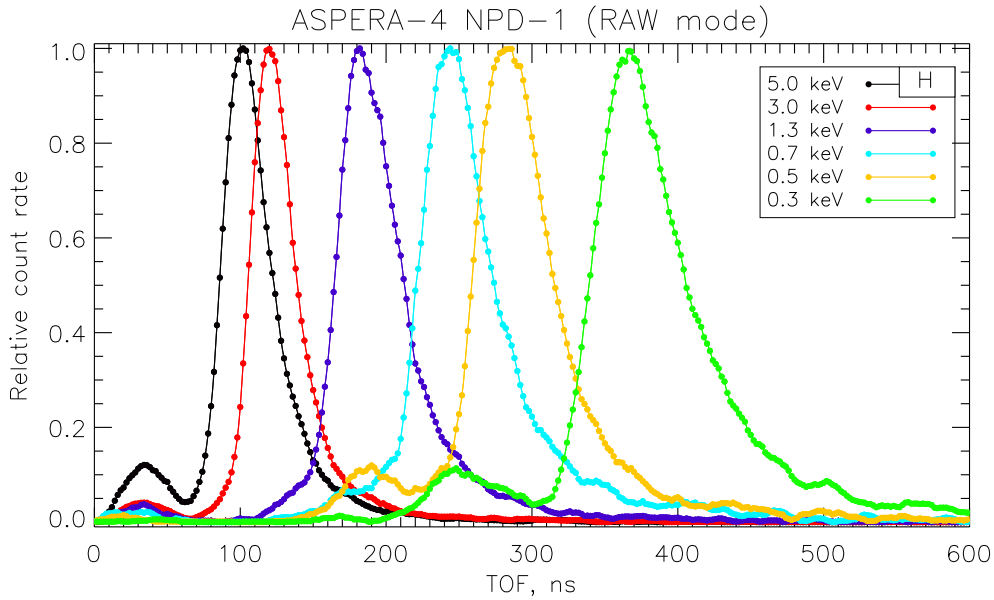

Figure 5.37: The NPD1 TOF spectra for *H* beams of different energies. The reason for the structures in the 0.3 keV TOF spectrum (at ~250 ns) and in the 0.5 keV TOF spectrum (at ~200 ns) is as yet unclear. It can perhaps be due to electronic disturbances.

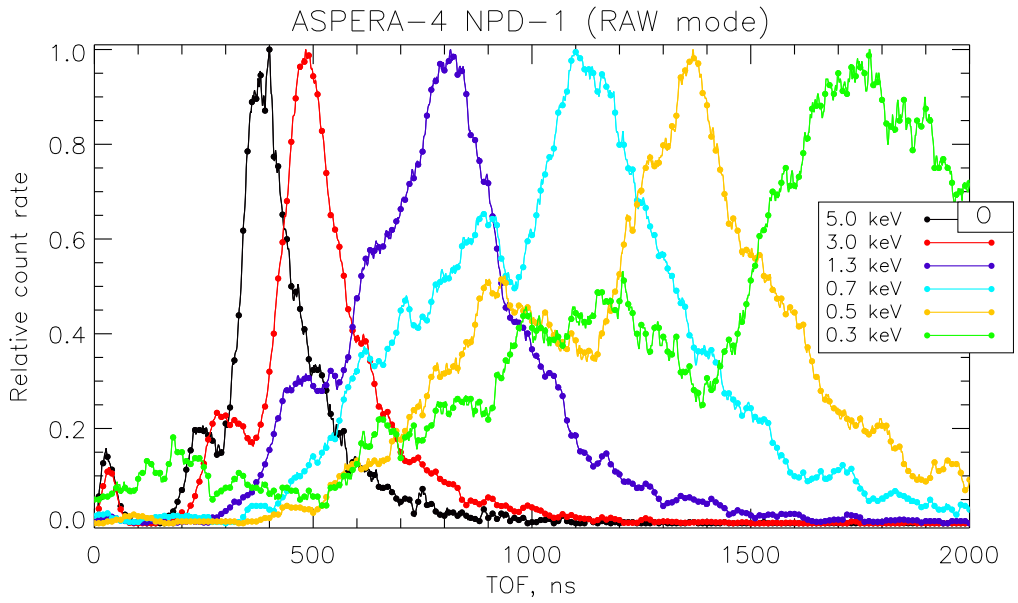

Figure 5.38: The NPD1 TOF spectra for *O* beams of different energies.

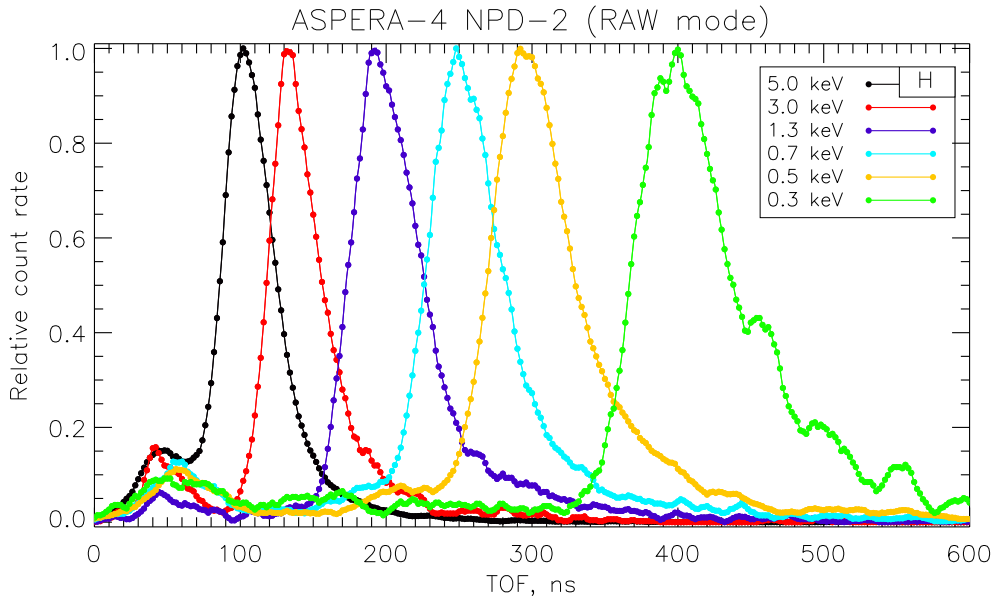

Figure 5.39: The NPD2 TOF spectra for *H* beams of different energies.

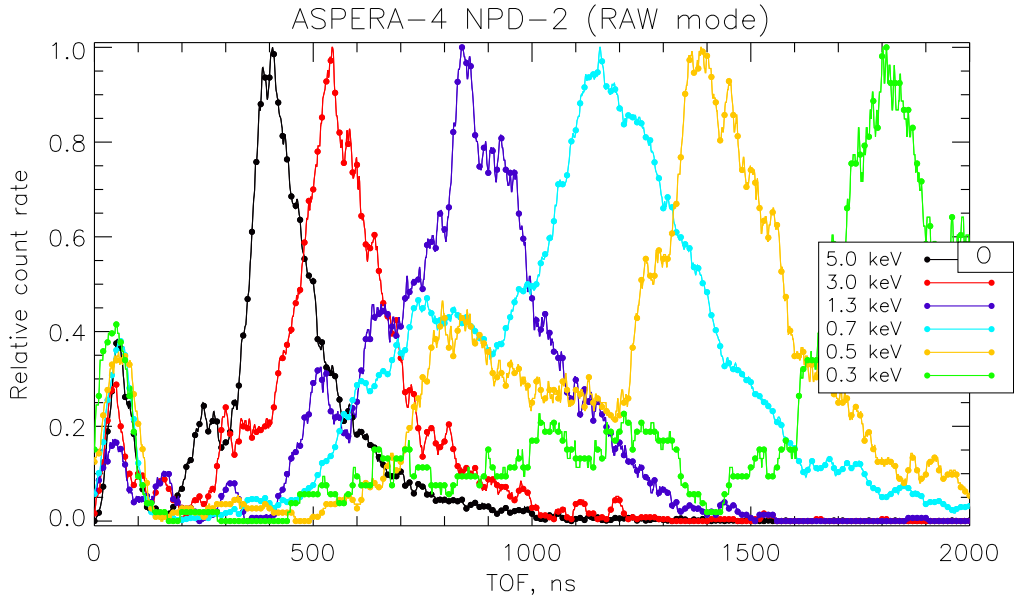

Figure 5.40: The NPD2 TOF spectra for *O* beams of different energies.

Figures 5.41 and 5.42 show the TOF spectrum maximum as a function of the incident ion beam energy for the NPD1 and NPD2 sensors, respectively. The error bars show FWHM of the TOF spectra. The dashed lines show ideal theoretical dependencies $T_M = f(E)$ (Equation 5.15) with no energy loss, i.e., ΔE_{loss}=0. The solid lines show the best fits, assuming the TOF distance L equal to 80 mm. These curves can be expressed by Equation 5.15.

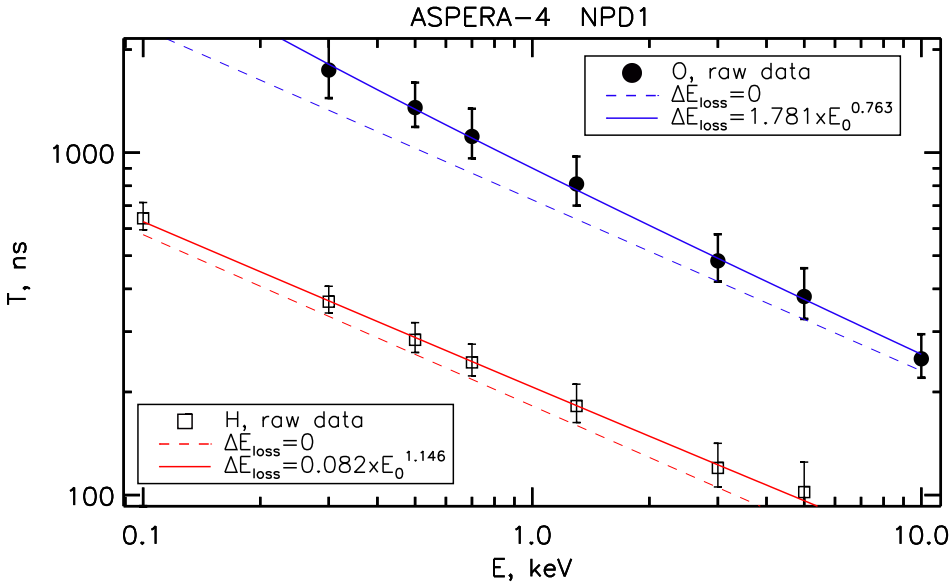

Figure 5.41: NPD1 TOF spectrum maximum as a function of the initial energy E_o. Open squares and solid circles show experimental data for H and O beam, respectively. The dashed lines depict the dependence with no energy loss, $\Delta E_{loss} = 0$. The solid lines show the best fit.

Table 5.34 shows ΔE_{loss} as a function of the initial particle energy E_o for both NPD sensors. The incident ion energy loss during interaction with the Start surface is clearly energy dependent.

Figures 5.43 and 5.44 show the energy loss ΔE_{loss} (panels a) and the relative energy loss $K = \Delta E_{loss}/E$ (panels b) of the NPD1 respectively NPD2 sensor graphically.

Figure 5.45 shows the estimation of the energy resolution of the NPD1 and NPD2 sensors. The energy resolution is defined as double FWHM of the TOF spectra, normalized to the TOF peaks.

	m	ΔE_{loss}		m	ΔE_{loss}
NPD1	O	$1.781E_o^{0.763}$	NPD2	O	$0.843E_o^{0.873}$
	H	$0.082E_o^{1.146}$		H	$0.124E_o^{1.128}$

Table 5.34: The energy loss ΔE_{loss} as a function of the initial energy E_o and ion species.

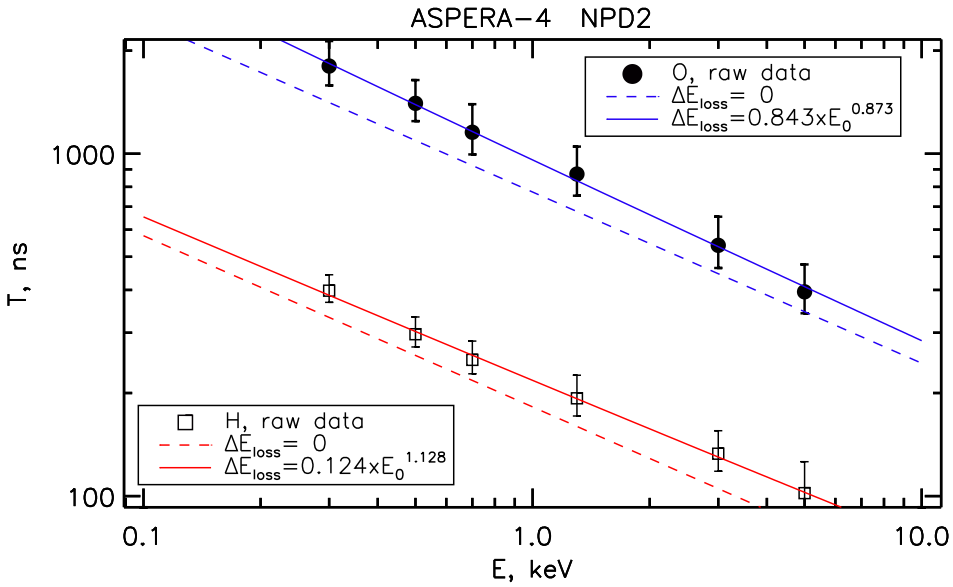

Figure 5.42: NPD2 TOF spectrum maximum as a function of the initial energy E_o. Open squares and solid circles show experimental data for H and O beams, respectively. The dashed lines depict the dependence with no energy loss, $\Delta E_{loss} = 0$. The solid lines show the best fit.

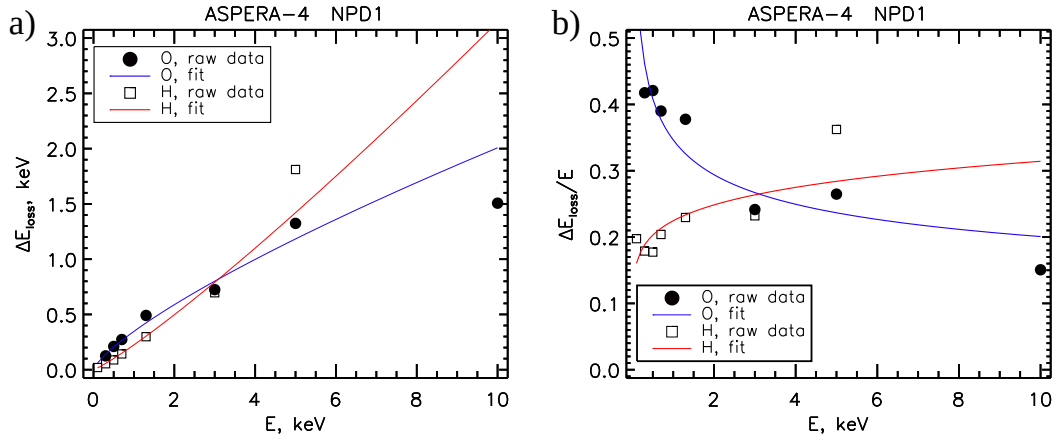

Figure 5.43: (a) Energy loss ΔE_{loss} and (b) relative energy loss $K = \Delta E_{loss}/E$ are plotted as a function of the initial energy E_o for NPD1.

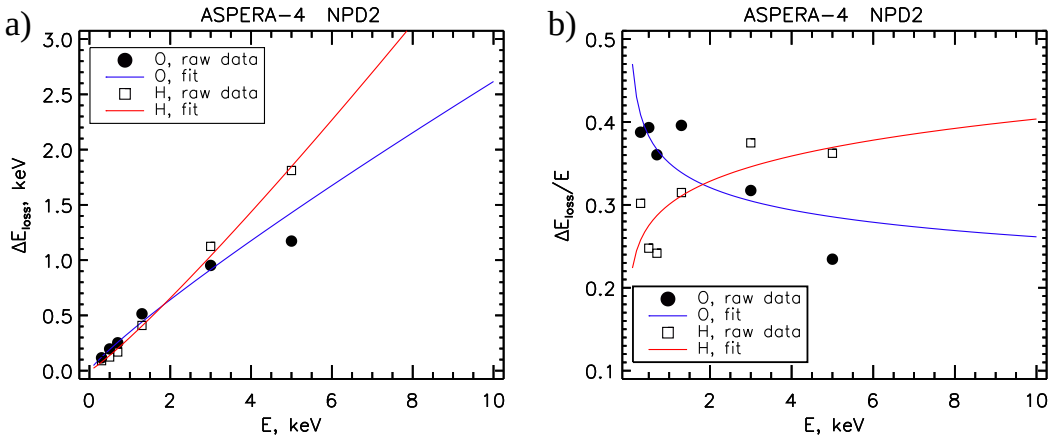

Figure 5.44: (a) Energy loss ΔE_{loss} and (b) relative energy loss $K = \Delta E_{loss}/E$ are plotted as a function of the initial energy E_o for NPD2.

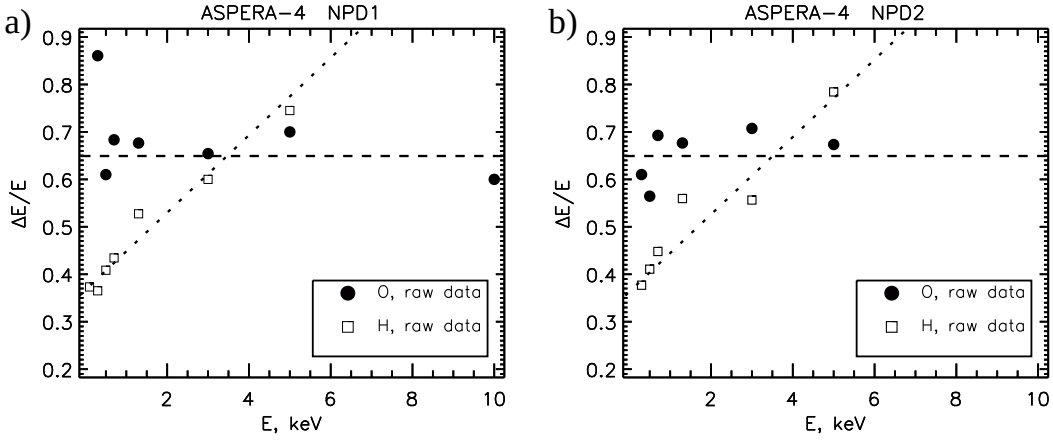

Figure 5.45: Energy resolution $\Delta E/E$ as a function of the initial energy E_o is plotted for different ion species; for a) the NPD1 and b) the NPD2 sensors. The dashed and dotted lines are to guide the eye.

5.5.7 Mass resolution

As seen in Figures 5.41 and 5.42, TOF for *H* and *O* overlaps in the range of ~260 - 650 ns for the energy range of 100 eV - 10 keV. Particles with TOF in the range of >650 ns are assumed to be *O*. Particles with TOF less than 260 ns are assumed to be *H*. Table 5.35 shows TOF ranges in which *O* and *H* species can be identified directly from TOF measurements. PH analysis is required to distinguish between the species inside this TOF range.

ASPERA-4				
	NPD1		NPD2	
	$T_M(RAW)$	T_M (BIN)	T_M (RAW)	T_M (BIN)
H	< 258 ns	< 7 ch	< 268 ns	< 7 ch
O	> 629 ns	> 10 ch	> 654 ns	> 10 ch

Table 5.35: Identification of *O* and *H* species from TOF measurements. TOF values are shown for two modes, RAW and BIN. T_M shows the TOF in ns in the RAW mode and the channel number in the BIN mode.

Table 5.36 shows the values of *N* indicating the channel number above which mostly *O* atoms give a considerable tail in the pulse height distribution, and P_H, P_O indicating probability for *H* and *O* atoms respectively to produce stop signals of a magnitude higher than level *N*. Channel *N* is defined in such a way as to minimize the value of $\frac{P_H}{P_O}$.

ASPERA-4						
	NPD1			NPD2		
	Dir0	Dir1	Dir2	Dir0	Dir1	Dir2
N	7	11	10	11	10	5
P_H, $\times 10^{-2}$	1.16	8.34	1.27	4.00	0.26	0.06
P_O, $\times 10^{-2}$	3.18	10.70	5.99	6.00	4.45	2.10

Table 5.36: Value *N* indicates a number of a channel above which mostly *O* atoms give a considerable tail in pulse height distribution. P_H and P_O are the probabilities for *H* and *O*, respectively, to produce stop signals of a magnitude higher than level *N*.

Figures 5.46 and 5.47 show pulse height distributions from 0.3 keV *H* (the red curve) and 5.0 keV *O* (the black curve) for the NPD1 and NPD2 sensors, respectively, in the logarithmic scale.

5.5.8 Heater and temperature sensor characterization

The heater is for the Start surface conditioning (Section 4.2.2). The heater increases temperature of the Start surface by 50° over the ambient temperature. It takes ~2 hours to reach the equilibrium maximum temperature of the Start surface. Temperature sensors were verified after the NPD integration with the ASPERA-4 package during TVAC test (Section 4.6).

5.5.9 Dark noise

Electromagnetic disturbances during communication of the DPU with the spacecraft were measured after the NPD integration with the ASPERA-4 package. Electromagnetically induced noise at biased MCP detectors is ⩽20 c/s for non-correlated counts. TOF coincidence totally removes this noise.

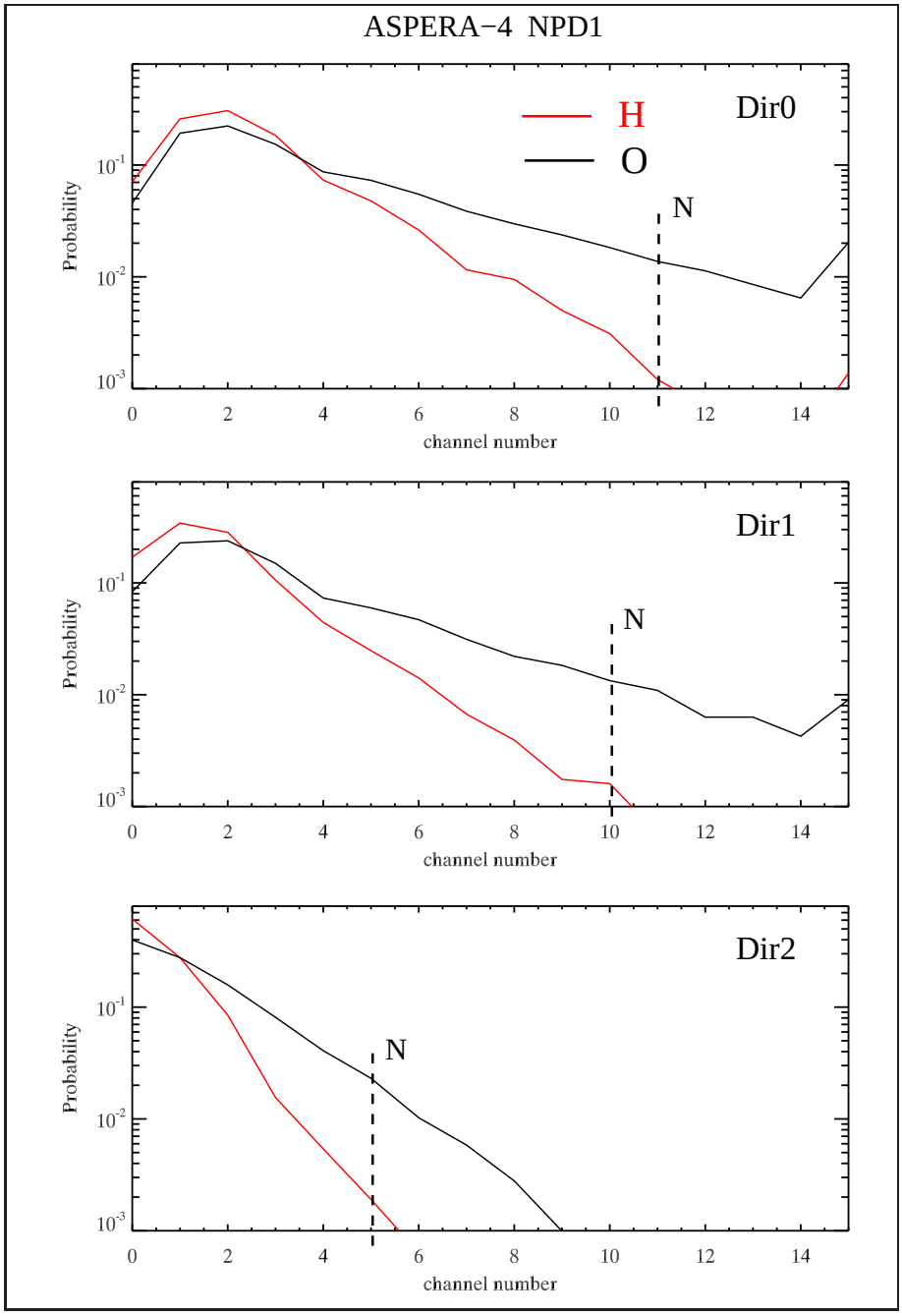

Figure 5.46: Pulse height distributions from 0.3 keV *H* (the red curve) and 5.0 keV *O* (the black curve) are shown for sectors Dir0, Dir1, Dir2 (from top to bottom) of the ASPERA-4 / NPD1. Plots are shown in the logarithmic scale. Both distributions are normalized to have the same area equal to 1. The dashed lines show channel *N* values.

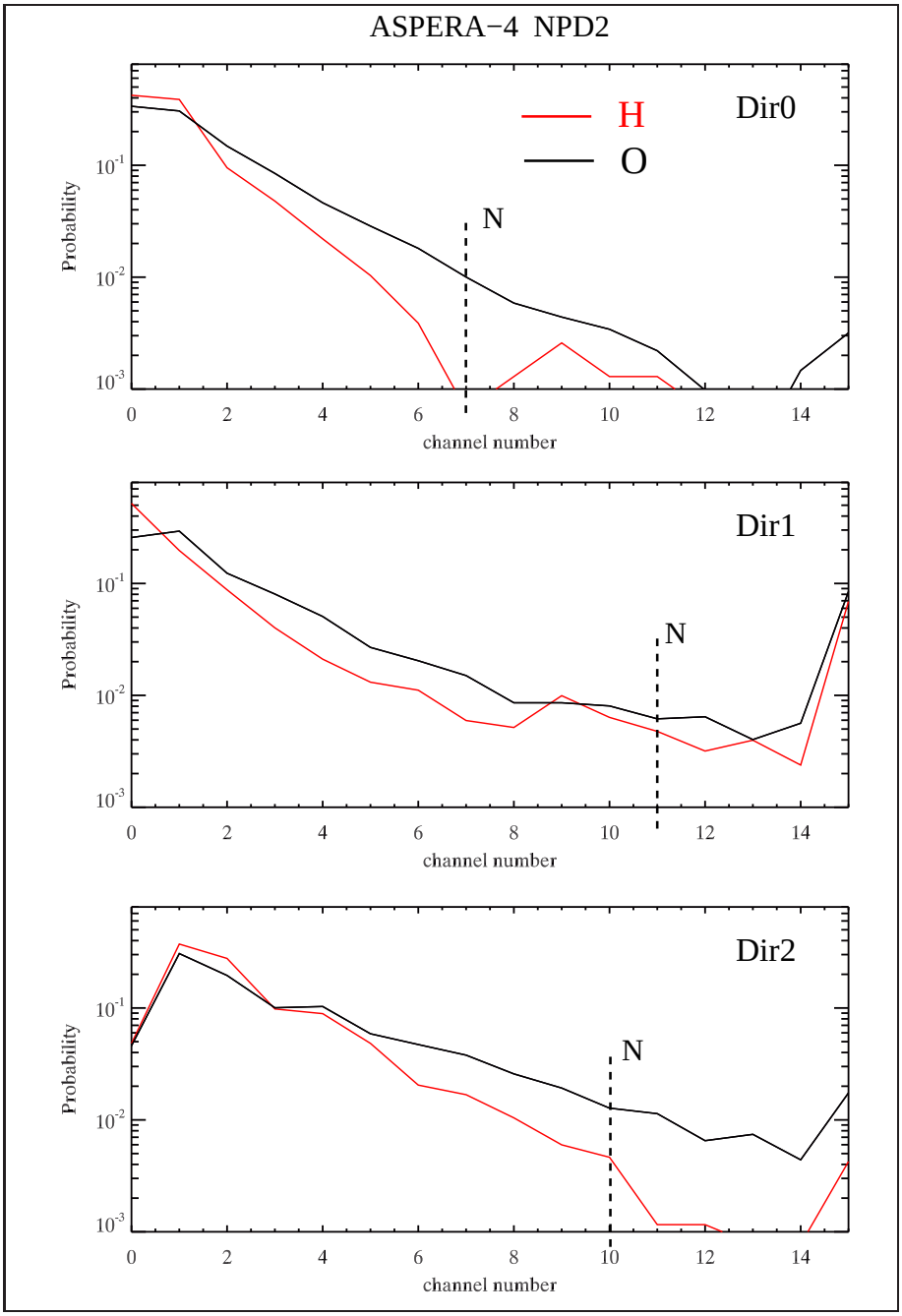

Figure 5.47: Pulse height distributions from *H* and *O* of about the same velocity are shown for the ASPERA-4 / NPD2 sensor. The format is the same as in Figure 5.46.

Chapter 6

Scientific results. The NPD measurements at Mars.

The ASPERA-3 / NPD is the first ENA sensor flown to Mars. In the meantime, the ENA environment of Mars was described using numerical simulations and models, based on Mars – solar wind interaction (see Section 1.3). In this chapter the observations and scientific findings by the ASPERA-3 / NPD are reviewed. One of the most important results from the NPD measurements is an observation of the ENA jet (cone) and its dynamics (*Futaana et al.*, 2006a; *Grigoriev et al.*, 2006), discussed in Sections 6.1, 6.2. In Section 6.3 other scientific results from the ASPERA-3 / NPD are briefly overviewed.

6.1 Subsolar ENA jet

6.1.1 Introduction

Futaana, Barabash, Grigoriev et al. (2006a) reported on the intensive ENA emission from the subsolar region of Mars, so-called ENA jet/cone, detected by the NPD instrument.

This study uses data recorded between May 24 and July 1, 2004, when the orbit and the attitude of Mars Express were optimal for investigating ENA emissions from the subsolar region. The NPD operations lasted ~30 minutes, starting ~20 minutes after the periapsis. During these time intervals, the Mars Express was nadir pointing and the ASPERA-3 scanner rotation axis pointed towards the center of Mars. NPD was running in the BIN mode. The TOF spectra observed by the NPD1 are used in this study since the subsolar region was out of the NPD2 field-of-view.

The NPD sensor is an open system, and thus UV photons entering the instrument result in non-correlated counts on the Start and Stop units. The non-correlated count rate on Start is ~10 kHz and on each Stop ~300 Hz. These non-correlated signals result in random correlated TOF signals as a background level. Since the TOF distribution of this signal is basically constant over the entire TOF window of NPD, we can estimate the background level from the TOF spectrum obtained. To recover absolute flux, this random correlated signal must be subtracted from the recorded signal.

Figure 6.1 shows a schematic view of the NPD configuration and viewing directions relative to the spacecraft body.

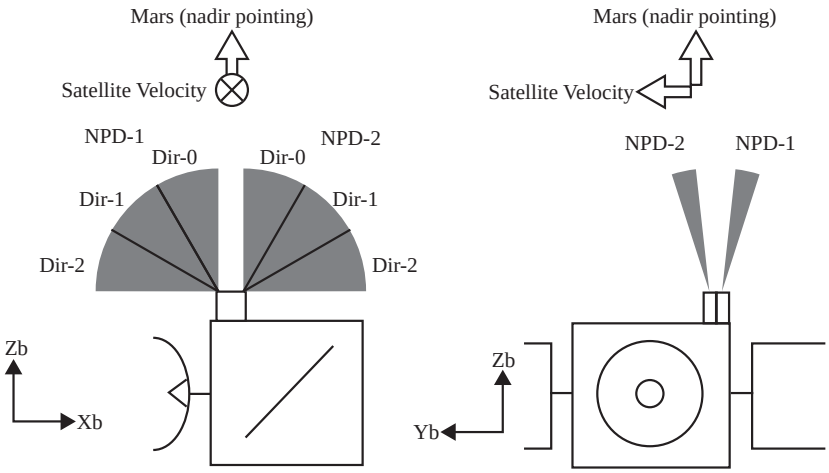

Figure 6.1: The configuration of the NPD instruments on board Mars Express seen from (left) the $-Y_b$ direction and (right) the $-X_b$ direction. The satellite coordinate system is used. Two NPD instruments are mounted on the Z_b plane and each has a $9°\times90°$ FOV. The FOV inclines $\pm15°$ in the Y_b direction for the NPD1 and NPD2 respectively. The attitude mode of the satellite during the observations discussed in this paper was nadir pointing, i.e., Z_b pointed toward the center of Mars. From *Futaana et al.* (2006a).

6.1.2 Observations

Figure 6.2 shows the Mars Express trajectory on June 2, 2004 (Orbit 466) in the cylindrical coordinate system, based on the Mars-Sun orbit (MSO) coordinate system, in which the *x*-axis is aligned from Mars to the Sun, the *z*-axis is perpendicular to the Martian orbital plane toward ecliptic north and the *y*-axis completes the right-handed system. In the cylindrical coordinate system, the horizontal axis corresponds to the *x*-direction of the MSO coordinates, and the vertical axis is the distance from the Mars-Sun line ($r = \sqrt{y^2+z^2}$).

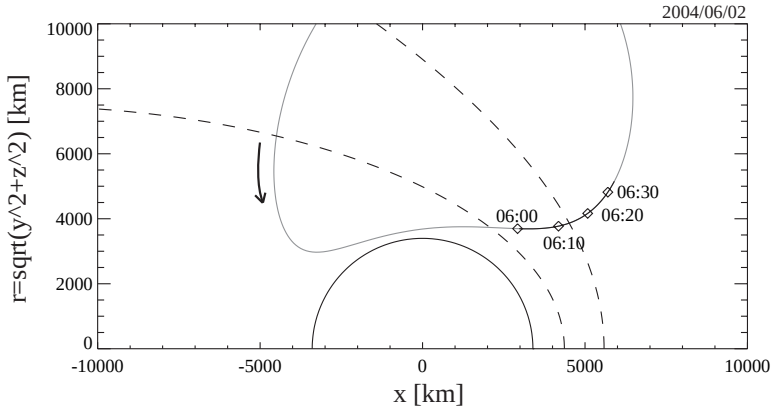

Figure 6.2: The Mars Express trajectory on June 2, 2004, (Orbit-466) in the cylindrical coordinate system: the horizontal axis corresponds to the *x*-direction of the MSO coordinates and the vertical axis is the distance from the Mars-Sun line. The dashed lines are the modeled BS and MPB (*Vignes et al.*, 2000). From *Futaana et al.* (2006a).

The pericenter height is 265 km (05:40 UT). NPD operated between 06:03 and 06:31 UT. Mars Express was located in the magnetosheath region at the start of the operations and moved to the solar wind region after a BS crossing at 06:05 UT as deduced from data recorded by the

ASPERA-3 IMA and ELS sensors. The BS was located closer to the planet than the modeled BS (shown in Figure 6.2).

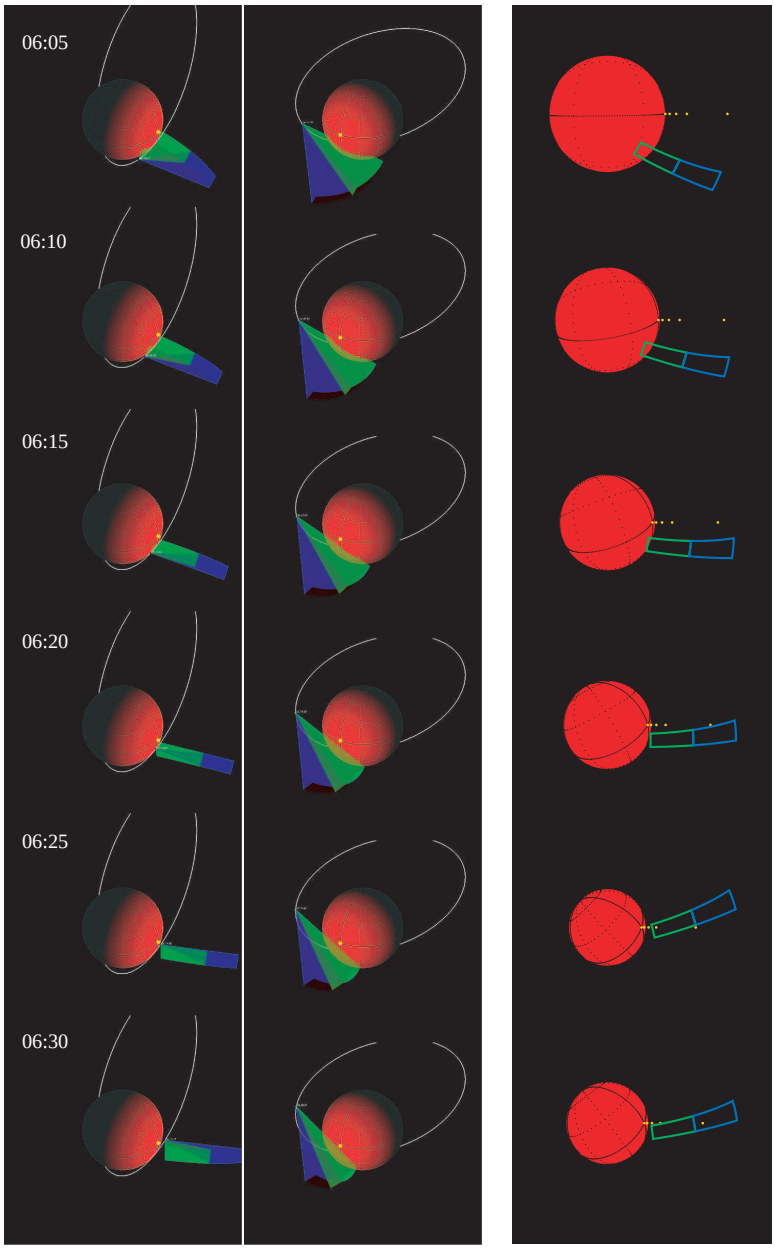

Figure 6.3: The viewing geometry of the NPD1 on June 2, 2004. The first and second columns are 3-D representations of the NPD1 FOV at different times seen from different view points. The green and blue fans are the Dir1 and Dir2 FOVs, respectively. The third column is a fish-eye projection of the same geometry (see text). The red sphere represents Mars and the green and blue rectangles show the Dir1 and Dir2 FOVs, respectively. The yellow dots are the directions toward points of 200 km, 500 km, 1000 km and 3397 km (=1R_M) above the subsolar point. From *Futaana et al.* (2006a).

The viewing geometry of the NPD1 is shown in Figure 6.3. The first and second columns are 3-D representations of the NPD1 FOV at different times along the Mars Express orbit (white ellipse) seen from different view points. The green and blue fans are the Dir1 and Dir2 FOVs and the yellow dots correspond to the subsolar point. The third column is a fish-eye projection

of the same geometry, i.e. an image as it would be seen by an observer located on the spacecraft with the boresight direction aligned toward the nadir. The red sphere represents Mars and the green and blue rectangles show the Dir1 and Dir2 FOVs, respectively. The yellow dots indicate the directions toward points of 200 km, 500 km, 1000 km and 3397 km (=1R_M) above the subsolar point.

Figure 6.4 shows measurements from the NPD1 sensor. The first and second panels from top are TOF spectrograms of Dir1 and Dir2, respectively. The right axis gives the corresponding energy per atomic mass 1 amu. Intense ENA signals with TOF less than 400 ns, corresponding to ⩾200 eV, are seen. The third panel shows the count rate of the Dir1 and Dir2 integrated over the TOF from 124.5 to 387 ns, which corresponds to the energy range 0.34-3.2 keV/amu.

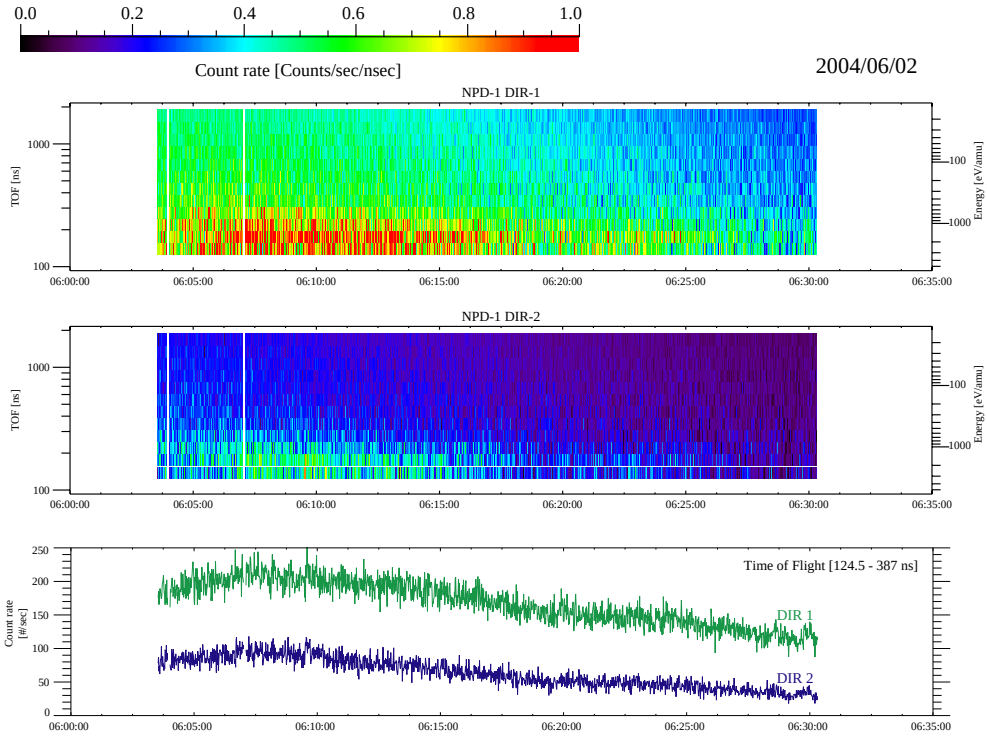

Figure 6.4: The NPD measurements between 06:03 and 06:31 UT on June 2, 2004. The first and second panels are TOF spectrograms of the Dir1 and Dir2, respectively. The right axis gives the corresponding energy per mass. The third panel shows the count rates of the Dir1 and Dir2 integrated over the TOF range of 124.5-387 ns (0.34-3.2 keV/amu). From *Futaana et al.* (2006a).

Figure 6.5 shows the TOF spectra of the NPD1/Dir1 averaged over the time periods 06:10-06:15 and 06:25-06:30 UT on June 2, 2004. The peak appears at an energy of ~1.5 keV/amu.

The total ENA count rate decreased as the spacecraft moved away from Mars (Figure 6.4). As seen in Figure 6.3, the FOVs of the NPD1/Dir1 and Dir2 covered the subsolar region during the observations.

The typical integrated count rate was ~200 counts/s (Figure 6.4). The random correlated count (a background level), is estimated to be ~0.48 counts/s per 1-ns bin from the spectrum (dashed line in Figure 6.5), which corresponds to ~130 counts/s in TOF range 124.5-387 ns. The effective ENA signal is then ~70 counts/s. Using the geometrical factor of the instrument ($G_0 \cdot \epsilon \sim (9.78 - 17.1) \times 10^{-5}$ cm^{2}sr for 0.7-1.3 keV hydrogen atoms, Chapter 5), the ENA differential flux, J, is calculated as J =(4-7)×10^5 cm^{-2}sr^{-1}s^{-1}, assuming the observed ENAs are

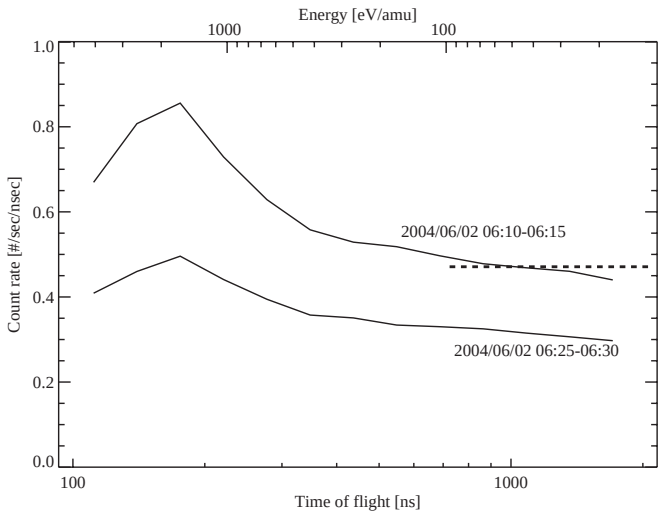

Figure 6.5: TOF spectra of the NPD1/Dir1 obtained during the time period 06:10-06:15 and 06:25-06:30 on June 2, 2004. The dashed line, 0.48 counts/s per 1-ns bin, depicts the background level of the period 06:10-06:15. From *Futaana et al.* (2006a).

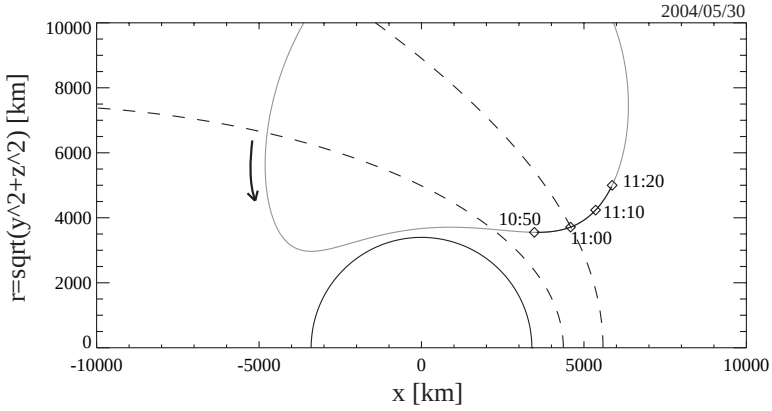

Figure 6.6: The trajectory of Mars Express (Orbit 456) in the same format as in Figure 6.2. From *Futaana et al.* (2006a).

hydrogen.

Another example of a similar NPD observation is discussed below. The observation was conducted on May 30, 2004. The orbit and the FOVs geometry are shown in Figures 6.6 and 6.7, respectively. They are almost the same as in the previous example from June 2. Figure 6.8 shows the NPD1 measurement. Instead of a gradual decrease of the count rate as in the previous example, NPD observed a sharp decrease in the count rate at ~11:03 UT within a time scale of the order of 1 minute. Figure 6.9 shows the TOF spectra at 10:56-11:00 (before the decrease) and at 11:12-11:16 (after the decrease). Their shapes are very similar to those obtained on June 2 (Figure 6.5).

Another characteristic signature is a short enhancement in the ENA count rate, observed at around 11:10 UT. Since the FOV pointed at the subsolar region and the TOF spectrum of these enhanced ENAs was almost the same as that observed before the sharp decrease, they probably originated from the same source and reflect a reconstruction of the interaction region (see Section 6.1.3).

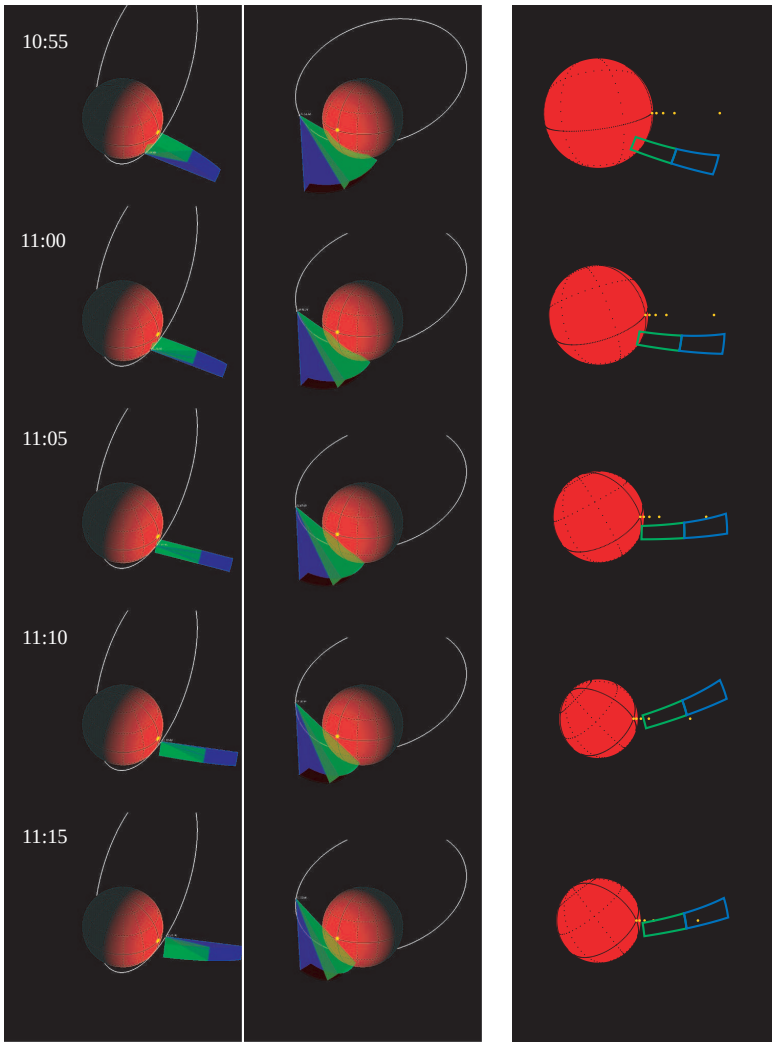

Figure 6.7: The viewing geometry of the NPD1 on May 30, 2004. The format is the same as in Figure 6.3. From *Futaana et al.* (2006a).

We searched through all of the TOF spectrograms obtained by the NPD1 between May 24, 2004, and July 1, 2004, when the trajectories and the attitude of the Mars Express were nearly the same, which means almost the same vantage points and observation directions. A total of 38 orbits were available, and the NPD observed an intense ENA flux in 36 cases. We used all the TOF spectrograms such as Figures 6.4 and 6.8 to divide the observations into two categories. The sharp changes in an ENA flux were observed in 23 orbits (64%), and the gradual decreases (i.e., no sudden change of an ENA flux) were seen in 13 orbits (36%).

6.1.3 Discussion

The ENA flux depends strongly on the position of the satellite, even though the FOVs of the NPD were always viewing toward the subsolar region. This observational fact can be explained in terms of a highly directional ENA emission around the subsolar region, i.e. a subsolar ENA jet (or cone). Figure 6.10 is a schematic representation of a concept of the subsolar ENA jet. Such an ENA flux can be detected when the sensor is within this ENA jet (case (a) in the

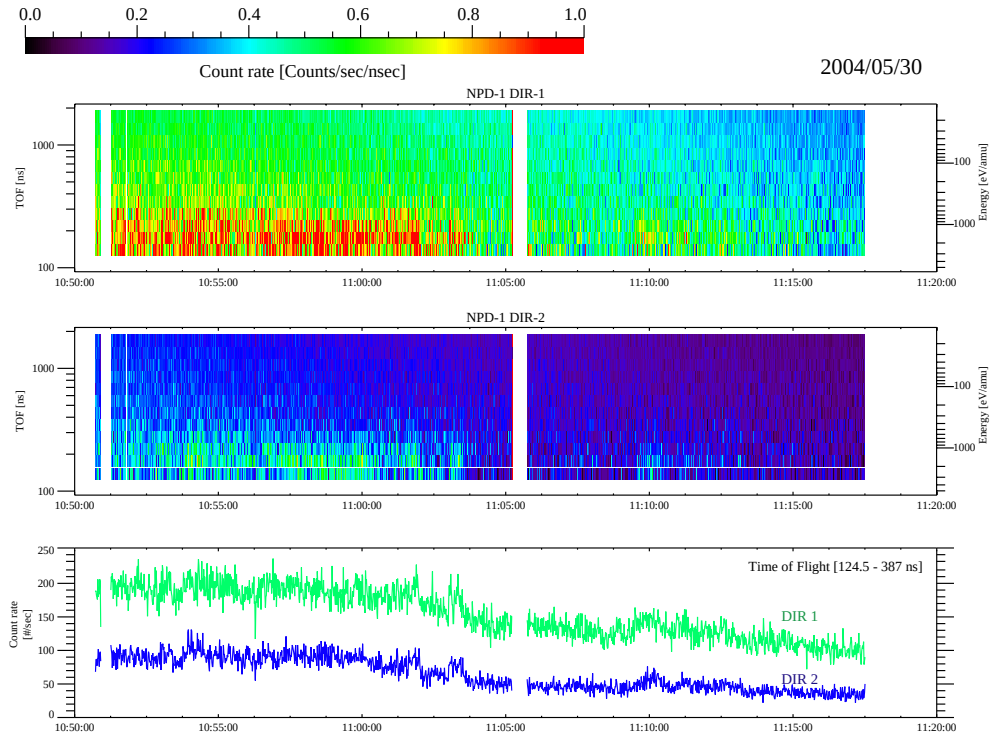

Figure 6.8: The NPD measurements recorded between 10:51 and 11:18 UT on May 30, 2004. The format is the same as in Figure 6.4. From *Futaana et al.* (2006a).

figure). As soon as the spacecraft leaves the jet (case (b) in the figure), the ENAs cannot be detected even though the instrument FOV covers the source region.

The region of the ENA generation and direction of ENA movement point to three possible origins, namely solar wind protons and ENAs back-scattered from the Martian exosphere (*Kallio and Barabash*, 2001), shocked solar wind protons charge-exchanged on the Martian hydrogen corona (*Holmström et al.*, 2002), and planetary hydrogen photo-ionized, accelerated and charge-exchanged in the exosphere (*Lichtenegger et al.*, 2002). These processes are all related to interactions between the solar wind and the Martian upper atmosphere, and the ENA generation is expected to be large in the subsolar region because the solar wind can penetrate to much lower altitudes, reaching altitudes with high neutral gas density.

Since back-scattered ENAs are expected to be emitted isotropically from the Martian upper atmosphere (*Kallio and Barabash*, 2001; *Futaana et al.*, 2006b), they are unlikely to result in the ENA jet generation.

We consider now shocked solar wind just above the IMB, which is defined as an envelope of the void of the solar wind (*Lundin et al.*, 2004). There the stream lines of the shocked solar wind are highly deflected, and an ENA jet can be formed by charge exchange with the dense atmosphere. This scenario is possible because the solar wind can actually reach altitudes as low as 300 km in the subsolar region, as evidenced by the recent results of the ASPERA-3 ion mass spectrometer (*Lundin et al.*, 2004). The size of the source, i.e., a region of the most intense ENA production by shocked solar wind charge exchanged with the exosphere, must be at least on the order of the scale height of the hydrogen, i.e., several hundred km. ENA production from the shocked solar wind is described in *Kallio et al.* (1997) and *Holmström et al.* (2002) in more detail. However the proton flux model has a singularity at the subsolar point, and cannot

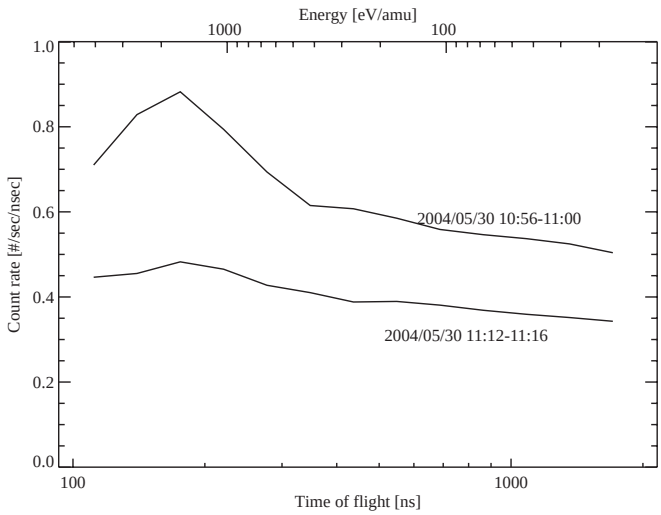

Figure 6.9: TOF spectra of the NPD1/Dir1 averaged over the time interval 10:56-11:00 and 11:12-11:16 on May 30, 2004. From *Futaana et al.* (2006a).

be used to simulate ENA productions there, while the ENA generation must be highest in the subsolar region.

The accelerated planetary protons, originated from exospheric hydrogen photo-ionization and then converted to ENAs through the charge exchange process, have been considered by *Lichtenegger et al.* (2002). Planetary protons transported to the magnetosheath are accelerated by the convection electric field. Such accelerated protons could form an ENA jet after they experience charge exchanges in the subsolar region. Somewhat similar jets of planetary oxygen ENAs were predicted by *Barabash et al.* (2002). *Lichtenegger et al.* (2002) concluded that the ENA flux produced by this mechanism would be as high as the shocked solar wind ENAs. These authors also compared the energy spectra of these two mechanisms, and concluded that careful analysis of the spectra can distinguish the accelerated planetary ENAs from the shocked solar wind ENAs. In the present instance it is difficult to discuss the spectra in detail because they are too coarse due to the observation mode employed.

The observation geometry over all 38 events was rather similar in the MSO coordinate system. During the observations, the NPD FOV plane was close to the ecliptic plane. Therefore, only a limited range of angles ($< 30°$) relative to the ecliptic plane was sampled, and we cannot thus conclude whether we are dealing with a jet or a cone. Existing MHD models of the solar wind – Mars interaction (e.g. *Tanaka and Murawski*, 1997) provide a rather cylindrically symmetric pattern of the solar wind proton flow around Mars, and thus one would be in favor of the conical ENA jet. On the other hand hybrid models (e.g., *Brecht*, 1997b) show asymmetric features of the proton flow in association with the interplanetary convection electric field direction ($E = -V_{SW} \times B_{IMF}$, where V_{SW} and B_{IMF} are the solar wind velocity and the interplanetary magnetic field, respectively). The analysis has not taken the electromagnetic direction into account because of the absence of a magnetometer aboard Mars Express. However, since the observations cover a long period (~40 days), the distribution of the IMF direction can be considered to be random. Therefore, a conical ENA jet geometry is rather plausible, and Figure 6.10 is considered as a cross-section of the axi-symmetric geometry of the conical ENA jet.

The ENA count rate was found to decrease very rapidly (~several tens of seconds) in two thirds of the orbits, as shown in Figure 6.8. This implies that the source of the ENA jet/cone

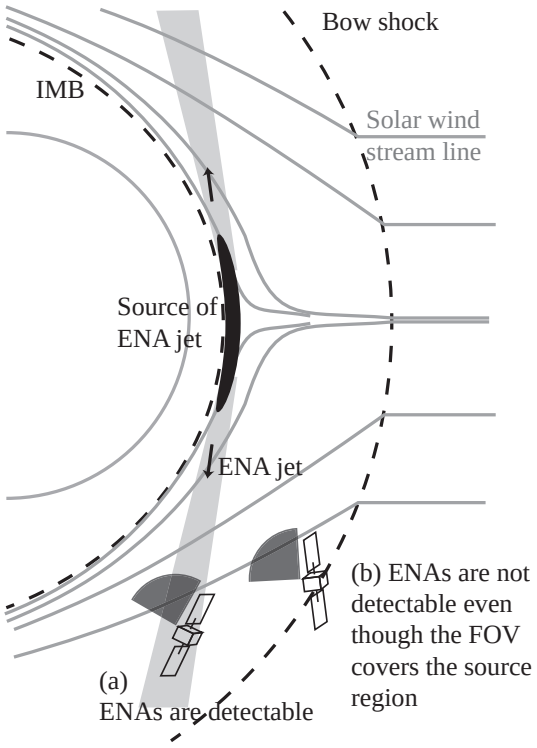

Figure 6.10: Geometry of the subsolar ENA jet. The subsolar jet can be detected when the sensor is within it (case a). As soon as the spacecraft leaves the jet (case b) the ENAs cannot be detected even though the instrument FOV covers the source region. From *Futaana et al.* (2006a).

should be confined in space. We do not have a clear explanation as to what controls its size and directionality. Existence of such a compact and directional ENA jet also raises a question with regard to the validity of current MHD models. In all MHD models, the subsolar point is a stagnation point with almost zero bulk velocity. The associated ENA emissions should be rather isotropic due to the high temperature of shocked solar wind. However the observations indicate highly anisotropic emission with solar wind energy. MHD models may not be valid in describing the Martian subsolar region, because the system size becomes comparable to the proton gyro-radius there. Therefore, one needs more detailed 3-D hybrid models dedicated particularly to this domain in order to investigate the physics of the sharp decrease of the ENA signal.

What causes the short bursty enhancements in the ENA signal such as were observed at 11:10 UT, May 30 (Figure 6.8)? These ENA bursts cannot be explained by changes in the observational geometry, which remained the same during the observation. The jet dynamics are discussed in Section 6.2.

6.1.4 Summary

The NPD, an ENA sensor of the ASPERA-3 experiment on board Mars Express, detected intense fluxes of ENAs emitted from the subsolar exosphere. Typical ENA fluxes were (4-7)$\times 10^5$ cm^{-2}sr^{-1}s^{-1} in the energy range of 0.3-3 keV/amu. These ENAs are likely to be generated through charge exchange between the shocked solar wind protons and the Martian exosphere in the subsolar region, where the solar wind plasma penetrates to its lowest altitude

and where the neutral gas density is high.

As the satellite moved away from Mars, the observed ENA signal decreased even though the subsolar region remained within the NPD FOV. These decreases are gradual in one third of the orbits, while the decreases are very sharp (on a scale of a few tens of seconds) in two thirds of the orbits in question. This behavior can be explained if the spacecraft crossed a spatially constrained ENA jet/cone, as shown in Figure 6.10. Such anisotropic ENAs indicate that the solar wind flow around the subsolar region is also highly anisotropic, and this cannot be explained in the frame of the existing MHD models.

6.2 Observations of the Martian subsolar ENA jet oscillations

6.2.1 Introduction

The initial ASPERA-3 / NPD observations revealed that an ENA flux is emitted anisotropically from the subsolar region of Mars (*Futaana et al.* (2006a); Section 6.1). This section reports on observed oscillations of the ENA jet (*Grigoriev et al.*, 2006).

The data set, used in this analysis, consists of 38 orbits recorded by the NPD1 detector during the period May 24 - July 1, 2004 when the orbit and the attitude of Mars Express were optimal to investigate ENA emissions from the subsolar region of Mars. During this observation period the NPD sensor was switched into BIN mode. Full spectrum accumulation time was 1 s.

The basic characteristics of the ENA jet/cone established earlier (see Section 6.1) are as follows: averaged energy ~1.5 keV/amu, energy range is from 0.34 to 3.0 keV/amu. ENA differential flux is estimated to be j~(4-7)$\times 10^5$ $cm^{-2}sr^{-1}s^{-1}$.

6.2.2 Observation geometry

A typical Mars Express spacecraft orbital position (orbit 499, on June 11, 2004) during the measurement cycle is shown in Figure 6.11. The orbital period during this time was about 6.5 hr. The NPD operation started ~20 minutes after the periapsis and lasted for ~30 minutes. The sensors were operational while Mars Express was moving on the dayside outbound through the magnetosheath region through the bow shock and the region of undisturbed solar wind. Figure 6.11(a) is in the cylindrical coordinate system, described in Section 6.1.2, scaled in Martian radii (R_M). Dashed curved lines show the MPB and the bow shock locations modeled by *Vignes et al.* (2000). A dotted line shows the Mars Express trajectory during the observation period. The orbital part where the NPD sensor was switched on (11:50 – 12:17 UT) is depicted as a thick line; diamonds along this line represent time intervals of 10 min. Figure 6.11(b) shows the spacecraft location projected on a YZ_{MSO} plane. Mars Express crosses the ecliptic plane, shown by a dot-dashed line, at the beginning of every measurement session.

Mars Express was nadir-pointing during the observations near the perigee. The plane where ASPERA-3 was mounted was perpendicular to the nadir, facing the planet (Figure 6.1). In this configuration, the symmetry axis between the channels Dir0 of the NPD1 and NPD2 detectors was pointing towards the center of Mars.

The NPD1 FOV was covering the subsolar region of Mars. Figure 6.12(a) shows the sensor observation geometry. In this plot, the spacecraft-centered ecliptical coordinate system of the epoch 2000 is employed. The northern hemisphere (positive ecliptic latitudes) is shown on the left side of the figure and the southern hemisphere (negative ecliptic latitudes) is shown on the right side. The vantage point is the origin of the coordinate system. The Martian limb is

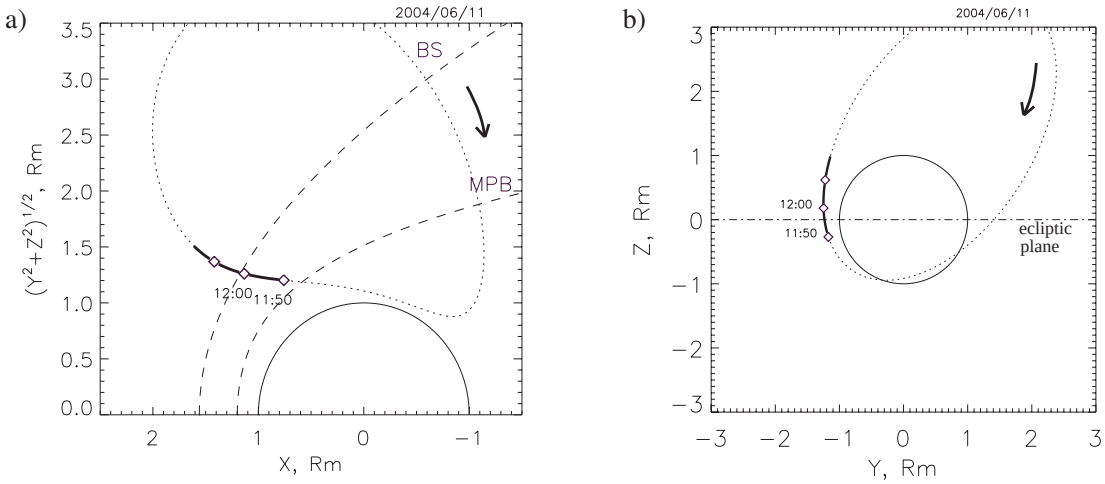

Figure 6.11: a) Mars Express trajectory on June 11, 2004 (orbit 499). The cylindrical coordinate system based on the MSO reference frame is used. The thick line depicts the measurement interval. Dashed lines are the modeled bow shock (BS) and magnetic pileup boundary (MPB, *Vignes et al.*, 2000). b) Mars Express trajectory, projected in YZ_{MSO} plane (seen from the Sun direction). Adapted from *Grigoriev et al.* (2006).

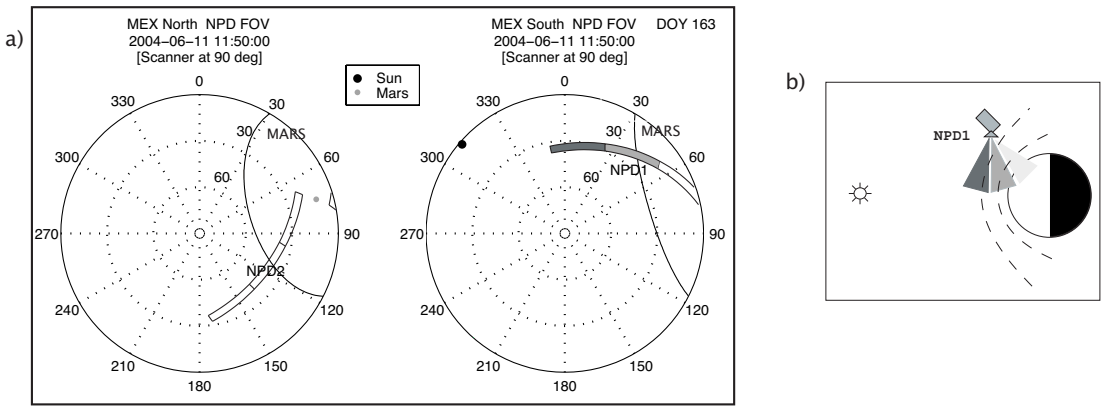

Figure 6.12: a) NPD sensor observation geometry in the spacecraft-centered ecliptical coordinate system taken for the epoch 2000. The Martian limb is shown by an ellipse. The elongated fans correspond to both NPD FOVs. The black and dark grey polygons depict viewing directions Dir1 and Dir2, respectively, of the NPD1 sensor. The filled dots show the location of the centers of the Sun (black) and Mars (light grey). b) A sketch (not in scale) emphasizes Mars Express location and the viewing direction of the NPD1 during the measurements. The black and dark grey numbered sectors correspond to the NPD1 channels Dir1 and Dir2 FOVs. A sun symbol shows the Sun direction. From *Grigoriev et al.* (2006).

shown by an ellipse. It is partially visible on both hemispheres. The elongated fans show the NPD1 and NPD2 FOV. The black and dark grey polygons depict viewing directions Dir1 and Dir2, respectively, of the NPD1 sensor. The filled dots show the location of the centers of the Sun (black) and Mars (light grey). Figure 6.12(b) represents a sketch that clarifies the NPD1 observation geometry, emphasizing the sensor's location and attitude during the measurement. The black and grey sectors correspond to the detector channels Dir1 and Dir2 FOV. These channels were observing the Martian subsolar region and therefore suited for investigation of subsolar ENA jet emission.

6.2.3 ENA jet fluctuation observation

The energy-time spectrograms obtained by the sensor channels Dir1 and Dir2 are shown in Figure 6.13(a, b). The data was recorded during 11:50-12:17 UT on June 11, 2004 (orbit 499). The count rate is color coded. The color bar, on the right side, is scaled in counts/read-out/ns or counts/s/ns, assuming 1 ns TOF resolution of the sensor's electronics. The left vertical axis gives the TOF of particles in ns. The right vertical axis is the energy scale, assuming particles as hydrogen. The jet peak energy is ~2.0 keV/amu in this case. One clearly sees oscillations of the ENA flux.

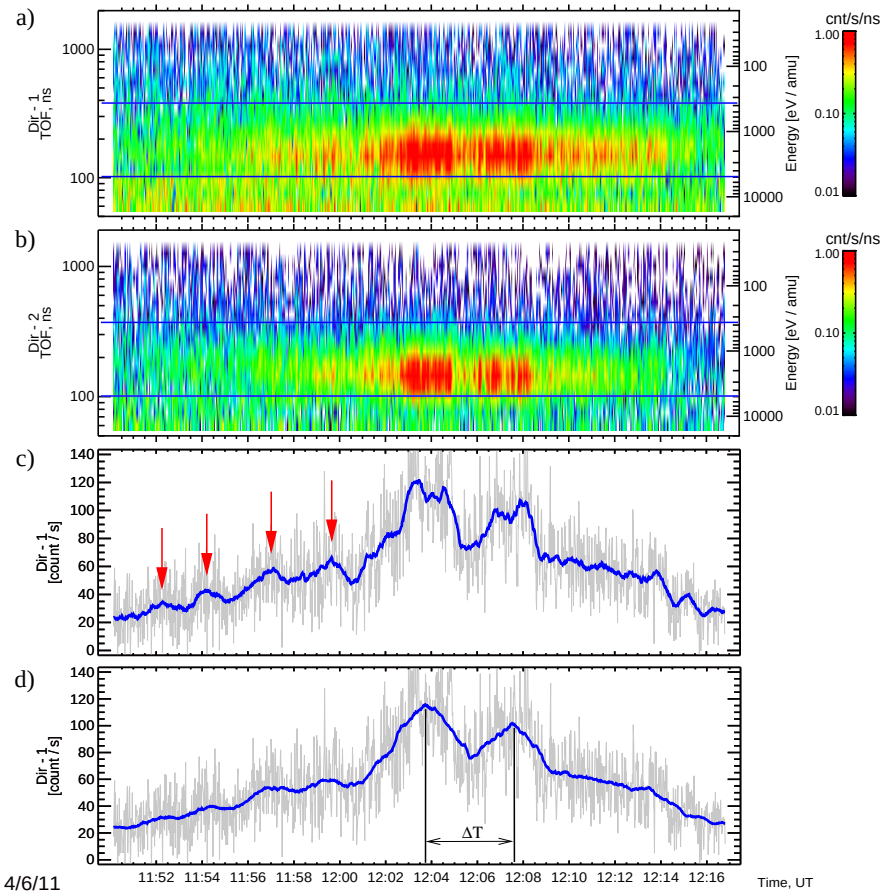

Figure 6.13: Panels a,b: TOF spectra of the NPD1 Dir1 and Dir2 channels. The corresponding energy is shown in the right axis assuming the mass 1 amu. Horizontal blue lines specify the TOF window ξ = 99 – 374 ns, which covers the ENA jet energy range. Panels c,d: integrated over the TOF window ξ correlated count rate. *Fast* variations are identified by red arrows. *Slow* variations are depicted by thin vertical black lines. Different low pass filter window is used: 40 s for panel c and 90 s for panel d. The peak-to-peak period is marked as ΔT. From *Grigoriev et al.* (2006).

In these panels, UV photon induced background noise has been subtracted from the spectra. As with any ENA instrument, NPD possesses a residual sensitivity to UV flux. This causes a background in the correlated count rate, which does not depend on the TOF. Therefore, to obtain the signal associated with ENAs only, we subtracted the UV-induced background, assumed to be equal to the count rate at the last TOF bin, where no ENAs are expected due to low sensitivity of the NPD sensor to low-energy ENA.

In order to investigate signal variations, we defined a TOF window ξ as follows: the ξ

consists of 6 TOF bins (99 – 374 ns), entirely covering the ENA jet energy range (0.34 - 5.1 keV/amu). The ξ window is marked by a pair of blue horizontal lines in panels (a) and (b).

Two panels, Figure 6.13(c, d), show the correlated count of the channel Dir1, integrated over ξ (grey line). Thick blue lines show the data, smoothed using the low-pass filter with 40 s (panel (c)) and 90 s (panel (d)) running averages.

As a general behaviour, the ENA jet intensity increases while the spacecraft enters the ENA jet region and decays as the spacecraft leaves the ENA jet region. At the same time, some periodic fluctuations of the signal appear during the first 10 - 12 minutes after the measurements start. The zoomed-in view of these signal variations is shown in Figure 6.14. Arrows emphasize the peaks. The peak-to-peak period is 150 - 180 s with the FWHM ~50 s. The FWHM of a peak is calculated between the peak maximum and a background reference level, which is estimated separately for each peak. The ENA jet long-term intensity variation is thus taken into account. The variations of the signal reach 30% of the maximum value. These are referred to as *fast* oscillations.

As the spacecraft moves further, another type of signal variation occurs. Two high-intensity peaks appear at approximately 12:04 and 12:08, as seen in Figure 6.13. These variations are different from the *fast* oscillations described earlier. The peak-to-peak period, ΔT, is ~270 s, and the FWHM is about 110 - 140 s. The variation depth is about 50%. This type of long-term signal variation is referred to as a *slow* variation.

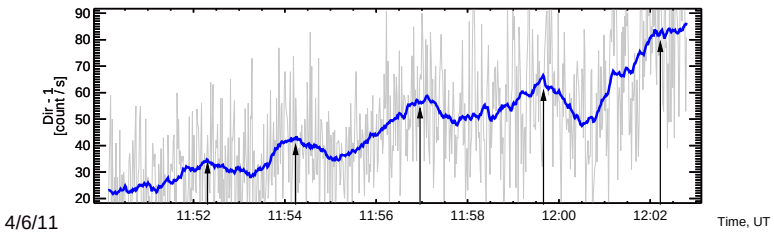

Figure 6.14: Typical flux variations due to *fast* oscillations. The picture is in the same format as Figure 6.13(c). The black arrows show the peaks of the *fast* oscillations. From *Grigoriev et al.* (2006).

The peak-to-peak times of the *slow* variation events do not depend on the window size of running average taken in a range of 20 to 120 s. That is reasonable, since a shorter running window retains statistical fluctuations while a longer than 120 s window smoothes out the oscillations. In case of the *fast* variations, changes in the steps of the running average length within a range of 20 to 50 s do not affect the periodicity of the variations.

6.2.4 Statistics on the intensity variations

Criteria for selecting *fast* and *slow* variation events are as follows: In case of *fast* oscillations signal depth amplitude variation must reach at least 20 - 30%. The number of peaks observed during an observation period is at least 3, with ΔT unchanged. Peak-to-peak period ΔT varies in the range of 40 - 180 s. In the case of *slow* variations, signal depth amplitude change is ~50-80%. The number of peaks detected during an observation period is 2 or more, and ΔT is ~300 s ±15%.

Figure 6.15 shows the statistical distributions of the peak-to-peak times for two different groups of ENA jet flux intensity variations. The histogram bin steps are equal to 20 sec and 60 sec for *fast* and *slow* oscillations, respectively. Each distribution is normalized to the maximum of the occurrence.

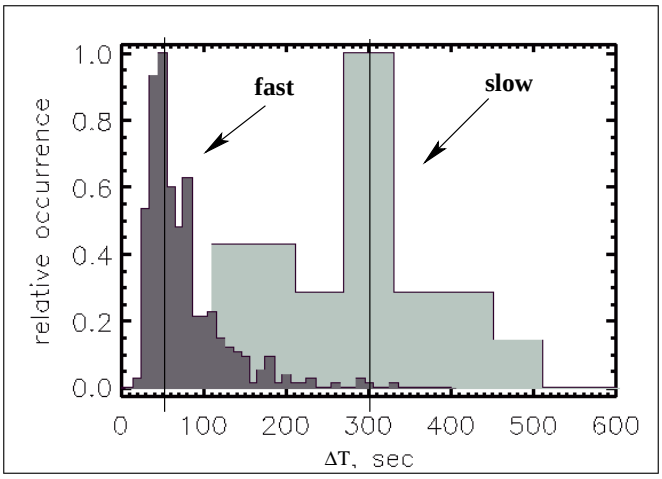

Figure 6.15: The peak-to-peak ΔT period distributions of both *fast* (dark-grey colored) and *slow* (light-grey colored) groups are shown. From *Grigoriev et al.* (2006).

The *fast* and *slow* oscillation distributions are shadowed by dark grey and light grey, respectively. The peak of the *fast* oscillation distribution is at ~50 sec and FWHM is ~30 s. These variations are periodic and are detected in every orbit. The signal peak-to-valley ratio can reach 20 - 30% of the maximum flux intensity. The peak of the *slow* oscillation distribution is at ~300 s and FWHM is ~30-80 s. The variations of the signal reach 60 - 80% of the maximum value. The *slow* variations are found in 15 of 38 orbits.

The distribution of FWHM of the signal peaks in the case of *slow* ENA jet variations is plotted in Figure 6.16. The histogram bin step equals to 40 s. Evidently, the majority of the detected peaks has FWHM of ~160 s. The shape and location of the peaks are highly variable from orbit to orbit. The number of peaks detected in one orbit is generally two – they occur in 30% of all orbits. Multiple peaks (three or more) appear only in 10% of the orbits.

Figure 6.17 shows the peak occurrence dependence on the angle between the $-Y$-axis and the position of the Mars Express spacecraft, defined as φ (positive if counting clockwise). There is no preferable direction of the intensified ENA flux. The peaks are detected with equal probability from different vantage points within the NPD observation region.

6.2.5 Discussion

NPD detected intense ENA fluxes with energies in the range 0.3-3.2 keV/amu when the FOV of NPD was pointed toward the subsolar region (*Futaana et al.*, 2006a). In all cases, the ENA flux intensity variations were detected. These variations can be categorized into two modes, namely *fast* and *slow* variations. The *fast* variations occur with a typical period of 28.5-200 sec and are detected on each orbit. The *slow* variations have a period of 143-500 sec and occur in 40% of the cases. We now discuss the possible generation mechanisms of the ENA jet intensity variations.

The MGS magnetometer team (*Espley et al.*, 2004) reported low-frequency (period ~25 s) magnetic field oscillations in the different plasma regions of Mars. One possible interpretation of the source of oscillations on the dayside of the magnetosheath is mirror mode instabilities. The important characteristic of the mirror modes is an anticorrelation between the magnetic field strength and the plasma density. Therefore, these kinds of magnetic field oscillations can represent one of the mechanisms of ENA jet *fast* oscillation generation. This is because the

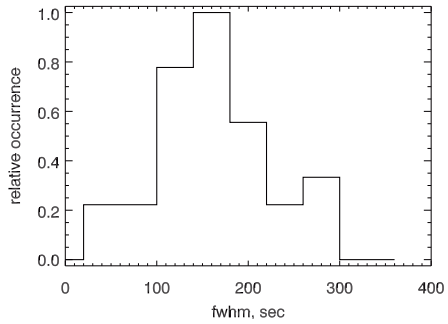

Figure 6.16: The distribution of FWHM of peaks in case of *slow* ENA jet variations. FWHM of a peak is expressed in seconds (X-axis). Y-axis marks the relative occurrence of cases. The histogram binning size is 40 s. From *Grigoriev et al.* (2006).

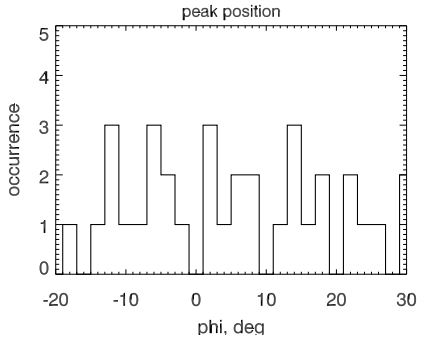

Figure 6.17: Location of the spacecraft during ENA peak detection and its occurrence is shown. Angular distance between the $-Y$-axis and the Mars Express spacecraft position is shown by φ (see text for details). φ is in degrees (X-axis). Y-axis marks the peak occurrence. From *Grigoriev et al.* (2006).

change of plasma density in the magnetosheath is reflected by the change in ENA production-rate through the change in the occurrence of the charge exchange process. However the predominant period of the main fluctuation of the magnetic field seems to be shorter than the period of the ENA *fast* oscillations (28.5-200 sec), derived from the NPD observations. The mirror-mode instability is thus a less plausible mechanism to explain the *fast* oscillations.

Another possible mechanism is the global oscillations of the IMB. *Futaana et al.* (2006c) discussed an example of a global response of the Martian plasma environment to an interplanetary shock. They used an ENA jet observation that shows an extremely intensive flux followed by a sudden decrease of the flux intensity. Using simultaneous plasma data, they concluded that the decrease is caused by the fast IMB displacement due to an interplanetary shock. They also reported oscillations of the ENA jet flux (period ~1 min) just after the abrupt decrease, regarded in this study as *fast* oscillations. However, to the best of our knowledge, there have been neither theoretical nor experimental reports on global oscillations of the Martian plasma obstacle.

Two peaks in the ENA jet *fast* oscillation distribution are apparent in our data set: ~50 and ~80 sec (Figure 6.15). Remarkably, these periods coincide with the typical time periods of the electron flux intensity oscillations observed by the ELS / ASPERA-3 instrument (between 50 and 100 s, *Winningham et al.*, 2006). Such oscillations of electron fluxes have been observed in different regions of Mars, but the dayside magnetosheath is one of the most active regions. The frequency range encompasses the typical O^+ ion gyro-frequency in the magnetosheath (*Espley et al.*, 2004). Cyclotron instability of the newly created planetary ion beams generates Alfvén waves with a frequency close to the local gyro-frequency (in the spacecraft frame of reference). The associated plasma density variations result in ENA flux oscillation. While it seems that the observed *fast* ENA oscillations are connected to the detected electron flux oscillations (plasma is quasi-neutral), it is not known whether the wave energy is sufficient to cause 20-30% plasma density variations.

The observed *slow* variations have a characteristic peak-to-peak time ~300 s. As shown in Section 6.2.4, the number of peaks in the case of *slow* ENA flux variations detected in one orbit is typically 2. It is rare for more peaks to occurs. Such differences between the ENA jet flux fluctuation signatures imply that these two types of fluctuations have different production

mechanisms.

It is important to emphasize that the observed variations can reflect either temporal variations of the generation region or spatial structure of the jet itself. Because of the spacecraft motion we cannot resolve this ambiguity. In the case of the temporal jet variations, such behavior can be explained by bursty intensification of the ENA source as a result of the temporal changes in the upstream conditions, mostly the solar wind dynamic pressure. *Holmström et al.* (2002) investigated the deflected solar wind ENA flux dependence on the solar wind and exosphere parameters. They concluded that the exospheric density is the most important parameter controlling the ENA flux. The IMB position is dependent on the exospheric density. Hence, if the ENA generation region moves closer to the planet, then the solar wind ions can reach denser part of the Martian exosphere, creating higher ENA flux.

The waves on the IMB resulting from Kelvin-Helmholtz instability could, in principle, cause the observed oscillations. However *Penz et al.* (2004) considered the development of the Kelvin-Helmholtz instability on the Martian boundary in one-fluid approximation and concluded that the subsolar ionopause of Mars is stable with respect to the Kelvin-Helmholtz instability.

The vantage points at the moments when the NPD1 sensor detected peaks of *slow* ENA jet intensity variations are distributed uniformly over the whole observation region, as shown in Figure 6.17. Meanwhile, the observation period is long (~40 days) and therefore the distribution of IMF direction and magnitude, as well as solar wind parameters, can be considered random. It is very likely that the ENA generation region is very sensitive to the exterior and is changeable under unsteady solar wind dynamic pressure and IMF direction. Unfortunately, lack of undisturbed solar wind measurements during the NPD observations (single point measurements) as well as *in situ* IMF measurements prevent us from making such a conclusion.

There is also a certain possibility that the *slow* variations of the ENA jet represent spatial structures of the jet itself. The majority of the detected peaks have the FWHM about 160 s, corresponding to 4-5° of an angular width of the ENA stream, taking into account the spacecraft velocity ~3 km/s and the distance to the generation region $\leqslant 2R_M$. If we assume existence of ENA "*sub-jets*" with an angular width of 4-5°, the observed *slow* variations can possibly be explained. This concept is shown in Figure 6.18. Such ENA sub-jets are likely to appear if the ENA generation source under certain conditions becomes patchy. What can cause the ENA generation source patchiness? Existence of small-scale magnetic field structures called magnetic flux ropes (e.g., *Russell and Elphic*, 1979; *Elphic and Russell*, 1983) is one possibility for such effects. The existence of these flux ropes at the Martian ionopause has been reported by *Vignes et al.* (2004). The magnetic character of the flux ropes at Mars appears chaotic. At the same time, these magnetic structures are stationary in time relative to the speed of the spacecraft. The width of the flux ropes is of the order of a few tens of kilometers. Most of the flux ropes have been detected at high solar zenith angles. A smaller number of flux ropes has been identified for solar zenith angles lower than 20° (*Vignes et al.*, 2004). Meanwhile, size of the region of the most intensive ENA generation was estimated to be ~6400 km (*Futaana et al.*, 2006c), i.e., within solar zenith angles lower than 40°. So, the existence of magnetic flux ropes is likely to affect the transport of planetary protons to the magnetosheath and consequently, the ENA production. Again, the mechanism of ENA formation through charge exchange of accelerated protons in the magnetosheath (*Lichtenegger et al.*, 2002) is one of the most probable ENA jet generation mechanisms (*Futaana et al.*, 2006a).

More detailed study of the ENA jet behavior should be the subject of future investigations. The next step would be to study the morphology of the ENA jet as a function of the upstream

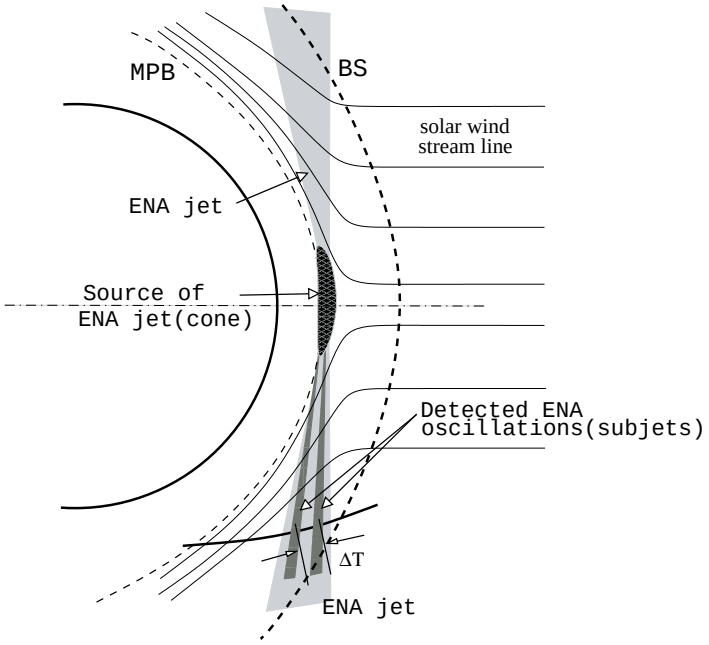

Figure 6.18: The schematic illustration of spatially resolved ENA sub-jets. From *Grigoriev et al.* (2006).

conditions such as the solar wind dynamic pressure and IMF direction. But to resolve the nature of the ENA jet oscillations and related dynamics of the Martian induced magnetosphere the key investigation would be multipoint measurements at Mars. These would allow us to make correct correlations of *in situ* measurements of the local plasma parameters and remote observations of the ENA flux emerging from the interaction region.

6.2.6 Summary

We presented observations of the Martian subsolar ENA jet intensity oscillations, made by NPD. We categorized the flux intensity variations into two groups. First group is *fast* oscillations with a characteristic peak-to-peak time ΔT ~50 s. These flux variations possess a periodic structure and are observed in all orbits. The second group is *slow* variations, whose time scale is of the order of ~300 s. These variations appear in 40% of all ENA jet observations.

The *fast* oscillations are possibly formed by low frequency ion waves (period ~50-100 sec) at the subsolar region. The observed period correlates with electron oscillation period detected by ELS which, in turn, is close to the oxygen gyro-period. However the energetics of the process is not clear.

The origin of the *slow* variations is a mystery. They might be related to temporal variations of the solar wind dynamic pressure. On the other hand, the *slow* oscillations can also be explained by a sub-jet structure as shown in Figure 6.18. Such structures could possibly appear due to the existence of magnetic flux ropes in the Martian ionosphere.

6.3 Other results by the ASPERA-3 / NPD

6.3.1 Global response of Martian plasma environment to an interplanetary structure: From ENA and plasma observations at Mars

The paper by *Futaana, Barabash, Grigoriev et al.* (2006c) presents a case study of the subsolar ENA jet (*Futaana et al.*, 2006a). The detailed investigations of the subsolar ENA jet would advance the understanding of the dynamics involved in the interaction between the solar wind and Mars. The event considered was interpreted as a global response of the Martian plasma environment (in a time scale of ~10 s) to a change in the solar wind conditions.

The measurements were conducted by the NPD sensor on June 7, 2004. The NPD data is treated together with *in situ* data of the ELS and IMA spectrometers. Figure 6.19 shows the NPD TOF spectrum (upper panel) and the ELS electron energy spectrum and fluxes (middle and lower panels), respectively. Three notable signatures of this unique event (at 13:58 UT) are discussed. The ENA flux is ~5 times higher than the nominal subsolar ENA jet flux of 4-7×10^5cm^{-2}sr^{-1}s^{-1} (*Futaana et al.*, 2006a). The jet outer boundary is very abrupt. It took ~10 s for Mars Express to cross this boundary, while the typical time scale is about 1 min. Additionally, there are three quasi-perioduc flux enhancements observed right after the spacecraft left the jet region.

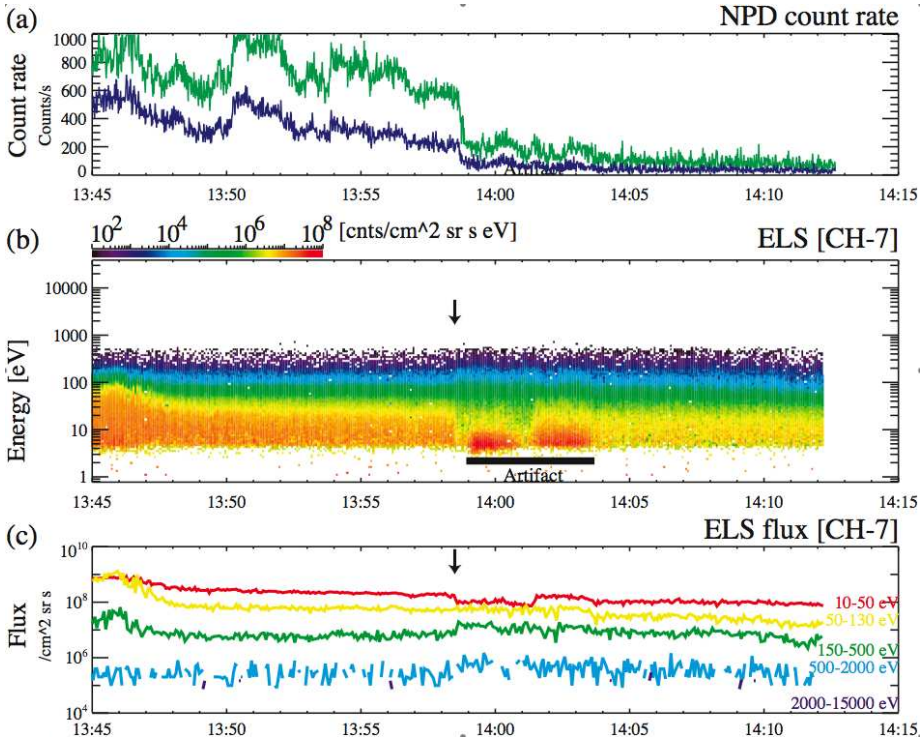

Figure 6.19: The observations from the NPD and ELS. Panel (a) is the count rate of the subsolar ENA flux integrated over the TOF window (50-1900 ns) for the directions Dir1 (green) and Dir2 (blue line) of the NPD1. Panel (b) shows the energy-time spectrogram observed by the ELS. Panel (c) shows the time series of counts within the energy range 10-50, 50-130, 150-500, 500-2000 and 2000-15000 eV from the ELS. The ENA flux is several times higher than the nominal subsolar ENA jet flux. Abrupt depletion of ENA fluxes occurred at 13:58:40 UT. Following are quasi-perioduc variations in flux observed right after the spacecraft left the jet region. Adapted from *Futaana et al.* (2006c).

This unusually high ENA flux can be interpreted as a result of a compressed Martian plasma obstacle. During this time interval, the Mars Global Surveyor (MGS) magnetometer recorded a strong increase of magnetic pressure inside the IMB. This means that the solar wind dynamic pressure outside the IMB increased by several times during this event, assuming that the magnetic field pressure in the induced magnetosphere region balances the incident solar wind dynamic pressure (*Crider et al.*, 2003). The BS and IMB locations, derived from the plasma spectrometers data, were much closer to the planet than the average locations (*Vignes et al.*, 2000).

The abrupt flux change is most likely to be caused by a quasi-perpendicular interplanetary shock, which led to a reconfiguration of the plasma obstacle shape and location, as illustrated in Figure 6.20. Consequently, the ENA jet generation region was relocated: it moved closer to the planet.

It has been suggested that the quasi-periodic ENA jet flux enhancements are due to a global vibration of the Martian plasma obstacle, caused by the interplanetary shock hit. Such vibrations can result in ENA flux variations as the ENA jet generation region displaces back and forth.

From the time difference between the changes of the Martian plasma obstacle and the ENA jet signal, the Martian subsolar ENA jet generation region size is estimated to be as large as $\sim 2R_M$.

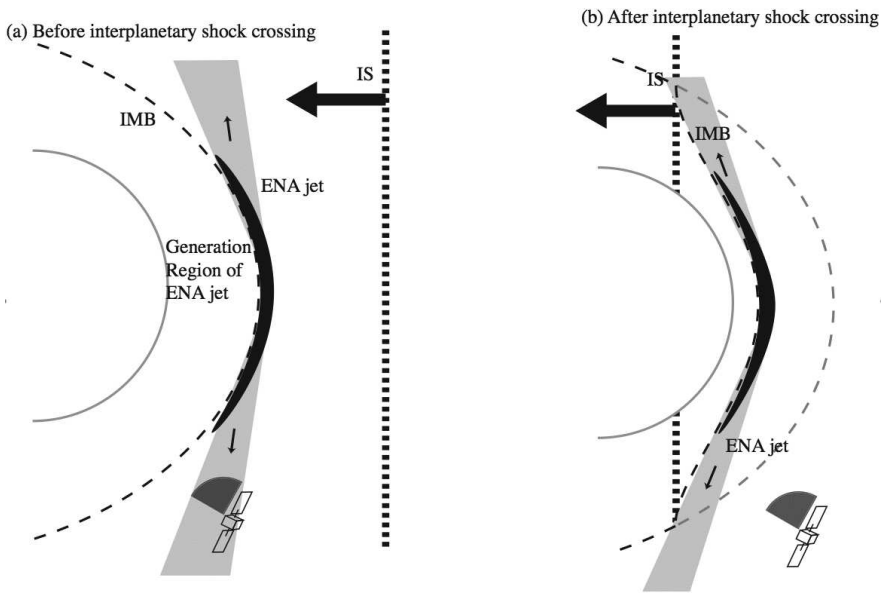

Figure 6.20: Illustration of an interpretation of the interplanetary shock interaction with the Martian plasma environment: (a) before and (b) after the shock crossing of the planetary ENA jet source. The source region of the subsolar ENA jet, which is very close to the IMB, was pushed toward the planet due to the high dynamic pressure of the interplanetary shock. The spacecraft went out of the subsolar ENA jet very quickly due to this reconfiguration of the Martian plasma obstacle. From *Futaana et al.* (2006c).

6.3.2 The Hydrogen Exospheric Density Profile Measured with ASPERA-3 / NPD

Galli et al. (2006c) discussed the exobase temperature and density of Mars during a period of

low solar activity, derived from the NPD measurements of Lyman-α limb emission from the exospheric hydrogen of Mars. These parameters are crucial for the models of atmospheric loss and ENA production (e.g., *Lichtenegger et al.*, 2002; *Barabash et al.*, 2002). The hydrogen exobase density and temperature were estimated to be $n_H = 10^{10}\mathrm{m}^{-3}$, and $T > 600$ K, respectively.

The analysis was based on the Lyman-α limb emission measurements at high altitudes. NPD was switched into the TOF mode during the measurements. The data obtained during the observation period (12:00 – 13:10 UT, on April 25, 2004) were integrated over 5 minutes intervals and a height of the UV-induced background in the TOF spectra for each measurement was retrieved. The NPD count rates, caused by UV photons, were converted into fluxes of UV emission of the neutral hydrogen, integrated along the line-of-sight through the Martian exosphere. The NPD sensor sensitivity to Lyman-α was calibrated using the all-sky UV map, based on the UV measurements by the Solar Wind Anisotropies (SWAN) experiment on the Solar and Heliospheric Observatory (SOHO) (NASA, 2006, *http://sohowww.nascom.nasa.gov*). Consequently, the non-planetary UV background was subtracted from the TOF spectra.

The measurements were interpreted by means of a numerical exosphere model, which yields a hydrogen density profile n_H(r) for a given exobase density and temperature. It is a one-dimensional Monte-Carlo model (*Wurz and Lammer*, 2003), for which the exobase density and temperature are the two free parameters. The model assumed an exobase location at 220 km (*Lichtenegger et al.*, 2006) above the surface, a fully thermalized hydrogen atom population at the exobase and a spherically symmetric distribution of neutral hydrogen with one single constant temperature. The modeled density profile was related to UV emission by means of a radiation transport equation. The UV emission was assumed to be entirely due to resonant scattering on hydrogen atoms.

The model was verified by evaluating the measurements by the Mariner 6 and 7 spacecraft (*Anderson and Hord*, 1971). The values of exospheric density and temperature derived with the Monte-Carlo model (*Wurz and Lammer*, 2003) were compared with results obtained by *Anderson and Hord* (1971). A good agreement within a factor of 2 was shown.

Afterwards, the model was used to evaluate the data obtained with the NPD sensor. A single hydrogen component exobase was assumed. The resulting exobase density of $n_H = 6\times10^9\mathrm{m}^{-3}$ was found to be 5 times lower and the temperature of T < 1000 K to be 2 times higher if compared with values derived by *Anderson and Hord* (1971). Figure 6.21 shows the measurements from both the NPD (from 2004) and Mariner 6 and Mariner 7 (from 1969) together with the modeled profiles. The difference can be explained either by different observation geometry or by asymmetry in the exobase due to high spatial variability (*Holmström*, 2006) or just by a generally thinner exobase.

So high exospheric temperature derived from the NPD measurements appears to be inconsistent with exospheric temperatures (<250 K) inferred from aero-braking maneuvers of recent spacecraft like Mars Odyssey (*Lichtenegger et al.*, 2006). This difference can be explained by the presence of a cold bulk component and a tenuous extended hot population of atoms that have been heated up in photo-dissociation and dissociative recombination processes (*Lichtenegger et al.*, 2006). If the two-component exobase approach is valid, then it is possible to assume that the Lyman-α airglow measurements are mostly affected by the hot component, while the measurements performed during aero-braking are affected by the hydrogen cold component of the exobase.

A two-component exobase approach was employed for evaluation of the NPD data; i.e., an exobase with two hydrogen components of distinct density and temperature was assumed.

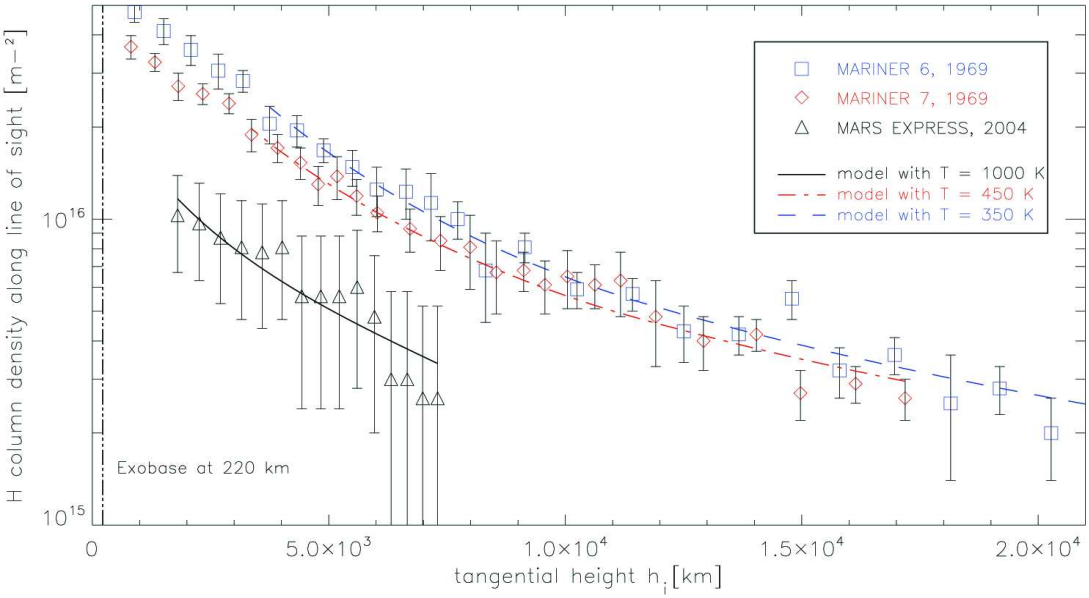

Figure 6.21: Measured column densities of neutral hydrogen (symbols) plotted against tangential height h_i. The thick lines represent modeled temperature and the exobase density. The most notable difference between the NPD measurements from 2004 (triangles) and the Mariner 6 data (rectangles) and Mariner 7 data (diamonds) is the diminished exosphere density. From *Galli et al.* (2006c).

A linear combination of two one-component models with different parameters was used. Resulted hot component remained the same as in the single component case, while a cold component was calculated to possess the exobase density $n_{H,cold} = 1.2 \times 10^{10} \mathrm{m}^{-3}$ and temperature $\mathrm{T}_{cold} = 180$ K.

A theoretical model (*Krasnopolsky*, 2002) of the Martian exosphere yields exobase densities of $n_H = 2 \times 10^{11}$ m^{-3} for a low solar activity, which is more than one order of magnitude away from the NPD observation. It is concluded that the limb emission measurement is dominated by a hydrogen component that is considerably hotter than the bulk temperature at the exobase, and the Martian hydrogen exosphere is considerably thinner than previously modeled for low solar activity (e.g., *Krasnopolsky*, 2002).

6.3.3 Energetic Hydrogen and Oxygen Atoms Observed on the Nightside of Mars

The paper by *Galli et al.* (2006a) presents measurements of hydrogen and oxygen ENAs on the nightside of Mars, performed by the NPD sensor. A global picture of the Martian ENA environment can improve our knowledge of interaction processes between the solar wind and the Martian atmosphere, as well as allowing us to infer the physical properties of the exosphere and to quantify atmospheric loss. Energy spectra of different H-ENA populations and the maps of H-ENA outflow are presented. The differential flux of H-ENAs can reach 10^5 cm^{-2}sr^{-1}s^{-1}. The global atmospheric loss rate of hydrogen and oxygen due to production of ENAs is estimated to be <1 g/s.

In this study only *H* and *O* species are considered due to their abundance and because the sensor favors detection of them. The study also attempts to distinguish between planetary and solar wind hydrogen ENAs by comparing the ENA differential intensity energy spectra

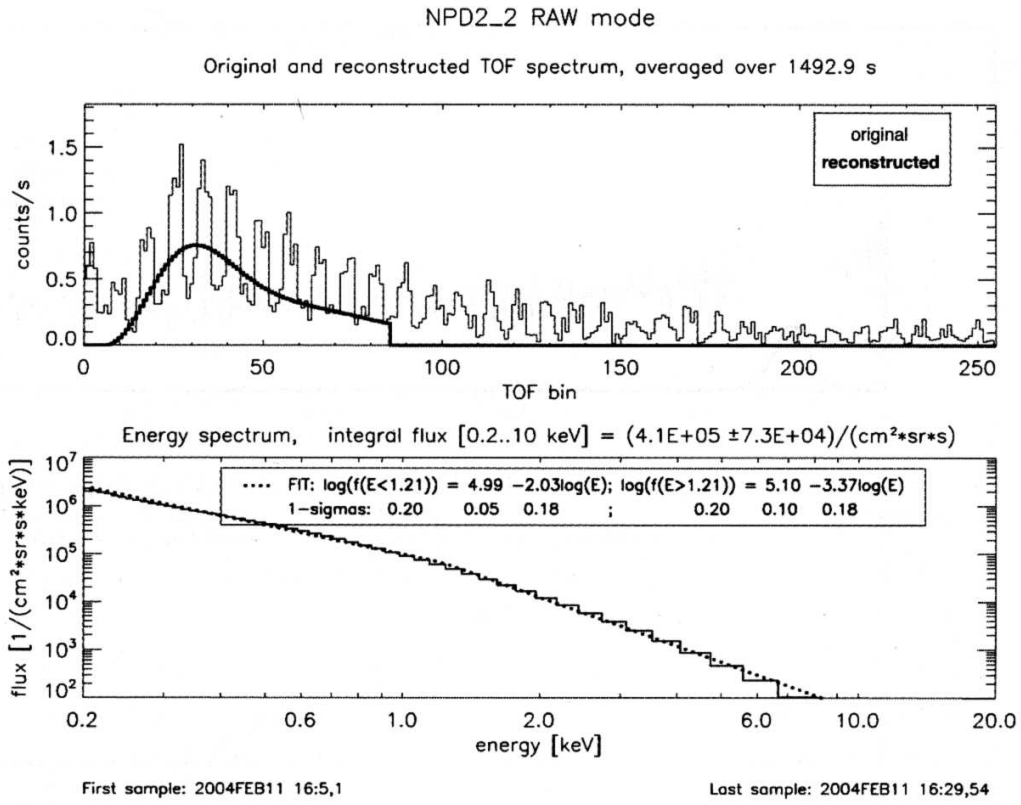

Figure 6.22: The NPD2 measurements (channel Dir2) on the nightside of Mars at the IMB, with FOV directed close to the tangential direction to the IMB surface. The measured integral intensity reaches several 10^5 $cm^{-2}sr^{-1}s^{-1}$. The measured (thin line) and the reconstructed (bold line) TOF spectrum is shown in upper panel. The lower panel shows the differential intensity energy spectrum (solid line) that corresponds to the reconstructed TOF signal, and a two-component power law distribution fit (dashed line). From *Galli et al.* (2006a).

measured in the region inside the IMB, at the IMB, in the subsolar region of Mars and in the magnetosheath region (X = -2.5 R_M).

Figure 6.22 shows the TOF and energy spectra obtained by the NPD2 sensor when the spacecraft was crossing the IMB. The position of the IMB refers to the plasma model of *Kallio et al.* (1997). Spectra of the tailward ENAs, obtained inside the IMB and at the IMB, can be approximated by two-compoinent power law with a roll-over at 1.1 keV (dashed line). The spectrum of the dayside solar wind can be parametrized by the Maxwell-Boltzmann distribution. Unfortunately, even though the energy spectrum of the nightside ENAs is much broader than that of the solar wind ENAs, it was found to be impossible to distinguish between the contributions of the solar wind and planetary protons to the typical ENA spectrum in general. The reason is that the ENA energy spectrum is a convolution of charge exchange processes along the line-of-sight intersecting several regions of varying temperature, density and flow directions. In the case of measurements in the magnetosheath (Figure 6.23), the energy spectrum has a bi-modal structure with a peak at 0.35 keV reproducible as slowed down and thermalized, neutralized solar wind with a thermal spread of 20 - 200 eV and bulk velocity < 300 km/s (dotted line in the energy spectrum). The other part is likely to be approximated by a two-component power law fit with a roll-over at 2.8 keV (dashed line). That part of the energy spectrum is concluded to be due to the planetary pick-up protons.

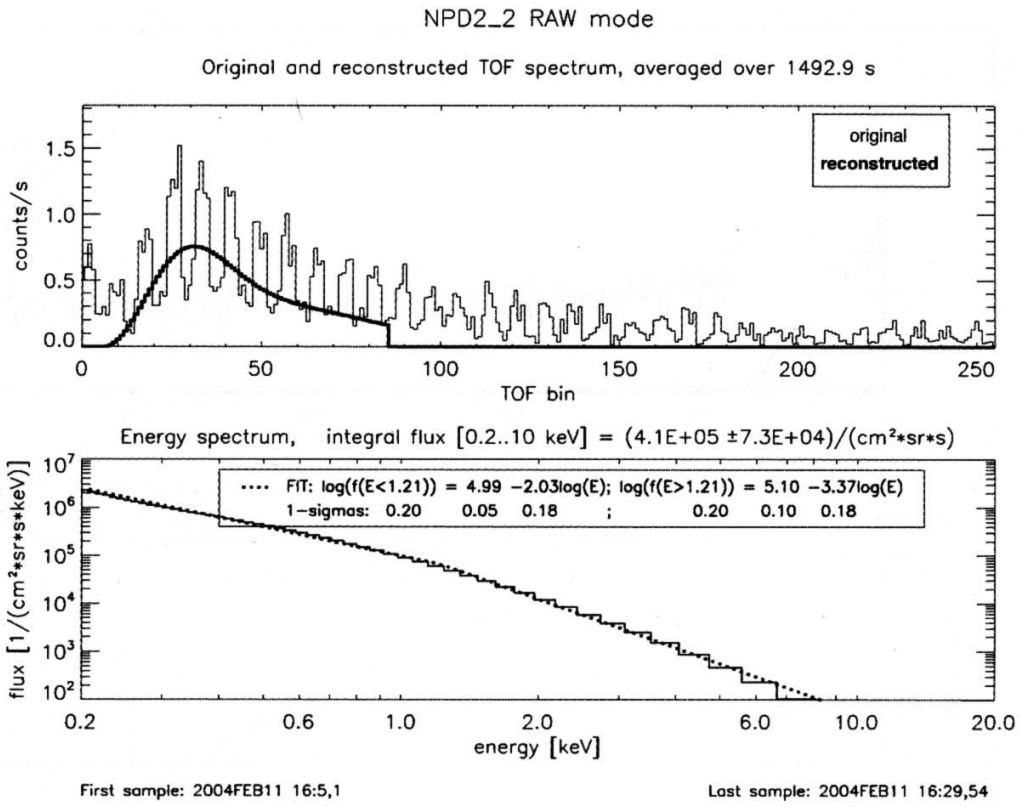

Figure 6.23: The NPD1 measurements (channel Dir2) in the magnetosheath. The measured (thin line) and the reconstructed (bold line) TOF spectrum is shown in upper panel. The lower panel shows the reconstructed differential intensity energy spectrum that corresponds to the reconstructed TOF signal. The dashed and dotted lines are fit curves for a maxwellian and a two-component power law distribution. From *Galli et al.* (2006a).

The ENA measurements were used to derive global ENA maps to be compared with theoretical models of solar wind ENAs (*Gunell et al.*, 2006) and of planetary ENAs (*Lichtenegger et al.*, 2002). The measured fluxes were found to be one or two orders of magnitude lower than the predicted ones. Such disagreement can result from the difference between the present exosphere properties and those assumed for the hydrogen exosphere models. As input parameters, the models used the hydrogen exobase density and temperature, predicted by *Krasnopolsky and Gladstone* (1996) for solar minimum, namely $n_H = 10^{12}\mathrm{m}^{-3}$ and T = 200 K. The recent UV Lyman-α limb emission measurements by ASPERA-3 / NPD indicated much thinner and hotter hydrogen exosphere (*Galli et al.*, 2006c), i.e., $n_H = 10^{10}\mathrm{m}^{-3}$ and T > 600 K. The spatial distribution and the integral intensity of the solar wind model from *Gunell et al.* (2006), being recalculated with hotter and less denser exobase, match the observations. The ENA flux intensity of a few $10^5\,\mathrm{cm}^{-2}\mathrm{sr}^{-1}\mathrm{s}^{-1}$ is consistent with solar wind ENAs. Therefore, it was concluded that the majority of the ENAs detected inside the IMB are due to the solar wind protons; the derived ENA maps give a representative image of the ENA flow at the Martian nightside for solar minimum conditions. Model calculations (*Lichtenegger et al.*, 2002) also indicate that the ratio of planetary-to-solar wind ENA fluxes should not exceed 20% at any time during the solar cycle.

Simulations predict significant oxygen ENA flow in the Martian tail (e.g., *Barabash et al.*, 2002; *Gunell et al.*, 2006). In contrast to theoretical predictions, no intense oxygen ENA signals

over the integral intensity of 2×10^4 $cm^{-2}sr^{-1}s^{-1}$ (detection limit) have been detected. This is one-two orders of magnitude lower that the simulations.

Finally, the total ENA production rates for both hydrogen and oxygen at Mars are computed to be 2-3$\times10^{24}s^{-1}$ and $<10^{22}s^{-1}$, respectively. Consequently, the corresponding atmospheric loss rate is estimated to be less than 1 g/s. It is comparable with an ion escape rate of a few g/s, as reported recently by *Barabash et al.* (2007a).

6.3.4 First ENA observations at Mars: ENA emissions from the Martian upper atmosphere

The paper by *Futaana et al.* (2006b) reports on the observations of backscattered H-ENAs (so-called ENA albedo), detected for the first time near the subsolar point of Mars. Knowledge about the particle flux and the energy flux of the backscattered ENAs provides information concerning energy and momentum transport from the solar wind into the Martian upper atmosphere. Basic characteristics of the observed ENA albedo are: H-ENAs are emitted from the broad region of Martian upper atmosphere, within solar zenith angles of 30° in the energy range of 0.2 - 2.3 keV with a peak energy of ~1.1 keV, differential flux is ~1.5 - 2.0 $\times10^6 cm^{-2}sr^{-1}s^{-1}$, energy flux is ~9.5 $\times10^9$eV $cm^{-2}s^{-1}$.

The precipitating particle flux generating this ENA albedo was estimated to be about 0.94 – 1.26$\times10^7 cm^{-2}s^{-1}$. The distribution and the energy of the ENA albedo was found to agree well with the results of a Monte-Carlo simulation by *Kallio and Barabash* (2001). The simulated flux is, however, lower by a factor of 3-4 than the detected one, likely due to different solar wind conditions, e.g., higher solar wind flux. Solar wind conditions were estimated from the IMA / ASPERA-3 *in situ* measurements in the shocked solar wind as 1.3 - 1.8 times higher than those used by *Kallio and Barabash* (2001) in simulations. At the same time the derived value could be overestimated, if the MHD shock theories are considered. The lower altitude of the IMB at Mars may also result in higher ENA albedo flux. Finally, part of the shocked solar wind protons can penetrate below the IMB due to finite gyro-radius, interact with the dense part of the exosphere and be scattered back as neutrals, contributing to the ENA albedo. It was shown that evaluation of the effects of this mechanism (also known as proton–ENA albedo) requires more precise models of the interaction between the solar wind and Mars.

The ENA albedo maps were suggested as a tool to investigate the distribution of the precipitating flux. Such maps can provide information concerning energy and momentum transport from the solar wind into the Martian upper atmosphere.

6.3.5 Direct Measurements of Energetic Neutral Hydrogen in the Interplanetary Medium

Galli et al. (2006b) reports on the NPD sensor observations of interplanetary ENAs within the energy range 200 eV to 10 keV over time range of 10 months, during the Mars Express cruise phase and also in orbit around Mars. Imaging these ENAs and deriving their energy spectra would reduce our uncertainties about the interaction of the heliosphere with the local interstellar medium. The paper also presents and discusses the energy spectra of the non-planetary ENA signal as well as the ENA flux spatial distribution.

In order to select only measurements of ENAs that have no Martian origin, observations with the NPD FOV as far as 45° away from the Martian limb are considered. Several tens of energy spectra in the data set were identified to attribute to energetic hydrogen atoms originating in the inner heliosheath. The spatial flux distribution in general supports this conclusion.

The following analysis showed that these ENAs are observed for all ecliptic longitudes with a typical flow direction between 90° and 180° away from the direction of the interstellar gas flow. The integrated ENA fluxes are found to be enhanced by a factor of two in the anti-apex direction.

The energy spectra of the detected ENAs are all very similar and are best described by a two-component power law. Figure 6.24 shows a typical energy spectrum of ENA flux of non-planetary origin. On average the energy spectra have a roll-over at E = 770 eV, a first and a second slope can be parameterized as $f(E) \sim E^{-1.61}$ and $f(E) \sim E^{-3.31}$, respectively. The ENA flux integrated over an energy range of 0.2 to 10 keV varies on a time scale of months in a range of $5{\times}10^3$ to $1.5{\times}10^5$ cm^{-2}sr^{-1}s^{-1}. The lower level of the flux intensity is defined by the detection threshold.

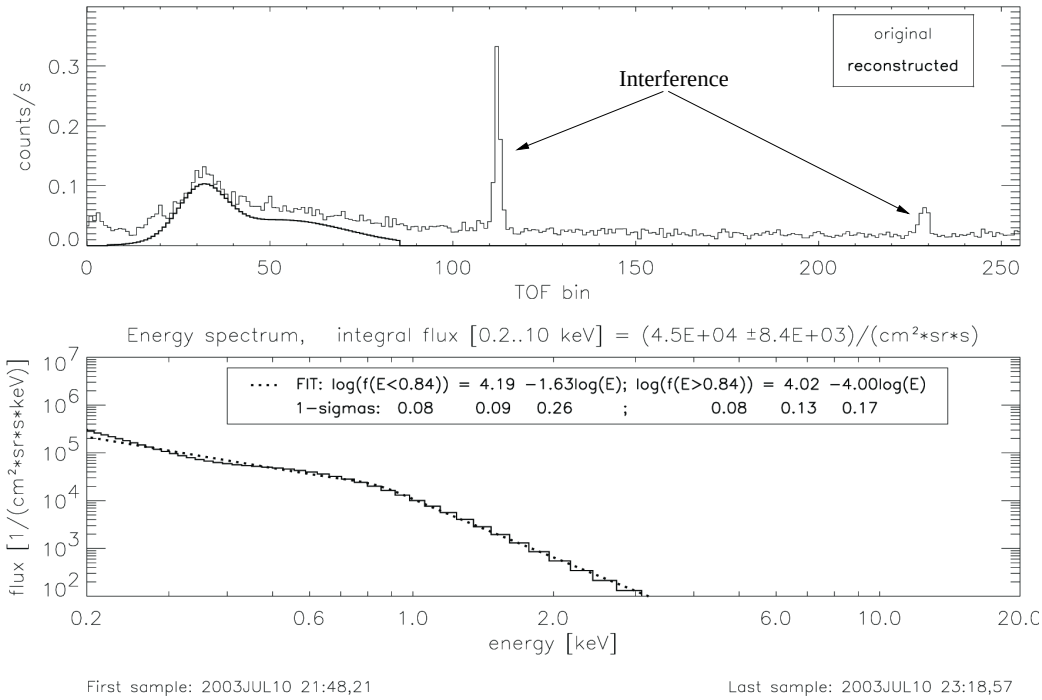

Figure 6.24: Typical example of a non-planetary ENA signal, measured during cruise phase. The top panel shows the original TOF spectrum (averaged over 86 minutes of data) and the reconstructed TOF signal after background removal and noise filtering. Narrow lines at TOF bin 112 and 229 are spikes introduced by the sensor electronics. They were removed from the TOF spectrum before further analysis. The bottom panel shows the energy spectrum calculated from the reconstructed TOF signal above, and a fit to this spectrum (dotted line). From *Galli et al.* (2006b).

Several alternative sources of the observed signal were considered. Solar wind-induced signal is ruled out, as the spectra are obtained when the NPD FOV was away from the Sun. Also, similar spectra were observed in the Martian eclipse. Planetary origin ENAs have a roll-over of the spectra above 1 keV and fluxes, reaching a few by 10^6 cm^{-2}sr^{-1}s^{-1} (see Section 6.3.3) and are, therefore, disregarded. Neutralized ions of co-rotating interaction regions (CIR) cannot be taken into account either, as the ion fluxes needed in the CIRs to account for the observed ENAs fluxes are three orders of magnitude higher than actual CIR fluxes. Signals related to UV bright stars cannot be related with these interplanetary ENAs, as the background spectra caused by UV photons are very different from the particle signal spectra, and we found no correlation

of the ENA signal with nearby UV bright stars coming into the FOV of the NPD sensor.

The similarity of the energy spectra can be due to smearing of the temporal variations in the ENA flux at the location of origin, i.e., the termination shock, by the time they arrive at Mars. The traveling time over such distances can be expected to vary from tenths of a year to several years.

6.3.6 Energetic Neutral Atoms from the Heliosheath

Wurz et al. (2006) continues analysis of the interplanetary ENA observations, reported by *Galli et al.* (2006b), following the idea of heliospheric origin of the ENA signal. Figure 6.25 shows energy spectra obtained by the NPD together with the data sets from the HENA instrument on IMAGE (*Kallenbach et al.*, 2005) and the High-Energy Suprathermal Time-of-Flight sensor (HSTOF) of the Charge Element and Isotope Analysis System (CELIAS) on the SOHO (*Hilchenbach et al.*, 1998). All three data sets showed good agreement in a comparison of energy spectra.

The ENA measurements were also compared with the theoretical heliospheric models (*McComas et al.*, 2004; *Fahr and Scherer*, 2004; *Chalov et al.*, 2003), which predict energy spectra of ENAs produced in the heliospheric interface region and travelling inward to Earth orbit. Interestingly, all these models predict ENA fluxes which are one – two orders of magnitude lower than the measured ENA fluxes. So far, none of the considered models can be chosen to describe the observed data.

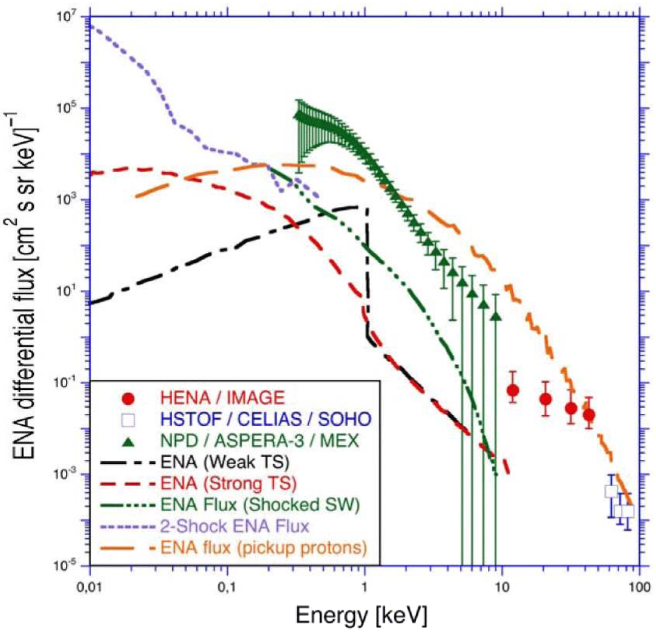

Figure 6.25: Modeled H-ENA energy spectra together with the measurements. The red dashed line and the dashed-dotted black line are from *McComas et al.* (2004) for a strong and a weak termination shock (TS), respectively; the dotted blue line is data from a two-shock model (Zank, private comm.); the dash-dot-dot-dot green line shows data from *Fahr and Scherer* (2004); and the long-dashed orange curve shows data from *Chalov et al.* (2003). Data points are from the NPD sensor of ASPERA-3 on Mars Express (green triangles), from the HENA instrument on IMAGE (red dots), and from the HSTOF sensor of the CELIAS instrument on SOHO (open squares). From *Wurz et al.* (2006).

Chapter 7

Summary and future prospects

The thesis is focused mainly on the development of NPD instrumentation. In chapter 1 it reviews the ENA basics including ENA production mechanisms and classification, and the ENA environments of Mars and Venus. It describes different ENA sources at Mars, namely neutral solar wind, shocked solar wind, accelerated planetary protons, back-scattered ENAs (ENA albedo), and sputtered atmospheric neutrals. The Venus ENA environment resembles that of Mars, though the different masses of the planets result in different scale heights. Consequently, the exospheric density profiles of the planets are different, making ENA fluxes at Venus generally lower than at Mars. NPD and NPI are the first instruments to conduct investigations of the ENA environment at Mars and Venus.

Chapter 2 describes the principles of ENA detection along with ENA detecting instrumentation. It presents different concepts to measure ENAs in different energy ranges. The new concept developed for NPD utilizes the surface interaction technique, making it possible to partially cover MENA and LENA energy ranges. The low energy detection limit of the sensor is defined as $\geqslant$100 eV because of the interaction of an incoming ENA with two surfaces.

Chapter 3 describes the ASPERA-3 and ASPERA-4 plasma and neutral particle packages, comprising the NPD sensors. Each package is a compact, highly integrated instrument including a scanner that allows sufficient coverage even on a 3-axis stabilized spacecraft platform. An internal digital processing unit provides data acquisition, preprocessing, compression, and packaging of telemetry packets.

Chapter 4 presents the NPD development process. Sensor integration, verification and testing were performed at IRF, Kiruna, Sweden. The chapter also describes the NPD mechanical design. It is important to emphasize that the sensor is of low density design in comparison with other sensors with similar characteristics, due to empty space in the field-free zone and especially in the electronics compartment. The latter can be used to accommodate a high voltage power supply internally, so the sensor can be used as a stand-alone unit for future missions. The NPD data is of a new type, requiring development of dedicated software. A quick look data display 'DVP' with a graphical user interface based on Interactive Data Language (IDL) was created. It is described in Appendix A.3.

Chapter 5 gives the calibration results for the NPD sensors. The sensors have a comparatively large geometrical factor with efficiency reaching 16% for ENAs of an energy of 6 keV. NPD is capable of distinguishing between low energy oxygen and high energy hydrogen atoms by TOF analysis only. The absence of high fluxes of high energy ($>$6 keV) O-ENAs at Mars makes this feature very important. The Start surface conditioning was shown to be not so critical.

The sensor possesses an open architecture, hence UV photon suppression is based on the Start surface coating optimization along with the TOF coincidence scheme. Eventually, the background in TOF spectra induced by UV photons leads to a decrease in the signal-to-noise ratio. However this feature can be used, and NPD can operate as a UV detector, if it is absolutely calibrated with an UV source, most promising against hydrogen Lyman-α. NPD was in-flight UV calibrated against interstellar sources and well-known Lyman-α fluxes scattered on interplanetary hydrogen. The UV photon rejection factor of the sensor was estimated to be $\sim 10^{-8}$.

Chapter 6 shows the first scientific results at Mars. For the first time several ENA sources were diagnosed, i.e., H-ENA jet/cone, back-scattered ENA (H-ENA albedo), interplanetary H-ENAs. The Martian ENA jet/cone dynamics were also investigated and jet oscillations with two different frequencies were identified. Again, due to single point measurements and the spacecraft movement, it is not possible to resolve an ambiguity whether the flux has temporal or spacial variations. To counter this, remote vantage points not affected by the spacecraft motion would be the ideal place for planetary ENA imaging on future missions. Spectra of the different ENA populations were obtained in various regions of Mars, including the subsolar region, the magnetic pile-up boundary, the magnetosheath, and the eclipse region. Martian exobase profiling was also performed using NPD as a UV detector. Correlation of the NPD measurements with ELS and IMA spectrometers data allowed us to investigate the dynamics of the entire Martian plasma environment. We confirmed that the latter is sensitive to the upstream solar wind conditions.

Finally, we summarize the main lessons learnt following the NPD design, development, operations, and data analysis. The ENA detection concept based on the surface interaction processes is well suited for neutral particle detection in an energy range partly covering the LENA and MENA regions, i.e., 100 eV – few keV. There is a very promising possibility of distinguishing between hydrogen and oxygen ENAs by means of TOF analysis only (in a certain energy range), in particular keeping in mind that no other techniques (e.g., pulse height analysis) are required. The UV photon-related count rate results in a rise of a background level in TOF spectra. Direct exposure to the Sun and Venus dayside limb saturates the Start and Stop counters. Therefore, the Sun and Venus surface avoidance techniques must be implemented to avoid a premature aging of MCPs. The scanner was not operated during the first several years of the Mars Express mission due to an unexpectedly cold environment. The drawback of this is that NPD – NPI data inter-comparison is somewhat difficult, as the NPD field-of-view plane is deflected 15° off the NPI field-of-view plane. In such a configuration both ENA sensors only pointed in the same direction when the spacecraft was changing attitude. Because of different instrument accommodation on Venus Express the ASPERA-4 scanner had to operate from the very beginning to avoid exposure to the Sun.

If making priorities for future development of an NPD-based instrument, we would emphasize the angular resolution. It can be improved down to 10° by mapping secondary electrons yielded from the Start surface to a position-sensitive detector.

Appendix A

NPD data processing

A.1 In addition to the NPD operation modes

The RAW mode. Table A.1 shows a bit allocation in a 32-bit event, generated by the DigTOF electronics in the RAW mode.

bit position	number of bits	parameter
31 : 25	7	spare
24 : 22	3	coincidence flag (COIN)
21 : 20	2	direction (DIR)
19 : 12	8	Pulse Height (PH)
11 : 0	12	TOF (0.5 ns resolution)

Table A.1: The RAW mode event bit layout.

Both the DigTOF electronics and the DPU have a 16-bit wide bus. Each 32-bit event generated in DigTOF is stored as two 16-bit values, which are composed back to 32-bit value in the DPU after data are transfered from DigTOF. A disadvantage of having a data size twice the data bus wide is possible data packet corruption during transfer from DigTOF to DPU. Each data entry is stored in a data packet sequentially, upper 16-bit, lower 16-bit word. Readout of the RAW data buffer of 512 values is carried out by the DPU through 2×512 read accesses to the respective 16-bit register of the DigTOF electronics. In total 1024 readouts are performed to obtain a data packet. There is a small probability for a read signal to be generated due to disturbances induced in the data bus, e.g., on a read-line. An additional fake read access results in a shift in the sequence of 16-bit words obtained by the DPU and consequently in the wrong data order, thus making the data packet unusable. DigTOF generates a certain hexadecimal value of '0x5555' for every read access exceeding 1024. Thus, special attention was paid to keeping the signal lines between the DPU and DigTOF clean from electromagnetic noise.

No data reduction is performed in the RAW mode because this mode was intended to be used for calibration purposes. Telemetry packets can be compressed by a lossy-less RICE algorithm in order to decrease the bit-rate. Optimization of RICE conversion during coding and decoding of telemetry packets is done in the DPU by splitting each 32-bit event into two 16-bit words, extracting certain information from the 32-bit event and forming two streams of data, according to Table A.2.

stream 1			stream 2		
bit position	number of bits	parameter	bit position	number of bits	parameter
15 : 14	2	DIR	7:0	8	PH
13 : 11	3	COIN	—	—	—
10 : 0	11	TOF (1 ns)	—	—	—

Table A.2: Structure of data streams in a telemetry packet containing RAW data is shown. Data streams are formed in order to optimize RICE (de-)compression.

The BIN mode. The TOF and pulse height of valid events are stored in compressed form in the BIN mode. Time-of-flight values are stored in logarithmically divided 16 TOF bins. Figure A.1 shows the size of the TOF bins and their location in the TOF space.

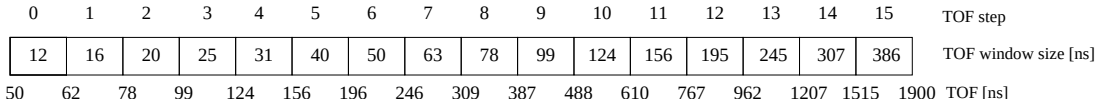

Figure A.1: TOF bins definition in the BIN mode

Pulse heights are stored in 16 linearly-divided PH bins, converted from 8-bit values to 4-bit by a 4 bit shift, i.e., scaled in 16 steps.

The data array consists of $16 \times 16 \times 3 = 768$ 16-bit counters addressed by TOF, pulse height, and direction values, respectively. Each valid event binned according to its TOF, pulse height and sector number increases by one a corresponding counter in the data array. The 16-bit counter values can be log-compressed (see Section A.2) to 8-bit values and RICE compressed by the DPU.

In order to decrease the bit-rate further, the $16_{TOF} \times 16_{PH}$ matrices can be compressed to $X_{TOF} \times Y_{PH}$ independently for each direction according to Table A.3.

Matrix No.	X	Y	interpretation
0	16	16	no compression of pulse height data
1	16	2	on board *H* and *O* discrimination
2	16	1	pulse height information is not used

Table A.3: Reduction matrices in BIN mode

The default matrix is No.=1, corresponding X=16, Y=2. In that case discrimination between *H* and *O* ENAs is done on board by the DPU. The reduction of 16 mass steps M_i to 2 is done according to the next algorithm.

$$M_i = \begin{cases} 0 & \text{if } T_i < 7 \\ 1 & \text{if } T_i > 10 \\ 0 & \text{if } 7 \leqslant T_i \leqslant 10,\ M \leqslant P \\ 1 & \text{if } 7 \leqslant T_i \leqslant 10,\ M > P \end{cases}$$

where T_i is a TOF step number, N the threshold, shows the PH channel number defined in Section 5.2.6. The principle of mass identification is discussed in Section 5.2.6.

Figure A.2 shows the algorithm graphically. The plot shows a TOF × PH matrix obtained in the BIN mode with 16 TOF steps as columns and 16 PH steps as rows.

All events outside the TOF interval 7 – 10 are treated according to their TOF values only. Events with TOF values less than 7 (more energetic) are treated as *H*, events with TOF values higher than 10 are treated as *O*. To distinguish between species within the TOF window 7 – 10 where both *H* and *O* events may occur, the PH analysis is used (see Section 5.2.6). The threshold *N*, separating areas where mostly *H* or *O* events occur, is commandable and is set separately for each direction. *N* is defined in on-ground calibrations. The calibrated thresholds are shown in Tables 5.19 and 5.36.

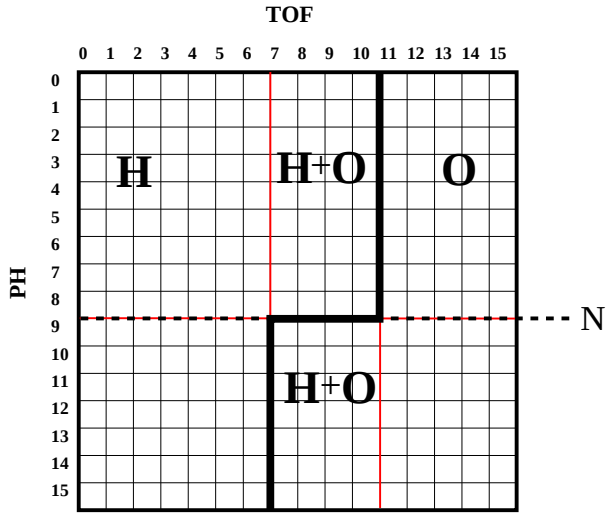

Figure A.2: PH reduction. TOF × PH matrix is shown. The black thick line separates two regions of the matrix. Events with TOF values less than 7 are treated as *H*, events with TOF values higher than 10 are treated as *O*. To distinguish between species within the TOF window 7 – 10 steps the PH analysis is used.

A.2 Log-compression algorithm

A 16-bit value can be log-compressed to 8 bits. The compressed value comprises a 4-bit exponent (*e*) and a 4-bit mantissa (*m*), and can be computed from *e* and *m* according to the following rules:

$$count = \begin{cases} m, & \text{if } e < 1 \text{ (no compression for count } \leqslant 32), \\ (m+16)\cdot 2^{e-1}, & \text{if } e \geqslant 1. \end{cases}$$

A.3 NPD data display

I wrote a quick look data display *DVP* was written by myself in IDL to display the NPD data. It is object-oriented and has a graphical user interface. Several examples of the data display window showing the NPD / ASPERA-4 data obtained in different modes are presented below. Initially, *DVP* was used to monitor the NPD status during TVAC tests. Then the program was further developed to display the NPD data obtained during flight. DVP can be used to plot not only housekeeping information (e.g., monitors of the temperature sensors, low voltages, bias HV, and a number of the NPD status registers) but even science data. Figure A.3 shows the TOF spectra and distributions, and linear counter data obtained by NPD1 in the TOF mode. Controlling buttons allow manipulation of the data files.

Figure A.4 shows the TOF and PH spectra as well as non-validated event counts (left panel) obtained by NPD1 in the RAW mode. The right panel shows the corresponding TOF and PH distributions.

Figure A.5 depicts house-keeping data obtained by NPD2 during one of the measurement sessions. The house-keeping data displayed includes several bias HV monitors, the respective HV reference settings, and the temperature profile.

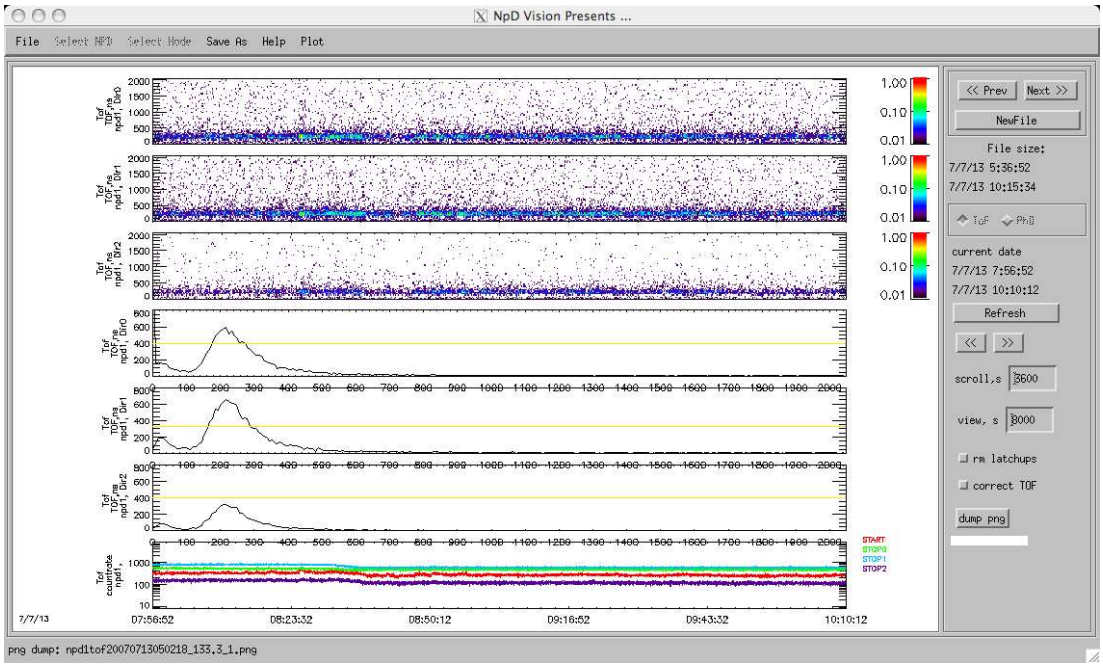

Figure A.3: DVP display. The TOF spectra and distributions obtained by the three sectors of the NPD1 (from top to bottom) in the TOF mode. The linear counter data is shown in the lower panel.

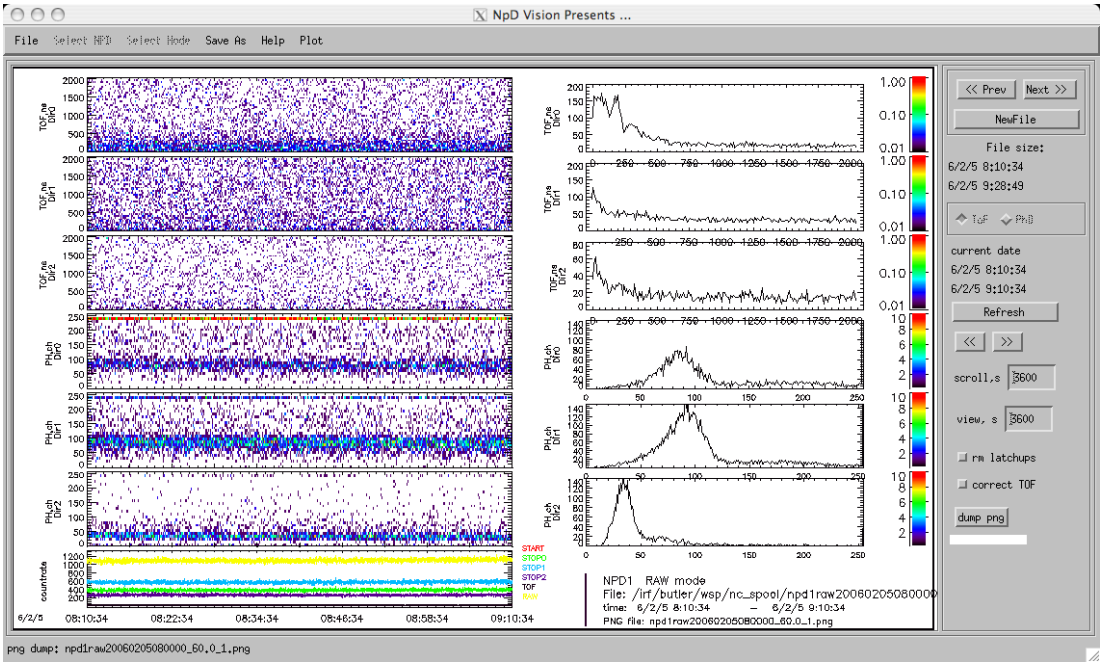

Figure A.4: DVP display. The NPD1 TOF and pulse height spectra for all three sectors (left panel from top to bottom) obtained in the RAW mode. Right panel shows the corresponding TOF and PH distributions. Lower left panel displays linear counters.

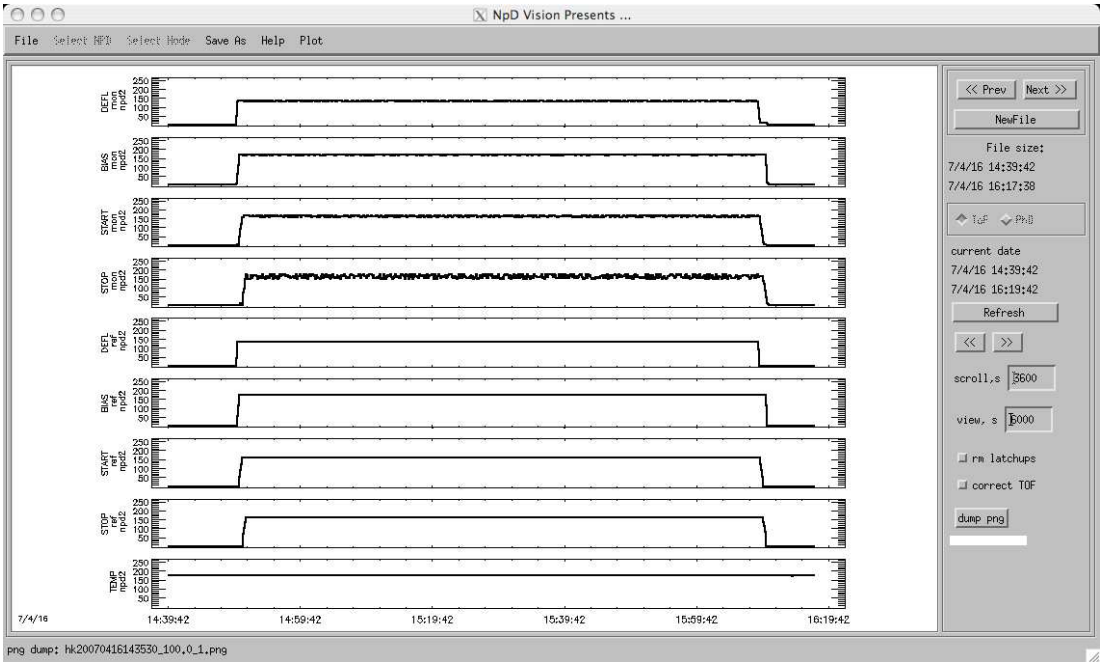

Figure A.5: DVP display. The house-keeping data collected by NPD2 during one of the measurement sessions with bias HV ramping up and down is displayed. The bias HV monitors of the deflector, Start, and Stop units are shown in the upper panels (from top to bottom). The corresponding HV references and the temperature profile are shown next.

This page is left intentionally blank

Bibliography

Bibliography

Acuña, M. H., J. E. P. Connerney, P. Wasilewski, R. P. Lin, K. A. Anderson, C. W. Carlson, J. McFadden, D. W. Curtis, D. Mitchell, H. Reme, C. Mazelle, J. A. Sauvaud, C. d'Uston, A. Cros, J. L. Medale, S. J. Bauer, P. Cloutier, M. Mayhew, D. Winterhalter, and N. F. Ness, 1998. Magnetic field and plasma observations at Mars: Initial results of the Mars Global Surveyor mission, *Science*, *279*, 1676–1680.

Amsif, A., J. Dandouras, and E. C. Roelof, 1997. Modeling the production and the imaging of energetic neutral atoms from Titan's exosphere, *J. Geophys. Res.*, *102*(A10), 22,169–22,182, doi:10.1029/97JA01597.

Anderson, D. E., and C. W. Hord, 1971. Mariner 6 and 7 ultraviolet spectrometer experiment: Analysis of hydrogen lyman-alpha data, *J. Geophys. Res.*, *76*, 6666–6673.

Barabash, S., 1995. Satellite observations of the plasma-neutral coupling near Mars and the Earth, Ph.D. thesis, Swedish Institute of Space Physics, Kiruna, Sweden.

Barabash, S., O. Norberg, R. Lundin, S. Olsen, K. Lundin, P. C. Brandt, E. C. Roelof, C. J. Chase, B. H. Mauk, H. Koskinen, and J. Rynö, 1998. Energetic neutral atom imager on the Swedish microsatellite Astrid, in *Measurement Techniques in Space Plasmas: Fields*, *Geophysical Monograph*, vol. 103, edited by R. F. Pfaff, J. E. Borovsky, and D. T. Young, pp. 257–262, AGU, Washington, DC.

Barabash, S., M. Holmström, A. Lukyanov, and E. Kallio, 2002. Energetic neutral atoms at Mars. 4. Imaging of planetary oxygen, *J. Geophys. Res.*, *107*(A10), 1280, doi: 10.1029/2001JA000326.

Barabash, S., R. Lundin, H. Andersson, J. Gimholt, M. Holmström, O. Norberg, M. Yamauchi, K. Asamura, A. J. Coates, D. R. Linder, D. O. Kataria, C. C. Curtis, K. C. Hsieh, B. R. Sandel, A. Fedorov, A. Grigoriev, E. Budnik, M. Grande, M. Carter, D. H. Reading, H. Koskinen, E. Kallio, P. Riihela, T. Säles, J. Kozyra, N. Krupp, S. Livi, J. Woch, J. Luhmann, S. McKenna-Lawlor, S. Orsini, R. Cerulli-Irelli, M. Maggi, A. Morbidini, A. Mura, A. Milillo, E. Roelof, D. Williams, J.-A. Sauvaud, J.-J. Thocaven, T. Moreau, D. Winningham, R. Frahm, J. Scherrer, J. Sharber, P. Wurz, and P. Bochsler, 2004. ASPERA-3: Analyser of space plasmas and energetic ions for Mars Express, in *Mars Express: The scientific payload*, vol. SP-1240, edited by A. Wilson, pp. 121–139, ESA Special Publication.

Barabash, S., R. Lundin, H. Andersson, K. Brinkfeldt, A. Grigoriev, H. Gunell, M. Holmström, M. Yamauchi, K. Asamura, P. Bochsler, P. Wurz, R. Cerulli-Irelli, A. Mura, A. Milillo,

M. Maggi, S. Orsini, A. J. Coates, D. R. Linder, D. O. Kataria, C. C. Curtis, K. C. Hsieh, B. R. Sandel, R. A. Frahm, J. R. Sharber, J. D. Winningham, M. Grande, E. Kallio, H. Koskinen, P. Riihelä, W. Schmidt, T. Säles, J. U. Kozyra, N. Krupp, J. Woch, S. Livi, J. G. Luhmann, S. Mckenna-Lawlor, E. C. Roelof, D. J. Williams, J.-A. Sauvaud, A. Fedorov, and J.-J. Thocaven, 2006. The Analyser of Space Plasmas and Energetic Atoms (ASPERA-3) for the Mars Express Mission, *Space Sci. Rev.*, *126*, 113–164, doi:10.1007/s11214-006-9124-8.

Barabash, S., A. Fedorov, R. Lundin, and J.-A. Sauvaud, 2007a. Martian Atmospheric Erosion Rates, *Science*, *315*(5811), 501–503, doi:10.1126/science.1134358.

Barabash, S., J.-A. Sauvaud, H. Gunell, H. Andersson, A. Grigoriev, K. Brinkfeldt, M. Holmström, R. Lundin, M. Yamauchi, K. Asamura, W. Baumjohann, T. Zhang, A. J. Coates, D. R. Linder, D. O. Kataria, C. C. Curtis, K. C. Hsieh, B. R. Sandel, A. Fedorov, C. Mazelle, J.-J. Thocaven, M. Grande, H. E. J. Koskinen, E. Kallio, T. Säles, P. Riihela, J. Kozyra, N. Krupp, J. Woch, J. Luhmann, S. McKenna-Lawlor, S. Orsini, R. Cerulli-Irelli, A. Mura, A. Milillo, M. Maggi, E. Roelof, P. Brandt, C. T. Russell, K. Szego, D. Winningham, R. A. Frahm, J. Scherrer, J. R. Sharber, P. Wurz, and P. Bochsler, 2007b. The Analyser of Space Plasmas and Energetic Atoms (ASPERA-4) for the Venus Express Mission, *Planet. Space Sci.*, doi:10.1016/j.pss.2007.01.014, in press.

Biernat, H. K., N. V. Erkaev, and C. J. Farrugia, 1999. Aspects of MHD flow about Venus, *J. Geophys. Res.*, *104*, 12,617–12,626, doi:10.1029/1999JA900032.

Biernat, H. K., N. V. Erkaev, and C. J. Farrugia, 2001. MHD effects in the Venus magnetosheath including mass loading, *Adv. Space Res.*, *28*, 833–839.

Bransden, B. H., and M. R. C. McDowell, *Charge Exchange and the Theory of Ion-Atom Collisions*, Oxford University Press, New York, 1992.

Brecht, S. H., 1997a. Solar wind proton deposition into the Martian atmosphere, *J. Geophys. Res.*, *102*(A6), 11,287–11,294.

Brecht, S. H., 1997b. Hybrid simulations of the magnetic topology of Mars, *J. Geophys. Res.*, *102*(A3), 4743–4750.

Brinkfeldt, K., P. Enoksson, M. Wieser, and S. Barabash, 2006a. Modelling of Microshutters for Space Physics Applications, *Eurosensors XX*, Göteborg, Sweden.

Brinkfeldt, K., H. Gunell, P. C. Brandt, S. Barabash, R. A. Frahm, J. D. Winningham, E. Kallio, M. Holmström, Y. Futaana, A. Ekenbäck, R. Lundin, H. Andersson, M. Yamauchi, A. Grigoriev, J. R. Sharber, J. Scherrer, A. J. Coates, D. R. Linder, D. O. Kataria, H. Koskinen, T. Säles, P. Riihela, W. Schmidt, J. Kozyra, J. Luhmann, E. Roelof, D. Williams, S. Livi, C. C. Curtis, K. C. Hsieh, B. R. Sandel, M. Grande, M. Carter, J.-A. Sauvaud, A. Fedorov, J.-J. Thocaven, S. McKenna-Lawler, S. Orsini, R. Cerulli-Irelli, M. Maggi, P. Wurz, P. Bochsler, N. Krupp, J. Woch, M. Fraenz, K. Asamura, and C. Dierker, 2006b. First ENA observations at Mars: Solar wind ENAs on the nightside, *Icarus*, *182*, 439–447.

Chalov, S. V., H. J. Fahr, and V. V. Izmodenov, 2003. Evolution of pickup proton spectra in the inner heliosheath and their diagnostics by energetic neutral atom fluxes, *J. Geophys. Res.*, *108*(A6), 1266, doi:10.1029/2002JA009492.

Chase, C. J., and E. C. Roelof, 1995. Extracting evolving structures from global magnetospheric images via model fitting and video visualization, *Johns Hopkins APL Technical Digest.*, *16*(2), 111–122.

Collier, M. R., T. E. Moore, K. W. Ogilvie, D. Chornay, J. Keller, S. Boardsen, J. Burch, B. E. Marji, M.-C. Fok, S. Fuselier, A. Ghielmetti, B. Giles, D. Hamilton, B. Peko, J. Quinn, E. Roelof, T. Stephen, G. Wilson, and P. Wurz, 2001. Observations of neutral atoms from the solar wind, *J. Geophys. Res.*, *106*, 24,893–24,906.

Crider, D. H., D. Vignes, A. M. Krymskii, T. K. Breus, N. F. Ness, D. L. Mitchell, J. A. Slavin, and M. H. Acuña, 2003. A proxy for determining solar wind dynamic pressure at Mars using Mars Global Surveyor data, *J. Geophys. Res.*, *108*(A12), 1461, doi:10.1029/2003JA009875.

Curtis, C. C., and K. C. Hsieh, 1989. Remote Sensing of Planetary Magnetospheres: Imaging via Energetic Neutral Atoms, in *Solar System Plasma Physics*, *Geophysical Monograph*, vol. 54, edited by J. H. Waite, Jr., J. L. Burch, and R. L. Moore, pp. 247–251, American Geophysical Union, Washington, DC.

Dandouras, J., and A. Amsif, 1999. Production and imaging of energetic neutral atoms from Titan's exosphere: a 3-D model, *Planet. Space Sci.*, *47*, 1355–1369.

Donahue, T. M., and R. E. Hartle, 1992. Solar cycle variations in H(+) and D(+) densities in the Venus ionosphere - Implications for escape, *Geophys. Res. Lett.*, *19*, 2449–2452.

Elphic, R., and C. Russell, 1983. Global characteristics of magnetic flux ropes in the Venus ionosphere, *J. Geophys. Res.*, *88*, 2993.

Espley, J. R., P. A. Cloutier, D. A. Brain, D. H. Crider, and M. H. Acuña, 2004. Observations of low-frequency magnetic oscillations in the Martian magnetosheath and magnetic pileup region and and tail, *J. Geophys. Res.*, *109*(A0), 7213, doi:10.1029/2003JA010193.

Fahr, H.-J., and K. Scherer, 2004. Energetic neutral atom fluxes from the heliosheath varying with the activity phase of the solar cycle, *Astrophys. Space Sci. Trans.*, *1*, 3–15.

Fedorov, A., E. Budnik, J.-A. Sauvaud, C. Mazelle, S. Barabash, R. Lundin, M. Acuña, M. Holmström, A. Grigoriev, M. Yamauchi, H. Andersson, J.-J. Thocaven, D. Winningham, R. Frahm, J. R. Sharber, J. Scherrer, A. J. Coates, D. R. Linder, D. O. Kataria, E. Kallio, H. Koskinen, T. Säles, P. Riihelä, W. Schmidt, J. Kozyra, J. Luhmann, E. Roelof, D. Williams, S. Livi, C. C. Curtis, K. C. Hsieh, B. R. Sandel, M. Grande, M. Carter, S. McKenna-Lawler, S. Orsini, R. Cerulli-Irelli, M. Maggi, P. Wurz, P. Bochsler, N. Krupp, J. Woch, M. Fränz, K. Asamura, and C. Dierker, 2006. Structure of the Martian wake, *Icarus*, *182*, 329–336, doi:10.1016/j.icarus.2005.09.021.

Fok, M.-C., T. E. Moore, M. R. Collier, and T. Tanaka, 2004. Neutral atom imaging of solar wind interaction with the Earth and Venus, *J. Geophys. Res.*, *109*(A18), 1206, doi:10.1029/2003JA010094.

Funsten, H., D. J. McComas, K. R. Moore, and E. E. Scime, 1995. Low Energy Neutral Atom Imaging Techniques for Remote Observations of the Magnetosphere, *J. Spacecraft and Rockets*, *32*, 899.

Funsten, H. O., D. J. McComas, and M. A. Gruntman, 1998. Neutral Atom Imaging: UV Rejection Techniques, in *Measurement Techniques in Space Plasmas: Fields, Geophysical Monograph*, vol. 103, edited by R. F. Pfaff, J. E. Borovsky, and D. T. Young, pp. 251–256, AGU, Washington, DC.

Futaana, Y., S. Barabash, A. Grigoriev, M. Holmström, E. Kallio, P. C:son Brandt, H. Gunell, K. Brinkfeld, R. Lundin, H. Andersson, M. Yamauchi, S. McKenna-Lawlor, J. D. Winningham, R. A. Frahm, J. R. Sharber, J. Scherrer, A. J. Coates, D. R. Linder, D. O. Kataria, T. Säles, P. Riihela, W. Schmidt, H. Koskinen, J. Kozyra, J. Luhmann, E. Roelof, D. Williams, S. Livi, C. C. Curtis, K. C. Hsieh, B. R. Sandel, M. Grande, M. Carter, J.-A. Sauvaud, A. Fedorov, J.-J. Thocaven, S. Orsini, R. Cerulli-Irelli, M. Maggi, P. Wurz, P. Bochsler, N. Krupp, J. Woch, M. Fraenz, K. Asamura, and C. Dierker, 2006a. First ENA observations at Mars: Subsolar ENA jet, *Icarus*, *182*, 413–423, doi: 10.1016/j.icarus.2005.08.024.

Futaana, Y., S. Barabash, A. Grigoriev, M. Holmström, E. Kallio, P. C:son Brandt, H. Gunell, K. Brinkfeld, R. Lundin, H. Andersson, M. Yamauchi, S. McKenna-Lawlor, J. D. Winningham, R. A. Frahm, J. R. Sharber, J. Scherrer, A. J. Coates, D. R. Linder, D. O. Kataria, T. Säles, P. Riihela, W. Schmidt, H. Koskinen, J. Kozyra, J. Luhmann, E. Roelof, D. Williams, S. Livi, C. C. Curtis, K. C. Hsieh, B. R. Sandel, M. Grande, M. Carter, J.-A. Sauvaud, A. Fedorov, J.-J. Thocaven, S. Orsini, R. Cerulli-Irelli, M. Maggi, P. Wurz, P. Bochsler, A. Galli, N. Krupp, J. Woch, M. Fraenz, K. Asamura, and C. Dierker, 2006b. First ENA observations at Mars: ENA emissions from the Martian upper atmosphere, *Icarus*, *182*, 424–430, doi:10.1016/j.icarus.2005.09.019.

Futaana, Y., S. Barabash, A. Grigoriev, D. Winningham, R. Frahm, and R. Lundin, 2006c. Global Response of Martian Plasma Environment to an Interplanetary Structure: From ENA and Plasma Observations at Mars, *Space Sci. Rev.*, *126*, 315–332, doi:10.1007/s11214-006-9026-9.

Galli, A., P. Wurz, S. Barabash, A. Grigoriev, H. Gunell, R. Lundin, M. Holmström, and A. Fedorov, 2006a. Energetic Hydrogen and Oxygen Atoms Observed on the Nightside of Mars, *Space Sci. Rev.*, *126*, 267–297, doi:10.1007/s11214-006-9088-8.

Galli, A., P. Wurz, S. Barabash, A. Grigoriev, R. Lundin, Y. Futaana, H. Gunell, M. Holmström, E. C. Roelof, C. C. Curtis, K. C. Hsieh, A. Fedorov, D. Winningham, R. A. Frahm, R. Cerulli-Irelli, P. Bochsler, N. Krupp, J. Woch, and M. Fraenz, 2006b. Direct Measurements of Energetic Neutral Hydrogen in the Interplanetary Medium, *Astrophys. J.*, *644*, 1317–1325, doi:10.1086/503765.

Galli, A., P. Wurz, H. Lammer, H. I. M. Lichtenegger, R. Lundin, S. Barabash, A. Grigoriev, M. Holmström, and H. Gunell, 2006c. The Hydrogen Exospheric Density Profile Measured with ASPERA-3/NPD, *Space Sci. Rev.*, *126*, 447–467, doi:10.1007/s11214-006-9089-7.

Grande, M., 1997. Investigation of magnetospheric interactions with the Hermean surface, *Adv. Space Res.*, *19*(10), 1609–1614, doi:10.1016/S0273-1177(97)00374-8.

Grigoriev, A., Y. Futaana, S. Barabash, and A. Fedorov, 2006. Observations of the Martian Subsolar ENA Jet Oscillations, *Space Sci. Rev.*, *126*, 299–313, doi:10.1007/s11214-006-9121-y.

Gruntman, M., 1993. A new technique for *in situ* measurement of the composition of neutral gas in interplanetary space, *Planet. Space Sci.*, *41*(4), 307–319.

Gruntman, M., 1997. Energetic neutral atom imaging of space plasmas, *Rev. Sci. Instrum.*, *68(10)*, 3617–3656.

Gunell, H., M. Holmström, H. K. Biernat, and N. V. Erkaev, 2005. Planetary ENA Imaging: Venus and a comparison with Mars, *Planet. Space Sci.*, *53*, 433–441, doi: 10.1016/j.pss.2004.07.021.

Gunell, H., M. Holmström, S. Barabash, E. Kallio, P. Janhunen, A. F. Nagy, and Y. Ma, 2006. Planetary ENA imaging: Effects of different interaction models for Mars, *Planet. Space Sci.*, *54*, 117–131, doi:10.1016/j.pss.2005.04.002.

Hilchenbach, M., K. C. Hsieh, D. Hovestadt, B. Klecker, H. Gruenwaldt, P. Bochsler, F. M. Ipavich, A. Buergi, E. Moebius, F. Gliem, W. I. Axford, H. Balsiger, W. Bornemann, M. A. Coplan, A. B. Galvin, J. Geiss, G. Gloeckler, S. Hefti, D. L. Judge, R. Kallenbach, P. Laeverenz, M. A. Lee, S. Livi, G. G. Managadze, E. Marsch, M. Neugebauer, H. S. Ogawa, K.-U. Reiche, M. Scholer, M. I. Verigin, B. Wilken, and P. Wurz, 1998. Detection of 55-80 keV Hydrogen Atoms of Heliospheric Origin by CELIAS/HSTOF on SOHO, *Astrophys. J.*, *503*, 916–921, doi:10.1086/306022.

Holmström, M., 2006. Asymmetries in Mars' Exosphere: Implications for X-ray and ENA Imaging, *Space Sci. Rev.*, *126*, 435–445, doi:10.1007/s11214-006-9036-7.

Holmström, M., S. Barabash, and E. Kallio, 2002. Energetic neutral atoms at Mars. 1. Imaging of solar wind protons, *J. Geophys. Res.*, *107*(A10), 1277, doi:10.1029/2001JA000325.

Hsieh, K. C., B. R. Sandel, V. A. Drake, and R. S. King, 1991. H Lyman-α transmittance of thin C and Si/C foils for keV particle detectors, *Nuclear Instruments and Methods in Physics Research B*, *61*, 187–193, doi:10.1016/0168-583X(91)95460-U.

Jans, S., Ionization of energetic neutral atoms for application in space instrumentation, Diplomarbeit, Universität Bern, 2000.

Johnstone, A. D., Alsop, C., Burge, S., Carter, P. J., Coates, A. J., Coker, A. J., Fazakerley, A. N., Grande, M., Gowen, R. A., Gurgiolo, C., Hancock, B. K., Narheim, B., Preece, A., Sheather, P. H., Winningham, J. D., Woodliffe, and R. D., 1997. PEACE: a Plasma Electron and Current Experiment, *Space Sci. Rev.*, *79*, 351–398.

Kallenbach, R., M. Hilchenbach, S. V. Chalov, J. A. Le Roux, and K. Bamert, 2005. On the "injection problem" at the solar wind termination shock, *Astron. & Astrophys.*, *439*, 1–22, doi:10.1051/0004-6361:20052874.

Kallio, E., 1996. An empirical model of the solar wind flow around Mars, *J. Geophys. Res.*, *101*(A5), 11,133–11,147.

Kallio, E., and S. Barabash, 2000. On the elastic and inelastic collisions between precipitating energetic hydrogen atoms and Martian atmospheric neutrals, *J. Geophys. Res.*, *105*(A11), 24,973–24,996, doi:10.1029/2000JA900077.

Kallio, E., and S. Barabash, 2001. Atmospheric effects of precipitating energetic hydrogen atoms on the Martian atmosphere, *J. Geophys. Res.*, *106*(A1), 165–177, doi: 10.1029/2000JA002003.

Kallio, E., and P. Janhunen, 2001. Atmospheric effects of proton precipitation in the Martian atmosphere and its connection to the Mars–solar wind interaction, *J. Geophys. Res.*, *106*(A4), 5617–5634, doi:10.1029/2000JA000239.

Kallio, E., and P. Janhunen, 2002. Ion escape from Mars in a quasi-neutral hybrid model, *J. Geophys. Res.*, *107*(A3), 1035, doi:10.1029/2001JA000090.

Kallio, E., J. G. Luhmann, and S. Barabash, 1997. Charge exchange near Mars: The solar wind absorption and energetic neutral atom production, *J. Geophys. Res.*, *102*(A10), 22,183–22,197, doi:10.1029/97JA01662.

Kallio, E., S. Barabash, K. Brinkfeldt, H. Gunell, M. Holmström, Y. Futaana, W. Schmidt, T. Säles, H, Koskinen, P. Riihelä, R. Lundin, H. Andersson, M. Yamauchi, A. Grigoriev, J. D. Winningham, R. A. Frahm, J. R. Sharber, J. Scherrer, A. J. Coates, D. R. Linder, D. O. Kataria, J. Kozyra, J. G. Luhmann, E. Roelof, D. Williams, S. Livi, P. C. Brandt, C. C. Curtis, K. Hsieh, B. R. Sandel, M. Grande, M. Carter, J.-A. Sauvaud, A. Fedorov, J.-J. Thocaven, S. McKenna-Lawler, S. Orsini, R. Cerulli-Irelli, M. Maggi, P. Wurz, P. Bochsler, N. Krupp, J. Woch, M. Fränz, K. Asamura, and C. Dierker, 2006. Energetic neutral atoms (ENA) at Mars: Properties of the hydrogen atoms produced upstream of the Martian bow shock and implications for ENA sounding technique around non-magnetized planets, *Icarus*, *182*, 448–463.

Kass, D. M., 1999. Change in the Martian Atmosphere, Ph.D. thesis, California Institute of Technology, California, United States.

Krasnopolsky, V. A., 2002. Mars' upper atmosphere and ionosphere at low, medium, and high solar activities: Implications for evolution of water, *J. Geophys. Res.*, *107*(E12), 5128, doi:10.1029/2001JE001809.

Krasnopolsky, V. A., and G. R. Gladstone, 1996. Helium on Mars : EUVE and PHOBOS data and implications for Mars' evolution, *J. Geophys. Res.*, *101*(A7), 15,765–15,772.

Lichtenegger, H., H. Lammer, and W. Stumptner, 2002. Energetic neutral atoms at Mars. 3. Flux and energy distributions of planetary energetic H atoms, *J. Geophys. Res.*, *107*(A10), 1279, doi:10.1029/2001JA000322.

Lichtenegger, H. I. M., H. Lammer, Y. N. Kulikov, S. Kazeminejad, G. H. Molina-Cuberos, R. Rodrigo, B. Kazeminejad, and G. Kirchengast, 2006. Effects of Low and High Energetic Neutral Atoms on Martian and Venusian Dayside Exospheric Temperature Estimations, *Space Sci. Rev.*, *126*, 469–501, doi:10.1007/s11214-006-9082-1.

Luhmann, J. G., 1992. Comparative studies of the solar wind interaction with weakly magnetized planets, *Advances in Space Research*, *12*, 191–203, doi:10.1016/0273-1177(92)90331-Q.

Luhmann, J. G., and J. U. Kozyra, 1991. Dayside pickup oxygen ion precipitation at Venus and Mars: Spatial distributions, energy deposition and consequences, *J. Geophys. Res.*, *96*(A4), 5457–5467.

Lukyanov, A., S. Barabash, and M. Holmström, 2004. Energetic neutral atom imaging at Mercury, *Adv. Space Res.*, *33*, 1890–1898, doi:10.1016/j.asr.2003.05.035.

Lundin, R., A. Zakharov, R. Pellinen, H. Borg, B. Hultqvist, N. Pissarenko, E. M. Dubinin, S. W. Barabash, I. Liede, and H. Koskinen, 1989. First measurements of the ionospheric plasma escape from Mars, *Nature*, *341*, 609–612.

Lundin, R., S. Barabash, H. Andersson, M. Holmström, A. Grigoriev, M. Yamauchi, J.-A. Sauvaud, A. Fedorov, E. Budnik, J.-J. Thocaven, D. Winningham, R. Frahm, J. Scherrer, J. Sharber, K. Asamura, H. Hayakawa, A. Coates, D. R. Linder, C. Curtis, K. C. Hsieh, B. R. Sandel, M. Grande, M. Carter, D. H. Reading, H. Koskinen, E. Kallio, P. Riihela, W. Schmidt, T. Säles, J. Kozyra, N. Krupp, J. Woch, J. Luhmann, S. McKenna-Lawler, R. Cerulli-Irelli, S. Orsini, M. Maggi, A. Mura, A. Milillo, E. Roelof, D. Williams, S. Livi, P. Brandt, P. Wurz, and P. Bochsler, 2004. Solar wind-induced atmospheric erosion at Mars: First results from ASPERA-3 on Mars Express, *Science*, *305*, 1933–1936, doi:DOI: 10.1126/science.1101860.

Ma, Y., A. F. Nagy, K. C. Hansen, D. L. DeZeeuw, T. I. Gombosi, and K. G. Powell, 2002. Three-dimensional multispecies MHD studies of the solar wind interaction with Mars in the presence of crustal fields, *J. Geophys. Res.*, *107*(A10), 1282, doi:10.1029/2002JA009293.

Massetti, S., S. Orsini, A. Milillo, A. Mura, E. de Angelis, H. Lammer, and P. Wurz, 2003. Mapping of the cusp plasma precipitation on the surface of Mercury, *Icarus*, *166*, 229–237, doi:10.1016/j.icarus.2003.08.005.

McComas, D., F. Allegrini, P. Bochsler, M. Bzowski, M. Collier, H. Fahr, H. Fichtner, P. Frisch, H. Funsten, S. Fuselier, G. Gloeckler, M. Gruntman, V. Izmodenov, P. Knappenberger, M. Lee, S. Livi, D. Mitchell, E. Möbius, T. Moore, D. Reisenfeld, E. Roelof, N. Schwadron, M. Wieser, M. Witte, P. Wurz, and G. Zank, 2004. The Interstellar Boundary Explorer (IBEX), in *Physics of the Outer Heliosphere*, *American Institute of Physics Conference Series*, vol. 719, edited by V. Florinski, N. V. Pogorelov, and G. P. Zank, pp. 162–181, AIP Conference Proceedings, doi:10.1063/1.1809514.

McComas, D. J., B. L. Barraclough, R. C. Elphic, H. O. Funsten III, and M. F. Thomsen, 1991. Magnetospheric imaging with low-energy neutral atoms, in *Proceedings of the National Academy of Sciences*, vol. 88, pp. 9598–9602.

McComas, D. J., H. O. Funsten, and E. E. Scime, 1998. Advances in Low Energy Neutral Atom Imaging, in *Measurement Techniques in Space Plasmas: Fields*, *Geophysical Monograph*, vol. 103, edited by R. F. Pfaff, J. E. Borovsky, and D. T. Young, pp. 275–280, AGU, Washington, DC.

McEntire, R. W., and D. G. Mitchell, 1989. Instrumentation for Global Magnetospheric Imaging via Energetic Neutral Atoms, in *Solar System Plasma Physics*, edited by J. H. Waite, Jr., J. L. Burch, and R. L. Moore, 54, pp. 69–80.

Mitchell, D. G., S. M. Krimigis, A. F. Cheng, S. E. Jaskulek, E. P. Keath, B. H. Mauk, R. W. McEntire, E. C. Roelof, C. E. Schlemm, B. E. Tossman, and D. J. Williams, 1998. The Imaging Neutral Camera for the Cassini Mission to Saturn and Titan, in *Measurement Techniques in Space Plasmas: Fields*, *Geophysical Monograph*, vol. 103, edited by R. F. Pfaff, J. E. Borovsky, and D. T. Young, pp. 281–287, AGU, Washington, DC.

Mitchell, D. G., S. E. Jaskulek, C. E. Schlemm, E. P. Keath, R. E. Thompson, B. E. Tossman, J. D. Boldt, J. R. Hayes, G. B. Andrews, N. Paschalidis, D. C. Hamilton, R. A. Lundgren, E. O. Tums, P. Wilson IV, H. D. Voss, D. Prentice, K. C. Hsieh, C. C. Curtis, and F. R. Powell, 2000. High Energy Neutral Atom (HENA) Imager for the IMAGE Mission, *Space Sci. Rev.*, *91*(1-2), 67–112.

Moore, T. E., D. J. Chornay, M. R. Collier, F. A. Herrero, J. Johnson, M. A. Johnson, J. W. Keller, J. F. Laudadio, J. F. Lobell, K. W. Ogilvie, P. Rozmarynowski, S. A. Fuselier, A. G. Ghielmetti, E. Hertzberg, D. C. Hamilton, R. Lundgren, P. Wilson, P. Walpole, T. M. Stephen, B. L. Peko, B. Van Zyl, P. Wurz, J. M. Quinn, and G. R. Wilson, 2000. The Low Energy Neutral Atom Imager for IMAGE, *Space Sci. Rev.*, *91*(1-2), 155–195.

Norberg, O., M. Yamauchi, R. Lundin, S. Olsen, H. Borg, S. Barabash, M. Hirahara, T. Mukai, and H. Hayakawa, 1998. The Ion Mass Imager on the Planet-B spacecraft, *Earth, Planets, and Space*, *50*, 199–205.

Penz, T., N. Erkaev, H. Biernat, H. Lammer, U. Amerstorfer, H. Gunell, E. Kallio, S. Barabash, S. Orsini, A. Milillo, and W. Baumjohann, 2004. Ion loss on Mars caused by the Kelvin-Helmholtz instability, *Planet. Space Sci.*, *52*, 1157–1167, doi:10.1016/j.pss.2004.06.001.

Perez, J. D., M.-C. Fok, and T. E. Moore, 2000. Deconvolution of Energetic Neutral Atom Images of the Earth's Magnetosphere, *Space Sci. Rev.*, *91*, 421–436.

Pollock, C. J., K. Asamura, J. Baldonado, M. M. Balkey, P. Barker, J. L. Burch, E. J. Korpela, J. Cravens, G. Dirks, M.-C. Fok, H. O. Funsten, M. Grande, M. Gruntman, J. Hanley, J.-M. Jahn, M. Jenkins, M. Lampton, M. Marckwordt, D. J. McComas, T. Mukai, G. Penegor, S. Pope, S. Ritzau, M. L. Schattenburg, E. Scime, R. Skoug, W. Spurgeon, T. Stecklein, S. Storms, C. Urdiales, P. Valek, J. T. M. van Beek, S. E. Weidner, M. Wüest, M. K. Young, and C. Zinsmeyer, 2000. Medium Energy Neutral Atom (MENA) Imager for the IMAGE Mission, *Space Sci. Rev.*, *91*(1-2), 113–154.

Roelof, E. C., and A. J. Skinner, 2000. Extraction of ion distributions from magnetospheric ENA and EUV images, *Space Sci. Rev.*, *91*, 437–459.

Rosenbauer, H., N. Shutte, A. Galeev, K. Gringauz, and I. Apathy, 1989. Ions of Martian origin and plasma sheet in the Martian magnetosphere - Initial results of the TAUS experiment, *Nature*, *341*, 612–614, doi:10.1038/341612a0.

Russell, C., and R. Elphic, 1979. Observation of magnetic flux ropes in the Venus ionosphere, *Nature*, *279*, 618–620.

Tanaka, T., and K. Murawski, 1997. Three-dimensional MHD simulation of the solar wind interaction with the ionosphere of Venus: Results of two-component reacting plasma simulation, *J. Geophys. Res.*, *102*(A9), 19,805–19,821.

Vignes, D., C. Mazelle, H. Rème, M. H. Acuña, J. E. P. Connerney, R. P. Lin, D. L. Mitchell, P. Cloutier, D. H. Crider, and N. F. Ness, 2000. The solar wind interaction with Mars: locations and shapes of the Bow Shock and the Magnetic Pile-up Boundary from the observations of the MAG/ER experiment on board Mars Global Surveyor, *Geophys. Res. Lett.*, *27*(1), 49–52, doi:10.1029/1999GL010703.

Vignes, D., M. Acuña, J. Connerney, D. Crider, H. Rème, and C. Mazelle, 2004. Magnetic Flux Ropes in the Martian Atmosphere: Global Characteristics, *Space Sci. Rev.*, *111*, 223–231, doi:10.1023/B:SPAC.0000032716.21619.f2.

Wieser, M., S. Barabash, M. Emanuelsson, K. Brinkfeldt, and P. Enoksson, 2006. Micromechanical shutter based mass spectrometers for charged and neutral particles, in *Proceedings Book of the International Conference on Future Perspectives of Space Plasma and Particle Instrumentation and International Collaborations*, Rikkyo, Japan.

Williams, D. J., E. C. Roelof, and D. G. Mitchell, 1992. Global magnetospheric imaging, *Reviews of Geophysics*, *30*(3), 183–208.

Winningham, J. D., R. A. Frahm, J. R. Sharber, A. J. Coates, D. R. Linder, Y. Soobiah, E. Kallio, J. R. Espley, R. Lundin, S. Barabash, M. Holmström, H. Andersson, M. Yamauchi, A. Grigoriev, J. R. Scherrer, S. J. Jeffers, D. O. Kataria, J. Kozyra, J. Luhmann, E. Roelof, D. Williams, S. Livi, C. C. Curtis, K. C. Hsieh, B. R. Sandel, H. Koskinen, T. Säles, P. Riihela, W. Schmidt, M. Grande, M. Carter, J.-A. Sauvaud, A. Fedorov, J.-J. Thocaven, S. McKenna-Lawler, S. Orsini, R. Cerulli-Irelli, M. Maggi, P. Wurz, P. Bochsler, N. Krupp, J. Woch, M. Fraenz, K. Asamura, and C. Dierker, 2006. Electron oscillations in the induced Martian magnetosphere, *Icarus*, *182*, 360–370, doi:10.1016/j.icarus.2005.10.033.

Witte, M., H. Rosenbauer, E. Keppler, H. Fahr, P. Hemmerich, H. Lauche, A. Loidl, and R. Zwick, 1992. The interstellar neutral-gas experiment on ULYSSES, *Astron. Astrophys. Suppl. Ser.*, *92*, 333–348.

Wiza, J. L., 1979. Microchannel plate detectors, *Nuclear Instruments & Methods*, *162*, 587–601.

Wurz, P., 2000. Detection of energetic neutral atoms, in *The Outer Heliosphere: Beyond the Planets*, edited by K. Scherer, H. Fichtner, and E. Marsch, pp. 251–288, Copernicus-Gesellschaft, Katlenburg-Lindau, Germany.

Wurz, P., and H. Lammer, 2003. Monte-Carlo simulation of Mercury's exosphere, *Icarus*, *164 (1)*, 1–13.

Wurz, P., A. Galli, S. Barabash, and A. Grigoriev, 2006. Energetic Neutral Atoms from the Heliosheath, in *Physics of the Inner Heliosheath, American Institute of Physics Conference Series*, vol. 858, edited by J. Heerikhuisen, V. Florinski, G. P. Zank, and N. V. Pogorelov, pp. 269–275, AIP Conference Proceedings, doi:10.1063/1.2359338.

Ziegler, J. F., J. P. Biersack, and U. Littmark, *The Stopping and Range of Ions in Solids*, Pergamon Press, New York, 1985.

Glossary of Acronyms

1D	one-dimensional
2D	two-dimensional
AIV	assembly, integration, and verification
ADC	Analog-to-Digit Converter
ASPERA	Analyzer of Space Plasma and EneRgetic Atoms
AU	Astronomical Unit
BS	Bow Shock
CELIAS	Charge, Element, and Isotope Analysis System
CEM	Channel Electron Multiplier
CIR	Co-rotating Interaction Region
DAC	Digit-to-Analog Converter
DC	Direct current
DigTOF	Digital Time-of-Flight electronics
DPU	Digital Processing Unit
EEPROM	Electrically Erasable Programmable Read Only Memory
ELS	ELectron Spectrometer
EMC	Electromagnetic compatibility
ENA	Energetic neutral atom
ESA	European Space Agency
EUV	Extreme Ultra Violet
FEE	Front-end Electronics
FOV	Field-of-View
FPGA	Field Programmable Gate Array
FWHM	Full Width at Half Maximum
HENA	High-energy neutral atoms
HK	Housekeeping
HSTOF	High-Energy Suprathermal Time-of-Flight
HV	High Voltage
HV PS	High Voltage Power Supply
IDL	Interactive Data Language
IMA	Ion Mass Analyzer
IMAGE	Imager for Magnetopause-to-Aurora Global Exploration
IMB	Induced magnetosphere boundary
IMF	Interplanetary magnetic field
IMI	Ion Mass Imager
IP	Ionopause
LENA	Low-energy neutral atoms
LOS	Line-of-Sight
MCP	MicroChannel Plate
MEMS	Micro-Electro-Mechanical System
MENA	Medium-energy neutral atoms
MGS	Mars Global Surveyor
MHD	Magnetohydrodynamics
MLI	Multi-layer insulation
MOS FET	Metal-Oxide-Semiconductor Field-Effect Transistor
MPB	Magnetic Pile-up Boundary
MSO	Mars-Sun orbit
NPI	Neutral Particle Imager
NPD	Neutral Particle Detector
NSW	Neutral Solar Wind
OSR	Optical secondary reflection
PIPPI	Prelude In Planetary Particle Imaging
PH	Pulse Height
SEY	Secondary Electron Yield
SOHO	Solar and Heliospheric Observatory
SRAM	Static Random Access memory
SRIM	Stopping and Range of Ions in Matter
SWAN	Solar Wind Anisotropies
SZA	Solar Zenith Angle
TC	Telecommand
TDC	Time-to-Digit Converter
TOF	Time-of-Flight
TS	Termination Shock
TVAC	Termo-vacuum
UV	Ultra Violet
VLENA	Very low-energy neutral atoms

Acknowledgments

First of all I express my sincere gratitude to my supervisor Professor Stas Barabash, for his support, continuous guidance, and criticism during the ASPERA-3 and ASPERA-4 projects, and for his inexhaustible patience during the writing phase of this dissertation. I appreciate highly his vast knowledge, expertise, and understanding which added considerably to my graduate experience.

I am deeply indebted to Andrei Fedorov who introduced me to and made me interested in the fields of space plasma physics and experimental science.

I thank Mats Holmström, Tima Sergienko, Martin Wieser, and Masatoshi Yamauchi for scientific support which helped enrich my experience. Special thanks go to Futaana Yoshifumi, who supported me with advanced knowledge on how to write and revise a scientific paper.

I am very grateful to Rick McGregor for the uphill work of proof-reading this thesis.

I would also like to thank the Swedish National Graduate School of Space Technology which provided financial support.

I thank the electronics lab staff involved in development, building and verification of the NPD sensors. Thanks also to the IRF workshop which manufactured different parts of the NPD sensor, and especially to Tero Saarijärvi for performing the tough job of making tens of holes with a thread for M1.2 screws in several NPD chassis.

I acknowledge the ASPERA team for making it possible to build the NPD instruments.

I am grateful to Leif Kalla for advice on software development, and to Grigory Nikulin for fruitful discussions about IDL tricks.

I am very thankful to my wife Daria whose love, patience, moral support, and editing assistance have sustained me, particularly in those many days in which I spent more time with my computer than with my family. I am in debt to my parents for their understanding, unending patience and encouragement when it was most required.

Finally, I say thank you to all colleagues and friends of mine at IRF in Kiruna for keeping a friendly work environment here.